Title

Mapping whole-brain inhibitory circuit reorganization and repair after brain injury

Author

Frankowski, Jan Christopher

Publication Date

2021

UNIVERSITY OF CALIFORNIA,
IRVINE

Mapping whole-brain inhibitory circuit reorganization and repair after brain injury

DISSERTATION

submitted in partial satisfaction of the requirements
for the degree of

DOCTOR OF PHILOSOPHY

in Biological Sciences

by

Jan Christopher Frankowski

Dissertation Committee:
Professor Robert F. Hunt, Chair
Professor Vijayalakshmi Santhakumar
Professor Andre Obenaus
Professor David C. Lyon

2021

DEDICATION

Do mojego ojca, Roman:

Tęsknię za tobą tato. Wiem że byłbys dumy.

Do mojej mamy, Ania:

Dziekuje za wszystko. Jestes najlepsza mama na swiecie.

TABLE OF CONTENTS

LIST OF FIGURES

LIST OF ABBREVIATIONS

3DISCO – three dimensional imaging of solvent cleared organs
AAV – adeno-associated virus
ACAd – anterior cingulate area, dorsal part
ACAv – anterior cingulate area, ventral part
ATP – adenosine triphosphate
BBB – blood-brain barrier
CA1 – cornu ammonis 1
CA3 – cornu ammonis 3
CCI – controlled cortical impact
CCK – cholecystokinin
CGE – Caudal ganglionic eminence
CHAPS – (3-((3-cholamidopropyl) dimethylammonio)-1-propanesulfonate)
CHAT – choline acetyltransferase
CLARITY – cleared lipid-extracted acryl-hybridized rigid immunostaining/in situ hybridization-compatible tissue hydrogel
CNS – central nervous system
CR – calretinin
CS – superior central nucleus raphae
DG – dentate gyrus
DNA – deoxyribonucleic acid
ENTl – lateral entorhinal cortex
ENTm – medial entorhinal cortex
EnvA - envelope protein of the subgroup A avian sarcoma and leukosis virus
FLEX – flip excision switch
fMRI – functional magnetic resonance imaging
GABA – gamma aminobutyric acid
GAD65 - Glutamate decarboxylase 65
GAD67 – Glutamate decarboxylase 67
GCL – granule cell layer
GFP – green fluorescent protein
hSYN – human synapsin
iDISCO – immunolabeling of three dimensional solvent cleared organs
ILA – infralimbic area
LGE – lateral ganglionic eminence
MA – magnocellular nucleus
MDEA – n-methyldiethanolamine
MGE – medial ganglionic eminence
ML – molecular layer
MOs – secondary motor area
MS – medial septal nucleus
MuVi SPIM – multi-view single-plane illumination microscope

NDB – diagonal band nucleus
nNOS – neuronal nitric oxide synthase
NPY – neuropeptite Y
oG – optimized rabies glycoprotein
ORBl – orbital area, lateral part
ORBm – orbital area, medial part
ORBvl – orbital area, ventrolateral part
PER – perirhinal area
PFA – paraformaldehyde
PFC – prefrontal cortex
PL – prelimbic area
PV – parvalbumin
RNA – ribonucleic acid
SDS – sodium dodecyl sulfate
SEM – standard error of the mean
SLM – stratum lacunosum-moleculare
SO – stratum oriens
SP – stratum pyramidale
SR – stratum radiatum
SST – somatostatin
TBI – traumatic brain injury
THF – tetrahydrofuran
TVA – avian tumor virus receptor A
UMAP – uniform manifold approximation
VIP – vasoactive intestinal peptide
VISpor – postrhinal area

ACKNOWLEDGEMENTS

To my mentor, Bobby: thank you for teaching me so much over the years. I have learned a tremendous amount from you, and I will always be grateful for all that you have done for me. Thank you for your patience and unwavering support over the years.

I am so thankful to my committee members Drs. Vijayalakshmi Santhakumar, David Lyon, and Andre Obenaus. I could not have asked for a better committee. Thank you for your guidance.

To my friends and family, thank you so much for your love and support. Thank you to my mom, Stasiu, Magda, and Tomek. A special thanks to my wonderful partner Miranda, who has done so much to keep me healthy and happy. I hope I can return the favor. Thank you to all of my friends who have made this journey easier, especially Josh, Nic, Rianne, Sunny, Crimps, and Claudia.

I would like to thank everyone who made intellectual contributions to my thesis work: Andrzej Foik, Young Kim, Jiana Machhor, Alexa Tierno, Shreya Pavani, David Lyon, and Robert Hunt. Andrzej Foik performed all electrophysiology experiments presented in Chapter 4. Jiana Machhor assisted with surgery and initial analyses in Chapter 4. Young Kim contributed to immunohistochemistry in Chapter 2. Alexa Tierno performed histology in Chapter 3 and immunostaining in Chapter 4. Shreya Pavani performed histology in Chapter 3. David Lyon provided consultation for all tracing experiments and contributed rabies virus. Robert Hunt contributed to writing, editing, analyses, and making figures.

VITA

Jan Christopher Frankowski

Education

University of California, Irvine, Irvine, CA 2015 – 2021
Ph.D., Biomedical Sciences
Advisor: Dr. Robert F. Hunt

University of Florida, Gainesville, FL 2011 – 2015
B.S., Neurobiological Sciences *(summa cum laude)*
Advisor: Dr. Eduardo Candelario-Jalil

Research Experience

Graduate Student 2015 – 2021
Department of Anatomy & Neurobiology, University of California – Irvine
Advisor: Robert F. Hunt Ph.D.

Undergraduate Research Assistant 2014
Department of Psychology, University of Florida
Advisor: Lori Knackstedt Ph.D.

Laboratory Technician 2012 – 2015
McKnight Brain Institute, University of Florida
Advisor: Eduardo Candelario-Jalil Ph.D.

Fellowships and Scholarships

F31 NINDS Ruth L. Kirschstein NRSA Individual Predoctoral Fellowship	2018 – 2021
T32 NINDS Training in Stem Cell Translational Medicine	2017 – 2018
UCI School of Medicine Travel Award	2018
UCI Graduate Dean Recruitment Fellowship	2015
Francisco J. Ayala Graduate Fellowship	2015
Ronald E. McNair Scholar	2014 – 2015
Howard Hughes Medical Institute Undergraduate Research Award	2012
Machen Florida Opportunity Scholarship	2011 – 2015

Honors and Awards

Alan Faden Award – National Neurotrauma Symposium	2021
National Neurotrauma Symposium Trainee & Diversity Award	2021
3rd Place Oral Presentation – UCI Elevator Pitch Competition	2018
1st Place Oral Presentation – Anatomy & Neurobiology Grad Day	2018
1st Place Oral Presentation – Anatomy & Neurobiology Grad Day	2017
3rd Place Oral Presentation – McNair Scholars Research Conference	2014
3rd Place Poster Presentation – Emory STEM Symposium	2014

Original Research

Peer-reviewed publications:

1. **Frankowski JC**, Tierno A, Pavani S, Lyon DC, Hunt RF. (2021). Brain-wide reconstruction of inhibitory circuits after traumatic brain injury. *Under review.*

2. **Frankowski JC**, Foik AT, Tierno A, Machhor JR, Lyon DC, Hunt RF. (2021). Traumatic brain injury to primary visual cortex produces long-lasting circuit dysfunction. ***Communications Biology***, *4,* 1297.

3. **Frankowski JC**, Kim YJ, Hunt RF. (2019). Selective vulnerability of hippocampal interneurons to graded traumatic brain injury. ***Neurobiology of Disease***, *129*, 208-216. PMID: 30031783

4. Kim YJ, Khoshkhoo S, **Frankowski JC**, Zhu B, Abbasi S, Lee S, Wu YE, Hunt RF. (2018). Chd2 is necessary for neural circuit development and long-term memory. ***Neuron***, *100*(5), 1180-1193. PMID: 30344048

5. Stennett BA, **Frankowski JC**, Peris J, Knackstedt LA. (2017). Ceftriaxone reduces alcohol intake in outbred rats while upregulating xCT in the nucleus accumbens core. ***Pharmacology Biochemistry and Behavior***. *159*, 18-23. PMID: 28687200

6. Hawkins KE, DeMars KM, Alexander JC, de Leon LG, Pacheco SC, Graves C, Yang C, McCrea AO, **Frankowski JC**, Garrett TJ, Febo M, Candelario-Jalil E. (2017). Targeting resolution of neuroinflammation after ischemic stroke with a lipoxin A4 analog: Protective mechanisms and long-term effects on neurological recovery. ***Brain and Behavior***, *7*(5), e00688. PMID: 28523230

7. **Frankowski, JC**, DeMars KM, Ahmad AS, Hawkins KE, Yang C, Leclerc JL, Doré S, Candelario-Jalil E. (2015). Detrimental role of the EP1 prostanoid receptor in blood-brain barrier damage following experimental ischemic stroke. ***Scientific Reports***, *5*, 17956. PMID: 26648273.

8. Hawkins KE, DeMars KM, Singh J, Yang C, Cho HS, **Frankowski JC**, Doré S, Candelario-Jalil E. (2014). Neurovascular protection by post-ischemic intravenous injections of the lipoxin A4 receptor agonist, BML-111, in a rat model of ischemic stroke. ***Journal of Neurochemistry***, *129*, 130-142. PMID: 24225006.

Pre-printed publication:

1. **Frankowski, JC**, Foik, AT, Machhor, JR, Lyon, DC, Hunt, RF. (2020). Primary visual cortex injury produces loss of inhibitory neurons and long-term visual circuit dysfunction. *bioRxiv*.

Technical report:

1. **Frankowski, JC**, & Hunt, RF. (2018). Modeling traumatic brain injury using controlled cortical impact injury. In *KOPF Carrier. #93*.

Oral presentations:

1. "Selective vulnerability of hippocampal interneurons to graded traumatic brain injury". (2018). *Anatomy & Neurobiology Graduate Student Research Day*.
2. "Characterization of a Chd2 haploinsufficient mouse". (2017). *Anatomy & Neurobiology Graduate Student Research Day*.
3. "Pharmacological blockade or genetic knockout of the prostaglandin E2 EP1 receptor reduces blood-brain barrier disruption and permeability in ischemic stroke". (2014). *20th Annual SAEOPP McNair/SSS Scholars Conference.*

Poster and Conference Presentations:

1. **Frankowski JC**, Lyon DC, Hunt RF. (2021). Whole-brain mapping of inhibitory circuits following traumatic brain injury. *National Neurotrauma Society Symposium*.
2. Tierno A, **Frankowski JC**, Foik AT, Machhor JR, Lyon DC, Hunt RF. (2021). Traumatic brain injury to primary visual cortex produces long-lasting circuit dysfunction. *National Neurotrauma Society Symposium.*
3. Kim YJ, Khoshkhoo S, Abbasi S, **Frankowski JC**, Lee S, Zhu B, Wu YE, Hunt RF. (2018). Chd2 is necessary for neural circuit development and long-term memory. *Society for Neuroscience Annual Meeting.*
4. **Frankowski JC,** Kim YJ., Hunt RF. (2018). "Selective vulnerability of hippocampal interneurons to graded traumatic brain injury" *Society for Neuroscience Annual Meeting.*
5. **Frankowski JC,** Kim YJ., Hunt RF. (2018). "Selective vulnerability of hippocampal interneurons to graded traumatic brain injury". *UCI School of Medicine Graduate Student Day.*
6. Kim YJ., **Frankowski JC,** Hunt RF. (2018). "Selective vulnerability of hippocampal interneurons to graded traumatic brain injury". *Epilepsy Gordon Conference.*
7. **Frankowski JC,** Kim YJ., Hunt RF. (2018). "Selective vulnerability of hippocampal interneurons to graded traumatic brain injury" *UCI EpiCenter Symposium.*
8. Abbasi S., **Frankowski JC,** Lee S., Smith S., Hunt R.F. (2016). "Modeling Chd2-linked epilepsy in mice". *American Epilepsy Society Annual Meeting.*
9. Abbasi S., **Frankowski JC,** Lee S., Gonzalez K., Smith S., Hunt R.F. (2016). "Role of Chd2 in cortical development and function". *Society for Neuroscience Annual Meeting.*
10. **Frankowski, JC,** DeMars, K.M., Hawkins, K. E., Ahmad, A., Doré, S. Candelario-Jalil, E. (2014). "Pharmacological blockade or genetic knockout of the prostaglandin E2 EP1 receptor reduces blood-brain barrier disruption and permeability in ischemic stroke". *College of Medicine Celebration of Research.*

11. **Frankowski, JC,** DeMars, K.M., Hawkins, K. E., Ahmad, A., Doré, S. Candelario-Jalil, E. (2014). “Pharmacological blockade or genetic knockout of the prostaglandin E2 EP1 receptor reduces blood-brain barrier disruption and permeability in ischemic stroke”. *Science, Technology, Engineering and Mathematics Symposium.*

12. **Frankowski, JC,** DeMars, K.M., Hawkins, K. E., Ahmad, A., Doré, S. Candelario-Jalil, E. (2014). “Pharmacological blockade or genetic knockout of the prostaglandin E2 EP1 receptor reduces blood-brain barrier disruption and permeability in ischemic stroke”. *Annual Society for Neurosciences Conference, University of Florida.*

13. **Frankowski, JC,** DeMars, K.M., Hawkins, K. E., Ahmad, A., Doré, S. Candelario-Jalil, E. (2014). “Pharmacological blockade or genetic knockout of the prostaglandin E2 EP1 receptor reduces blood-brain barrier disruption and permeability in ischemic stroke”. *Florida Undergraduate Research Conference, Florida International University.*

14. **Frankowski, JC,** DeMars, K.M., Hawkins, K. E., Candelario-Jalil, E. “Understanding and Treating Stroke: The Contribution of the EP Receptors”. (2013). *Annual Society for Neurosciences Conference, University of Florida.*

15. **Frankowski, JC,** DeMars, K.M., Hawkins, K. E., Candelario-Jalil, E. “Understanding and Treating Stroke: The Contribution of the EP Receptors”. (2013). *Creativity in Arts & Sciences Event, University of Florida.*

ABSTRACT OF THE DISSERTATION

Mapping whole-brain inhibitory circuit reorganization & repair after brain injury

by

Jan Christopher Frankowski

Doctor of Philosophy in Biological Sciences

University of California, Irvine, 2021

Professor Robert F. Hunt, Chair

Traumatic brain injury produces a range of long-lasting cognitive deficits. The underlying causes of these deficits could be in part due to reorganization of normal neural connectivity within brain regions critically important for cognition. Inhibitory interneurons play critical roles in normal circuit function, are known to be vulnerable in disease states, and are highly plastic in response to injury. The overall goal of my thesis work is to understand how traumatic brain injury affects brain circuitry from the microscopic to the mesoscopic scale with a particular focus on somatostatin-expressing (SST+) neurons. First, I show that SST+ neurons are the most vulnerable population of neuron to traumatic brain injury. Second, I use rabies virus tracing and novel brain clearing techniques to create whole-brain maps of the sources of input onto SST+ neurons both in hippocampus and prefrontal cortex, two brain regions involved in cognition. Analysis of brain-wide connectivity changes after trauma reveal profound changes both in long-range and local patterns of connectivity, even in regions distal from the site of injury. Finally, I use interneuron progenitor transplantation and the same mapping approach to identify the sources of input onto grafted interneurons in the injured brain. My results provide the first

comprehensive characterization of brain-wide circuit reorganization of a single a well-defined neuronal subtype after traumatic brain injury, and reveal that new SST neurons introduced into the injured brain environment maintain the capacity to rewire in the correct ways.

INTRODUCTION

1.1 Fundamentals of brain circuit organization

Mammalian brains are comprised of billions of individual neurons whose activity generates the perception of sensory experience, planning and execution of goal-directed motor programs, and the ability to encode and recall the memory of sensory experiences. The capability of our brains to perform these operations is underpinned by an exquisite diversity of neurons with unique patterns of connectivity and specialized functions. Here, I will overview the fundamental principles of brain circuit organization illustrated with examples from hippocampus. I will introduce traumatic brain injury as a brain circuit disorder, and in three subsequent chapters I will demonstrate how injury fundamentally changes the structure and function of circuits in hippocampus and in visual cortex, and how brain circuits may be reconstructed following injury using neuronal progenitor transplantation. I will conclude with remarks on mechanisms and potential future experiments based on the results of the work described here.

The hippocampus is the gateway for spatial and associative information coming from the cortex and is critically involved in the formation of episodic memory. Axons from the entorhinal cortex form the perforant pathway, the major source of cortical input to the hippocampus (Andersen et al., 1969; Andersen et al., 1966). Perforant path axons cross the hippocampal fissure and ‘perforate’ the subiculum and terminate in the outer two-thirds of the molecular layer of the dentate gyrus where they terminate on the distal dendrites of dentate granule cells (Steward, 1976). The dentate gyrus acts as a filter for activity propagation through the rest of the limbic system (Heinemann et al., 1992; Lothman et al., 1992). Granule cells integrate excitatory input and project through the mossy fiber pathway, forming large synapses on the proximal dendrites of CA3 pyramidal neurons. CA3 pyramidal neurons project to other brain regions through the fimbria, and project myelinated Schaffer collateral axons to the apical dendrites of CA1 pyramidal neurons.

CA1 in turn projects to the subiculum and other brain regions through the fimbria. Together, these regions form the trisynaptic excitatory pathway of the hippocampus.

Neurons are the fundamental information processing unit in the brain. Neurons rely on electrical potentials to integrate information from other neurons and to transfer information to other neurons. Neurons can be broadly classified as “excitatory” if they synthesize neurotransmitters such as glutamate or acetylcholine which depolarize the post-synaptic cell potential and increase the probability of generating an action potential. Alternatively, neurons can be classified as “inhibitory” if they release gamma-aminobutyric acid (GABA) or glycine, which hyperpolarize the post-synaptic membrane potential and decrease the probability of action potential firing (Kandel, 2000).

Inhibitory interneurons are a morphologically and functionally heterogeneous population of neurons that make up approximately 20% of all neurons in the neocortex and hippocampus (Wonders and Anderson, 2006). In the hippocampus, interneurons regulate integration of excitatory inputs to principal neurons, generate network oscillations, and are essential for higher-order cognitive functions such as memory retrieval and attention (Freund, 2003; Jonas et al., 2004). Early classification of interneurons in the dentate hilus revealed the presence of more than twenty morphologically distinct types (Amaral, 1978). More recent efforts using single cell sequencing to describe the breadth of neural diversity have identified more than 40 distinct subtypes based on their transcriptional profile (Zeisel et al., 2015), highlighting the incredible diversity of interneurons found in the brain.

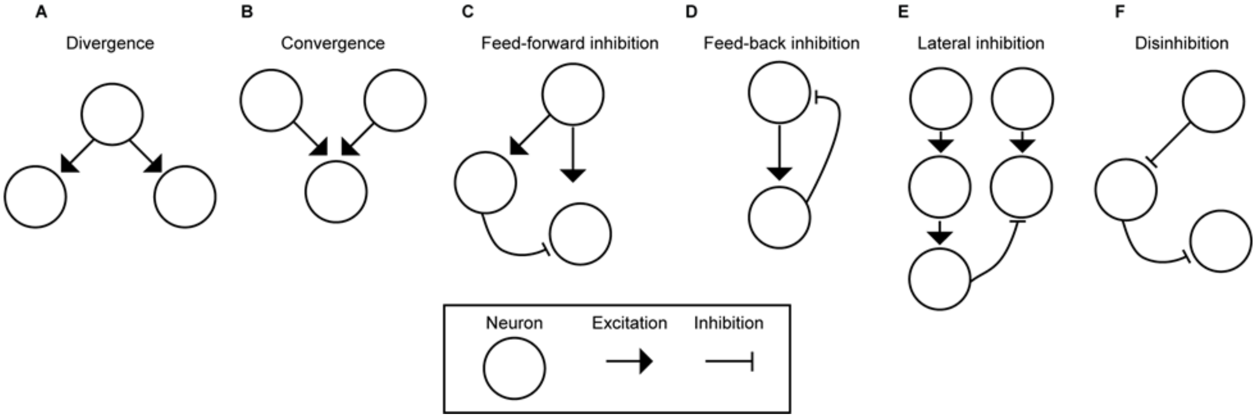

Figure 1.1 Microcircuit motifs in brain. **A.** Divergence sends information from one neuron to multiple neurons. **B.** Input from multiple neurons integrated onto one neuron is convergence. **C.** Feed-forward inhibition recruits an interneuron to inhibit neurons further down the microcircuit. **D.** Excitatory neurons target inhibitory neurons that synapse on the source neuron. **E.** A neuron's response to a stimulus is inhibited by the activation of a neighboring neuron. **F.** An inhibitory neuron inhibits another, exciting the second-order neuron.

Although individual neurons can send and receive information, higher-order brain functions arise from the coordinated activity of ensembles of neurons which interact to create more complex circuit motifs. Excitatory neurons may communicate with other excitatory neurons, creating a feed-forward excitatory circuit. These circuits are useful for passing information from one brain region to another. In hippocampus, feed-forward excitation underlies the largely unidirectional flow of information from the cortex through the hippocampal formation that supports episodic memory formation. For example, dentate granule cells excite CA3 pyramidal neurons through the mossy fiber pathway (Amaral et al., 2007). Feed-forward excitation gives rise to divergence and convergence, where information is propagated from one neuron to several others, or integrated from multiple sources to a single neuron, respectively. (**Fig 1.1**). An example of divergence in hippocampus is a single dentate granule cell contacting hilar interneurons and basal dendrites of CA3 pyramids (Frotscher et al., 2006). An example of convergence in hippocampus is a single dentate granule cell receiving input from thousands of neurons in entorhinal cortex (Rennó-Costa et al., 2010). Circuits involving only excitatory components lack the ability to regulate and refine their activity. Inhibitory neurons substantially increase the complexity of brain circuits through motifs such as feed-forward, feed-back, lateral, and dis- inhibition. Feed-forward inhibition involves excitation of a presynaptic neuron, which then depolarizes the intermediate interneuron, which in turn hyperpolarizes the next post-synaptic neuron. For example, a dentate granule cell activates an interneuron in CA3, which in turn hyperpolarizes a CA3 pyramidal neuron (Acsády et al., 1998). Feedback inhibition involves an excitation of an interneuron which in turn inhibits the initial excitatory neuron. Dentate granule cells are excited by input arriving on their distal dendrites, mossy fiber synapses then activate hilar interneurons, which in turn inhibit the distal dendrites of granule cells (Leranth et al., 1990). Lateral inhibition involves activation of a neuron within a cell layer, which projects to an intermediate interneuron, which then inhibits another neuron within the original cell layer. Dentate granule cells activate hilar interneurons, which then suppress the activation of neighboring granule cells, contributing to their sparse activity (Stefanelli et al., 2016). Disinhibition involves an initial interneuron which targets other inhibitory interneurons, producing a net excitatory effect on the targets of the intermediate interneuron. Vasoactive intestinal peptide-expressing interneurons inhibit somatostatin interneurons in the cortex, exciting pyramidal neurons targeted by the intermediate somatostatin interneuron (Karnani et al., 2016). Through these circuit mechanisms, the activity of interconnected neurons allows for the processing, transfer, and refinement of information on the both the global and local scale. However, in the case of damage to the circuit, such as that observed in traumatic brain injury (TBI), these inhibitory interneuron circuits reorganize. My work, presented here, addresses three fundamental questions pertaining to this reorganization: (1) what interneurons are most vulnerable to injury, (2) what happens on both the local and global brain-wide scale following injury, (3) can damage be repaired following injury using neuronal transplantation?

1.2 Definition, mechanisms, epidemiology, and brief history of traumatic brain injury (TBI)

Traumatic brain injury (TBI) occurs when an external mechanical force disrupts brain function (Centers for Disease Control and Prevention, 2014). The most frequent causes of TBI include falls, motor vehicle accidents, sports-related injuries, and assault (Rutland-Brown et al., 2006). Immediately following a TBI, affected individuals experience a decreased level of consciousness, seizures, changes in mental state including confusion or disorientation, coma or death depending on injury severity (Faul and Coronado, 2015).

TBIs are inherently heterogeneous with features that evolve over space and time depending on the type and severity of initial injury and the associated histopathological and behavioral outcomes. TBIs can be described by several classification systems that include clinical symptoms, pathophysiology, or the mechanism of initial injury. Injury severity can be classified from mild to severe. The most frequently used clinical measure is the Glasgow Coma Scale which classifies patients into mild, moderate, or severe categories based on the patient's verbal, motor, and ocular responses to commands (Teasdale and Jennett, 1974). Spontaneous and oriented responses score higher, while reflexive or non-responses score lower with a score or 8 or less out of 15 points considered severe. Glasgow Coma Scale scores are frequently used as a primary outcome measure in clinical trials where treatments are targeted to the most severe cases, although this scale does not capture anatomical or mechanistic differences between patients that are important considerations for successful treatment. Injury severity can also be classified by loss of consciousness, memory loss, and neurological deficits affecting sensation and perception. Mild TBI typically involves a concussive injury producing no overt structural lesion with a loss of consciousness that does not exceed thirty minutes and post-traumatic amnesia that does not exceed 24 hours (Alexander, 1995; Ruff and Jurica, 1999). Anatomical classifications describe the features of injury to inform treatment based on the location and type of injury. Mild injuries may present with no overt damage to the skull or lesions detectable by computed tomography, although functional imaging and diffusion tensor imaging are often more sensitive measures to detect damage after mild injury (Fox et al., 2013). Moderate to severe injuries involve skull fracture, hemorrhage within the meninges or parenchyma, contusions, and axonal injury. Anatomical classification paired with computed tomography can help predict clinical outcomes and inform treatment (Saatman et al., 2008). In addition, the mechanism of initial injury can inform expected injury severity and anatomical features of injury. Focal injuries resulting from the head striking an object produce contusions, skull fractures, and epidural hematomas. Non-contact forces from acceleration or blast injuries involve diffuse axonal injury and subdural hematomas (Saatman *et al.*, 2008). Injury classification schemes will likely continue to evolve over time with more detailed and non-invasive diagnostic measures that include genetic or metabolic biomarkers to inform treatment and patient outcomes.

TBI is significant public health concern with significant economic burden. In 2000, costs associated with TBI were ~ 60 billion dollars, with ~ 51 billion dollars associated with productivity losses (Corso et al., 2006). Approximately 2.5 million TBI-related emergency room visits, hospitalizations, and deaths occur each year in the US (Centers for Disease Control and Prevention, 2014). Approximately 1% of the US population is living with a chronic disability brought about by a TBI (Zaloshnja et al., 2008). TBI is most common in children under four years of age and in young adults between the ages of 15 and 24 and in elderly 75 years and older. TBI incidence rates double for every additional 10 years of age starting at age 65 (Coronado et al., 2005; Rutland-Brown *et al.*, 2006). Mortality rates are higher for older people compared to younger people with similar injuries (Ferrell and Tanev, 2002) The aging of the United States population will further increase the incidence and associated disability of non-fatal TBI (Brown et al., 2004).

Long-term cognitive and motor dysfunctions have been recognized as the most debilitating consequences of TBI (Klein et al., 1996) and it is the leading cause of acquired disability in children (Cronin, 2001). The majority of individuals affected by severe injury live with residual disability and show deficits in learning, memory, and executive function 10 years after initial injury (Ponsford et al., 2008). Between 5 and 10 year follow ups, only 7% of individuals improved while 37% had deteriorated, and 56% showed no change in global outcome (Forslund et al., 2019). Many individuals do not work or go to school and are dependent on long-term care provided by the family (Jacobs, 1988) This highlights that TBI is a serious chronic health condition with no effective treatments that prevent chronic disability.

TBI is a significant risk factor for the development of other neurological disorders. The incidence of post-traumatic epilepsy has been reported to be between ~2% - ~40% depending on injury severity and is more frequently associated with hemorrhagic temporal lobe injury, penetrating injury, and early post-injury seizures (Annegers and Coan, 2000; Caveness et al., 1979; Salazar et al., 1985; Tubi et al., 2019). In a cohort of ~180,000 older veterans, TBI was found to be associated with a 60% increased risk of developing Alzheimer’s disease over a nine-year period (Barnes et al., 2014). TBI also significantly increases the risk for psychiatric co-morbidities such as generalized anxiety, depression, bipolar disorder, post-traumatic stress disorder, and substance use disorders (Vaughn et al., 2019).

Public awareness of the devastating consequences of TBI prominently came into public view after "shell-shocked" veterans of WWI suffered from amnesia, sensory hypersensitivity, tremors, and other cognitive deficits despite the lack of an obvious head injury (Jones et al., 2007). More recently, conflict in Afghanistan and Iraq subjected veterans to blast-related injuries. Approximately 7% of the Afghanistan and Iraq war veterans who used VA services carried a diagnosis of TBI, and those with TBI had extremely high incidence of co-morbid PTSD and pain diagnoses (Taylor et al., 2012). Sports-related injuries have also been a major driver of public awareness of the consequences of TBI. The incidence of neurological symptoms in boxers led Dr. Harrison S. Martland to publish his seminal report describing the neuropathology related to repeated blows to the head: "*I am of the opinion that in punch drunk there is a very definite brain injury due to single or repeated blows on the head or jaw which cause multiple concussion hemorrhages in the deeper portions of the cerebrum*" (Martland, 1928). In recent years, there has been increasing focus on the consequences injuries sustained during contact sports such as American football. In one report, the majority of retired NFL football players who sustained at least one concussion during their careers showed incidence of memory problems and diagnosis of mild cognitive impairment (Guskiewicz et al., 2005). Post-mortem evaluation of brain tissue donated by former football players across all levels of play revealed that even high-school level players showed evidence of chronic traumatic encephalopathy, with nearly universal (99%) incidence in professional players (Mez et al., 2017). Evidence of contact-related brain injury pathology is emerging in other sports, including rugby (Zimmerman et al., 2021), soccer (Grinberg et al., 2016), and hockey (Schwab et al., 2021). Growing public awareness of the widespread incidence of TBI and the associated risks has driven the development of safety equipment to better protect at-risk populations such as athletes and soldiers from the devastating consequences of brain injury. The mechanisms by which TBI damages the brain will outlined below.

1.3 Primary and secondary mechanisms of TBI (or neurotrauma)

The behavior of the skull and brain in response to the application of external forces is based on their material properties (Holbourn, 1943). Two major types of forces are involved: contact forces and shear-strain forces. Contact forces involve the interaction of elastic brain tissue against the rigid skull and can produce local contusions, while shear-strain forces arise from linear and rotational acceleration and contribute to axonal injury. Brain tissue has a very small modulus of rigidity, which means brain is highly susceptible to shear-strain deformation (a change in shape without a change in volume). The brain is most susceptible to injury at the junction of tissues of different rigidities i.e. skull/brain or dura/brain (Gentry et al., 1988). Following a TBI, a series of inter-related mechanisms contribute to injury that evolve over space and time. Primary injury refers to immediate and irreversible damage to brain tissue occurring as a result of the biomechanics of initial injury (Werner and Engelhard, 2007). Focal injuries include contusions, lacerations, epidural, subdural, and intracerebral hematomas (Saatman *et al.*, 2008). Diffuse axonal injury due to acceleration-induced shearing and tearing occurs within minutes of injury, while intact but perturbed axons may swell and disconnect within several hours of injury (Maxwell et al., 1993). In humans, diffuse axonal injury and cerebral contusions are the most common primary injuries observed, most frequently affecting the frontal and temporal lobes (Gentry *et al.*, 1988). Secondary injury is a consequence or response to primary injury, and includes inflammation, cerebral edema, intracranial hypertension, blood-brain barrier disruption, and apoptosis (Werner and Engelhard, 2007). The immediate effects of TBI include impaired cerebral blood flow and metabolism, which induce an ischemic state (Clark et al., 1997; Cunningham et al., 2005; Nilsson et al., 1990). The buildup of metabolic waste and impaired glycolysis lead to insufficient ATP generation, and ionic imbalances occur due to the failure of ATP-dependent ionic pumps. These mechanisms lead to increased membrane permeability, cellular edema, increases in extracellular potassium, and influx of intracellular calcium (Nilsson et al., 1993; Soares et al., 1992; Werner and Engelhard, 2007). Ion pump failure and increases in extracellular potassium leads neurons to terminally depolarize, leading to unregulated release of neurotransmitter into the extracellular space (Bullock et al., 1998; Katayama et al., 1990). Increases in excitatory neurotransmitter concentrations in the extracellular space promotes a feed-forward loop, further exacerbating injury. Increases in intracellular calcium in turn activate proteases, phospholipases, and caspases to further perturb intracellular homeostasis and contribute to DNA fragmentation and apoptosis (Werner and Engelhard, 2007). The blood-brain barrier (BBB) is comprised of specialized networks of tight junction proteins that prevent the extravasation of blood components including red blood cells and leukocytes into the brain parenchyma (Zlokovic, 2008) Increased BBB permeability occurs in two phases after injury, with an immediate increase after injury related to shear forces disrupting endothelial cells (Rodríguez-Baeza et al., 2003), and a delayed phase that occurs several days after insult as a result of secondary inflammatory processes (Shlosberg et al., 2010). BBB disruption leads to uncontrolled exchange of excitatory amino acids, blood-derived leukocytes, hemoglobin, and other toxic serum components which trigger neuroinflammation, edema, and hyperexcitability (Baldwin et al., 1996; Faden et al., 1989; Morganti-Kossmann et al., 2001; Shlosberg *et al.*, 2010). Inflammation after injury involves the production of chemokines and prostaglandins that upregulate endothelial adhesion molecules such as ICAM-1 which promotes adhesion of immune cells to the endothelial cell wall and subsequent infiltration into the brain parenchyma (Balabanov et al., 2001). T-cells, macrophages, natural killer cells, and neutrophils contribute to oxidative and nitrosative stress and produce proteinases, prostaglandins, and other pro-inflammatory cytokines. These peripheral-derived cells and their associated cytokines activate resident microglia and astrocytes, which in turn produce and secrete their own cytokines and exacerbate the inflammatory response (Allan and Rothwell, 2001). Altogether, injury after TBI involves a complex and inter-related series of events that each make individual contributions over space and time. To better understand these complex relationships in a clinically relevant model of TBI, we used a method to produce consistent injuries that reproduce the features of TBI seen in affected individuals.

1.4 Controlled cortical impact model of TBI

The overall goal of experimental TBI models is to produce consistent injuries that reproduce the physiological, behavioral, and anatomical changes seen clinically. Numerous strategies have been tested across species, many using custom-build apparatuses spring-loaded guns (Ommaya et al., 1971) weight drop (Feeney et al., 1981), acceleration injury using a pneumatically-actuated cylinder (Gennarelli et al., 1982), or acceleration using a gas- actuated cylinder (Nilsson et al., 1977). While these approaches were effective, many of these devices lacked the ability to tightly control experimental parameters and were not commercially available. Devices for acceleration injury in primates required custom-fitting to each primates skull geometry (Gennarelli *et al.*, 1982). The need for an injury device that could produce reproducible injuries lead to the development of fluid percussion injury, delivered by a fluid pulse to the epidural space through a port in the cranium (Dixon et al., 1987; Hayes et al., 1987). While fluid percussion models produced anatomical and behavior changes consistent with those seen in human patients, the model is not amenable to producing focal contusive injuries restricted to particular brain regions (Lighthall, 1988). The need for a focal injury device that gave a high degree of control over experimental parameters led to the development of controlled cortical impact (CCI) as a model of experimental head injury and much research has been done since regarding the histopathological and behavioral outcomes as well as its clinical relevance.

1.5 Histopathological and behavioral outcomes, and clinical relevance of CCI

CCI was first used in ferrets as a new experimental model of mechanical brain injury (Lighthall, 1988). A steel small bore, stroke-constrained, pneumatically-driven and electronically controlled impactor was mounted on an adjustable crossbar. Crossbar height was adjusted such that upon retraction, the impactor would compress the surface of the brain through a craniotomy to the desired depth. Impactor speed was measured by the latency to break a pair of laser beams separated in space. The velocity of the impactor was adjusted by varying air pressure delivered to the cylinder. CCI injury produced physiological changes including hypertension and increased heart rate. Histopathological outcomes included contusion, axonal injury, subdural hematoma, subarachnoid hemorrhage, and herniation of the brainstem. CCI injury has since been scaled for use in small lissencephalic animals such as mice (Smith et al., 1995), rats (Dixon et al., 1991), and larger gyrencephalic animals such as pigs (Duhaime et al., 2000), sheep (Anderson et al., 2003), and non-human primates (King et al., 2010). One of the advantages of the scalability of CCI is the ability to test hypotheses not feasible in rodents. Examples include measuring altered functional connectivity in a gyrated neocortex using fMRI (Simchick et al., 2021), testing resuscitation strategies after trauma (Halaweish et al., 2016), or testing recovery of skilled motor function in non-human primates (Barbay et al., 2021). CCI can be adapted to study trauma across the lifespan by using juvenile animals (Adelson et al., 2013; Semple et al., 2017; Statler et al., 2009). CCI can also be used in a closed-skull configuration, hitting the skull directly to studying the consequences of repetitive injuries (Gold et al., 2018).

One of the features of CCI is precise control over injury parameters that influence injury severity. Since the initial description of the method, there has been a concerted effort to determine how manipulating these variables affect injury severity. Increasing impactor velocity alone can increase the severity of motor and cognitive deficits (Fox et al., 1998), produce more extensive hemorrhaging, more widespread contusions, and herniation of the brainstem and spinal cord in some cases (Lighthall, 1988). Impactor shape also significantly changes the characteristics of injury. Beveled tips create higher degree of principle strain in compressed tissue, leading to more rapid tissue loss, greater numbers of fluorojade-positive neurons in CA1 and DG (Mao et al., 2010a; Mao et al., 2010b; Pleasant et al., 2011). Beveled tips are more likely to cause hippocampal cavitation, the presence of which is associated with more pronounced mossy fiber sprouting (Hunt et al., 2012). Increasing impact depth is a commonly used approach to grade injury severity. Compared to 0.5 mm compression depths, 1 mm depth injuries in mice produce higher incidence of post-traumatic epilepsy (Hunt et al., 2009), greater motor and memory deficits, greater degree hippocampal cell death, and increases the rate of IgG extravasation into the hippocampus (Saatman et al., 2006). In ferrets, 2 mm compressions produced minor physiological and morphological changes, while 4 mm impacts were often fatal (Lighthall, 1988).

In humans, TBI produces interneuron loss in the neocortex (Buriticá et al., 2009; Schiavone et al., 2017) and hippocampus (Swartz et al., 2006). Neuron loss after CCI occurs rapidly in multiple brain regions and gradually declines. Neurodegeneration measured by fluorojade or terminal deoxynucleotidyl transferase dUTP nick end labeling peaks between 24 and 48 hours after injury (Hall et al., 2008; Kaya et al., 1999). Stereological quantification in of hippocampal neuron density at progressive time points after injury shows that cell loss is detectable within one hour and peaks two days after injury (Baldwin et al., 1997). Two days after injury, cell loss is detectable in multiple subfields of the hippocampus (Saatman *et al.*, 2006; Smith *et al.*, 1995). CCI rapidly upregulated markers of microglial activation (IBA1) and astrogliosis (GFAP) within hours that are detectable up to one year after injury (Littlejohn et al., 2020; Madathil et al., 2013; Pischiutta et al., 2018; Semple *et al.*, 2017; Zhu et al., 2019) In the neocortex, PV+ and SST+ cell loss occurs in the perilesional zone (Cantu et al., 2015; Koenig et al., 2019). CCI also reduces $GABA_A$ receptor δ subunit density in dentate gyrus and impairs $GABA_B$ receptor signaling (Parga Becerra et al., 2021). In summary, CCI produces widespread cell loss and neuroinflammation in both neocortex and hippocampus.

Electrophysiological changes in neocortex and hippocampus occur after CCI injury. In the neocortex, both pyramidal neurons and interneurons receive increased excitatory input and decreased inhibitory input after injury (Cantu *et al.*, 2015; Koenig *et al.*, 2019; Nichols et al., 2018;

Nichols et al., 2015). In hippocampus, dentate granule cells receive increased excitatory input (Butler et al., 2015; Hunt et al., 2010) and decreased inhibitory input (Boychuk et al., 2016; Butler et al., 2016; Hunt et al., 2011; Parga Becerra *et al.*, 2021), while hilar interneurons receive greater excitatory input after injury (Butler et al., 2017; Hunt *et al.*, 2011). Post-traumatic epilepsy is a frequency consequence of TBI, with up ~40% incidence (Annegers and Coan, 2000; Caveness *et al.*, 1979; Salazar *et al.*, 1985; Tubi *et al.*, 2019). CCI has been developed as a reliable animal model of post-traumatic epilepsy, with injured rodents showing spontaneous seizures at rates comparable to human patients (Hunt *et al.*, 2009). In adult mice, PTE incidence has been reported to be 36% after 1mm impact and 20% after 0.5 mm impact (Hunt *et al.*, 2009), 63% after 1 mm impact (Zhu *et al.*, 2019), 40% after 1 mm impact (Butler *et al.*, 2015) 50% after 2 mm impact (Guo et al., 2013) 9% after 0.5 mm impact (Bolkvadze and Pitkänen, 2012), and 27% after 1 mm impact (Szu et al., 2020). In juvenile mice, PTE incidence was 95% after 1.73 mm injury (Semple *et al.*, 2017). In rats, PTE incidence was 20% after 2.8 mm impact (Kelly et al., 2015), 20% after 3 mm injury (Sun et al., 2018), and 13% after 2 mm injury in juveniles (Statler *et al.*, 2009). Differences between groups may be due to differences in impact depth, tip geometry (beveled vs. rounded), impactor orientation (parallel to midline or perpendicular to the dura), and type of CCI device (pneumatic vs. electromagnetic).

Mossy fiber sprouting is the formation of aberrant recurrent excitatory connections between dentate granule cells and is a hallmark feature of epileptic hippocampus in both rodent models of epilepsy (Scharfman et al., 1999; Shibley and Smith, 2002) and human patients (Sutula et al., 1989). Mossy fiber sprouting is visualized and scored using Timm’s stain to precipitate zinc ions present in granule cell axons and the degree of staining in the supragranular region and the inner molecular layer of the dentate gyrus (Sloviter, 1982). Mossy fiber sprouting occurs after severe CCI, is almost always confined to the ipsilateral hemisphere and is more pronounced in septal dentate gyrus compared to temporal dentate gyrus (Hunt *et al.*, 2009; Hånell et al., 2010; Semple *et al.*, 2017), and occurs in a variety of inbred and outbred mouse strains (Hunt *et al.*, 2012). Although mossy fiber sprouting indicates circuit reorganization has occurred in damaged hippocampus, sprouting alone is not necessary and sufficient for developing PTE. Average Timm's scores are not different between epileptic and non-epileptic mice after CCI (Hunt *et al.*, 2012). Rapamycin treatment targets mTOR signaling pathways and attenuates post-traumatic mossy fiber sprouting (Butler *et al.*, 2015; Guo *et al.*, 2013) and network excitability in dentate gyrus (Butler *et al.*, 2015). Notable, mossy fiber sprouting does not correlate with the frequency or duration of seizures in kainite-induced epilepsy (Buckmaster and Dudek, 1997) and suppression of mossy fiber sprouting with rapamycin does not reduce spontaneous seizure frequency after pilocarpine-induced status epilepticus (Buckmaster and Lew, 2011).

1.6 Roles of GABA neurons in circuit function based on neurochemical identity and laminar position

Interneuron diversity emerges from highly their heterogeneous morphological and electrophysiological features. Classification schemes differentiate interneuron subtypes based on neurochemical marker expression, physiological properties, and post-synaptic targets (Ascoli et al., 2008; Freund and Buzsáki, 1996; Houser, 2007; Pelkey et al., 2017). A consistent feature across nearly all interneurons is the expression of GAD65 or GAD67, which catalyze the production of GABA from glutamate (Houser, 2007; Houser and Esclapez, 1994). Numerous other calcium binding proteins and peptides including parvalbumin (PV), calretinin (CR), neuronal nitric oxide synthase (nNOS), reelin, neuropeptide Y (NPY), somatostatin (SST), and vasoactive intestinal peptide (VIP) label different interneuron subtypes. Some of these markers label largely mutually exclusive populations (SST, PV, VIP), while others are frequently co-expressed (NPY, CR) (Freund and Buzsáki, 1996; Pelkey *et al.*, 2017; Rudy et al., 2011).

Interneurons can also be classified based on the laminar position of their soma, the localization of their post-synaptic targets, and where their dendrites arborize (Freund and Buzsáki, 1996; Halasy and Somogyi, 1993). These features determine what types of inputs interneurons receive and what cellular domain they target, which determine their respective contribution to local circuit operations. Interneurons with somas within the hilus and axons that innervate the molecular layer of the dentate gyrus directly oppose excitatory input from the perforant pathway and are called hilar perforant path-associated (HIPP) cells (Freund and Buzsáki, 1996). These neurons frequently express SST and project to the outer two-thirds of the molecular layer, targeting the distal dendrites of granule cells (Houser, 2007). HIPP cells have dendrites in the hilus, where they receive mossy fiber input and are positioned to mediate feed-back inhibition onto dentate granule cells (Freund and Buzsáki, 1996). Neurons that have their soma, axon, and dendrites within the molecular layer receive input from perforant path axons and are termed molecular layer perforant path-associated (MOPP) cells (Freund and Buzsáki, 1996; Overstreet-Wadiche and McBain, 2015). MOPP cells have exceptionally high presynaptic bouton density and a relatively compact axonal and dendritic arborization, which provide low-frequency inhibitory volume transmission to granule cell dendrites. While most interneurons mediate $GABA_A$ receptor-mediated inhibition through phasic mechanisms, MOPP cells mediate tonic inhibition by releasing GABA into the extracellular space (Overstreet-Wadiche and McBain, 2015). This mechanism mediates slower and longer-lasting inhibition. Interneurons with their cell bodies in the hilus and project to the inner one-third of the molecular layer are termed hilar commissural-association pathway (HICAP) cells. HICAP cells provide feed-back inhibition to dentate granule and receive mossy cell input from the contralateral dentate gyrus as well as input from the entorhinal cortex (Freund and Buzsáki, 1996; Han et al., 1993). The heterogeneity of interneuron morphologies give rise to distinct patterns of connectivity within the hippocampus. The specific patterns of connectivity of SST-expressing interneurons will be described below.

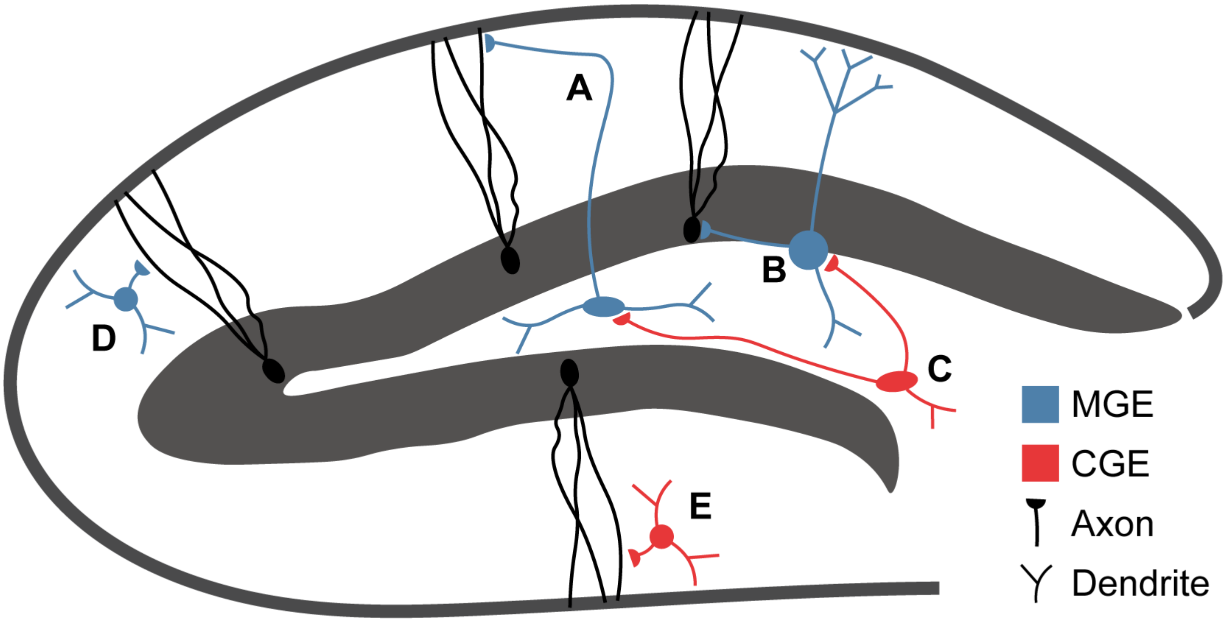

Figure 1.2 Interneurons in dentate gyrus. A-E. A. HIPP cells with hilar dendrites target distal granule cell dendrites and express SST. **B.** Basket cells with hilar and molecular layer dendrites target somas and axon initial segments and express PV. **C.** Interneuron-selective cells disinhibit other interneurons and express VIP. **D.** MOPP cells arborize in the molecular layer and target distal dendrites and express nNOS. **E.** Reelin-expressing MOPP cells arborize in the molecular layer and target distal dendrites. Blue color indicates MGE-derived neurons and red color indicates CGE-derived neurons.

1.7 SST+ neuron function and connectivity in hippocampus

Somatostatin is a neuropeptide first described in hypothalamus as an inhibitor of pituitary growth hormone release (Brazeau et al., 1973). While expression is highest in hypothalamus, somatostatin is expressed across the entire brain including neocortex, septum, thalamus, midbrain, brain stem, cerebellum, striatum, and olfactory bulb (Brownstein et al., 1975). Nearly all SST+ neurons co-express glutamate decarboxylase and GABA (Somogyi et al., 1984), and SST is a useful neurochemical marker for identification a largely distinct population from parvalbumin- and 5HT3a-expressing interneurons, which together label nearly all neocortical GABAergic interneurons (Rudy *et al.*, 2011). SST+ neurons are one of the largest neurochemically-defined neuron subtypes found in the dentate gyrus, with ~55% of hilar GABAergic neurons co-expressing SST (Esclapez and Houser, 1995). SST+ neuron cell bodies are located in the polymorphic layer (hilus) of the dentate gyrus, with greater abundance towards the temporal pole (Bakst et al., 1986; Buckmaster et al., 1994; Leranth *et al.*, 1990). SST+ axons project to outer two-thirds of the molecular layer where they form symmetric synapses on the heads and necks of granule cell dendritic spines, directly opposing the excitatory input arriving from the entorhinal cortex (Bakst *et al.*, 1986; Leranth *et al.*, 1990). SST+ axons are most prominently found in the outer-third of the molecular layer, with decreasing immunoreactivity moving towards the granule cell layer (Bakst *et al.*, 1986; Leranth *et al.*, 1990). This pattern of expression is conserved across rodent, non-human primates, and humans (Amaral et al., 1988; Bakst et al., 1985). Some SST+ axons leave the hippocampus and project to the contralateral dentate gyrus through an axon that enters the fimbria and approaches the septal pole (Buckmaster et al., 2002), with synaptic terminals predominantly targeting granule cell apical dendrites (Bakst *et al.*, 1986; Eyre and Bartos, 2019; Léránth and Frotscher, 1987). SST+ axons are also found on granule cell bodies, albeit infrequently (Leranth *et al.*, 1990). SST+ axons also innervate the hilus, forming axo-somatic and axo-axonic symmetric synapses and occasionally dendrite of other hilar interneurons (Leranth *et al.*, 1990). SST+ dendrites most prominently arborize in the hilus, however occasionally they extend into the molecular layer (Leranth *et al.*, 1990). Hilar dendrites receive input from mossy fiber synapses originating in the granule cell layer, CA3 pyramidal cells, and CA3 interneurons, mossy cells, and interneurons in contralateral dentate gyrus (Eyre and Bartos, 2019; Freund and Buzsáki, 1996; Hajos et al., 1996; Hunt *et al.*, 2011; Katona et al., 1999; Leranth *et al.*, 1990; Morgan et al., 2007; Wittner et al., 2006). Some SST+ dendrites project through the granule cell layer to the outer molecular layer of the dentate gyrus, where they receive direct excitatory input from the entorhinal cortex (Leranth *et al.*, 1990). Hilar SST+ neurons are innervated by symmetric axo-somatic and axodendritic CHAT+ synapses originating in the basal forebrain, including the medial septum and diagonal band nucleus of Broca (Léránth and Frotscher, 1987). In summary, the anatomy of hilar SST+ neurons endows them with the ability to participate in feed-forward and feed-back inhibitory circuit motifs and prominently control the integration of input along dentate granule cell dendrites. SST neurons also make important contributions to circuit function in other brain regions outside the hippocampus, including the neocortex.

1.8 SST+ neuron functions and presynaptic inputs in PFC

The prefrontal cortex integrates input from across the entire brain to learn associations between contextual and spatial cues and support adaptive decision making to plan goal-directed behavior (Euston et al., 2012). The ventral division of the PFC includes the prelimbic and infralimbic areas which are involved in emotional and autonomic regulation with reciprocal interactions with the amygdala, striatum, insular areas, hypothalamus, and neuromodulatory areas in the brain stem (Allen et al., 1991; Gabbott et al., 2005; Heidbreder and Groenewegen, 2003). Input from the hippocampal formation provides spatial information about external cues to provide contextual information to guide decision making in addition to synchronizing network oscillations between the two regions (Abbas et al., 2018; Euston *et al.*, 2012). SST+ interneurons specifically receive input from over 150 discrete brain regions including neocortex, olfactory areas, hippocampal formation, thalamus, hypothalamus, and brain stem (Sun et al., 2019b; Ährlund-Richter et al., 2019). Compared to other interneuron subtypes, SST+ interneurons receive less input from lateral orbital cortex and secondary motor areas, more input from CA1, and more input from the basal forebrain (Sun *et al.*, 2019b). Within local microcircuits, SST+ interneurons target PV interneurons and are targeted by VIP and PV interneurons (Ährlund-Richter *et al.*, 2019). PFC SST+ interneurons receive significantly more cholinergic input from than other interneuron subtypes (Ährlund-Richter *et al.*, 2019). Functionally, PFC SST+ neurons have been implicated in a wide range of behaviors including social interaction (Liu et al., 2020), social fear (Xu et al., 2019), affective state discrimination (Scheggia et al., 2020), and encoding fear memory (Cummings and Clem, 2020). SST-, but not PV-expressing interneurons in prelimbic cortex show potentiation after cued fear learning, are active during memory acquisition, and their activity is necessary for memory expression (Cummings and Clem, 2020). SST interneurons can increase the output of prefrontal pyramidal neurons by inhibiting PV interneurons, thus disinhibiting the excitatory cell population (Cummings and Clem, 2020). Altogether, SST neurons make important contributions to circuit function in the cortex, however unlike excitatory neurons, SST neurons arise from outside the cortex, which I will discuss next.

1.9 GABA neuron development in the MGE and the origin of SST+ neurons

The medial, caudal, and lateral ganglionic eminences are structures in the developing telencephalon that generate interneuron progenitors along their respective ventricular zones. These progenitors generate immature interneurons that migrate tangential to the radial glial scaffold to populate the neocortex, hippocampus, and olfactory bulb (Anderson et al., 1997; Anderson et al., 2001; de Carlos et al., 1996; Nery et al., 2002; Tamamaki et al., 1997). Anderson et. al demonstrated that cortical interneurons originate outside the cortex by labeling striatal cells with dye at E12.5 that are later found in neocortex (Anderson *et al.*, 1997). When the neocortex was separated from the ganglionic eminence, GABAergic interneuron density in the neocortex was reduced five-fold. Dlx1 and Dlx2 homeobox genes drive the transition from proliferation to migration which begins around E12.5. Migrating cells travel tangential to the radial glial scaffold, in contrast to excitatory cortical neurons that are born in the cortical ventricular zone and require the guidance of the radial glial scaffold (Anderson *et al.*, 1997). Wichterle et. al demonstrated the migratory potential of neuronal progenitors derived from the medial ganglionic eminence (MGE) by transplantation into the adult brain (Wichterle et al., 1999). Cells from the neocortical subventricular zone, lateral ganglionic eminence (LGE) and medial ganglionic eminence (MGE) were dissected at E14 and transplanted into the striatum or thalamus, revealing that while neocortical and LGE progenitors remained mostly confined to the injection site, MGE progenitors migrated extensively and very few cells were found at the injection site (Wichterle *et al.*, 1999). The MGE and CGE generate nearly all of the interneurons in the neocortex and hippocampus. Interneurons born in both regions migrate extensively from the ventral telencephalon to populate the neocortex and hippocampus (Marín and Rubenstein, 2001; Rudy *et al.*, 2011; Tricoire et al., 2011). Interneuron cell fate is specified by the spatiotemporal origin during development and driven by genetic programs that guide the development of each subtype of interneuron (Kessaris et al., 2014). The MGE produces interneuron subtypes found in deeper cortical layers including parvalbumin-(PV), somatostatin- (SST), and neuronal nitric oxide (nNOS)-expressing cells, while the CGE produces interneurons found more often in superficial layers including cholecystokinin (CCK)-, vasoactive intestinal peptide (VIP)-, and reelin-expressing cells (Butt et al., 2005; Nery *et al.*, 2002; Tricoire and Vitalis, 2012; Wichterle et al., 2001; Wonders and Anderson, 2006; Xu et al., 2004). The majority of SST-expressing interneurons are generated by E12.5, with a sharp decline by E15.5 (Miyoshi et al., 2007). In the ventricular zone of the MGE, expression of the homeodomain transcription factor NKX2.1 is essential for specifying the neuroepithelial domain and the first step towards initiating SST interneuron development (Kessaris *et al.*, 2014). NKX2.1 is only transiently expressed and downregulated by the time progenitors start to migrate out of the ventricular zone (Hernández-Miranda et al., 2010; Miyoshi *et al.*, 2007). NKX2.1 activates downstream genetic programs involved in migration, positioning, and maturation. The transcription factor LHX6 has a critical role for migration and laminar positioning of SST-expressing interneurons (Fogarty et al., 2007; Miyoshi *et al.*, 2007; Zhao et al., 2008). Transcriptional regulators of the DLX family have roles in patterning and differentiation of SST interneurons, as well as laminar positioning, dendritic maturation, and survival (Kessaris *et al.*, 2014; Long et al., 2009). Many other transcription factors are involved in the specification, migration and maturation of SST+ interneurons including SOX6, DLX5-6, LHX7-8, Arx, and NKX6.2 (Hernández-Miranda *et al.*, 2010; Kessaris *et al.*, 2014; Miyoshi *et al.*, 2007; Wonders and Anderson, 2006). Our understanding of the origin of cortical interneurons within the ganglionic eminences has paved the way for studying how interneuron transplantation can be used to modify the function of mature circuits by microdissection and transplantation of these progenitors, which I will discuss below.

1.10 MGE cell transplantation

When grafted into wild-type mice, MGE or CGE interneuron progenitors maintain their ability to migrate, differentiate, and functionally integrate into host-brain networks as mature interneurons (Alvarez-Dolado et al., 2006; Hunt et al., 2013b; Larimer et al., 2016). MGE explants transplanted into the postnatal neocortex or hippocampus migrate extensively, show morphology of mature interneurons, and express neurochemical markers such as GABA, PV, CR, SST, and NPY (Alvarez-Dolado *et al.*, 2006). Starting four weeks after transplantation, grafted interneurons show mature firing properties and host-brain cortical pyramidal neurons show increased synaptic inhibition, indicating that transplanted interneurons formed functional synapses in the host brain (Alvarez-Dolado *et al.*, 2006). The first demonstration of therapeutic efficacy of MGE transplantation was shown in a mouse lacking a Shaker-like potassium channel (Kv1.1-/-) (Baraban et al., 2009). Bilateral cortical transplantation of MGE progenitors into juvenile mice elevated inhibition onto host-brain pyramidal neurons and reduced both the frequency and duration of spontaneous seizures. The first demonstration of therapeutic efficacy of MGE transplantation into adult animals was shown in pilocarpine-treated mice who had already shown at least one spontaneous seizure (Hunt *et al.*, 2013b). This study demonstrated that MGE progenitors can migrate and survive in the injured hippocampus, reduce seizure frequency by 92%, and correct spatial memory deficits. These effects were specific to the hippocampus, as transplantation into the basolateral amygdala has no effect on spontaneous seizures, or spatial memory behaviors. Other studies have demonstrated therapeutic efficacy in other models of CNS disease, such as Alzheimer's disease (Martinez-Losa et al., 2018; Tong et al., 2014), neuropathic pain (Bráz et al., 2012), stroke (Daadi et al., 2009), Parkinson's disease (Martínez-Cerdeño et al., 2010), and severe traumatic brain injury (Zhu *et al.*, 2019), and genetic epileptic encephalopathy (Kim et al., 2018). Interneuron grafts survive long-term and continue to have beneficial effects on circuit function at chronic time points. After grafting into pilocarpine-treated mice, spontaneous seizure suppression persisted 6-7 months after transplantation and elevations in synaptic inhibition persisted 9 months after transplantation (Casalia et al., 2017). MGE transplants have been demonstrated to integrate into host-brain networks using multiple modalities including electron microscopy (Daadi *et al.*, 2009), dual patch clamp recording and stimulation (Howard and Baraban, 2016), and optogenetics (Hsieh and Baraban, 2017). While these techniques have elucidated the organization of local circuits, viral tracing techniques are useful tools in order to understand long-range connectivity of transplanted interneurons.

1.11 Monosynaptic rabies virus tracing

Rabies lyssavirus is a neurotropic single-stranded negative sense RNA virus that has been repurposed as useful tool for trans-neuronal tracing. The rabies viron is made up of only five proteins: nucleoprotein (N) which encapsulated the viron and serves as a template for replication (Albertini et al., 2011), RNA polymerase (L) and its cofactor phosphoprotein (P) which replicated and amplify virons (Albertini *et al.*, 2011), matrix protein (M), and glycoprotein (G), which are required for the cellular transfer of viral particles (Mebatsion et al., 1999). Rabies virus is transmitted across synapses (Iwasaki and Clark, 1975) and is largely confined to neurons, although astrocytes are occasionally infected (Tsiang et al., 1983). Rabies virus is propagated exclusively in the retrograde direction in the CNS (Kelly and Strick, 2000). Using G-protein from different rabies virus strains improves trans-synaptic efficiency (Mori and Morimoto, 2014). An optimized rabies glycoprotein (oG) has been developed by incorporating a codon-optimized version of the extracellular domain of Pasteur strain glycoprotein with the cytoplasmic domain of the SAD B19 glycoprotein, resulting in up to 20-fold increase in synaptic efficacy compared to the original SAD B19 glycoprotein (Kim et al., 2016). Rabies virus infection is cytotoxic after approximately two weeks after infection (Wickersham et al., 2007a), which has prompted investigators to find alternative approaches for longer survival of infected neurons.

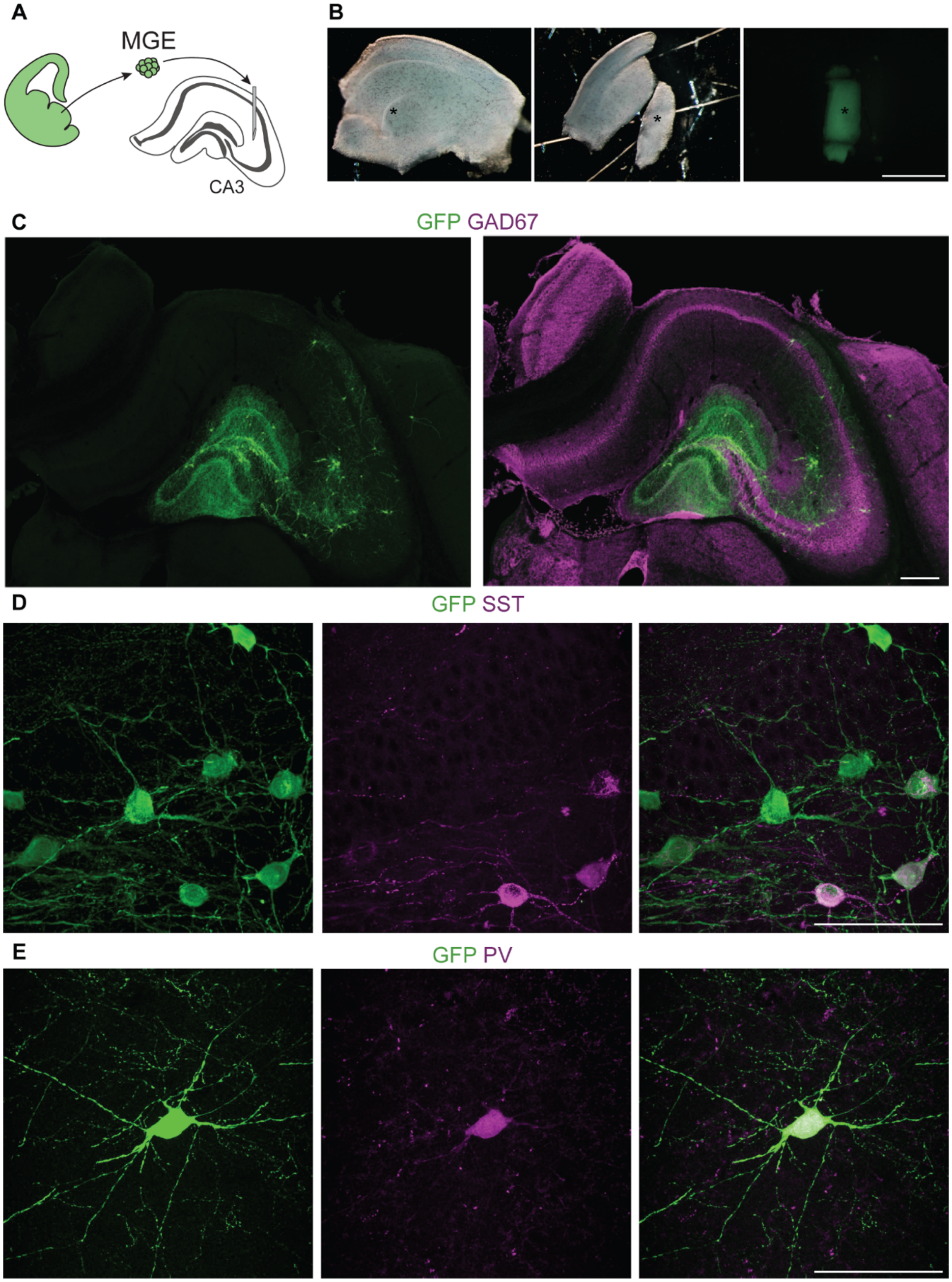

Figure 1.3 Transplantation of interneuron progenitors. A-E. A. Schematic depicting microdissection of MGE cells and transplantation into CA3 after brain injury. **B.** The MGE in E13.5 embryos (black asterisk, left panel) is separated from the LGE, CGE, and cortical plate (middle panel). MGE cells express GFP (right panel). Scale bar, 500 μm. **C.** MGE cells grafted into CA3 of brain-injured mouse migrate and develop into mature interneurons (green) that express GAD67 (magenta). Scale bar, 500 μm. **D.** Grafted GFP-expressing MGE cells in the hilus (green) express somatostatin and parvalbumin (**E**). Scale bar, 100 μm.

One approach is to use the CVS-N2c rabies virus strain, which shows reduced cytotoxicity and increased trans-synaptic efficiency (Reardon et al., 2016). Another approach involves reducing the ability for rabies to replicate once it has infected a neuron. Deletion of the gene coding for RNA polymerase (L) protein reduces viral expression to low levels, permitting infected cells to survive up to a year after infection with no morphological abnormalities (Chatterjee et al., 2018). However, due to reduced expression of rabies virus fluorescent reporter intensity is greatly reduced. This approach replaces the gene coding for a fluorophore with a gene coding for Cre or Flp recombinase and must be paired with a recombinase-dependent reporter. One advantage of this Cre/Flp dependent-system is that retrogradely-labeled neurons can be specifically targeted to silence or drive the expression of floxed alleles, allowing for more involved circuit manipulations besides expressing a fluorophore. Another advance involves driving the expression of channelrhodopsin using rabies virus. This allows for optogenetic stimulation of inputs arriving onto a target population, which has been used validate the functional connectivity of cholinergic synapses onto newborn granule cells (Zhu et al., 2017).

Rabies virus tracing has been used to create cell-type specific whole-brain maps of inputs in many brain regions. Rabies tracing paradigms have elucidated the connectivity of dopaminergic neurons in midbrain (Watabe-Uchida et al., 2012), serotonergic neurons in brain stem (Pollak Dorocic et al., 2014), parvalbumin-expressing interneurons in barrel cortex (Hafner et al., 2019), striatal cholinergic interneurons (Klug et al., 2018), and parvalbumin- and somatostatin-expressing interneurons in hippocampus (Sun et al., 2014). Limitations to rabies virus tracing exist. Not all neurons are susceptible to rabies virus infection (Albisetti et al., 2017). Trans-synaptic tracing experiments in the lateral hypothalamic area have revealed that retro-AAVs show preference for cortical transmission, while rabies virus shows preference for basal ganglia and hypothalamus (Sun et al., 2019a). While most rabies virus tracing studies have used traditional slice immunohistochemistry, modern approaches using tissue clearing have enabled analysis of rabies virus tracing data in three dimensions.

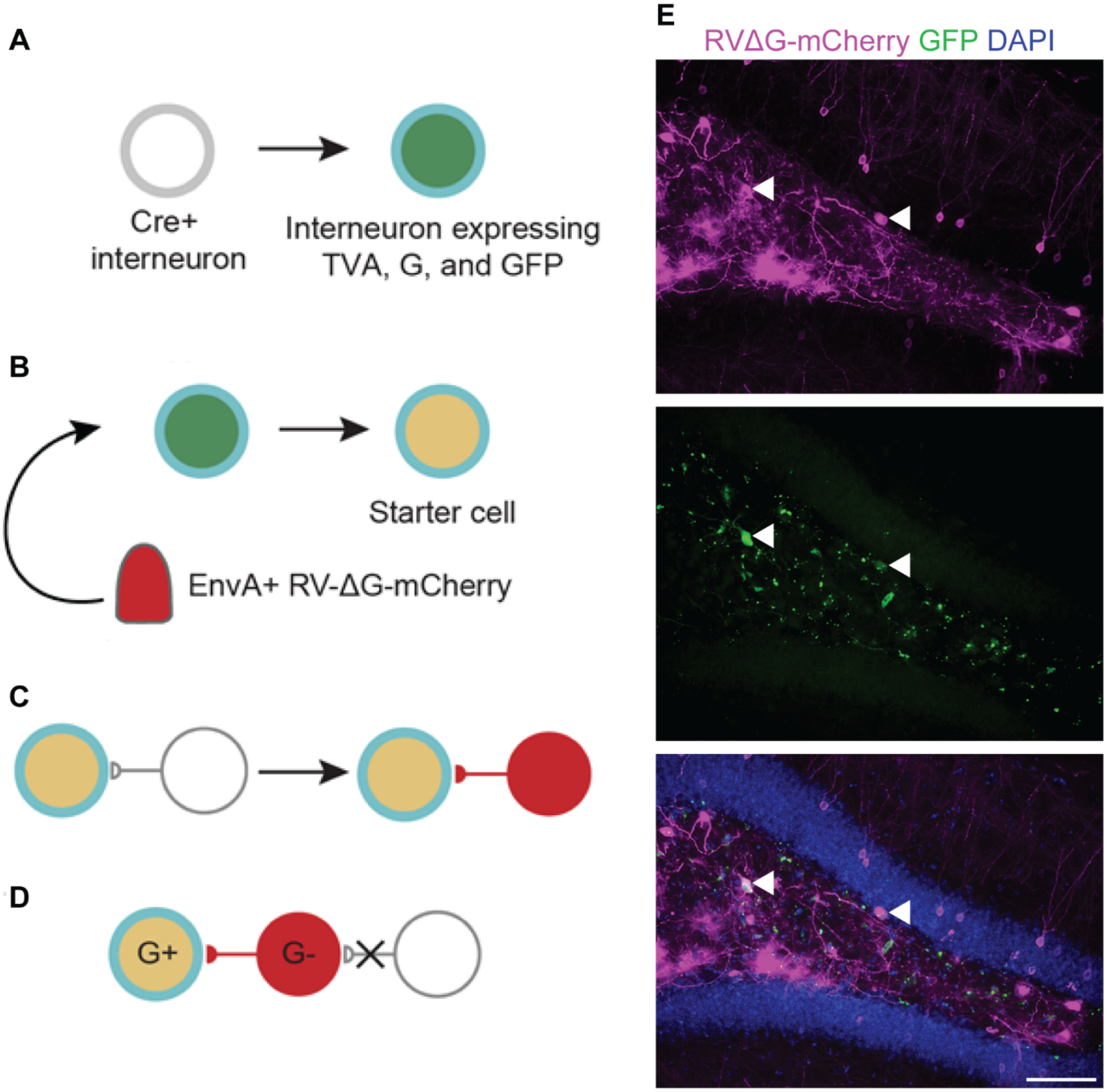

Figure 1.4. **Monosynaptic rabies tracing in dentate gyrus**. **A-E. A.** SST-Cre expressing neurons are infected with a cre-dependent AAV expressing TVA (blue ring), G protein, and GFP (green fill). **B.** EnvA-pseudotyped rabies virus expressing mCherry (red fill) infects TVA-expressing neurons, generating starter cells (yellow fill). **C.** Rabies virus infects neurons directly connected to starter cells (red fill). **D.** Trans-synaptic spread is dependent on G protein, thus limited to one monosynaptic step from starter cells. **E.** Monosynaptic tracing of SST-expressing neurons in dentate gyrus. Rabies-labeled cells (magenta, top panel), GFP-expressing hilar SST+ neurons (green, middle panel), and overlaid images with DAPI counterstain (bottom panel). Scale bar, 500 μm.

1.12 Tissue clearing theory and approaches

Tissue clearing involves maximizing the transmission of light passing through a sample by refractive index matching while minimizing light absorption and scattering. Mammalian tissues are opaque due to light absorption in the visible spectrum by organic components such as lipids (van Veen et al., 2005) and inorganic components such as hemoglobin (Faber et al., 2003). Heterogeneous distribution of tissue components with variable refractive indices such as lipids (RI ~ 1.45), water (RI ~ 1.33), proteins and amino acids (RI ~ 1.6) leads to incoherent random scattering of light passing as it passes through tissue (Schmitt and Kumar, 1996).

Tissue clearing broadly refers to approaches involving dehydration, dilapidation, and refractive index matching. The leftover proteins and carbohydrates are refractive index matched to an immersion solution such that light passing through the immersion media is not scattered when it passes through tissue, rendering the tissue optically transparent. The earliest tissue clearing method was developed by Werner Spalteholz who rendered human organs transparent using a combination of ethanol and benzene for clearing and equal parts methyl salicylate and benzyl benzoate for refractive index matching (Spalteholz, 1911). Spalteholz succeeded in clearing entire human organs, however for nearly a century after the development of the Spalteholz method, tissue clearing had few applications in biology. Starting in the early 2000's, numerous novel tissue clearing methods emerged as a valuable tool to probe the intact structure of the nervous system. Broadly, these novel methods can be classified into distinct categories including hydrophobic, hydrophilic, and hydrogel-based methods (Ueda et al., 2020b).

Hydrophobic methods use organic solvents for dehydration and delipidiation and can rapidly clear large specimens. Ali Ertürk and Hans-Ulrich Dodt's group developed 3D imaging of solvent-cleared organs (3DISCO) and applied this method to rapidly render brain, spinal cord, immune organs and tumors optically transparent using a THF-based protocol (Ertürk et al., 2012). 3DISCO was modified by to incorporate immunolabeling (immunolabeling-enabled three-dimensional imaging of solvent-cleared organs – iDISCO) which was found to be compatible with a wide range of antibodies and used to image entire mouse brains, embryos and kidneys (Renier et al., 2014). However, THF-based approaches lead to disproportionate shrinking of the cortex compared to subcortical structures. This led to the development of iDISCO+ by Nicolas Renier and Marc Tessier-Lavigne's group, which replaced THF with a methanol and dichloromethane-based method to produce isotropic shrinkage and permitted accurate registration of the brain to standardized brain atlases (Renier et al., 2016). DISCO-based approaches have taken advantage of the tissue-shrinking effects to image increasingly larger specimens. uDISCO (ultimate DISCO) has the advantages of shrinking tissue, but also preserves endogenous fluorescence. uDISCO replaces THF (containing an ether group that is prone to reactivity) with tert-butanol, a tertiary alcohol that is more stable. Another change is replacing dibenzy ether (which contains benzylic C-H and C-O bonds that can form peroxides) with diphenyl ether, which is less prone to peroxidation and free-radical formation. Since uDISCO can shrink tissues by up to 65%, this method was used to image entire mouse and rat bodies, permitting tracking of stem cells injected into circulation across the entire body (Pan et al., 2016). vDISCO (v for the variable-domain of heavy-chain antibodies, i.e. nanobodies) involves continuous perfusion of nanobodies throughout the sample. The molecular weight of nanobodies is on the order of ~15kDa, compared to traditional IgGs which are on the order of ~150kDa. Smaller molecular weight enables greater diffusion into tissue, which was used to label and image the intact nervous system of an entire mouse – the first whole body connectome. This method was used to reveal that a central TBI can produce peripheral degeneration distal from the injury site (Cai et al., 2019). The most recent development in solvent-based methods is SHANEL (small-micelle-mediated human organ efficient clearing and labeling), which incorporated new developments in permeabilization chemistry to render an entire human brain transparent and immunolabel large chunks of tissue (Zhao et al., 2020). Since human tissue contains residual blood, an amine-based decolorization step incorporated was incorporated to chelate and precipitate heme, which scatters and absorbs light and hinders tissue transparency. The second major change was the incorporation of acetic acid and guanidine hydrochloride treatment to denature the extracellular matrix, which hinders antibody penetration. Lastly, the addition of a novel detergent that produces micelles of much smaller diameter compared to traditional detergents such as Tween-20, Triton-X, or SDS allowed for enhanced permeabilization into deeper parts of large tissue chunks. These improvements permitted immunolabeling of centimeter-thick chunks of human cortical tissue for the first time. One of the drawbacks to DISCO-based methods is quenching of endogenous fluorophores. However, recently developed FDISCO has been shown to preserve endogenous fluorescence by pH buffering the THF solution prior to use (Qi et al., 2019).

Hydrogel-based clearing methods involve cross-linking proteins within the sample to form a polymer, followed by accelerated clearing using detergents and electrophoresis. In 2013, Kwanghun Chung and Karl Deisseroth developed the cleared lipid-extracted acryl-hybridized rigid immunostaining/in situ hybridization-compatible tissue hydrogel (CLARITY) method which covalently bonds proteins to an acrylamide polymer network (Chung et al., 2013). Lipids are actively removed using a combination of boric acid, SDS, and electrophoresis, or passively without the use of electrophoresis by circulating the detergent solution using a peristaltic pump. The acrylamide polymer network prevents excessive loss of protein compared to tissue fixed with PFA alone (10% versus 70%) (Chung *et al.*, 2013). One of the advantages of hydrogel-based methods is the ability to label nucleic acids, which is not possible using solvent-based methods (Ueda *et al.*, 2020b). One of the drawbacks of hydrogel-based methods is reduced penetration of molecules and probes such as antibodies due to the presence of the crosslinked polymer network. This has led to the development of strategies to enhance probe penetration using electrokinetic, centrifugation, and convection-based methods. Stochatic electrotransport involves using a rotating electric field to increase the diffusion of charged molecules without affecting the proteins and nucleic acids fixed in the hydrogel network (Kim et al., 2015b). This method significantly decreases the amount of time needed to clear tissue samples and enhances penetration of dyes and probes uniformly into polymerized tissue (Kim *et al.*, 2015b). However, one of the downsides of electrokinetic-based approaches is the need for specialized equipment. Active clarity technique-pressure related efficient and stable transfer of macromolecules into organs (ACT-PRESTO) relies on the same acrylamide and PFA-linked hydrogel network to fix proteins used in the original CLARITY protocol, with enhanced antibody labeling using centrifugation or convective flow delivered via a syringe pump. Either centrifugal or convective flow produce similar results, with 3 hours of either method producing superior antibody penetration compared to 48 hours of free diffusion (Lee et al., 2016), albeit lower penetration than with enhanced solvent-based methods (Zhao *et al.*, 2020). Taken together, there are many effective clearing methods however the selection of the ideal protocol depends on the nature of the scientific question. In order to image cleared tissue, traditional microscopes are not suitable due to their limited working distance and slow image acquisition. Light-sheet microscopy has emerged as an ideal approach to rapidly image cleared tissue to produce high-resolution three dimensional image volumes for analysis.

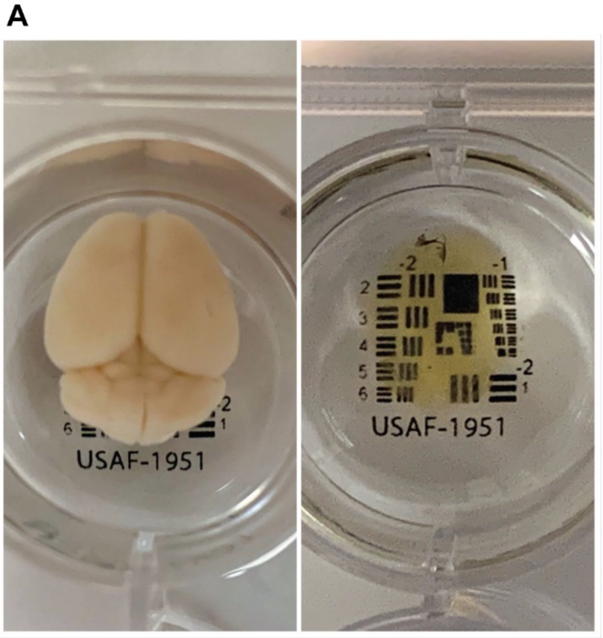

Figure 1.5. **Cleared mouse brain**. **A.** Whole mouse brain before (left panel) and after (right panel) iDISCO clearing and refractive index matching.

1.13 Light sheet microscopy

Advances in sample preparation and imaging over the course of hundreds of years enabled neuroanatomists to visualize and understand the nervous system. In the mid-19th century, the development of the microtome and the use of formalin fixation enabled scientists to produce thin sections of tissues for observation with light microscopes, giving rise to the field of histopathology. Advances such as the development of immunofluorescence have enabled selective contrast enhancement of proteins of interest (Coons et al., 1941).

High-resolution imaging of tissue hundreds of micrometers thick has been made possible through advances including confocal microscopy to remove out-of-focus light using a physical aperture (Minsky, 1988), and two-photon microscopes increase 3D resolution by exciting fluorophores with two different colored photons simultaneously (Denk et al., 1990). In order to image larger volumes such as a mouse brain (~ $1cm^3$ in volume), methods of reconstructing 3-dimensional volumes from 2-dimensional sections have been developed over the past decade. Serial two-photon tomography (Ragan et al., 2012) and fluorescence micro-optical sectioning tomography (Gong et al., 2013) utilize two-photon or confocal microscopy paired with a microtome to acquire optical sections while tissue is continuously removed. While these methods have permitted high-resolution acquisition of large tissue volumes, they are computationally intensive and destructive to the sample.

Light sheet microscopy uses a different approach but with many of the advantages of the methods above: rapid image acquisition, high signal-to-noise ratio, and low phototoxicity. A sheet of laser light illuminates a thin section of a cleared sample, and a lens orthogonal to the laser is used to detect emitted light. Out-of-focus light is minimized by illumination using a sheet of laser light thinner than a typical tissue section (~1,5 μm -10 μm thick). Photobleaching is reduced due to illumination of only a thin slice of the sample, in contrast to confocal or widefield illumination. Rapid volumetric imaging is made possible by programming a moveable stage to pass different parts of the sample through the laser light. While the basic principle of imaging orthogonal to the illumination objective was demonstrated over 100 years ago, the lack of digital imaging approaches prevented application until recently (Ueda et al., 2020a). The first demonstration of optical sectioning paired with digital imaging and 3D reconstruction involved imaging a guinea pig cochlea stained with fluorescein (Voie et al., 1993). Development of commercial light-sheet microscope platforms started with the Ultramicroscope, which was the first application of light-sheet imaging in cleared brain tissue (Dodt et al., 2007). In recent years, advances in optics and camera acquisition speed have rapidly expanded the applications of light-sheet microscopy to ultra-fast imaging of live specimens and super-resolution imaging (Ueda *et al.*, 2020a). Light sheet microscopy has enabled high-throughput imaging of entire organs (Ertürk *et al.*, 2012) embryos (Renier *et al.*, 2014), and organisms (Cai *et al.*, 2019) at resolutions much greater than traditional structural imaging methods. 9.4T structural MRI can achieve 350 μm resolution compared to 300 nm resolution of modern light-sheet microscopes such as the MuVi SPIM, a 100-fold difference (Kemper et al., 2018; Krzic et al., 2012). Fast high-resolution light-sheet imaging paired with advances in automated detection have allowed investigators to quantify millions of neurons in intact brains, which would otherwise by prohibitively costly using manual approaches (Matsumoto et al., 2019; Zhao *et al.*, 2020).

Visual cortex structure and function

Reflected light from the external environment enters the eye and is sampled by photoreceptors in the retina that transmit to retinal ganglion cells, which are the first stage of visual processing before signal transmission through the optic nerve. The optic nerve transmits visual information to the lateral geniculate nucleus of the thalamus (LGN), before being relayed to the primary visual cortex (V1). Layer 4 is the main target of input neurons from the LGN, with both excitatory neurons and PV-expressing neurons receiving nearly all LGN input (Ji et al., 2016). SST and VIP-expressing neurons receive little input from layer 4 compared to other neuron types (Ji *et al.*, 2016). Layer 4 excitatory neurons receive most of their input from the LGN and other neurons in layer 4, thus serving as the major input layer for visual information entering V1 (Seeman et al., 2018). Excitatory neurons in layer 4 project to layers 2/3 and layer 5 of V1, in addition to other neocortical structures (Callaway, 1998; Harris et al., 2019; Olivas et al., 2012). Excitatory neurons in layers 2/3 receive excitatory feed-forward input from layer 4, layer 5, LGN, as well as recurrent circuits within layers 2/3 (Olivas *et al.*, 2012; Seeman *et al.*, 2018). SST+ neurons in layer 2/3 do not receive input from layer 4, but do receive input from layer 2/3 excitatory neurons, and provide input to nearly all other types of neurons except other SST neurons (Adesnik et al., 2012). While VIP-expressing interneurons in layer 2/3 do not receive substantial excitatory input from layer 4, they do receive input from other sensory areas and facilitate cross-modal sensory processing by modulating visual responses in response to auditory stimuli (Ibrahim et al., 2016). Layer 2/3 excitatory neurons are the major source of output to other visual areas (Harris *et al.*, 2019). Layer 5 excitatory neurons receive feed-forward input from layer 4, layer 2/3, LGN, and recurrent input from within layer 5 (Ji *et al.*, 2016). Layer 5 excitatory neurons are the major source of output from the visual cortex to subcortical areas including the pulvinar thalamus and superior colliculus (Kim et al., 2015a; Lur et al., 2016). Layer 6 contains two excitatory cell types cortico-cortico and cortico-thalamic projection neurons (Vélez-Fort et al., 2014). Cortico-cortico projection neurons receive input from layers 5 and 6, show broad stimulus selectivity, and project to the deep layers of V1 and V2. Cortico-thalamic neurons receive input from retrosplenial cortex and superficial layers of V1 and V2, show sharp orientation tuning, and project to superficial layers of V1 and the thalamus (Vélez-Fort *et al.*, 2014). Layer 1 is nearly entirely comprised of GABAergic interneurons of four different classes: NDNF+/NPY+ neurogliaform cells, NDNF+/NPY- canopy cells, alpha-7 expressing cells, and VIP-expressing cells (Ibrahim et al., 2020; Schuman et al., 2019). These interneurons receive input from other sensory areas which endows them with the ability to modulate visual responses across sensory domains. Excitatory neurons in layer 5 of auditory cortex project directly to layer 1 interneurons (Ibrahim *et al.*, 2016). Sound alone activate layer 1 V1 interneurons and sharpens orientation selectivity of excitatory neurons in layer 2/3, an effect that is abolished by suppressing layer 1 interneuron activity (Ibrahim *et al.*, 2016). These results demonstrate how GABA neurons in layer 1 are involved in multi-modal sensory processing. Taken together, cell-type and layer-specific roles of excitatory and inhibitory neurons in visual cortex make distinct contributions to visual information processing.

CHAPTER TWO

Selective vulnerability of hippocampal interneurons to graded traumatic brain injury

Abstract

Traumatic brain injury is a major risk factor for many long-term mental health problems. Although underlying mechanisms likely involve compromised inhibition, little is known about how individual subpopulations of interneurons are affected by neurotrauma. Here we report long-term loss of hippocampal interneurons following controlled cortical impact (CCI) injury in young-adult mice, a model of focal cortical contusion injury in humans. Brain injured mice displayed subfield and cell-type specific decreases in interneurons 30 days after impact depths of 0.5 mm and 1.0 mm, and increasing the depth of impact led to greater cell loss. In general, we found a preferential reduction of interneuron cohorts located in principal cell and polymorph layers, while cell types positioned in the molecular layer appeared well preserved. Our results suggest a dramatic shift of interneuron diversity following contusion injury that may contribute to the pathophysiology of traumatic brain injury.

Introduction

Traumatic brain injury (TBI) is a serious neurological disorder that occurs after an external mechanical force damages the brain (e.g., from a bump, blow, or jolt to the head) and afflicts nearly 6 million Americans (Centers for Disease Control and Prevention, 2014). Trauma greatly increases the risk for a number of physical, cognitive, emotional, social and psychiatric health problems, and it is one of the most common causes of medically intractable epilepsy in humans (Centers for Disease Control and Prevention, 2014; Frey, 2003; Herman, 2002; Rao and Lyketsos, 2000; Scholten et al., 2015). Following TBI, damaged neural circuits undergo major reorganization that includes progressive neuron loss, synaptic circuit remodeling and changes in the cellular environment (Hunt et al., 2013a).

As the primary source of inhibition in the brain, GABAergic interneurons coordinate information processing within cortical circuits by precisely timing and synchronizing excitatory principal populations. Such spatiotemporal control over input-output activity is achieved by a remarkable diversity of interneurons, each with distinct molecular, anatomical and electrophysiological properties (Freund and Buzsáki, 1996; Pelkey *et al.*, 2017). In hippocampus, deficits in interneuron number or function have been implicated in a wide range of neurodegenerative disorders, such as epilepsy (de Lanerolle et al., 1989) Alzheimer's disease (Satoh et al., 1991) and stroke (Liepert et al., 2000). Studies examining brain tissue samples from patients with TBI have also found reductions in the number of interneurons in hippocampus (Swartz *et al.*, 2006) and neocortex (Buriticá *et al.*, 2009). These clinical findings are supported by a growing body of experimental data using in vivo rodent TBI models that display reductions in GABAergic neurons (Butler *et al.*, 2016; Cantu *et al.*, 2015; Gupta et al., 2012; Huusko et al., 2015; Lowenstein et al., 1992; Nichols *et al.*, 2018; Santhakumar et al., 2000; Toth et al., 1997) and/or a marked loss of inhibition within injured regions of the brain (Almeida-Suhett et al., 2014; 2015; Butler *et al.*, 2016; Hunt *et al.*, 2010; Li and Prince, 2002; Nichols *et al.*, 2018; Pavlov et al., 2011). However, it is unclear whether certain interneuron cohorts are preferentially lost after TBI as most studies focus on only a single cell type, and the effect of graded contusive injury has not been systematically evaluated.

Identifying how molecularly-distinct classes of interneurons are altered by mechanical injury is critical to understanding cortical network dysfunction in TBI and for designing precision therapies. Here, we took advantage of a widely used model of focal cortical contusion injury to directly compare and contrast the long-term effect of graded mechanical trauma on hippocampal interneuron subpopulations. We found a dramatic change in the diversity of hippocampal interneurons after contusive injury.

Methods

Animals

All experiments were first approved by the University of California, Irvine Animal Care and Use Committee and adhered to National Institutes of Health guidelines and regulations for the Care and Use of Laboratory Animals. Wild-type CD1 mice (Charles River, cat no. 022) were crossed with a hemizygous glutamic acid decarboxylase - enhanced green fluorescence protein (GAD67-GFP) knock-in line (Tamamaki et al., 2003). All animals were bred in house under a normal 12 h/12 h light/dark cycle and maintained on a CD1 background strain for >10 generations before their use in experiments. Water and food were available ad libitum. At P60, male littermates were randomly assigned for brain injury, sham injury or no injury and experiments were performed 30d later.

Controlled cortical impact (CCI) injury

Male mice (P60) were subjected to a unilateral cortical contusion injury by controlled cortical impact (CCI) as previously described (Hunt *et al.*, 2012; Hunt *et al.*, 2009; 2010; 2011). Briefly, mice were anesthetized by 2% isoflurane inhalation and placed in a stereotaxic frame. The skull was exposed by midline incision, and a 4–5 mm craniotomy was made lateral to the sagittal suture and centered between bregma and lambda. The skull cap was removed, leaving the exposed underlying dura intact. The contusion device consisted of a computer-controlled, pneumatically driven impactor fitted with a beveled stainless-steel tip 3 mm in diameter (Precision Systems and Instrumentation). Brain injury was delivered using this device to compress the cortex to a depth of 0.5 mm or 1.0 mm at a velocity of 3.5 m/s and 500 ms duration. The incision was sutured, and the animal was allowed to recover for 30d. A qualitative postoperative health assessment was performed daily for 5d after TBI and periodically thereafter. All animals that received surgery were treated with buprenorphine hydrochloride (Buprenex; 0.05 mg/kg, delivered i.p.) at the time of surgery and then once daily for 3 d. We used a total of 33 mice subjected to CCI (13 at 0.5 mm depth and 20 at 1.0 mm depth), 11 mice subjected to craniotomy only (sham controls) and 7 uninjured controls. A percentage of identically treated mice have previously been shown to exhibit spontaneous seizures (Hunt *et al.*, 2009; 2010), but mice in the present study were not monitored for seizure activity. All brain-injured mice survived and remained otherwise healthy until the day of experimentation.

Immunostaining

At P90 (30 days after CCI injury), animals were perfused transcardially with 4% paraformaldeyde (PFA) in 0.1 M PBS, pH 7.4. Brains were removed and post-fixed overnight in the same solution. Free-floating vibratome sections (50 µm) were processed using standard immunostaining procedures according to our published protocols (Dinday et al., 2017; Hunt *et al.*, 2013b). Primary antibody dilutions were as follows: chicken anti-green fluorescent protein (GFP; 1:1000; Aves, Cat No. GFP1020); mouse anti-neuronal nuclei (NeuN; 1:1000; Millipore, Cat No. MAB377), mouse anti-parvalbumin (PV; 1:500; Sigma, Cat No. P3088); rabbit anti-somatostatin (SST; 1:200; Santa Cruz, Cat No. SC-7819); rabbit anti-calretinin (CR; 1:1000; Millipore, Cat No. AB5054); rabbit anti-neuronal nitric oxide synthase (nNOS; 1:1000; Millipore, Cat No. AB5380); mouse anti-reelin (1:500; Millipore, Cat No. MAB5364). Secondary antibodies included Alexa Fluor 488 and 594 (1:1000; Life Technologies). Sections were then mounted on charged slides (Superfrost plus; Thermo Fisher Scientific) with Aqua-Mount medium.

Volumetric analysis

Volumetric analysis was performed 30 days after CCI to estimate the volume of the remaining neocortical tissue as previously described (Hall et al., 2005a). Sections were imaged using a Leica DM6 widefield fluorescence microscope with an x5 objective equipped with a motorized stage.

Cortex volume was quantified by tracing the borders of the neocortex in a series of 8 NeuN-stained coronal sections containing the lesion (50 µm thick, 300 µm apart) using Imaris 9.1 software. Neocortex was defined as the region between the dorsal aspect of the corpus callosum and the pial surface. Regions of the cortical subplate (e.g., amygdala, endopiriform nucleus) were excluded from analysis. The % of the ipsilateral cortex remaining for each animal was calculated using the following formula:

$$\%\ \text{Cortex Remaining} = \left(\frac{\sum i_n}{\sum c_n}\right) \times 100$$

where i = the area of the ipsilateral cortex and c = the area of the contralateral cortex and n = the section number.

Cell quantification

Fluorescently labeled sections (50 µm) were imaged using a Leica DM6 widefield fluorescence microscope with an x10 objective and cell counts were performed using Imaris 9.1 or ImageJ software, as described previously (Dinday *et al.*, 2017; Hunt *et al.*, 2013b). All cells that expressed GFP (or subtype marker) were counted in every sixth coronal section in all layers of the hippocampus (300 µm apart). To define the border of hilus/CA3, straight lines were drawn from the ends of the granule cell to the proximal end of the CA3 pyramidal cell layer. For quantification of GFP+ cells in each hippocampal sub-region, four (CA3 analysis) to five (dentate gyrus and CA1 analysis) sections of the dorsal hippocampus surrounding the injury epicenter were analyzed per hemisphere for each animal and the values averaged to obtain a mean cell density (cells/mm^2). To quantify laminar distribution of GFP+ cells and interneuron subtypes, three sections surrounding the injury epicenter were analyzed per hemisphere for each animal.

Statistics

Data analysis was performed using Imaris 9.1, Microsoft Excel, Graphpad Prism 6 or Systat 14 programs. Experimental groups were compared by one-way ANOVA, two-way repeated measures ANOVA followed by a Tukey's post hoc test for multiple comparisons or Chi-Square analysis. Cell layer distributions were compared by Chi-Square analysis, using the cell density for each layer (cells/mm^2). Corresponding pie charts expressed cell densities for each layer as a proportion of the sum of all layers. Data are expressed as mean ± SEM, and significance was set at $P < 0.05$.

Results

Histological responses to graded CCI injury

We first examined gross damage to the brain 30 days following either 0.5 mm or 1.0 mm depth of impact at P60. Uninjured controls and sham-injured animals showed no overt cortical lesion in any animal examined (**Figure 2.1A**). In all mice injured at 0.5 mm impact depth, the lesion consisted of a cortical cavity restricted to neocortex (*n* = 4 animals, **Figure 2.1B**). In mice injured at 1.0 mm depth, the injury extended through the thickness of the neocortex and included substantial distortion of the principal cell layers in hippocampus. At the impact site, loss of NeuN staining in hippocampus was evident as a thinning of the pyramidal cell layer in CA1 as well as the granule cell layer in dentate gyrus (*n* = 4 animals, **Figure 2.1C**). Quantification of the % of ipsilateral cortex remaining at 30 days post-injury, a commonly used measure of cortical damage, revealed a significantly greater lesion in both the 0.5 mm and 1.0 mm impact groups compared to uninjured or sham-injured animals, and significantly greater cortical damage after 1.0 mm injury as compared to 0.5 mm impact depth (uninjured control: 100 ± 1%; sham: 101 ± 1%, 0.5 mm: 84 ± 3%, 1.0 mm: 71 ± 1%, $F_{(3,11)}=49.5$, P= 1.1E-06, one-way ANOVA; **Figure 2.1D**). This pattern of hippocampal cell loss and cortical damage is consistent with prior studies demonstrating graded morphological and histological injury responses following 0.5 mm or 1.0 mm impact depths (Hunt *et al.*, 2009; Pleasant *et al.*, 2011; Saatman *et al.*, 2006).

Regionally localized interneuron loss in hippocampus after CCI

To visualize the long-term effect of contusion injury on hippocampal interneurons, we used a GAD67-GFP knock-in reporter line labeling nearly all GABAergic interneurons (Tamamaki *et al.*, 2003). We first quantified the density of GFP+ neurons in dentate gyrus, CA3 and CA1 sub-regions of the hippocampus 30d following CCI (**Figure 2.2**). Comparisons were made between age-matched uninjured controls, animals that received only a craniotomy (sham injury) and brain injured animals that received either 0.5 mm or 1.0 mm impact. Both injury severities produced a significant reduction in GFP+ cell densities ipsilateral to the injury. In dentate gyrus, the density of GFP+ neurons was reduced by ~20% following 0.5 mm impact and ~40% following 1.0 mm impact ($F_{(7,34)}$= 16.97, P= 2.04E-09, n=5-6 mice per group, one-way ANOVA; **Figure 2.2B**). Cell loss was more robust after 1.0 mm injury as compared to 0.5 mm impact depth (q=6.03, P=0.003, Tukey's post hoc test), suggesting there is a correlation between increasing contusion severity and interneuron loss. In CA3, GABA neuron density was reduced only following 1.0 mm injuries (~21% reduction, $F_{(7,34)}$= 4.77, P= 8.11E-04, n=5-6 mice per group, one-way ANOVA; **Figure 2.2C**). Finally, in CA1, the density of GFP+ neurons was reduced by ~26% following 0.5 mm impact and ~36% following 1.0 mm impact ($F_{(7,34)}$= 18.02, P= 1.86E-09, n=5 mice per group, one-way ANOVA; **Figure 2.2D**). We did not observe a difference between the two injury severities (q=2.82, P=0.5, Tukey's post hoc test), suggesting CCI leads to an "all or none" loss of GABAergic cells in this region. GABA cell loss was only observed ipsilateral to the injury and was not observed in the contralateral hemisphere for any treatment group.

To further visualize the extent of interneuron loss following CCI, we next evaluated interneuron density as a function of distance from the injury epicenter for each hippocampal sub-region. For this analysis, we analyzed GFP+ cell density in the ipsilateral hemisphere at the injury site and ±600µm in rostral and caudal directions (i.e., transverse sections through 1200 µm of dorsal hippocampus surrounding the injury). To limit bias, sections of CA3 that were 600µm caudal to the injury were excluded from analysis, because CA3 was no longer orientated in the coronal plane at this distance. In dentate gyrus, interneuron density was significantly reduced throughout the entire dorsal hippocampus (**Figure 2.2E**).

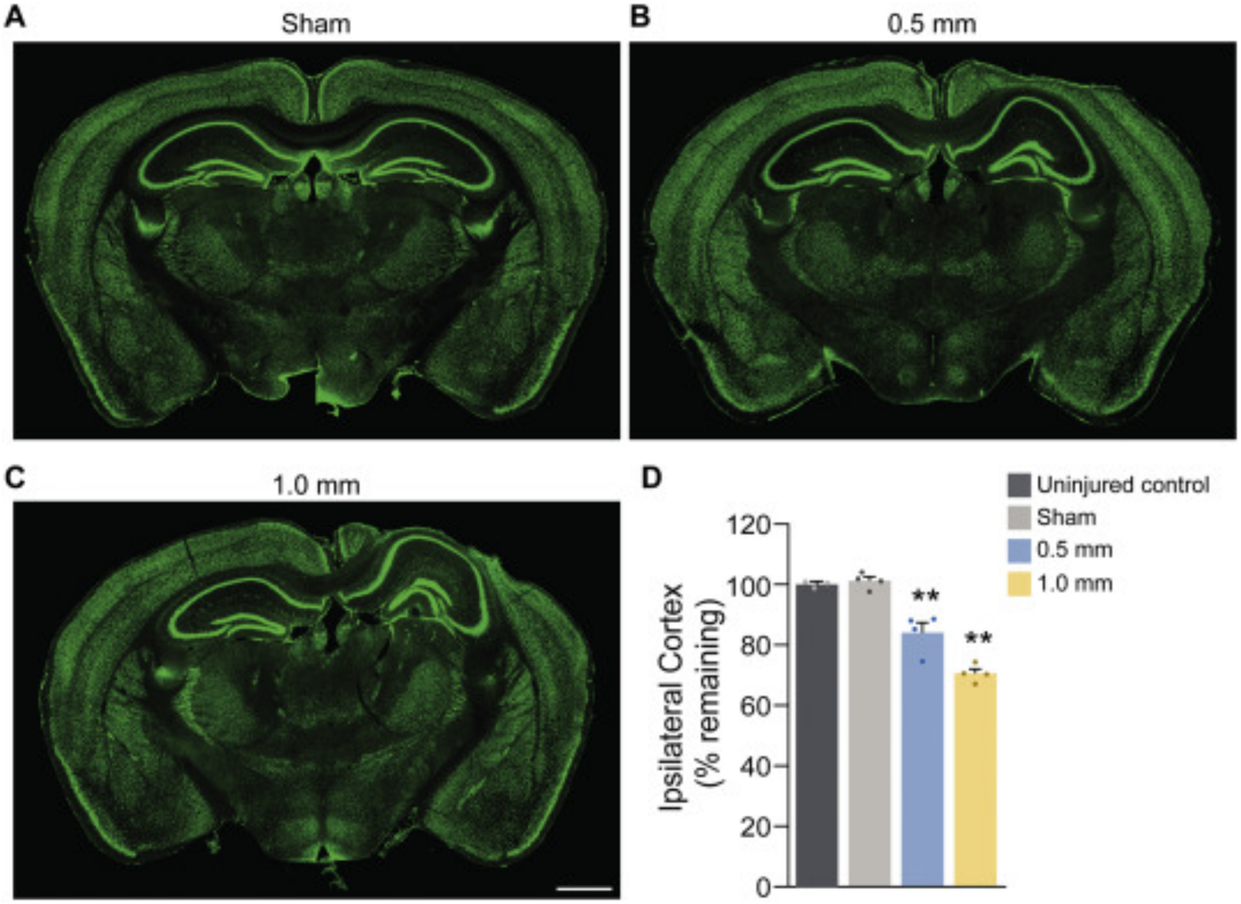

Figure 2.1. Tissue damage following graded cortical contusion injury. A-C, Immunostaining for NeuN (green) in coronal sections taken from the injury epicenter in a sham-injured animal (**A**) and 30d following impact depths of 0.5 mm (**B**) or 1.0 mm (**C**). Quantification of percent cortex remaining ipsilateral to the injury. Scale bar, 1000 µm; error bars, s.e.m.; ** $p < 0.01$.

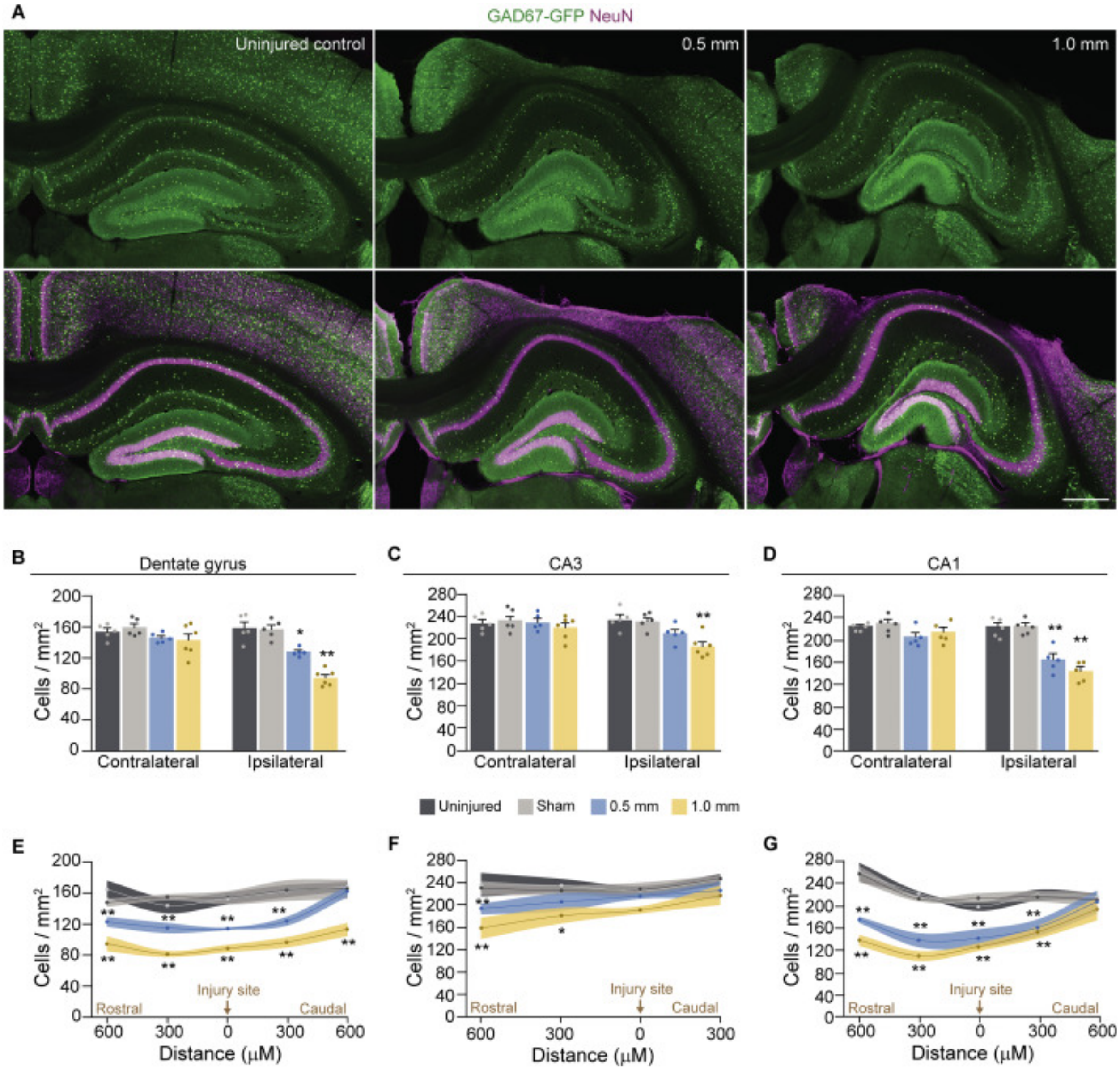

Figure 2.2 Long-term reduction in interneuron density following CCI injury. A. Immunostaining for GAD67-GFP (green) and NeuN (magenta) in coronal sections taken from the injury epicenter of an uninjured animal and 30d following impact depths of 0.5 mm or 1.0 mm. **B-D.** Quantification of GAD67-GFP cell density contralateral and ipsilateral to the injury in dentate gyrus (**B**), CA3 (**C**) and CA1 (**D**). **E-G.** Quantification of GAD67-GFP cell density with distance from the injury site (zero on the *x*-axis) in ipsilateral hemisphere of dentate gyrus (**E**), CA3 (**F**) and CA1 (**G**). Scale bar, 500 □m; error bars, s.e.m.; * $p < 0.05$, ** $p < 0.01$.

However, in CA3 and CA1, the most robust reduction in GFP+ cell density was found within 600 µm rostral to the injury epicenter and GFP+ cell density was not significantly different between injured and uninjured control animals 600 µm caudal to the injury site (**Figure 2.2F,G**). Thus, graded CCI injury produces focal and sub-region specific changes in inhibitory interneuron density in hippocampus.

Hippocampal interneurons show distinct laminar position preferences according to cell type (Freund and Buzsáki, 1996; Klausberger and Somogyi, 2008; Pelkey *et al.*, 2017). Therefore, we next assessed the laminar distribution of GAD67-GFP interneurons 30 days after CCI injury (**Figure 2.3**), focusing on cells in dentate gyrus or CA1 subfields where interneuron diversity has been well characterized and laminar location anatomically defines specific interneuron subtypes. In dentate gyrus, we found a significant loss of GFP+ cell bodies positioned in the hilus ($F_{(3,17)}$= 29.03, P= 6.49E-07, n=5-6 mice per group, one-way ANOVA) and granule cell layer ($F_{(3,17)}$= 25.00, P= 1.83E-06), but GFP+ cell density was not changed in the molecular layer ($F_{(3,17)}$= 0.75, P= 0.54) (**Figure 2.3A**). Loss of GFP+ cells was more extensive following 1.0 mm as compared to 0.5 mm impact depths in this region, consistent with our finding of graded interneuron loss to increasing injury severity. In CA1, we found a reduction in GFP+ cell bodies positioned in all four cell layers: stratum oriens ($F_{(3,16)}$= 5.96, P= 6.30E-03, n=5 mice per group, one-way ANOVA), stratum pyramidale ($F_{(3,16)}$= 66.91, P= 2.85E-09), stratum radiatum ($F_{(3,16)}$= 21.61, P= 7.15E-06) and stratum lacunosum-moleculare ($F_{(3,16)}$= 16.69, P= 3.50E-05) (**Figure 2.3B**). Loss of GFP+ cells was most extensive in the pyramidal cell layer, where both 0.5 mm and 1.0 mm impact depths led to ~50% reduction in GFP+ interneurons.

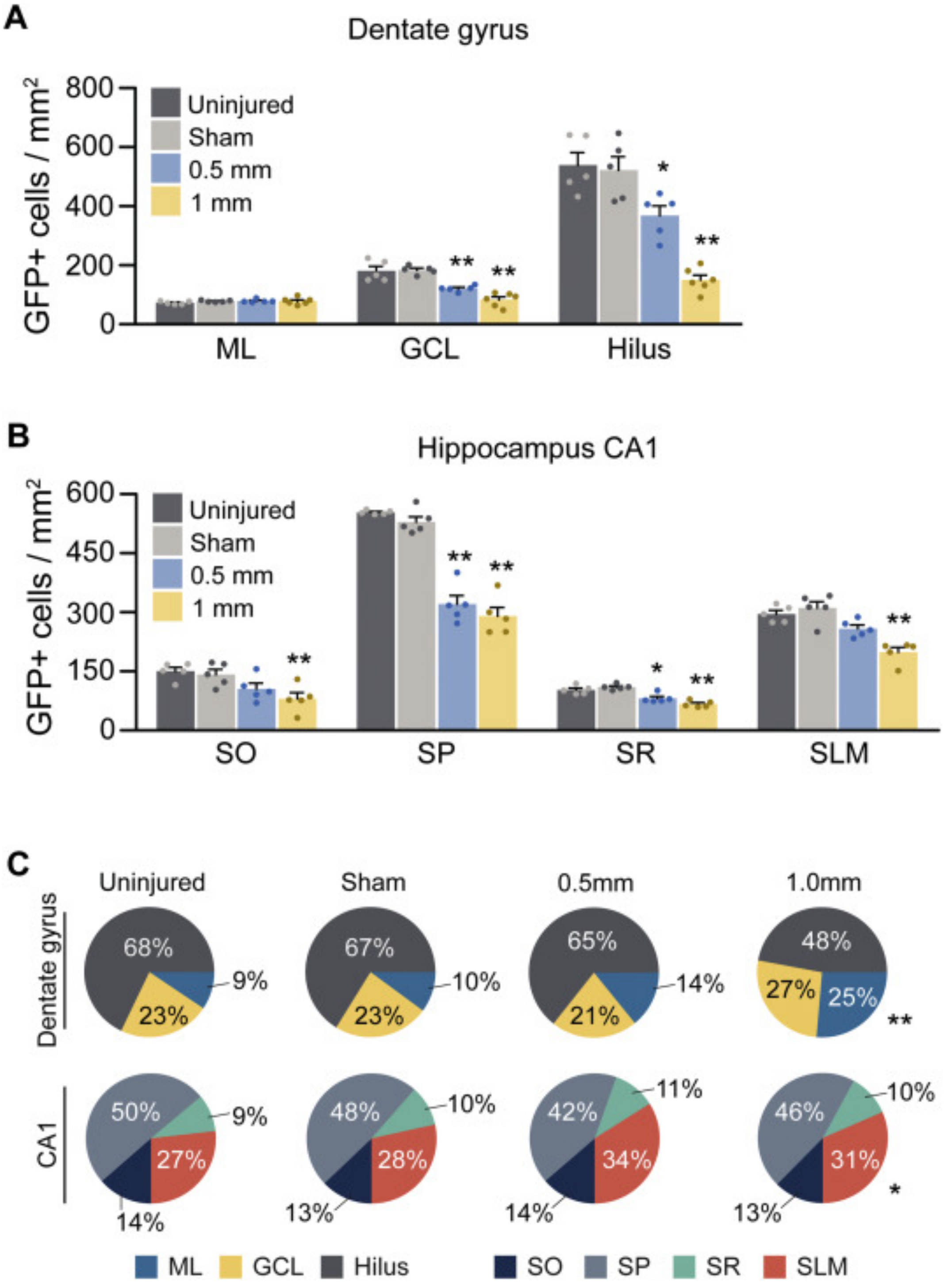

Figure 2.3. Laminar distribution of hippocampal interneurons following graded CCI injury. A. Quantification of GAD67-GFP cell density in dentate gyrus ipsilateral to CCI injury. **B.** Quantification of GAD67-GFP cell density in CA1 ipsilateral to CCI injury. **C.** Relative proportion of interneurons found in each cell layer of the dentate gyrus (top) and CA1 (bottom). ML, molecular layer; GCL, granule cell layer; SO, stratum oriens; SP, stratum pyramidale; SR, stratum radiatum; SLM, stratum lacunosum-moleculare. Error bars, s.e.m.; * $p < 0.05$, ** $p < 0.01$.

Selective loss of molecularly-distinct classes of interneurons after CCI

The constitutive expression of GFP in cells of the GAD67-GFP transgenic mice allows for a systematic investigation of interneurons following neurotrauma. However, interneurons have classically been distinguished based on their unique neurochemical signatures (Freund and Buzsáki, 1996; Pelkey *et al.*, 2017). To delineate the effect of CCI injury on neurochemically-distinct subtypes of interneurons, we performed a series of immunostaining studies 30d after 0.5 mm or 1.0 mm CCI injury using well established markers for hippocampal interneurons (**Figure 2.4**). In dentate gyrus and CA1, we found significant reductions in all cohorts examined (**Figure 2.5**). Interneuron loss was generally more extensive following 1.0 mm as compared to 0.5 mm impact depths in dentate gyrus, but this was not apparent in CA1. It is important to note that we likely overestimated the loss of CR-containing GABAergic interneurons in dentate gyrus, because large numbers of CR-containing mossy cells are found within the hilus, which are glutamatergic interneurons and especially susceptible to brain injury (Toth *et al.*, 1997). In CA3, we found a significant reduction in the density of neurons expressing PV or SST after 1.0 mm impact, while the density of CR-, nNOS- and reelin--expressing neurons were not changed (**Figure 2.5C-E**). Finally, we examined the laminar distribution of each neurochemical marker, focusing on cells within the dentate gyrus and CA1 where interneuron loss is most extensive. In dentate gyrus, there was a significant shift in distribution of markers for PV, nNOS and Reelin following CCI (**Figure 2.6**). For each cell type, the relative proportion of hilar neurons was reduced and molecular-layer neurons increased (PV: X^2= 13.3, d.f. = 6; P = 0.04; nNOS: X^2= 40.4, d.f. = 6; P <0.001; Reelin: X^2= 52.0, d.f. = 6; P <0.001; n=5-6 mice per group; Chi-square), consistent with our findings for GAD67-GFP+ neurons.

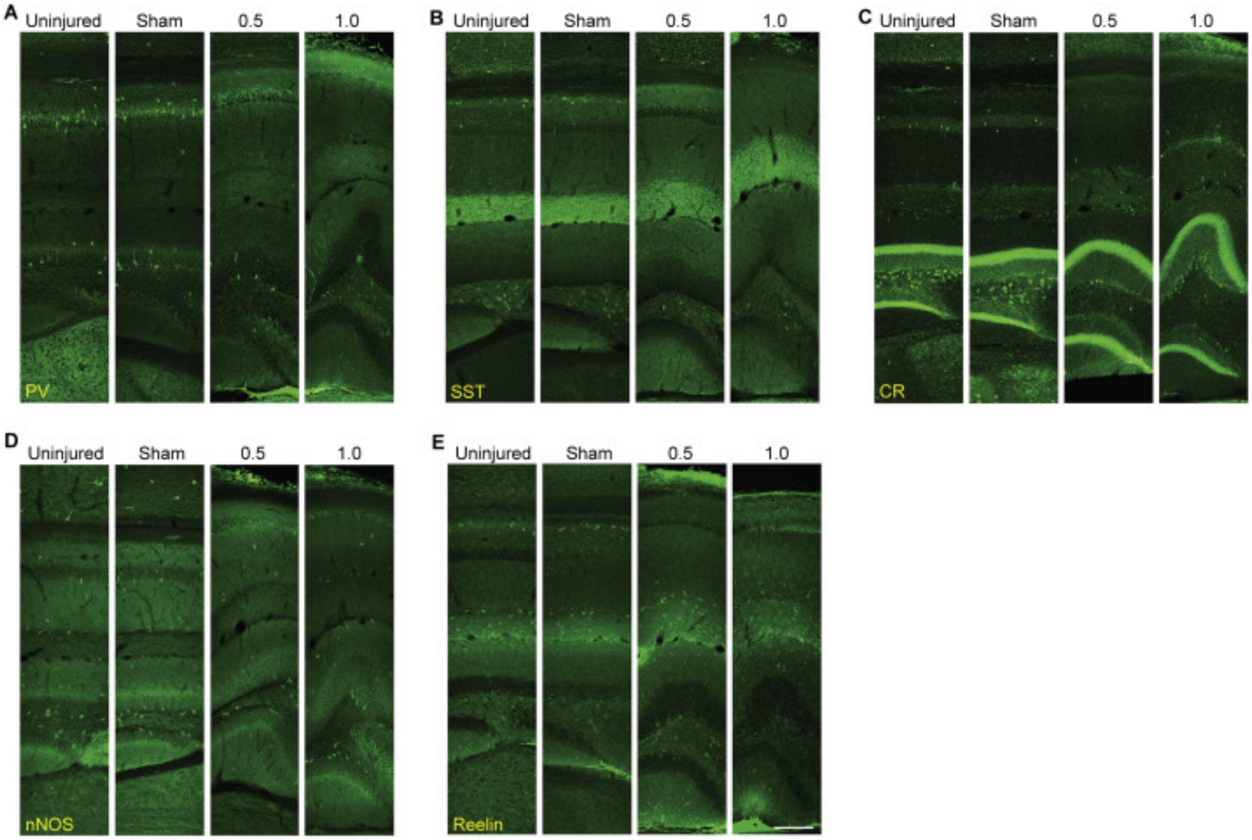

Figure 2.4. Neurochemical markers of hippocampal interneurons in control and brain injured animals. A-E. Immunostaining for PV, SST, CR, nNOS and Reelin in coronal sections of hippocampus at the injury epicenter. Scale bar, 200 μm.

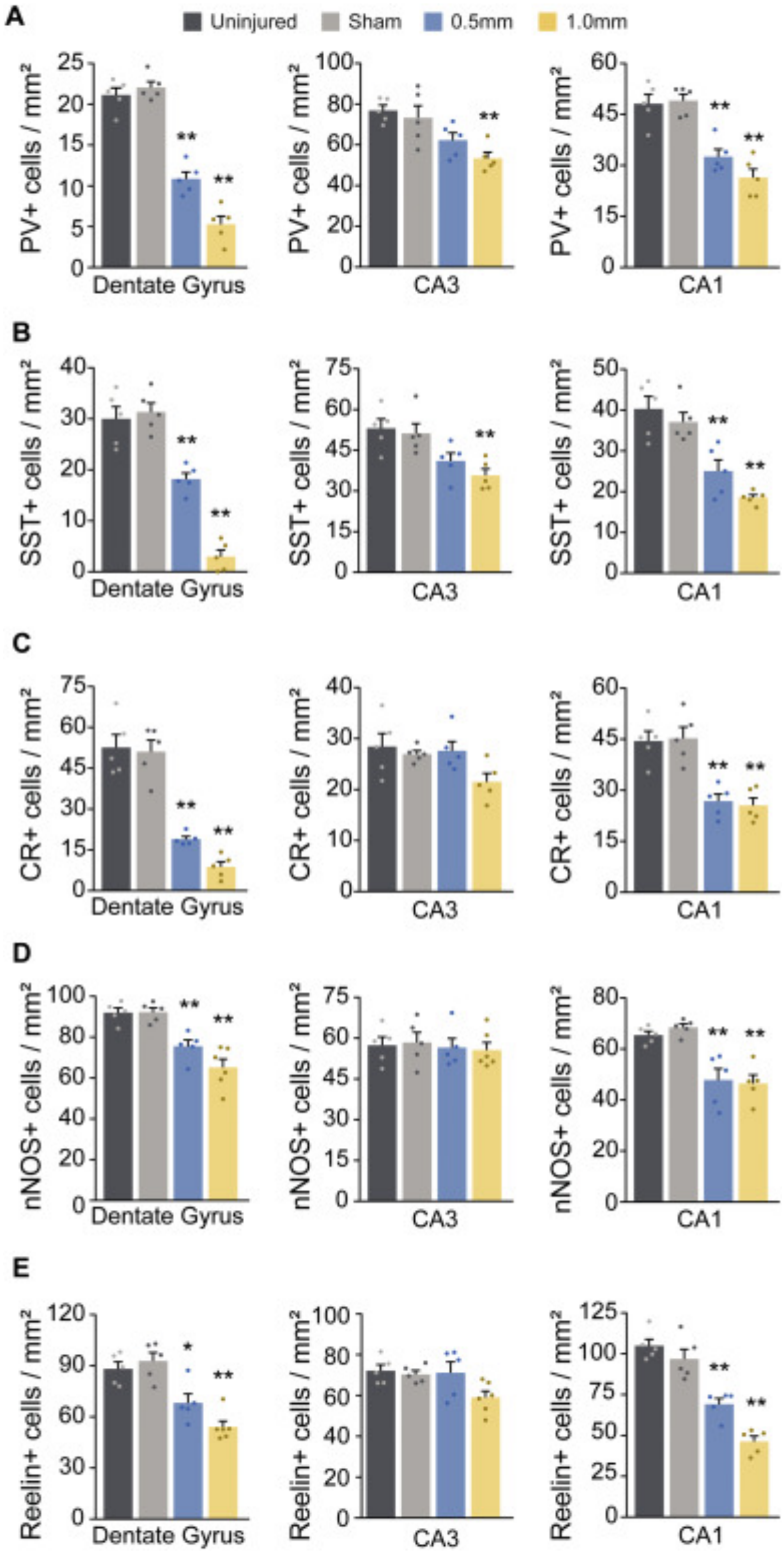

Figure 2.5. Selective loss of molecularly-distinct interneuron cohorts following CCI injury. A-E. Quantification of cell density for PV, SST, CR, nNOS and Reelin ipsilateral to the injury in dentate gyrus, CA3 and CA1. Error bars, s.e.m.; * $p < 0.05$, ** $p < 0.01$.

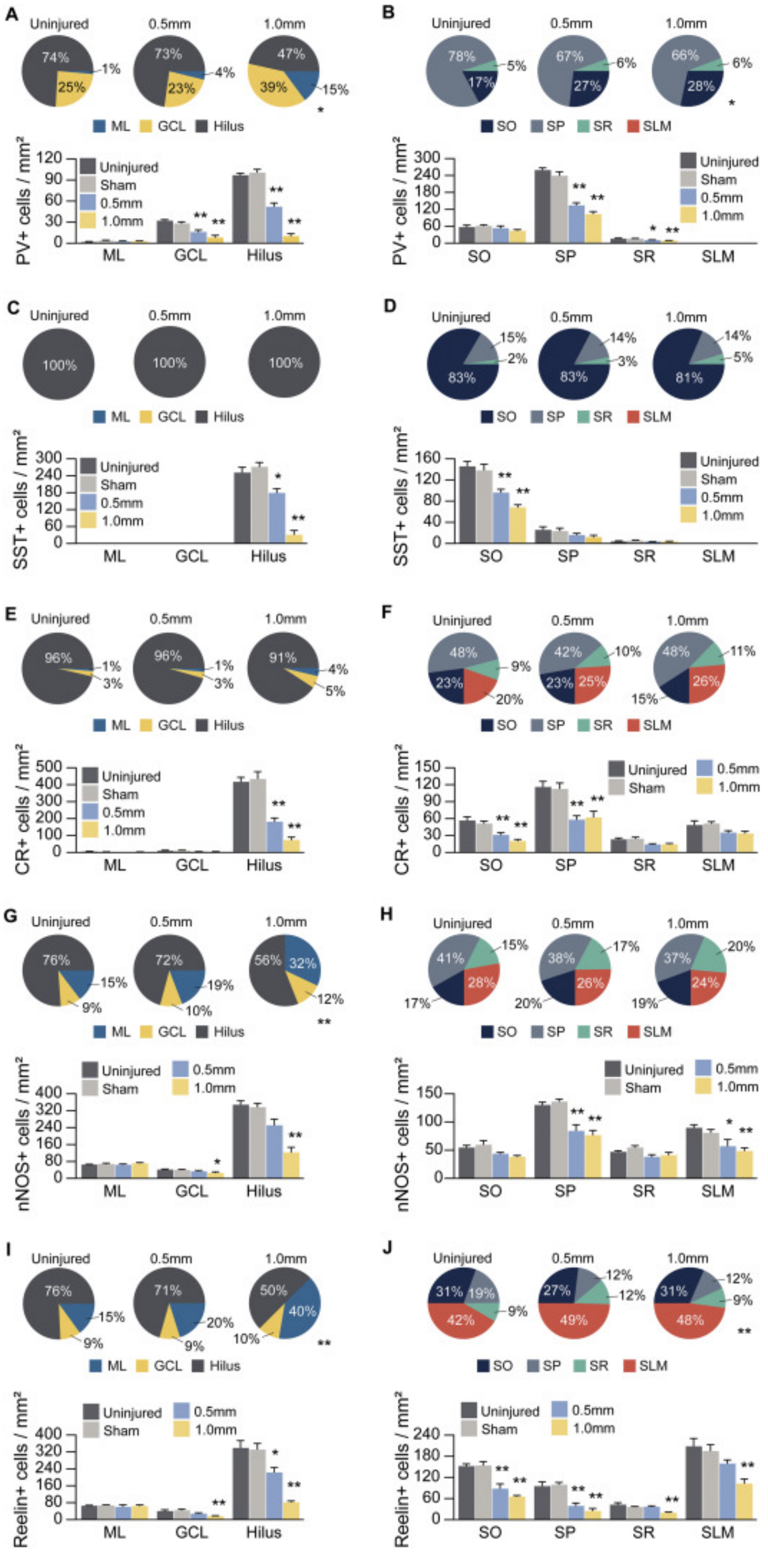

Figure 2.6. CCI produces cell type-specific changes in interneuron distribution. A,C,E,G,I. Quantification of neurons expressing PV, SST, CR, nNOS and Reelin in dentate gyrus ipsilateral to the injury. Pie charts show proportion of neurons found in each cell layer, and bar plots show cell densities in each layer. **B,D,F,H,J.** Quantification of neurons expressing PV, SST, CR, nNOS and Reelin in CA1 ipsilateral to the injury. Pie charts show relative proportion of neurons found in each cell layer, and bar plots show cell densities in each layer. ML, molecular layer; GCL, granule cell layer; SO, stratum oriens; SP, stratum pyramidale; SR, stratum radiatum; SLM, stratum lacunosum-moleculare. Error bars, s.e.m.; * $p < 0.05$, ** $p < 0.01$.

In CA1, there was also a change in the laminar distribution of PV- and Reelin-expressing cells due to disproportionate reduction of these cell types in the pyramidal cell layer after CCI (PV: X^2= 13.3, d.f. = 6; P = 0.04; Reelin: X^2= 22.4, d.f. = 9; P =0.008; n=5 mice per group; Chi-square). Thus, there are graded, regional and cell-type specific changes in the density of hippocampal interneurons following contusive brain injury.

Discussion

Neuron loss is a major feature of TBI in both rodents and human (Anderson et al., 2005; Baldwin *et al.*, 1997; Buriticá *et al.*, 2009; Hall et al., 2008; Hall *et al.*, 2005a; Hall et al., 2005b; Swartz *et al.*, 2006), but the loss of interneurons following contusive injury has not been systematically evaluated. Our results provide the first comprehensive analysis of hippocampal interneurons following graded CCI injury. We found a dramatic reduction in interneuron density that was dependent on impact depth, hippocampal sub-region and laminar position. In agreement with these findings, analysis of neurochemically distinct cohorts of interneurons revealed cell type-specific vulnerability to head injury. Interneurons located in the principal cell and polymorph layers (e.g., PV and SST) were generally more vulnerable to injury than cell types occupying the molecular layer (e.g., nNOS and Reelin). This was observed most clearly in dentate gyrus. Overall, our results demonstrate a reorganization of interneuron diversity following contusion injury that may substantially alter information processing within hippocampal circuits.

Each sub-region of hippocampus displayed a different histological response to CCI injury. In dentate gyrus, interneuron loss correlated quantitatively with contusion depth, consistent with our prior work demonstrating mossy fiber sprouting and seizures are more robust with increasing impact depths (Hunt *et al.*, 2012; Hunt *et al.*, 2009; 2010). While mossy fiber sprouting does not correlate with seizure frequency (Buckmaster and Dudek, 1997), loss of interneurons does (Buckmaster et al., 2017). This may explain the relatively high incidence of seizures following CCI injury as compared to other neurotrauma models (Hunt *et al.*, 2009; 2010; Nichols *et al.*, 2015; Semple *et al.*, 2017). Although previous studies have reported substantial neuron dystrophy and loss in the CA3 sub-region (Anderson *et al.*, 2005; Baldwin *et al.*, 1997), we found interneurons in CA3 were relatively well preserved compared to other hippocampal regions. These differences might be explained by the histological analyses employed (e.g., Fluoro-Jade and NeuroSilver staining versus markers for interneurons). Indeed, most prior studies evaluating regional hippocampal damage have focused on principal neurons, and Fluoro-Jade B staining appears most robust in principal neuron populations in the first week after CCI (Anderson *et al.*, 2005; Hall *et al.*, 2008). Another possibility is that varying external injury parameters between studies might produce differences in regional cell damage after CCI. In our studies, we positioned the impactor tip parallel to midline, which in our hands leads to a substantial lesion to granule cells and CA1 pyramids, but not CA3 (Hall *et al.*, 2008; Hunt *et al.*, 2012; Hunt *et al.*, 2009). Prior studies reporting extensive CA3 damage have angled the head (or impactor) to deliver an injury perpendicular to the surface of the cortex (Anderson *et al.*, 2005; Saatman *et al.*, 2006). Computer models show shifting the angle of impact applies more tissue strain to the CA3 region (Mao *et al.*, 2010a; Mao and Yang, 2011). However, further investigation is needed to clarify the role of tissue level biomechanics on regional interneuron loss.

Functionally, CCI injury leads to a reduction in synaptic inhibition in hippocampus (Hunt et al., 2010; Almeida-Suhett et al., 2014, 2015; Butler et al., 2016). This is likely due to loss of interneurons as well as changes in the expression of $GABA_A$ receptor subunits (Raible et al., 2015) and subtype-specific modifications of inhibitory circuits. We previously reported a shift from somatic to dendritic inhibition in dentate granule cells following CCI injury (Hunt *et al.*, 2011). Our current data reveal a proportional preservation of molecular layer interneurons, which primarily target dendrites. Together, these findings suggest there may be a domain-specific shift from feedback to feedforward GABAergic inhibition after TBI, at least in dentate gyrus circuits. The computational consequences of such a shift are unknown, but at a circuit level, one might expect inhibitory drive is more capable of shunting excitatory input than synchronizing principal cell populations in the injured dentate gyrus. Alternatively, dendrite-projecting GABA neurons are involved in timing rhythmic cortical cell discharges (Szabadics et al., 2001) and can drive ictogenesis (Wendling et al., 2002). Thus, network level studies are ultimately necessary to determine how long-term changes in interneuron diversity affects the activity dynamics of principal neurons *in vivo*.

Successful therapeutic approaches for TBI will ultimately depend on cellular mechanisms of the initial insult and cell type-specific modifications of injured neural circuitry (Hunt *et al.*, 2013a). As such, it is critically important to understand which cell populations are sensitive to neurotrauma and how the cellular environment changes. Our results provide an important step in understanding the response of hippocampal interneurons to contusive brain injury.

CHAPTER THREE

Brain-wide reconstruction of inhibitory circuits after traumatic brain injury

Introduction

Brain function relies on an extremely diverse group of inhibitory interneurons that control the input and output of local networks (Kepecs and Fishell, 2014; Klausberger and Somogyi, 2008; Tremblay et al., 2016). In the cerebral cortex, one of the largest populations of interneurons expresses the neuropeptide, somatostatin (SST) (Ascoli *et al.*, 2008; Freund and Buzsáki, 1996; Pelkey *et al.*, 2017). These neurons inhibit dendrites and thereby regulate the integration of glutamatergic input to local principal neurons. This endows them with unique roles in shaping synaptic plasticity, learning and memory (Cummings and Clem, 2020; Larkum et al., 1999; Lovett-Barron et al., 2014; Morales et al., 2021; Royer et al., 2012; Spruston, 2008; Stefanelli *et al.*, 2016; Udakis et al., 2020). However, SST interneurons are among the most vulnerable to cell death following a brain injury, and their loss has been well documented in experimental models of epilepsy, traumatic brain injury (TBI) and Alzheimer's disease (Butler *et al.*, 2016; Cantu *et al.*, 2015; Frankowski et al., 2019; Lowenstein *et al.*, 1992), and in humans (Beal et al., 1986; de Lanerolle *et al.*, 1989). In hippocampus, surviving SST interneurons receive more excitatory drive, form new inhibitory synapses onto glutamatergic neurons and even grow into territories they normally do not occupy (Halabisky et al., 2010; Hunt *et al.*, 2011; Peng et al., 2013; Zhang et al., 2009). This pattern of local circuit rewiring raises the question of whether brain damage reorganizes interneuron connectivity on a much larger scale.

To address this challenge in an unbiased manner, we took advantage of a retrograde monosynaptic rabies virus system and enhanced whole-brain tissue clearing techniques to create brain-wide maps of the direct input to SST interneurons in a mouse model of focal TBI. We found dramatic quantitative differences in both the local and long-range input to hippocampal SST interneurons at the injury site. However, there was no neuron loss within the distant input regions themselves, and the proportion of neuron subtypes targeting starter neurons was stable. To our surprise, we uncovered a similar pattern of circuit reorganization far away from the injury in prefrontal cortex (PFC), which interacts with hippocampus bidirectionally (Jin and Maren, 2015) but was not directly damaged by the initial insult. Interneuron progenitors grafted into the lesioned hippocampus successfully established appropriate long-range connections; however, graft-derived interneurons retained the enhanced local input seen after TBI. Thus, our experiments provide new insights about large-scale circuit remodeling following brain injury and suggest that brain damage, even when focally restricted, has a far broader impact on neural circuit function across the entire brain than previously appreciated.

Methods

Mice

All animal procedures were performed under Institutional Animal Care and Use Committee (IACUC) approval by the University Laboratory Animal Resources at the University of California, Irvine and adhered to National Institutes of Health Guidelines for the Care and Use of Laboratory Animals. Experiments were performed on adult mice of both sexes maintained in standard housing conditions on a 12 h light/dark cycle with food and water provided *ad libitum*. For SST cell quantifications, we used GIN mice maintained on a FVB background (Jax Stock No: 003718). For retrograde circuit tracing, we used Sst-IRES-Cre mice maintained on a C57BL/6J background (Jax Stock No: 018973). We used C57BL/6J mice (Jax Stock No: 000664) for fluoro-jade C experiments. For cell transplantations, embryonic donor tissue was produced by crossing Sst-IRES-Cre J mice with C57BL/6J mice (Jax Stock No: 000664) or Ai6-ZsGreen reporter mice (Jax Stock No: 007906).

Experimental Design

Experiments were performed on male and female littermates between P55 and P139. Upon weaning, animals were coded and randomly assigned into uninjured (naïve control), TBI or MGE-injected treatments groups. Brain injured mice and age-matched controls were housed together (2–5 animals per cage) within a temperature- (21–22 °C), humidity- (40–51%), and light- (12-h light:dark cycle) controlled vivarium. The order of injury, virus injection and cell transplantation was also randomized. Blinding was not possible due to the presence of an injury in TBI treatment group. CHAT immunostaining experiments were replicated using a separate, independent cohort of control and brain injured animals. No other replication studies were performed.

Brain injury

CCI injury was performed on adult male mice at P55 (Frankowski et al., 2019). Briefly, mice were anesthetized by 2% isoflurane inhalation and placed in a stereotaxic frame. The skull was exposed by midline incision, and a 4–5 mm craniotomy was made ~1 mm lateral to the sagittal suture and centered between bregma and lambda. The skull cap was removed without damage to the exposed underlying dura. The contusion device consisted of a computer-controlled, pneumatically driven impactor fitted with a beveled stainless-steel tip 3 mm in diameter (Precision Systems and Instrumentation; TBI-0310). Brain injury was delivered using this device to compress the cortex to a depth of 1.0 mm at a velocity of 3.5 m s^{-1} and 500 ms duration. The incision was sutured, without replacing the skull cap, and the animal was allowed to recover. A qualitative postoperative health assessment was performed daily for 7 d after TBI and periodically thereafter. All animals that received surgery were treated with buprenorphine hydrochloride (Buprenex; 0.05 mg/kg, delivered i.p.) at the time of surgery and then once daily for 3d. All brain-injured mice survived and remained otherwise healthy until the day of experimentation.

Virus injections

AAV8-hSyn-FLEX-TVA-P2A-GFP-2A-oG with a titer of 1.2 x 10^{13} genome copies/mL was obtained from the GT3 Core Facility of the Salk Institute and diluted to a titer of 2.4 x 10^{11}genome copies/mL in sterile 0.9% NaCl prior to use, to prevent impairments in tracing performance (Lavin et al., 2020). RV-ΔG-mCherry was produced as previously described (Wickersham et al., 2007b) with a titer of 5 x 10^9 infectious units/mL. Virus was front loaded into beveled glass micropipettes (40 µm tip diameter, Wiretol 5 µl, Drummond Scientific) and injected into the brains of adult control and brain injured mice at a rate of 15 nL min^{-1} and the needle was left in place for 5 min before retraction. Target coordinates were first verified in a series of preliminary dye injection studies into control and brain injured mice. AAV injections (200 nL) were made into hilus of dentate gyrus at the following stereotaxic coordinates: anterior-posterior (AP) -2.0 mm, medial-lateral (ML) 1.35 mm, dorsal-ventral (DV) -1.9 mm. In separate cohort of animals, injections were made into prelimbic cortex: AP 1.8 mm, ML 0.35 mm and DV -1.4 mm. RV-ΔG-mCherry (100nL) was injected 3 weeks later at the same location.

Tissue clearing and whole brain immunostaining

Mice were transcardially perfused with 0.1M PBS containing 1uL/mL of 10mg/mL heparin sodium (Serva cat no. 24590.01) followed by 4% PFA in 0.1M PBS. Samples were post-fixed overnight in 4% PFA in 0.1M PBS. Subsequent steps were performed in 5mL centrifuge tubes (Eppendorf cat. No 0030119401) with 0.01% sodium azide added to each solution. First, samples were decolorized in 10% 3-[(3-Cholamidopropyl)dimethylammonio]-1-propanesulfonate (CHAPS, Anatrace cat. no. C316S) and 25% N-methyl diethanolamine (MDEA, Alfa-Aesar cat. no. L15712) in 0.1M PBS for 48 hr at 37°C with nutation. Samples were then washed in 0.1M PBS for 24h, dehydrated in a methanol/water gradient (20%, 40%, 60%, 80%, 100%, 100%) for 1h each and delipidiated in 2:1 DCM:MeOH overnight. The next day, samples were washed twice in 100% MeOH for 4 hr to remove DCM:MeOH and bleached in 5% H_2O_2 in 80% MeOH overnight at 4°C without shaking. Samples were then rehydrated in 60% MeOH, 40% MeOH, 20% MeOH and

0.1M PBS for 1 hr, incubated in 4M guanidine hydrochloride (Alfa-Aesar cat. no. A13543-30) and 1% CHAPS in 0.1M PBS for 24 hrs and washed overnight in 0.1M PBS with three solution changes. Next, samples were permeabilized in 10% CHAPS/25% MDEA in 0.1M PBS overnight at 37°C with nutation and blocked in 3% normal donkey serum in 0.1M PBS containing 0.2% Tween-20 at 37°C with nutation for 24 hr. Primary antibody incubations were performed in heparinized 0.1M PBS with Tween-20 (PTwH) containing 0.25% CHAPS and 1:1,000 rabbit anti-DsRed (1:1,000) and chicken anti-GFP antibodies (1:1,000) for 7 days at 37°C with nutation. Samples were then washed in PTwH overnight with five solution changes. Secondary antibody diluent was prepared in PTwH containing 0.25% CHAPS, donkey anti-rabbit 546 (1:1,000) and goat anti-chicken antibodies (1:1,000), syringe filtered at 0.2µm and incubated for 7 days at 37°C with nutation before washing in PTwH overnight with shaking at room temperature. The next day, samples were dehydrated in increasing methanol/water gradients (20%, 40%, 60%, 80%, 100% for 1h each) and allowed to sit in 100% MeOH overnight at 4°C. Samples were then washed in 2:1 DCM/MeOH for 3 hrs, followed by two 100% DCM washes for 15 min each and cleared in dibenzyl ether (DBE) overnight at 4°C. DBE was changed four additional times before imaging for refractive index matching.

Light-sheet imaging

Cleared samples were mounted in DBE using a 3D-printed sample holder in a custom imaging chamber and imaged using a Zeiss Z1 light-sheet microscope. Samples were imaged in the sagittal orientation with single-sided illumination using a x5/0.1 illumination objective and a x5/0.16 detection objective at 0.91 µm/pixel resolution with 4.97µm step size. mCherry-labeled input neurons were imaged using a 561 nm laser coupled to a 575-625nm BP filter. GFP and auto-fluorescence channels were acquired simultaneously with 488 nm and 638 nm laser lines coupled to 505-545nm BP and 660nm LP filters. Laser power was set to 40% intensity for all laser lines with 200 ms exposure. Tile overlap was set to 10%.

Whole-brain 3D image registration and analysis

Raw data (.czi) were converted into hierarchical format (.ims) using Imaris File Converter 9.1 (Bitplane). The 561 nm channel data was downsampled by a factor of two in each dimension and exported as numpy arrays (.npy) using custom Python scripts. Individual tiles were stitched non-rigidly using WobblyStitcher (Kirst et al., 2020). Stitched arrays were exported as .tif series with a background subtraction value determined for each animal. Individual cell positions were manually annotated using cellfinder (Tyson et al., 2021). Image stacks were downsampled to 10 μm resolution and registered to the Allen Reference Atlas (Wang et al., 2020) using brainreg, a Python port of aMAP (Niedworok et al., 2016). Atlas boundaries were upsampled to the original high resolution image, and image planes containing cells were inspected for accuracy. To correct for whole-brain registration error, pairs of correspondence points were manually marked where atlas boundaries diverged from anatomical landmarks. Average vector length was calculated, and annotated cell positions were linearly transformed based on the correspondence point vector length. Coronal atlas plates were rendered at selected positions along the anterior/posterior axis and individual cells positions ± 125 μm (hippocampus tracing) or ± 50 μm (PFC tracing) to the selected atlas plate were plotted using brainrender (Claudi et al., 2021).

Whole-brain quantification

Registered cell positions for each animal were summarized using cellfinder (Tyson et al., 2021). All subsequent analyses were performed using custom Python scripts. Cell counts were combined for laminated cortical strucutures. Ipsilateral and contralateral cell counts were analyzed as separate regions except for brain structures that were fused at midline, which were considered one structure. For Euclidian distance calculation, the starter cell centrioid was calculated by averaging the atlas coordinates of each registered starter cell and rounding the result to the nearest integer. Three dimensional Euclidian distance was calculated between the starter cell centriod and each presynaptic cell position using the following formula:

$$d = \sqrt{(x_2 - x_{1)} + (y_2 - y_1) + (z_2 - z_1)}$$

where (x_2, y_2, z_2) represents the starter cell centriod and (x_1, y_1, z_1) represents each registered presynaptic cell position and *d* represents the length of the calculated distance vector. For AP and DV distance analyses, cell counts were binned at 200 μm intervals and normalized to the total number of cells for each animal. For ML analysis, cell counts were binned at 300 μm to produce an even number of bins for each hemisphere. For Gaussian kernel density plots, bandwidth was determined for each plot using Scott's Rule:

$$b = n^{(-\frac{1}{d+4})}$$

where *n* represents the number of points, *d* represents the number of dimensions, and *b* represents kernel bandwidth.

Reverse clearing

Cleared samples were removed from DBE and washed in DCM twice for 15 min followed by overnight incubation in 2:1 DCM/MeOH. Samples were then rehydrated in 100%, 80%, 60%, 40%, 20% MeOH/water and 0.1M PBS for 1hr each. Free-floating vibratome sections (50 μm) were cut using a vibratome at room temperature in 0.1M PBS containing 0.05% Triton-X.

Immunostaining

Mice were transcardially perfused with 4% paraformaldehyde (v/v) and free-floating vibratome sections (50 μm) were processed using standard immunostaining procedures (Zhu et al., 2019). Primary antibodies were as follows: chicken anti-green fluorescent protein (GFP; 1:1000; Aves, cat no. GFP1020), rabbit anti-somatostatin (SST; 1:200; Santa Cruz, cat no. SC-7819), mouse anti-reelin (1:500; Millipore, cat no. MAB5364), goat anti-choline acetyltransferase (CHAT; 1:500;

Millipore, cat no. AB144P) and rabbit anti-DsRed (1:1000; Clontech, cat no. 632496). All antibodies have been previously used for immunostaining analysis in brain. For secondary antibodies (1:1000, Life Technologies), we used Alexa 488–conjugated goat antibody to chicken IgG (cat. no. A11039), goat antibody to mouse IgG (cat. no. A11029), donkey antibody to goat IgG (cat. no. A11055; Alexa 546-conjugated goat antibody to rabbit IgG (cat. no. A11035), donkey antibody to rabbit IgG (cat. no, A10040), Alexa 594–donkey antibody to goat IgG (cat. no. A11058) and Alexa 647–conjugated goat antibody to chicken IgG (cat. no. A32933). Sections were then mounted on charged slides (Superfrost plus, Fisher Scientific) with Fluoromount-G containing DAPI. Confocal images were obtained with an Olympus FV3000 laser scanning microscope. Epifluorescent images were obtained using a Leica DM6 microscope. Brightness and contrast were adjusted manually using Image J, as needed.

Cell quantification

Fluorescently labeled sections (50 μm) were imaged using a Leica DM6 microscope with a ×10 or ×20 objective or Olympus FV3000 confocal microscope with a ×20 or ×40 objective and counted using FIJI (ImageJ) (Zhu et al., 2019). All cells were counted in every sixth coronal section through the entire brain (that is, 300 μm apart). All sections containing labeled cells were analyzed per animal and the values averaged to obtain a mean cell density (cells/mm^2).

Fluoro-jade C staining

Mice were transcardially perfused with 4% paraformaldehyde (v/v) and free-floating vibratome sections (50 μm) were processed for fluoro-jade C staining according to manufacturer instructions (Schmued et al., 2005). Briefly, brain sections were dried on gelatin-coated slides for 30 min at 50^{o}C. Slides were immersed in 1% NaOH in 80% ethanol for 5 min, 70% ethanol for 2 min, dH_2O for 2 min, 0.06% potassium permanganate for 10 min, dH_2O for 2 min, 0.00015% fluoro-jade C (Histo-Chem Inc., cat no. 1FJC) and 0.0001% DAPI in 0.1% acetic acid for 10 min, followed by three washes in dH_2O for 1 min each. Slides were then dried at 50°C for 5 min and cleared in xylenes before coverslipping with Eukitt mounting medium (Sigma, cat. no 03989).

Tissue dissection and transplantation

Ventricular and subventricular layers of the MGE were harvested from E13.5 embryos. The time point at which the sperm plug was detected was considered E0.5. Embryonic MGE explants were dissected in Leibovitz L-15 medium, mechanically dissociated by repeated pipetting in L-15 medium and concentrated by centrifugation (3 min at 600 × *g*). Concentrated cell suspensions were front loaded into beveled glass micropipettes (50 μm tip diameter, Wiretol 5 μl, Drummond Scientific) and injected (3×10^4 cells per injection) into the hippocampus of adult brain injured mice 7 d after CCI injury. Cell injections were made into stratum radiatum of the CA3 subfield at the following stereotaxic coordinates: AP -2.0 mm, ML 2.45 mm, DV -1.8 mm.

Quantification and statistical analysis

All statistical tests were performed with Graphpad Prism 9 and Microsoft Excel. Data were compared by two-tailed student's t-test, one-way ANOVA followed by a Tukey's post hoc test for multiple comparisons, two-way ANOVA followed by a Tukey's post hoc test for multiple comparisons, two-way repeated measures ANOVA followed by a Bonferroni's post hoc test, Chi-Square analysis or Fisher's exact test. Data are expressed as mean ± SEM, *n* = animals and significance was set at $P < .05$.

Results

Long-term loss of SST interneurons after TBI

Despite their important role in shaping local network activity and memory (Morales *et al.*, 2021; Stefanelli *et al.*, 2016), the precise brain-wide input to SST interneurons in dentate gyrus has not been systematically defined. We first quantified SST+ neuron density during the chronic period after TBI using reporter mice that label nearly all SST interneurons with GFP (Oliva et al., 2000). A unilateral controlled cortical impact (CCI) injury was delivered to young-adult mice at P60, and animals were processed for immunostaining eight weeks later. This period corresponds to a time when long-term neuropathology and behavioral phenotypes are well established. In all brain injured mice, the lesion consisted of a cavity extending through the thickness of the neocortex and included substantial distortion and thinning of the principal cell layers in hippocampus (**Fig 3.1A**). We observed ~65% reduction in GFP+ cells in the hilus (**Fig 3.1B**), consistent with short-term loss of SST interneurons reported in previous studies (Butler et al., 2016; Frankowski et al., 2019).

Visualization of input neurons to hippocampal SST+ interneurons

To label monosynaptic input to SST interneurons in the chronically injured brain, we used a genetically restricted two-virus approach to anatomically reveal their putative inputs (**Fig 3.1C**). We first injected a Cre-dependent helper virus (AAV8-hSyn-FLEX-TVA-P2A-eGFP-2A-oG) into dentate gyrus of adult SST-Cre mice 4 weeks after TBI. This helper virus provides the receptor that allows EnvA-coated rabies virus to enter only Cre-positive neurons and glycoprotein for rabies virus to transfer retrogradely to monosynaptic input neurons. Three weeks later, we injected a G-deleted and EnvA-pseudotyped rabies virus coding mCherry into the same location (RVΔG-mCherry). Because SST+ interneurons in dentate gyrus are exclusively located in the polymorph layer (that is, the hilus), we targeted this region for virus injection. After 7 days, we identified neurons that were positive for both fluorescent reporters at the injection site (starter cells) and neurons infected with the rabies virus were tagged with mCherry (pre-synaptic input neurons). Substantial numbers of neurons in different brain areas were labeled by rabies virus (**Fig 3.2**). To confirm the specificity of virus labeling, we performed immunostaining against SST at the injection site. We found 97.4% of the GFP-labeled neurons were SST+ (152 of 156 cells, *n* = 3 mice) (**Fig 3.1F, G**). To evaluate potential leakage expression of the virus, we performed a series of control experiments. To confirm the dependence of Cre recombination, we injected AAV8-hSyn-FLEX-TVA-P2A-eGFP-2A-oG helper and RVΔG-mCherry virus into Cre- littermates. No neurons were labeled anywhere in the brain (**Fig 3.3A**). In Cre+ animals, GFP+ neurons were only labeled at the injection site and no GFP+ neurons were found outside the injection site (**Fig 3.3B**). In both control and brain injured animals, starter cells were almost exclusively confined to the hilus (**Fig 3.1H**). Only occasional starter cells were found in the adjacent CA3 region; no GFP+ cells were found in CA1, CA2 or neocortex.

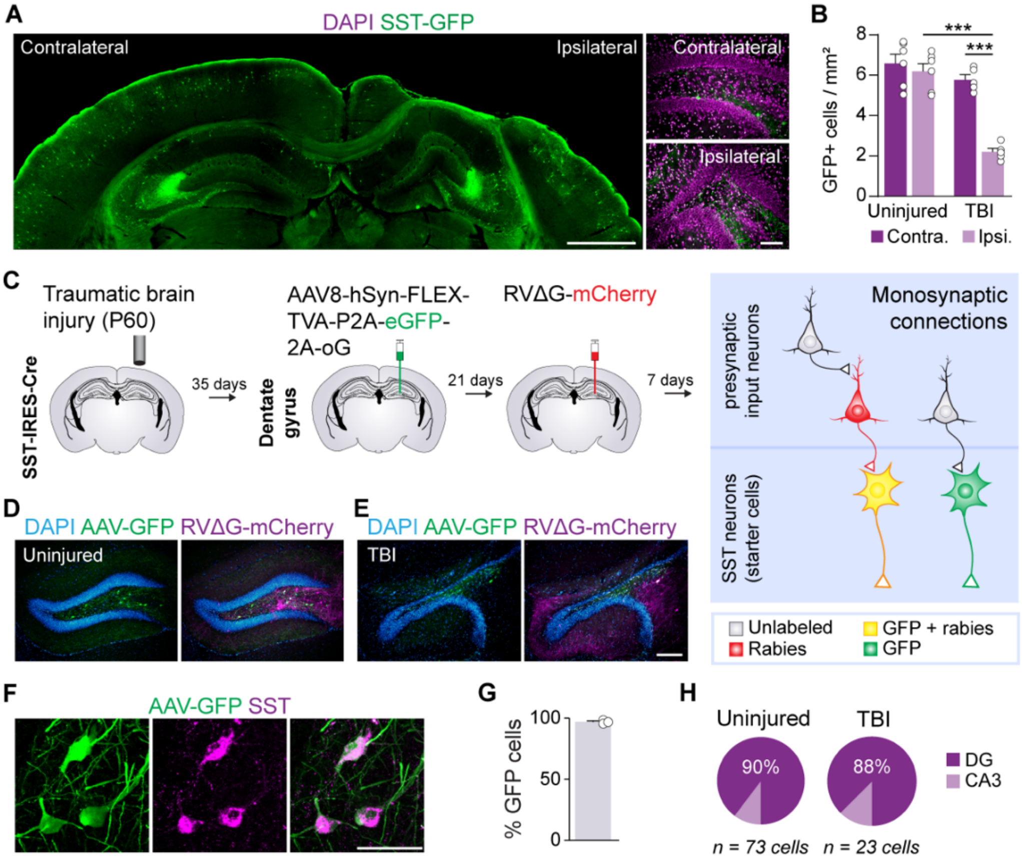

Figure 3.1. SST interneuron loss after focal TBI. A. Coronal section 8 wks after TBI labeled for SST-GFP (green) and DAPI (magenta). **B.** Quantification of SST-GFP interneurons in uninjured control and brain injured animals. ***P = 1.31E-05, ipsilateral TBI versus contralateral TBI, ***P = 1.62E-06, ipsilateral TBI versus ipsilateral uninjured control; two-way ANOVA with Tukey's post-hoc test, *n* = 5-6 mice per group. **C.** Schematic showing the two-virus experimental retrograde tracing strategy. **D, E.** Dentate gyrus of an uninjured control (D) and CCI injured animal (E) labeled for DAPI (blue), AAV helper virus (green) and RVΔG-mCherry (magenta). **F.** Coronal section of dentate gyrus labeled for AAV helper virus (green) and somatostatin (magenta). **G.** Quantification of SST expression in neurons labeled with AAV helper virus. **H.** Distribution of dual color-labeled starter cells in hippocampus (*n* = 73 cells from 3 controls, *n* = 23 cells from 2 animals with TBI). Error bars, s.e.m.; scale bars, 1 mm (A, left), 100 µm (A, right; D and E) and 50 µm (F). See also **Fig 3.2, 3.3**.

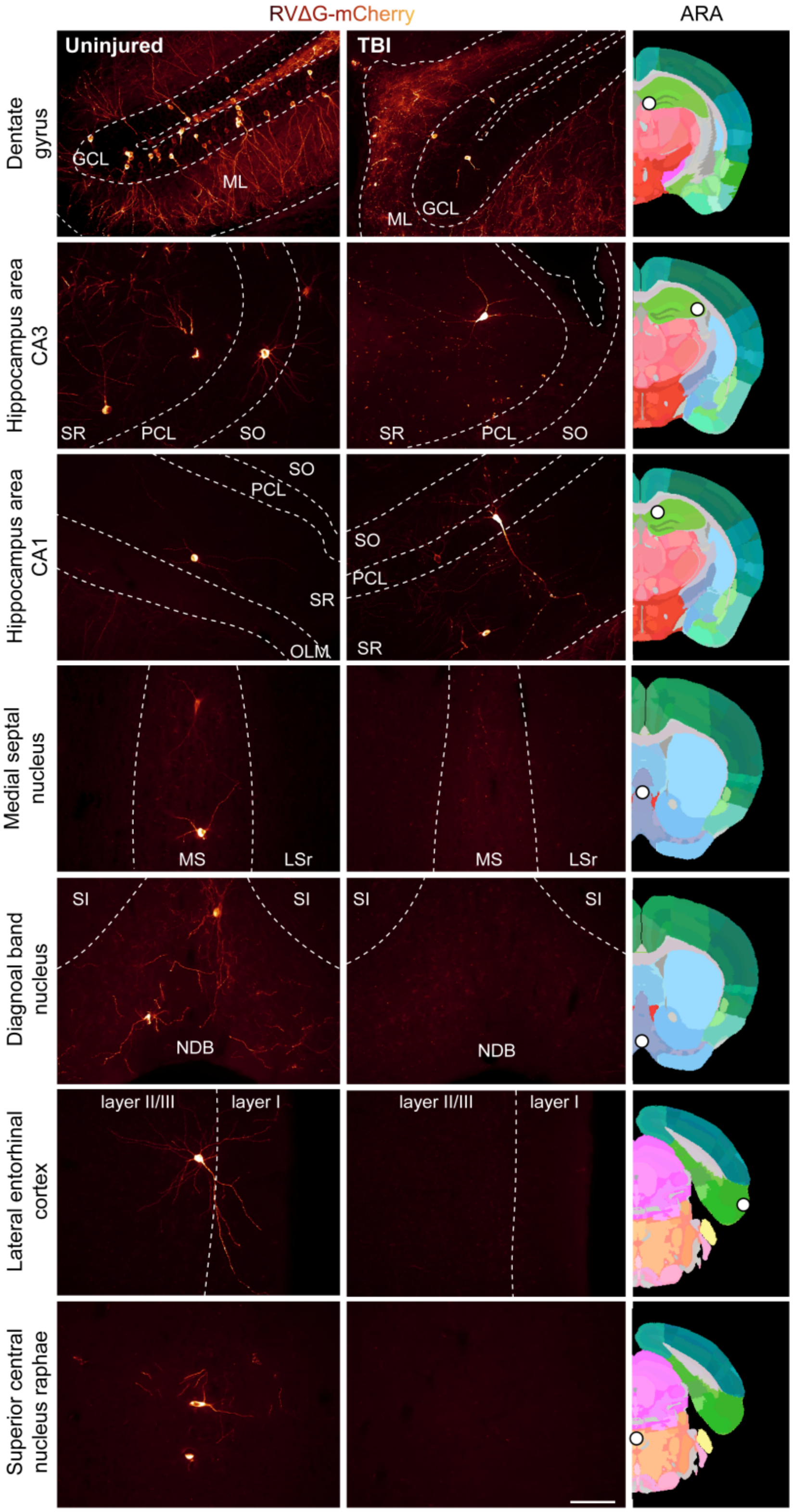

Figure 3.2: Input neurons to hilar SST interneurons. Coronal sections labeled for input neurons (red) in an uninjured control (left) and 8 wks after TBI (right). Image location is indicated by a white dot overlaid onto the corresponding atlas plate from the Allen Reference Atlas (ARA). GCL, granule cell layer; ML, molecular layer; SR, stratum radiatum; PCL, pyramidal cell layer; SO, stratum oriens; OLM, oriens lacunosum moleculare; MS, medial septal nucleus; LSr, lateral septal nucleus, rostroventral part; NDB, diagonal band nucleus; SI, substantia innominata. Scale bar, 100 µm.

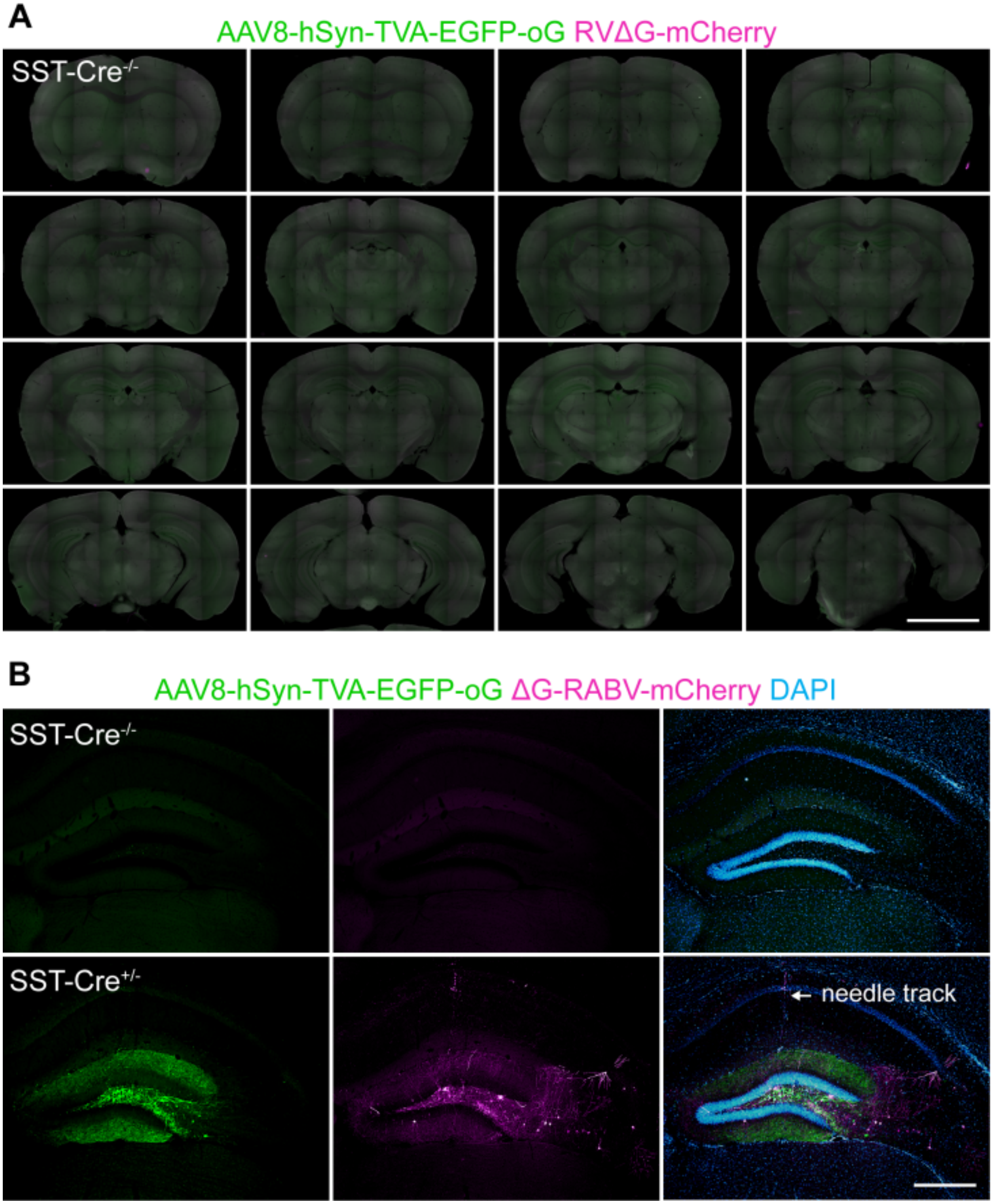

Figure 3.3: Virus specificity in hippocampus. A. Serial coronal sections every 300 μm through the entire brain of an adult SST-Cre-negative mouse labeled for AAV helper virus (green) and RVΔG-mCherry (magenta). **B.** Coronal section of hippocampus labeled for helper virus (green) and rabies (magenta) in SST-Cre-negative mouse (top) and SST-Cre-positive mouse (bottom). Scale bar, 2 mm (A); 500 μm (B).

Whole-brain input to SST-positive neurons is reorganized by TBI

Next, we generated whole-brain maps of neurons sending monosynaptic input to SST interneurons using iDISCO brain clearing and whole-brain light-sheet imaging (**Fig 3.4A)**. One of the major challenges to these techniques has been accessing input neurons deep within the tissue (Ueda *et al.*, 2020b). Building on existing iDISCO protocols and recent advances in permeabilization chemistry (Renier *et al.*, 2016; Zhao *et al.*, 2020), we therefore modified the clearing conditions to achieve deep tissue immunolabeling in a traumatically injured brain. We made three key improvements in iDISCO sample preparation and imaging procedures (**Fig 3.4A** and **Fig 3.5)**. First, we incorporated an initial wash using N-methyl diethanolamine (MDEA) to decolorize residual unperfused blood, which absorbs light (Faber et al., 2003). Second, we denatured the extracellular matrix using a concentrated guanidine hydrochloride solution prior to immunolabeling. Third, we incorporated an additional detergent (3-[(3-cholamidopropyl) dimethylammonio]-1-propanesulfonate, CHAPS) to the antibody diluent to enhance penetration of antibodies deeper into the tissue. These optimizations enabled whole-brain immunolabeling without need for separating the brains into two separate hemispheres, as is commonly done. The raw data acquired from imaging were registered to the Allen Common Coordinate Framework (CCF) and cell positions were annotated and analyzed using tools from the BrainGlobe suite (Claudi et al., 2021; Tyson et al., 2021) (**Fig 3.6)**. As expected, the number of starter neurons was reduced in brain injured animals (control: 46.3 ± 4.7 cells, TBI: 9.4 ± 0.9 cells, P = 5.2E-05, two-tailed t-test), consistent with the loss of SST interneurons, and there was a correlation between the number of input neurons and starter cells (**Fig 3.4B**). Whole-brain mapping of rabies-labeled neurons revealed input from 14 distinct brain regions (**Fig 3.4C, Fig 3.7, Fig 3.8**). The majority of input came from dentate gyrus and CA3, as expected (Hunt *et al.*, 2011; Katona *et al.*, 1999; Wittner *et al.*, 2006) followed by medial entorhinal cortex (ENTm), diagonal band nucleus (NDB) and lateral entorhinal cortex (ENTl).

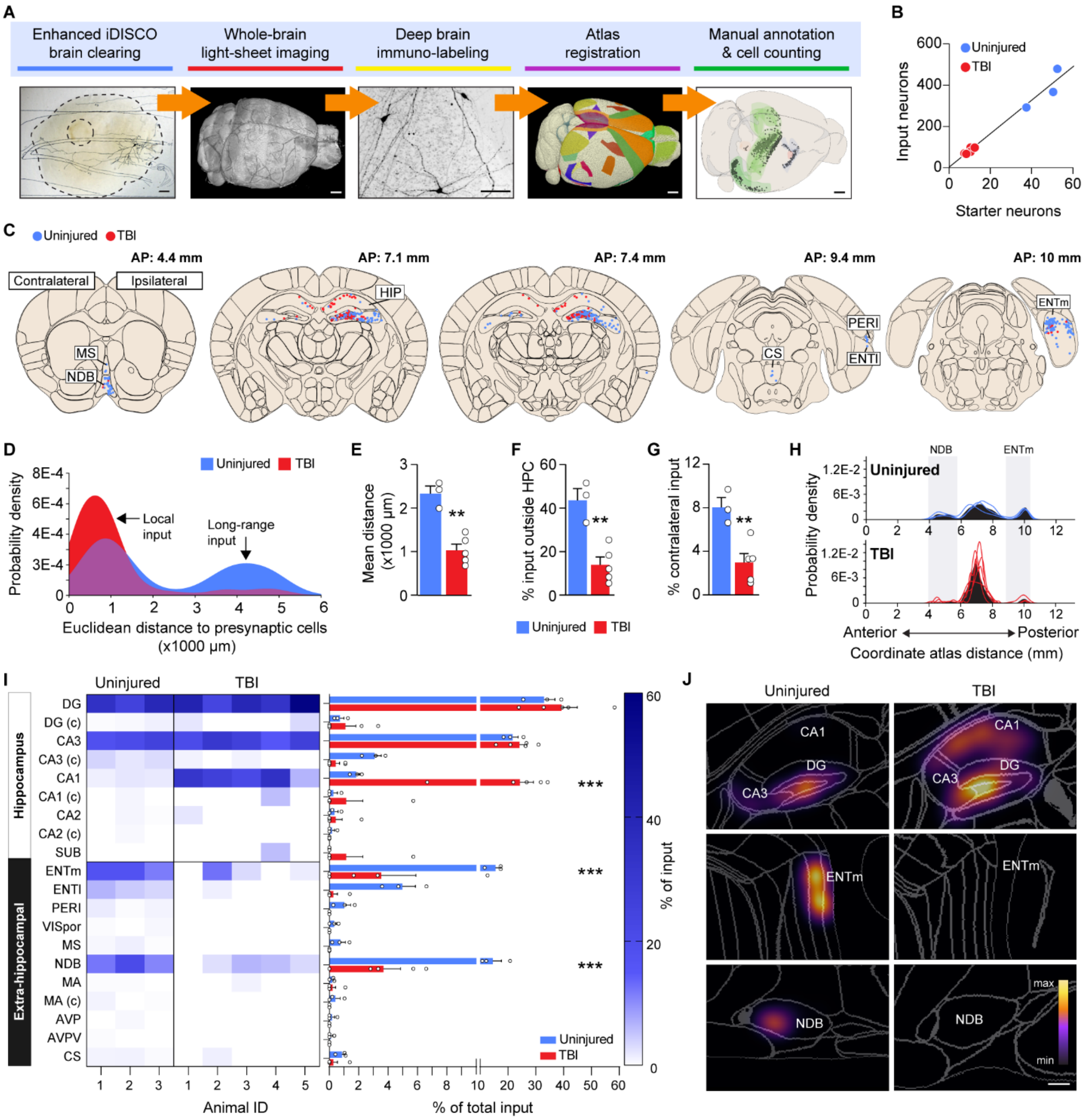

Figure 3.4. Reorganization of brain-wide input to hippocampal SST interneurons after TBI. A. Experimental design for enhanced iDISCO brain clearing and whole-brain light-sheet imaging. **B.** Linear regression analysis for number of starter cells and pre-synaptic input neurons (*n* = 3 controls, 5 TBI mice; R^2 = 0.97). **C.** Schematic coronal sections (250 μm) showing individual rabies-labeled cells registered in standardized atlas space for uninjured controls (blue) and brain injured animals (red). One dot represents one neuron. *n* = 3 control and 5 TBI animals. **D.** Gaussian kernel cell density plots showing pooled Euclidian distances of input neurons to nearest starter neuron. **E.** Quantification of average Euclidian distance between starter cell centroid and input neuron positions. Control: 2331 ± 174.1 μm, *n* = 3 mice; TBI: 1029 ± 142.5 μm, *n* = 5 animals; **P = 1.30E-3; two-tailed t-test. **F.** Proportion of input neurons found outside hippocampus. Control: 43.5 ± 5.4%, n=3 mice; TBI: 13.9 ± 3.6 %, n = 5 mice; **P = 3.0E-3; two-tailed t-test. **G.** Proportion of input neurons found in contralateral hemisphere. Control: 6.6 ± 0.9%, n = 3 mice; TBI: 3.0 ± 0.8 %, n = 5 mice; **P = 7.40E-3; two-tailed t-test. **H.** Gaussian kernel cell density plot of the whole-brain distribution of input neurons along the anterior-posterior axis. Black shading represents the pooled population with individual lines representing each animal. **I.** Proportion of input neurons found in each discrete brain area. ***P = 2.00E-15, control versus TBI (CA1), ***P = 4.26E-05, control versus TBI (ENTm), ***P = 2.98E-04, control versus TBI (NDB); two-way repeated measures ANOVA with Bonferroni's post-hoc test; n = 3-5 mice per group. **J.** Heatmaps of rabies-labeled input neuron density in hippocampus (top), ENTm (middle) and NDB (bottom). Error bars, s.e.m.; scale bars, 1 mm (A, except deep immunolabeling, 100 μm), 200 μm (J). See also **Fig 3.4** to **3.9**. MS, medial septal nucleus; NDB, diagonal band nucleus; HIP, hippocampus; PERI, perirhinal area; ENTl, lateral entorhinal cortex; ENTm, medial entorhinal cortex; DG, dentate gyrus; CA3, cornu ammonis 3; CA1, cornu ammonis 1; CA2, cornu ammonis 2; SUB, subiculum; PSUB, prosubiculum; VISpor, postrhinal area; MA, magnocellular nucleus; AVP, anteroventral preoptic nucleus; AVPV, anteroventral periventricular nucleus; CS, superior central nucleus raphe.

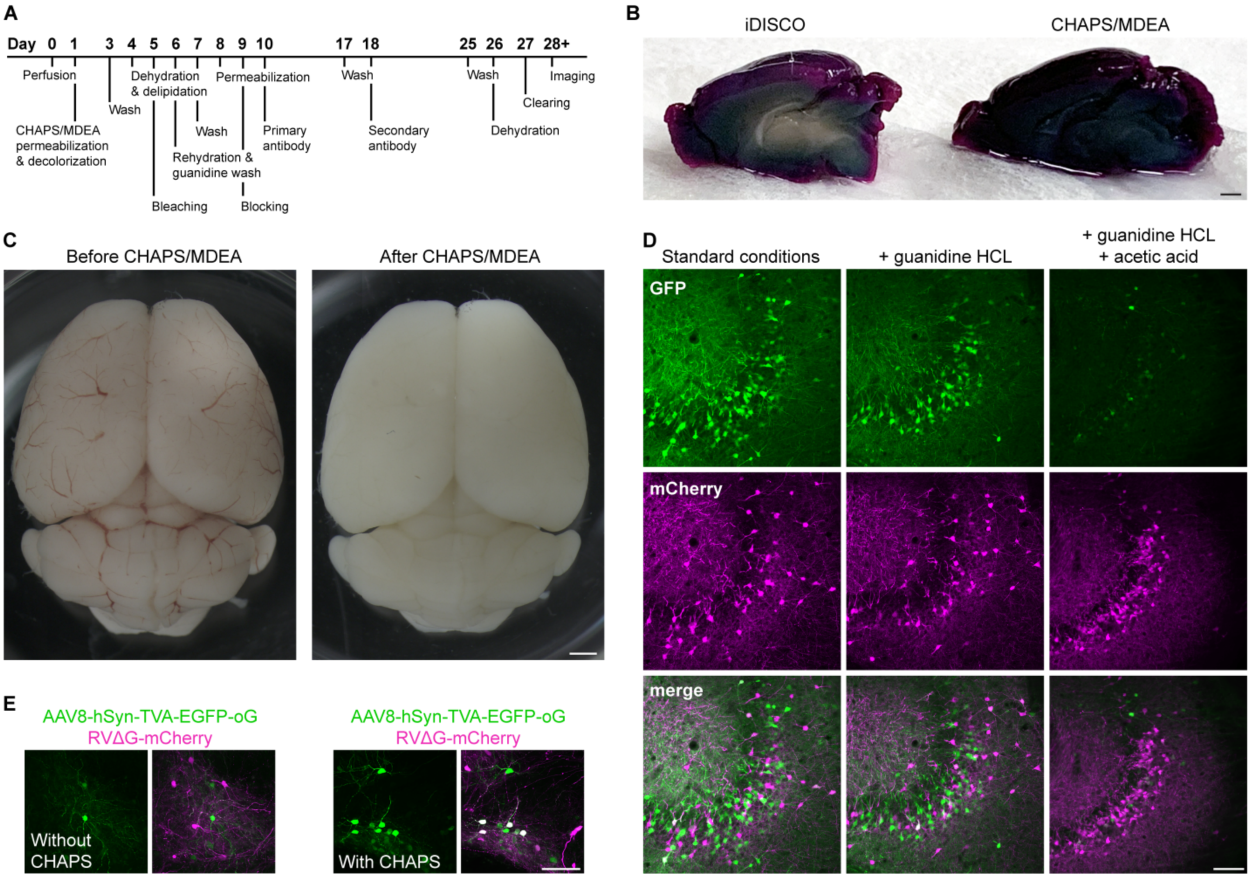

Figure 3.5: Optimization of enhanced iDISCO protocol. A. Timeline of brain clearing and immunolabeling. **B.** Whole mouse brains incubated with purple food coloring overnight after permeabilization with iDISCO+ buffer or CHAPS/MDEA buffer for 48 h. **C.** Unperfused mouse brain drop-fixed in 4% PFA overnight (left) and the same brain after 48 h of decolorization in 10% CHAPS/25% MDEA in PBS (right). **D.** Coronal section of hippocampus labeled for AAV helper virus (green) and input neurons (magenta) using standard immunostaining conditions, immunostaining with 4M guanidine HCl treatment or with 4M guanidine HCl and acetic acid treatment. **E.** Coronal section of hippocampus labeled for AAV helper virus (green) and input neurons (magenta) with standard antibody diluent (left) and diluent containing 0.25% CHAPS (right). Scale bar, 1mm (B, C); 100 µm (D, E).

Of note, this pattern of input is different from previous retrograde tracing results in dentate granule cells, which receive considerably weaker projections from ENTm than ENTl and prominent input from mammillary nuclei (Li et al., 2020; Vivar et al., 2012), as well as SST interneurons in CA1, which receive very little input from entorhinal cortex (Sun *et al.*, 2014). After TBI, there was a significant reduction in the mean distance of rabies-labeled neurons to the starter cell centroid (**Fig 3.4D, E**), suggesting input neurons were substantially closer to starter cells after brain injury.

An increase in local connectivity was confirmed when we analyzed the input to SST interneurons in greater detail. In control animals, approximately half of the input neurons were detected outside the hippocampus, and 8% of input neurons were located in the contralateral hemisphere. These long-range inputs were significantly reduced in animals with TBI (**Fig 3.4F, G**). Furthermore, we analyzed the probability density of input neurons in 200 μm bins along the entire anterior-posterior axis, from 0 mm (olfactory bulb) to 13 mm (cerebellum) (**Fig 3.4H**). This revealed significant increases in the percentage of input neurons between 6.8 mm to 7.4 mm at the level of hippocampus (6.8-7 mm, control: 5.84 ± 0.17 %, TBI: 18.55 ± 5.26 %, P = 4.97E-12; 7-7.2 mm, control: 6.73 ± 1.16 %, TBI: 17.43 ± 4.26 %, P = 1.37E-08; 7.2-7.4 mm, control: 8.87 ± 2.22 %, TBI: 16.66 ± 4.09 %, P = 1.82E-04; Two-way ANOVA with Bonferroni's post-hoc test) and decreases at 10 mm to 10.2 mm at the level of ENTm (control: 10 ± 1.09 %, TBI: 1.90 ± 1.03 %, P = 7.57E-05; Two-way ANOVA with Bonferroni's post-hoc test). After TBI, massive input labeling was detected within the hippocampus, with a significant increase in input from area CA1 and input arising from a new brain region, subiculum, which was not detected in any of the controls (**Fig 3.4I, J**). Nearly all of the labeled CA1 neurons were found in the pyramidal layer (**Fig 3.8**). However, distant brain areas providing the most input to SST interneurons in controls, such as ENTm and NDB, were found to contain significantly fewer input neurons after TBI (**Fig 3.4I, J**). To directly compare changes in the number of input neurons rather than proportion of input, we calculated the convergence index for each animal, defined as the number of mCherry-labeled input neurons divided by the number of GFP- and mCherry-labeled starter cells. This analysis also revealed a significant increase in CA1 input, and decreases in long-range input from ENTm and NDB (**Fig 3.9**). Thus, there is a dramatic shift in both the number and relative proportion of local and long-distance input to hippocampal SST interneurons after TBI.

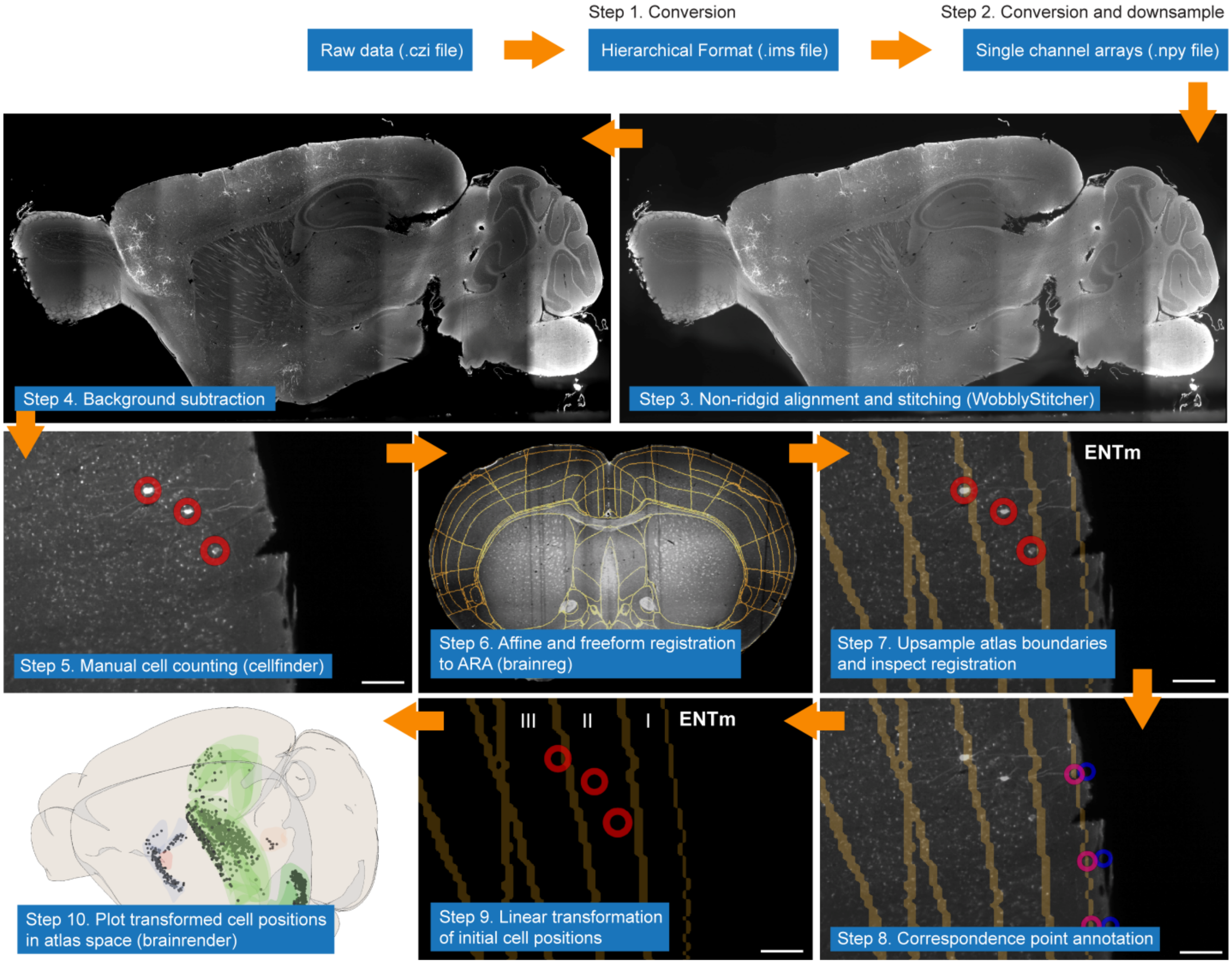

Figure 3.6: Protocol for image registration and analysis. Raw data were initially converted from .czi to .ims file format. For each channel, data were downsampled by a factor of two in each dimension and converted to .npy format. 561 nm channel data was stitched using WobblyStitcher and exported as a stack of .tif files. For each animal, background intensity was measured and subtracted from all images in the stack. Individual cell positions were annotated using the graphical interface in cellfinder. 561 nm channel data were then down sampled to 10 μm isotropic resolution and registered to the Allen Reference Atlas. Atlas boundaries were upsampled to the original imaging resolution and overlaid over 561 nm channel data. For each image plane containing cells, atlas boundaries were manually inspected for accuracy. Registration error was corrected by annotating pairs of points corresponding to region boundaries (blue) and the respective atlas location to correct (magenta) to calculate transformation vector length. ENTm, medial entorhinal area.

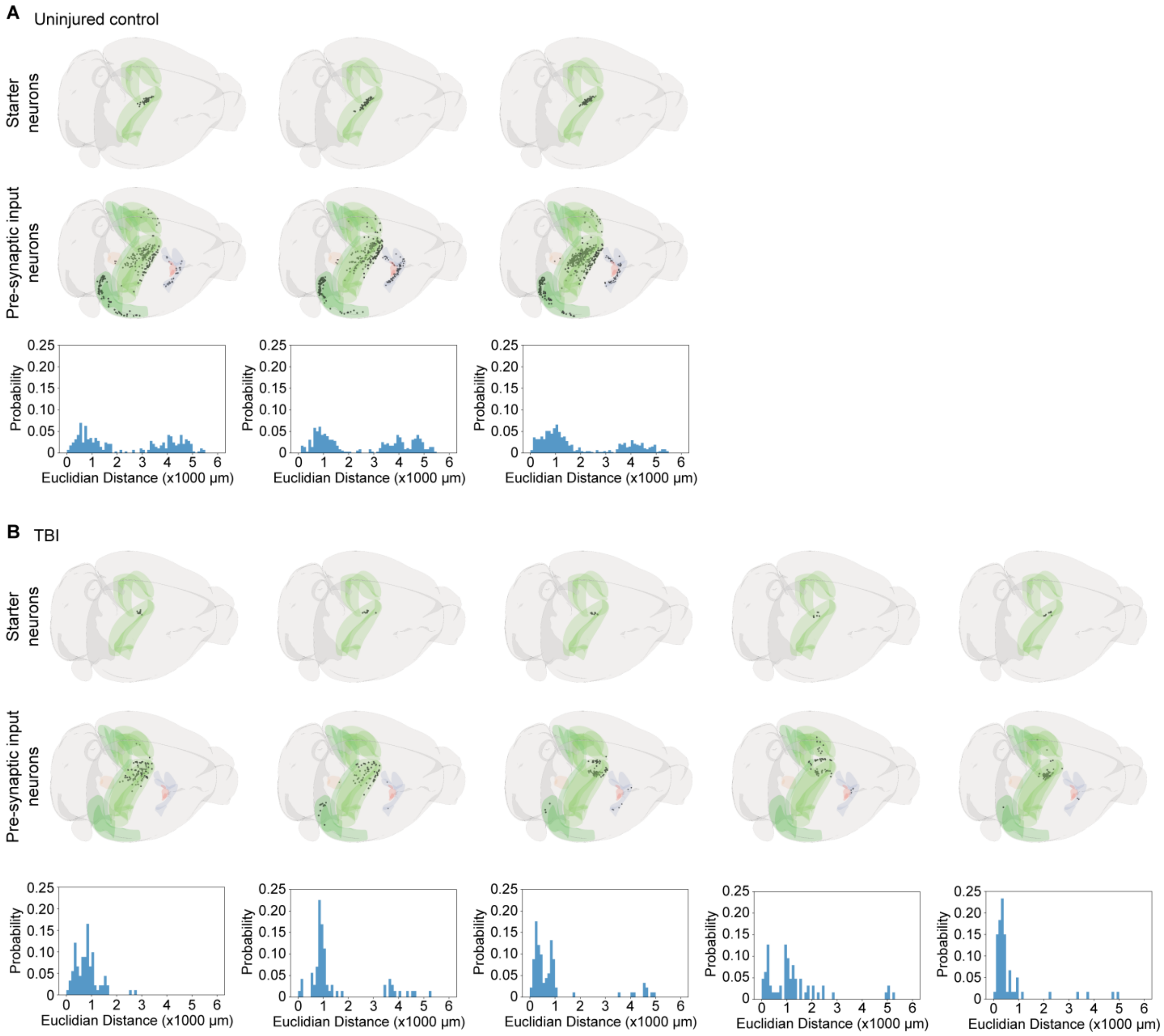

Figure 3.7: Individual animal plots of input to hilar SST interneurons. A, B. Top: whole-brain plots of starter cells and pre-synaptic input neurons annotated in standardized atlas space. Bottom: histograms showing Euclidian distances at 100 µm bins in uninjured controls (A) and brain injured animals (B). Black dots represent individual cells registered in standardized atlas space. Shading indicated hippocampal formation (green), pallial regions (blue) and hypothalamus (red).

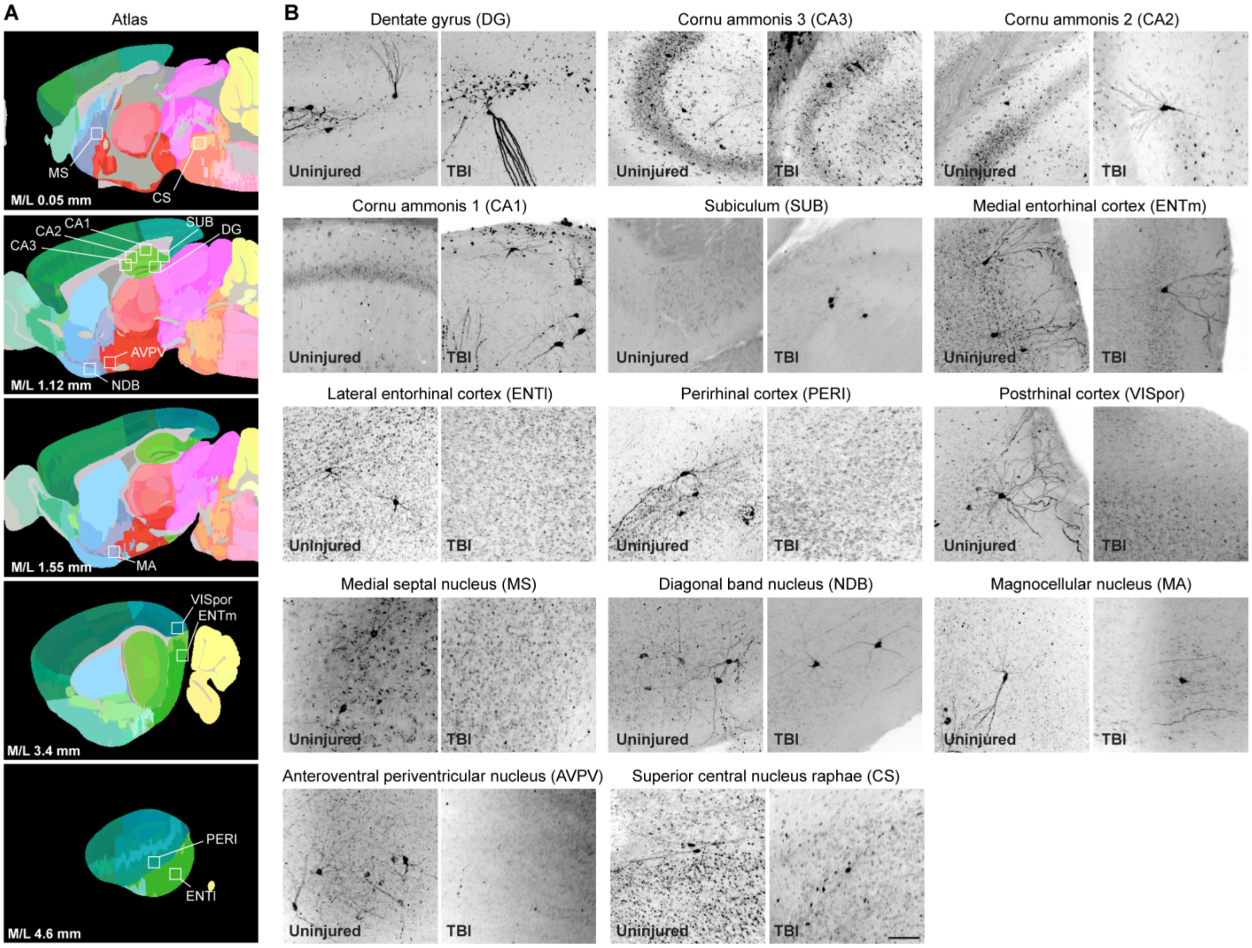

Figure 3.8: Input neurons innervating hilar SST interneurons in hippocampus. A. Sagittal sections obtained from the ARA indicating brain regions where rabies-labeled cells were found. **B.** Maximum intensity projections (100µm) of neurons in whole brains providing direct input to hilar SST interneurons in the intact and damaged brain. Scale bar, 100 µm.

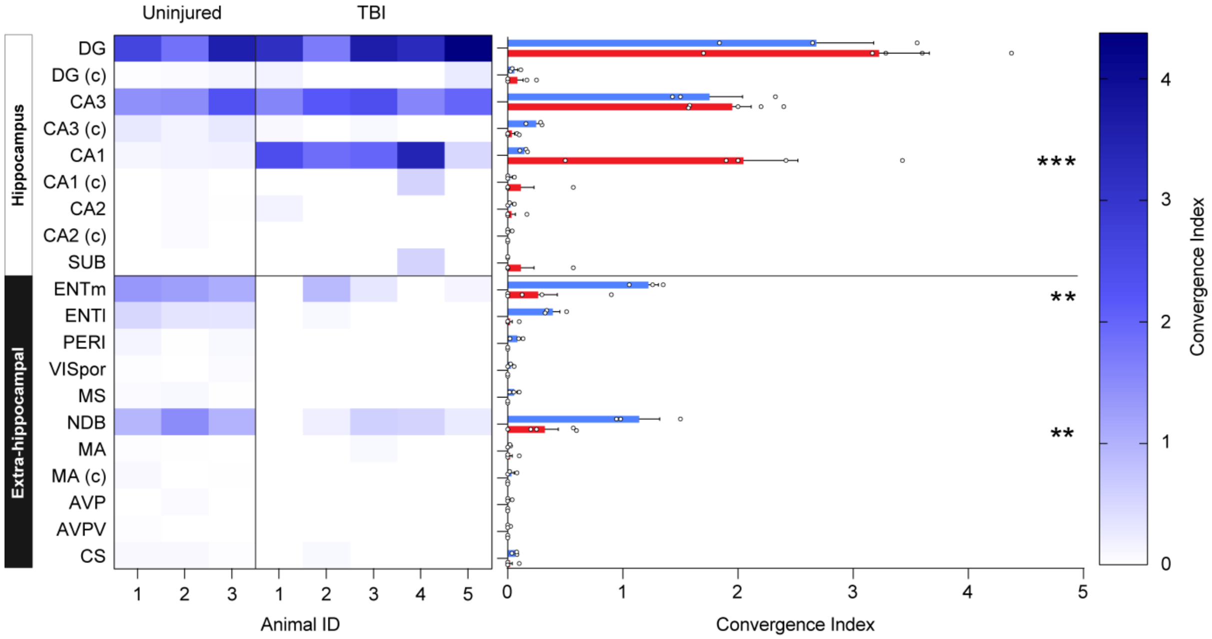

Figure 3.9: Retrograde circuit tracing data represented as a convergence index. The number of rabies-labeled input neurons in each brain area were divided by the total number of starter cells counted for each animal to derive a convergence index for each brain area. Left: individual values for each animal represented by a heat-map. Right: Average convergence index for each brain area. ***P = 6.00E-15, control versus TBI (CA1), **P = 2.02E-04, control versus TBI (ENTm), **P = 3.07E-03, control versus TBI (NDB); two-way repeated-measures ANOVA with Bonferroni's post-hoc test; *n* = 3-6 mice per group. Error bars, s.e.m. MS, medial septal nucleus; NDB, diagonal band nucleus; HIP, hippocampus; PERI, perirhinal area; ENTl, lateral entorhinal cortex; ENTm, medial entorhinal cortex; DG, dentate gyrus; CA3, cornu ammonis 3; CA1, cornu ammonis 1; CA2, cornu ammonis 2; SUB, subiculum; PSUB, prosubiculum; VISpor, postrhinal area; MA, magnocellular nucleus; AVP, anteroventral preoptic nucleus; AVPV, anteroventral periventricular nucleus; CS, superior central nucleus raphe.

Long-range input is proportionally stable

The loss of long-range input after TBI could result from a loss of neurons at distant sites or a loss of anatomical connections. To test this, and to characterize the neurochemical identities of the input to hilar SST interneurons, we developed a method for rehydrating the same brains used for light-sheet imaging and processing them for traditional double-immunofluorescence immunostaining (**Fig 3.10A, B**). Because long-range input to hilar SST interneurons arrives primarily from basal forebrain and ENTm, we quantified neuron populations in these areas.

The basal forebrain contains multiple cell types that project long-distances via the fimbria/fornix pathway to hippocampus, including cholinergic, glutamatergic and GABAergic neurons (Do et al., 2016). In both control and injured animals, the absolute majority of NDB input neurons to hilar

SST interneurons expressed choline acetyltransferase (CHAT) (control: 67.1 ± 6.8 %, *n* = 3 mice; TBI: 79.2 ± 12.5 %, *n* = 4 mice; P = 0.99, Fisher's exact test; **Fig 3.10B-E**). This is different from inhibitory interneurons in CA1, which primarily receive GABAergic input from basal forebrain (Sun et al., 2014). We did not find a difference in the density of CHAT+ neurons in NDB between control and brain injured animals (**Fig 3.10F**), suggesting CHAT+ neurons were not reduced in basal forebrain after focal TBI.

This result was unexpected, because a loss of CHAT immunoreactive neurons has been reported in basal forebrain of diffuse injury models (Leonard et al., 1994; Schmidt and Grady, 1995). To rule out the possibility that cell quantifications were influenced by rabies circuit mapping or brain clearing procedures, we examined a second, independent cohort of control and brain injured animals that did not undergo these procedures (*n* = 6 controls, *n* = 4 TBI animals). In this replication experiment, we also found similar numbers of CHAT+ neurons in NDB of age-matched control and TBI mice (**Fig 3.11**).

In both control and brain injured animals, input neurons in ENTm were found almost exclusively in layer II (**Fig 3.10G, H**). Approximately 90% of these cells co-expressed reelin and had large multipolar stellate cell morphologies (control: 86.8 ± 0.34 %, *n* = 3 mice; TBI: 95.2 ± 4.8 %, *n* = 3 mice; P = 0.99, Fisher's exact test; **Fig 3.10G, H**). These results are consistent with prior studies showing that reelin-expressing stellate cells in ENTm give rise to the main associational glutamatergic pathway known as the perforant path that projects to the dentate gyrus, CA3 and CA2 regions of hippocampus (Pesold et al., 1998; Steward, 1976; Varga et al., 2010). We did not find a difference in the density of reelin+ neurons in ENTm between control and brain injured animals (**Fig 3.10I**), similar to our results in basal forebrain. Together, our results demonstrate there is a reduction in the amount of input to hilar SST interneurons from both of the major distant brain regions innervating dentate gyrus after focal TBI, but these areas remain structurally intact.

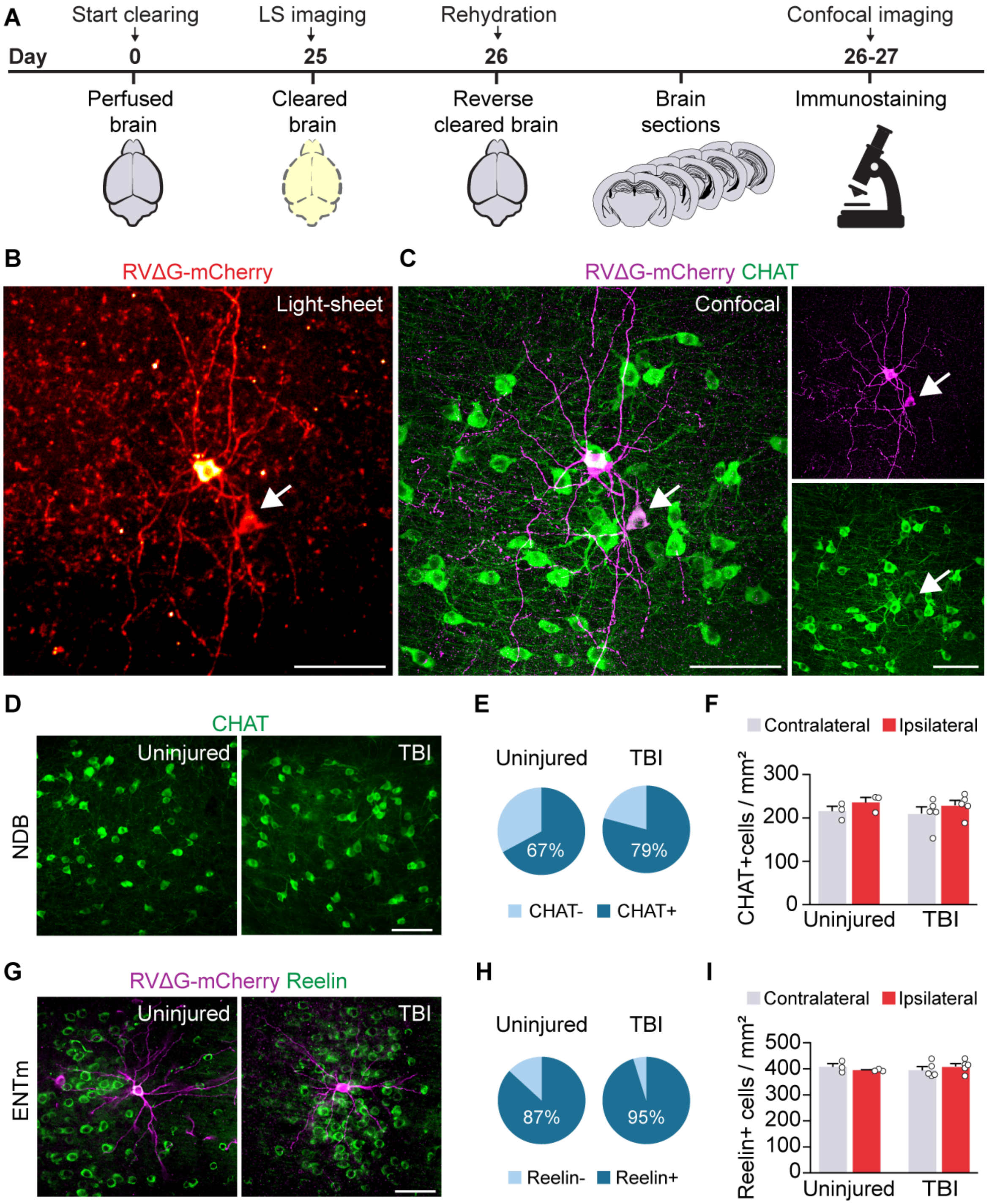

Figure 3.10: Distant brain regions remain structurally intact. A. Schematic showing experimental protocol for reverse brain clearing and immunolabeling. **B.** Two rabies-labeled input neurons (red) identified in a sagittal optical section of NDB in an intact control brain. 50 µm maximum intensity projection obtained by whole-brain light-sheet imaging. **C.** Sagittal section containing the same input neurons (magenta) labeled for CHAT (green) after processing for traditional immunostaining and confocal imaging. Arrow indicates co-labeled cell. **D.** NDB of uninjured control (left) and brain injured animal (right) labeled for CHAT (green). Scale bar, 100 µm. **E.** Proportion of mCherry+ rabies-labeled input neurons that expressed CHAT. **F.** Quantification of CHAT+ neuron density in ipsilateral and contralateral NDB in uninjured controls and brain injured animals. *n* = 3 control and 5 TBI animals. **G.** ENTm of uninjured control (left) and brain injured animal (right) labeled for reelin (green) and mCherry (magenta). **H.** Proportion of mCherry+ rabies-labeled input neurons that expressed reelin. **I.** Quantification of reelin+ cell density in ipsilateral and contralateral ENTm. *n* = 3 control and 5 TBI animals. Error bars, s.e.m.; scale bars, 100 µm. See also **Fig 3.11**. NDB, diagonal band nucleus; ENTm, medial entorhinal area.

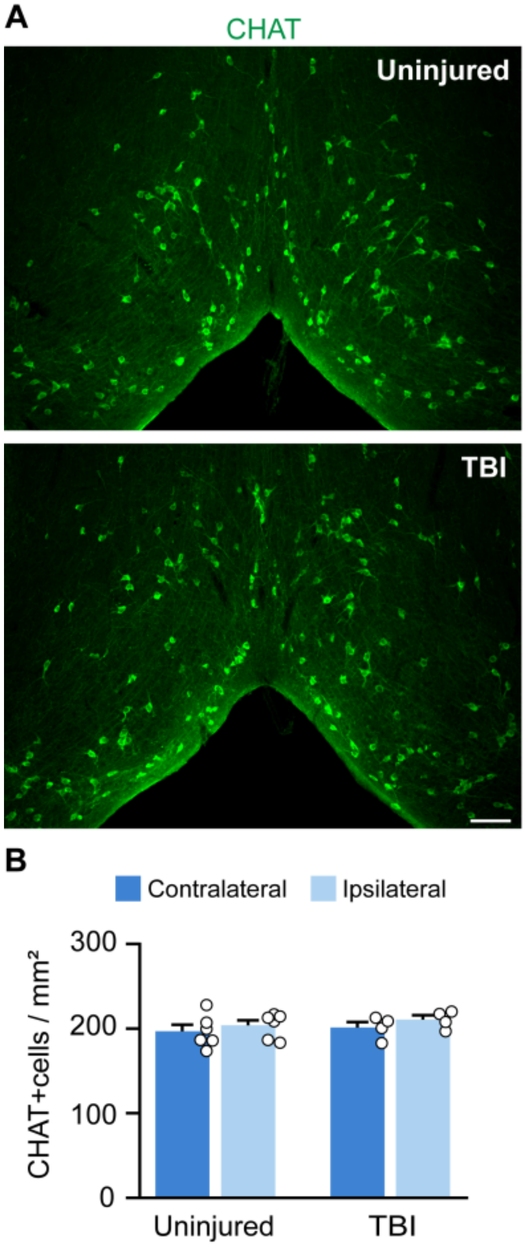

Figure 3.11: Replication of CHAT immunostaining with conventional immunostaining in a separate cohort of animals. A. Coronal sections of NDB labeled for CHAT in an uninjured control and a brain injured animal. Scale bar, 100 µm. **B.** Quantification of CHAT+ cell density.

Whole-brain connectivity is reorganized far from the injury

Having observed dramatic brain-wide reorganization of hippocampal SST interneuron circuitry, we next asked whether the input to SST neurons was also rewired far away from the injury. The PFC is a critical higher-order limbic site that is central to memory retrieval and decision making and receives a highly diverse pattern of inputs spanning the entire brain, including direct input from hippocampus (Le Merre et al., 2021). At 24 hrs after injury, fluoro-jade C staining revealed degenerating neurons in hippocampus and neocortex at the injury epicenter, but no labeled cells were detected at distant sites, such as PFC, entorhinal cortex, basal forebrain or thalamus (**Fig 3.12**). We also did not find a difference in SST+ neuron density in PFC eight weeks after TBI (**Fig 3.13**). These results are consistent with producing a highly focal contusive brain injury.

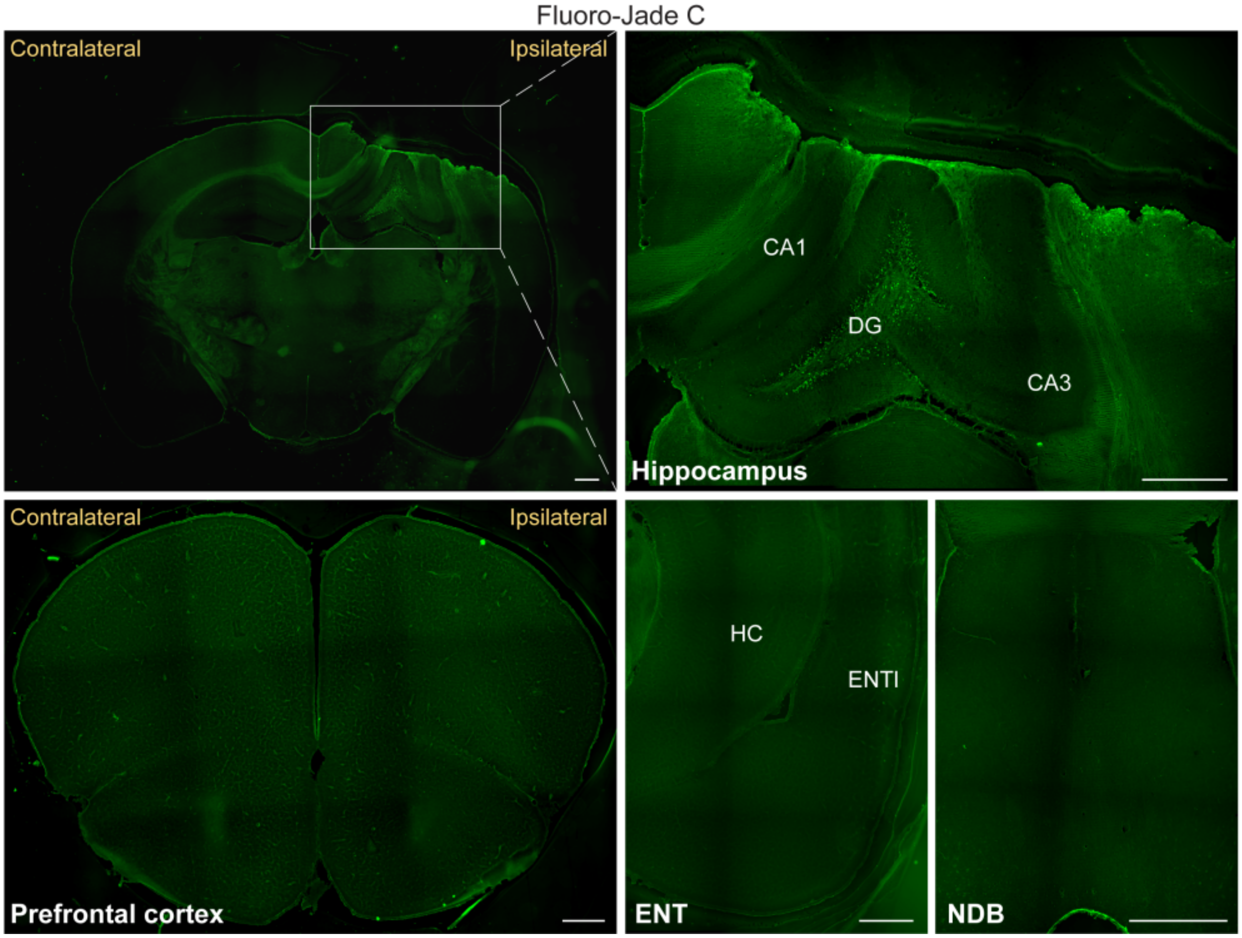

Figure 3.12: TBI produces highly focal neurodegeneration. Coronal sections through dorsal hippocampus (HC), prefrontal cortex, entorhinal cortex (ENT) and diagonal band nucleus (NDB) labeled for fluoro-jade C 24 h after TBI. Scale bar, 500 μm. CA1, cornu ammonis 1; DG, dentate gyrus; CA3, cornu ammonis 3; ENTl, lateral entorhinal area.

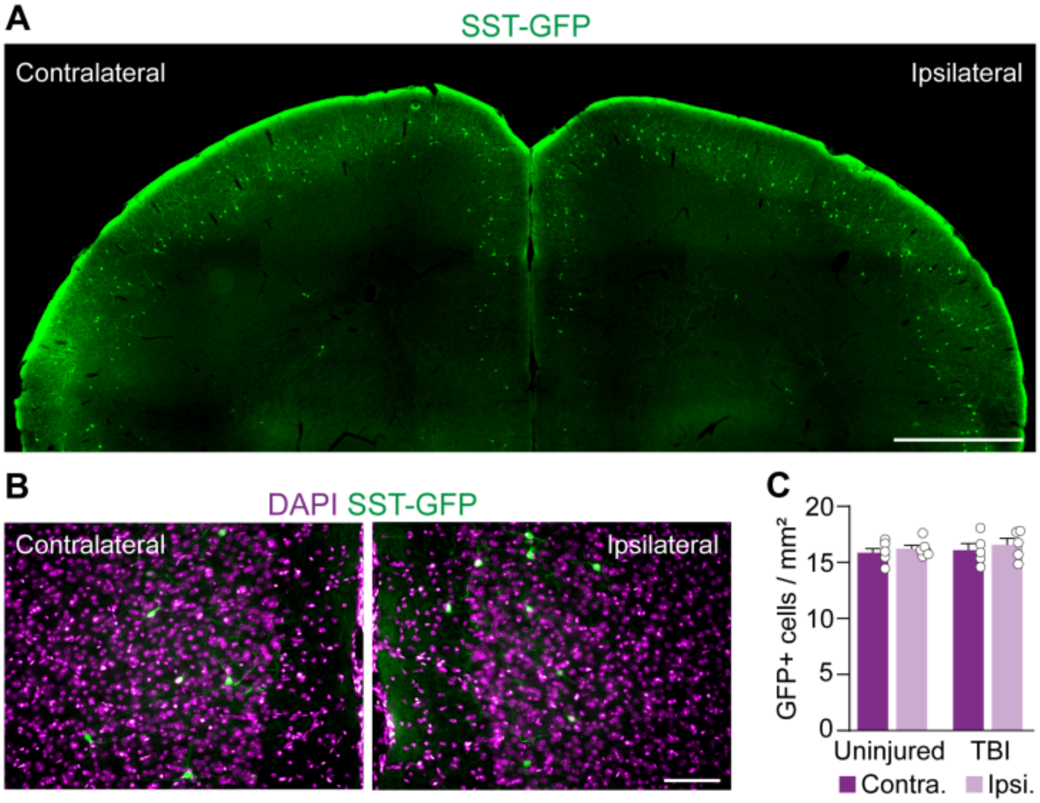

Figure 3.13: SST interneurons are not reduced in PFC after TBI. A, B. Coronal section 8 wks after TBI labeled for SST-GFP (green) and DAPI (magenta). **C.** Quantification of SST-GFP interneurons in uninjured and brain injured animals. Error bars, s.e.m.; scale bars, 1 mm (A), 100 μm (B).

To generate whole-brain maps of the input to SST interneurons in PFC, we used the same two-virus rabies-based approach to label dual-color starter cells and mCherry-labeled input neurons in SST-Cre mice (**Fig 3.14A, B**). For these studies, PFC was defined as including the following subregions based on a consensus drawn from the literature (Le Merre et al., 2021): secondary motor area (MOs), anterior cingulate areas dorsal and ventral (ACAd and ACAv), prelimbic area (PL), infralimbic area (ILA), orbital areas medial, lateral and ventrolateral (ORBm, ORBl and ORBvl). Injections were made into the ipsilateral hemisphere (that is, the injured side of the brain). We found 96.5 % of the GFP-labeled neurons were SST+, and no neurons were labeled anywhere in the brain after injecting AAV8-hSyn-FLEX-TVA-P2A-eGFP-2A-oG helper and RV-ΔG-mCherry virus into Cre- animals (**Fig 3.15**). In both control and brain injured animals, starter cells were almost exclusively located inside the PFC (**Fig 3.14C-F**). Regional distributions of the starter cells were similar to what has previously been published for PFC (Ährlund-Richter et al., 2019), and no differences were detected between groups in the dorsal–ventral location of the starter neurons (**Fig 3.14D**) or layer distribution (**Fig 3.14E**), indicating there was no major bias in the location of the starter cells. As expected, there was a correlation between the number of input neurons and starter neurons, but unlike hippocampus, the number of starter neurons were not reduced in brain injured animals (control: *n* = 283.6 ± 69.5 cells; TBI: *n* = 178.8 ± 18.2 cells, P = 0.2, two-tailed t-test, *n* = 5 animals per group; **Fig 3.14G**).

Next, we quantified the input to SST interneurons in PFC. Whole-brain retrograde tracing revealed input from 160 distinct brain regions (**Figs 3.16A, Fig 3.17, Fig 3.18**). The majority of input was detected within the isocortex, especially in the injected hemisphere, followed by thalamus, hippocampus and pallidum. These results are comparable to previous retrograde tracing results in control animals (Ährlund-Richter et al., 2019; Sun et al., 2019). Within isocortex, PFC subregions provided the most prominent input; the agranular insular area and hippocampus area CA1 also provided prominent input. Analysis of probability density of input along the AP axis showed significant increases in the percentage of input neurons found between 3 and 3.6 mm (PFC) in brain-injured animals (3-3.2 mm, control: 7.25 ± 0.55 %, TBI: 9.39 ± 1.14 %, P = 9.37E-03; 3.2-3.4 mm, control: 5.58 ± 0.68 %, TBI: 9.1 ± 1.15 %, P = 4.23E-08; 3.4-3.6 mm, control: 4.08 ± 0.69 %, TBI: 7.23 ± 0.68 %, P = 1.84E-06; Two-way repeated measures ANOVA with Bonferroni's post-hoc test). Along the ML axis, we detected significant increases in input neurons between midline and 0.6 mm lateral to midline in the ipsilateral hemisphere (5.1-5.4 mm, control: 28.42 ± 1.54 %, TBI: 34.95 ± 3.31 %, P = 8.12E-05; 5.4-5.7 mm, control: 16.75 ± 2.83 %, TBI: 21.39 ± 5.71 %, P = 2.57E-02; Two-way repeated measures ANOVA with Bonferroni's post-hoc test), and significant decreases in input neurons were found between 0.3 and 0.6 mm lateral to midline in the contralateral hemisphere (6-6.3 mm, control: 7.98 ± 0.77 %, TBI: 3.56 ± 0.58 %, P = 4.55E-02; Two-way repeated measures ANOVA with Bonferroni's post-hoc test; **Fig 3.16B**).

There was a significant decrease in the overall percentage of contralateral input to SST interneurons after TBI (**Fig 3.16C**), similar to what we observed in hippocampus. However, no differences were detected in the mean distance of rabies-labeled neurons to the starter cell centroid (**Fig 3.16D**) or the overall percentage of input neurons located outside the PFC (**Fig 3.16E**).

Input neurons were initially grouped according to large functional divisions, i.e. isocortex, cortical subplate, olfactory areas, hippocampal formation, striatum, pallidum, thalamus, hypothalamus, midbrain and hindbrain. In brain injured animals, we found that SST interneurons in PFC received significantly greater percentage of total input from the ipsilateral isocortex as compared to controls, but the percentage of input neurons in contralateral isocortex and ipsilateral thalamus were both reduced (**Fig 3.16F**). In thalamus, only the anterior thalamic nuclei showed a significant reduction in input neurons after TBI (**Fig 3.16G**). Whole-brain analysis of the input neurons in all discrete brain areas revealed that six of the seven areas with altered input after TBI were in isocortex (**Fig 5H**). Notably, not all PFC regions in the ipsilateral hemisphere showed increased input; input from PL and ACAd were both significantly reduced after TBI. Similar results were obtained by analyzing the convergence index for each animal (**Fig 3.19**). This pattern of enhanced local connectivity and reduced long-range input is similar to what we observed in brain injured hippocampus, suggesting that even in brain regions very far away from the injury site, the topographic organization of inhibitory neurons is dramatically rewired after a focal brain injury.

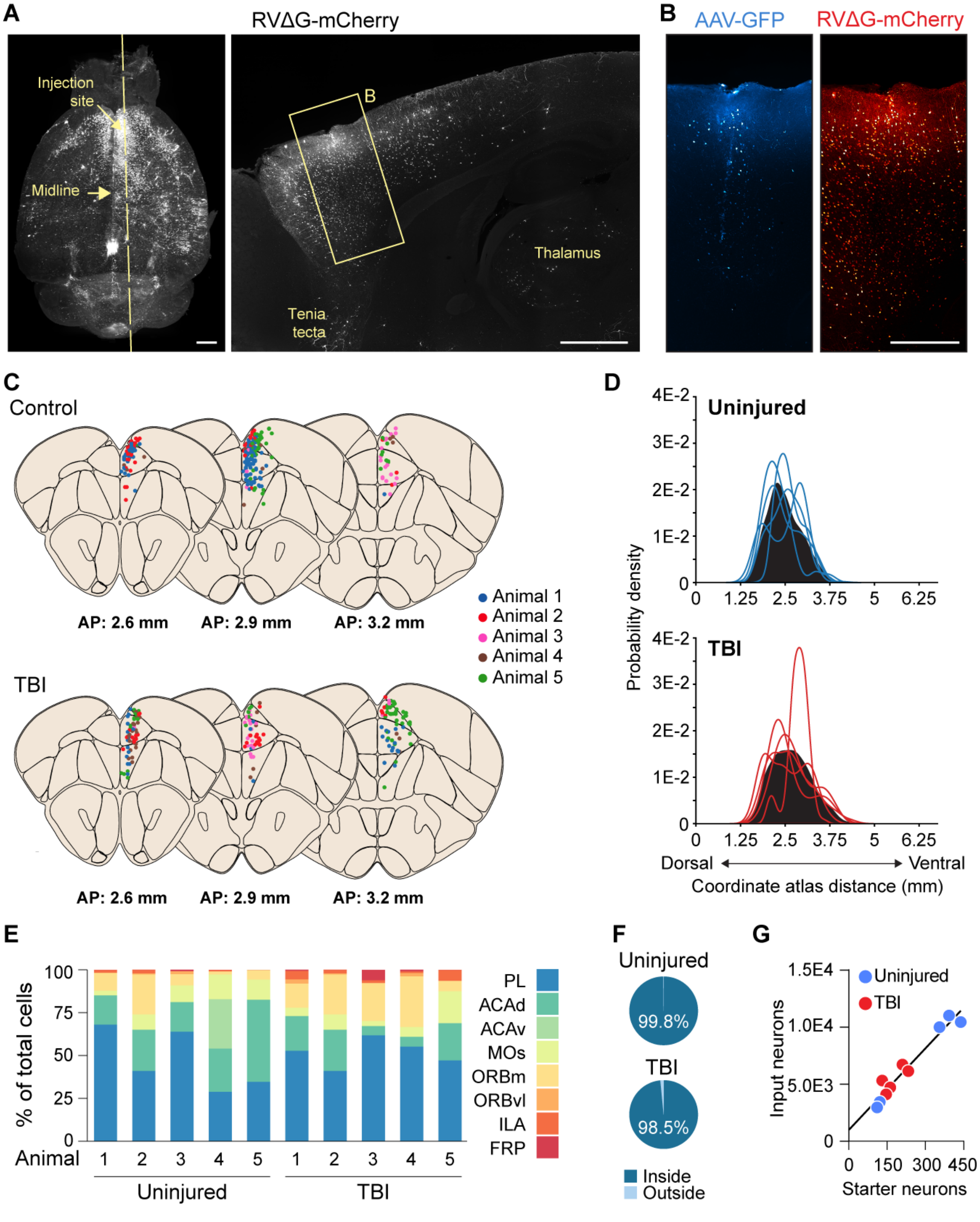

Figure 3.14: Distribution of starter neurons in PFC. A. Left: Whole brain cleared using iDISCO and labeled for neurons providing input to prelimbic SST interneurons (white). Right: 100 µm sagittal optical section of the same brain showing rabies-labeled input neurons at the injection site. Scale bars, 1 mm. **B.** Boxed region shown in A labeled for starter cells (blue) and input neurons (red). Scale bar, 500 µm.. **C.** Schematic coronal sections (100 µm) showing individual starter cells registered in standardized atlas space for uninjured controls and brain injured animals. Each color corresponds to a different animals. One dot represents one neuron. n = 5 control and 5 TBI animals. **D.** Gaussian kernel cell density plots of the whole-brain distribution of starter neurons along the dorsal-ventral axis. Black shading represents the pooled population with individual lines representing each animal. **E.** Regional distribution of starter cells in uninjured controls and brain injured animals. **F.** Proportion of starter cells identified within PFC (PL, ACAd, ACAv, MOs, ORBm, ORBvl, ILA). **H.** Linear regression analysis for number of starter cells and pre-synaptic input neurons (n = 5 mice per group; R^2 = 0.94). See also **Fig 3.12**, **3.13** and **3.15**. PL, prelimbic area; ACAd, anterior cingulate area, dorsal part; ACAv, anterior cingulate area, ventral part; MOs, secondary motor area; ORBm, orbital area, medial part; ORBvl, orbital area, ventrolateral part; ILA, infralimbic area, FRP, frontal pole.

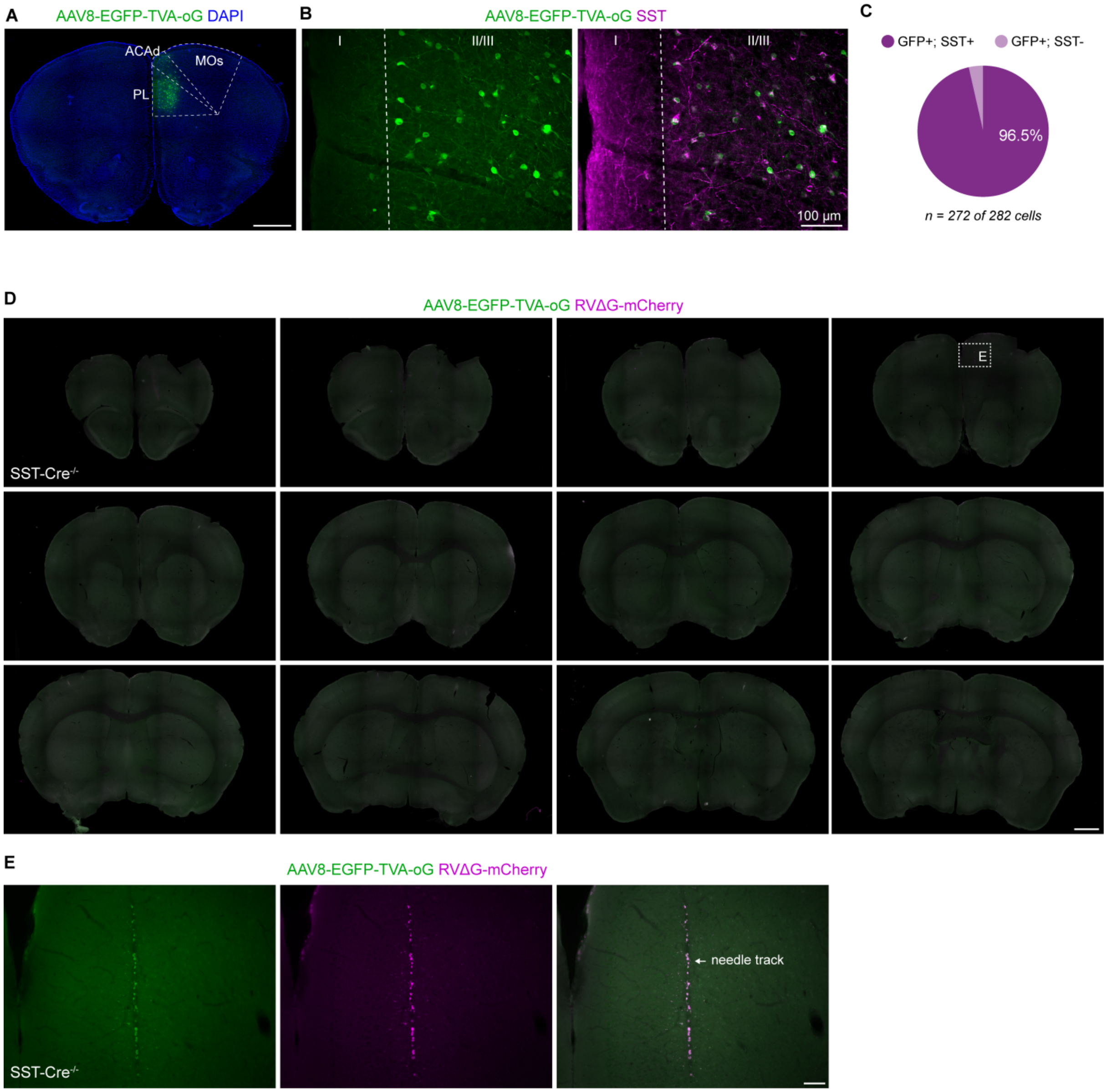

Figure 3.15: Virus specificity in PFC. A, B. Coronal section of a control animal labeled for AAV-GFP helper virus (green), SST (magenta) or DAPI (blue) 3 wks after AAV injection into PFC. **C.** Proportion of GFP+ cells that express SST. **D.** Serial coronal sections every 300 µm through the entire brain of an adult SST-Cre-negative mouse labeled for AAV helper virus (green) and rabies (magenta). **E.** High magnification image of the injection site in PFC of the same SST-Cre-negative mouse shown in D. Scale bars, 1 mm (A, D), 100 µm (B, E). PL, prelimbic area; ACAd, anterior cingulate area, dorsal part; MOs, secondary motor area.

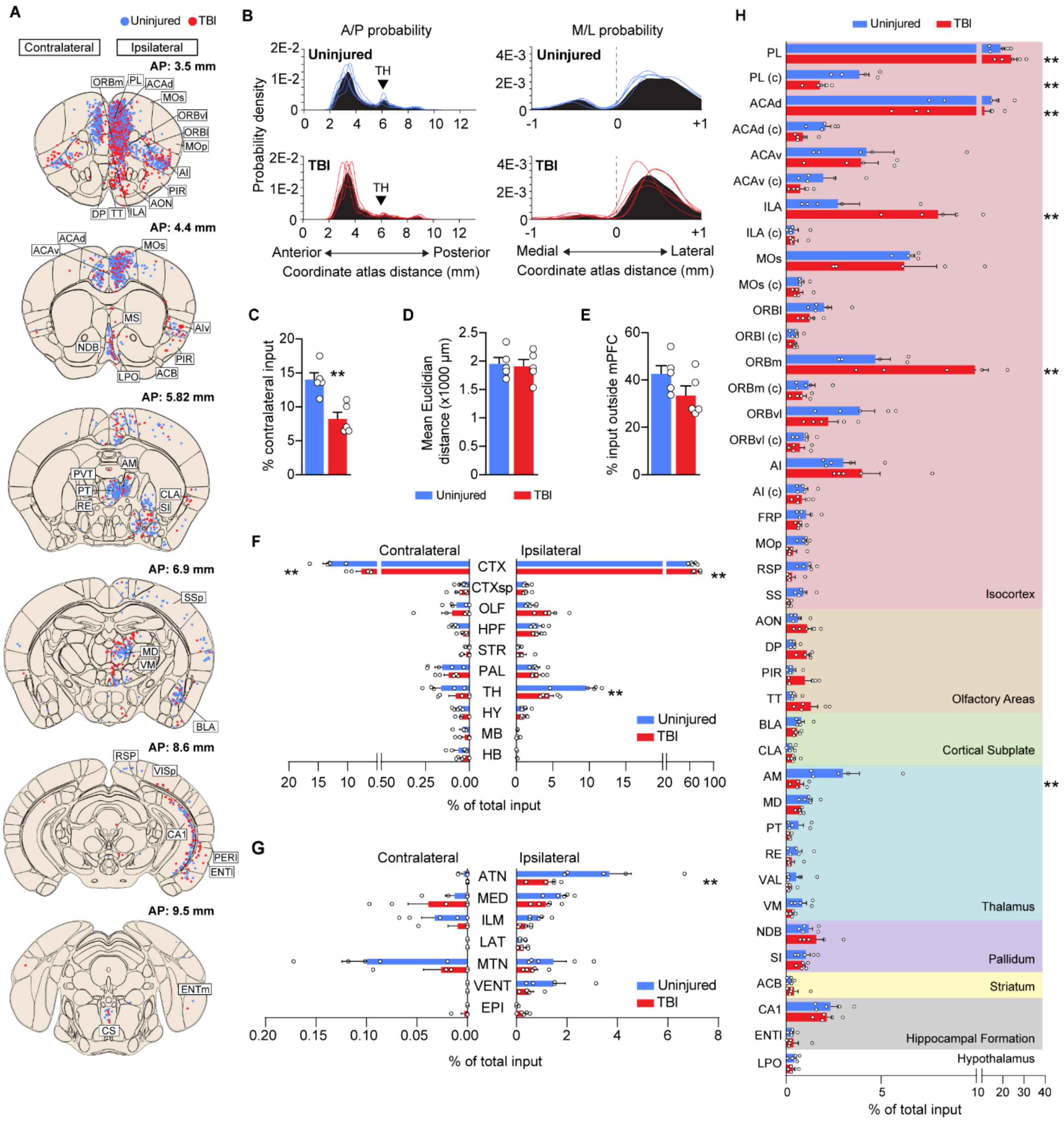

Figure 3.16: Input to SST interneurons in PFC is reorganized after TBI. A. Schematic coronal sections (100 µm) showing individual input neurons registered in standardized atlas space for uninjured controls (blue) and brain injured animals (red). One dot represents one neuron. *n* = 5 control and 5 TBI animals. **B.** Gaussian kernel cell density plots of the whole-brain distribution of input neurons along the anterior-posterior (A-P) and medial-lateral (M-L) axis. Black shading represents the pooled population with individual lines representing each animal. TH, thalamus. **C.** Proportion of input neurons found in contralateral hemisphere. Control: 11.17 ± 1.02%; TBI: 8.22 ± 0.98 %; *n* = 5 mice per group; **P = 3.40E-3; two-tailed t-test. **D.** Quantification of average Euclidian distance between starter cell centroid and input neuron positions. **E.** Proportion of input neurons found outside PFC. **F.** Proportion of total input arising from high-level brain regions. **P = 4.43E-10, control versus TBI (CTX, ipsilateral), **P = 2.88E-06, control versus TBI (CTX, contralateral),**P = 4.68E-05, control versus TBI (TH, ipsilateral); *n* = 5 mice per group; Two-way repeated measures ANOVA with Bonferroni's post-hoc test. **G.** Proportion of total presynaptic input arising from thalamic areas. **P = 5.86E-10, control versus TBI (ATN, ipsilateral); *n* = 5 mice per group; Two-way repeated measures ANOVA with Bonferroni's post-hoc test. **H.** Proportion of input neurons identified in the top 40 discrete brain regions innervating PFC. **P = 1.00E-15, control versus TBI (PL, ipsilateral),**P = 1.82E-03, control versus TBI (PL, contralateral),**P = 4.38E-12, control versus TBI (ACAd, ipsilateral),**P = 1.00E-15, control versus TBI (ILA, ipsilateral),**P = 1.00E-15, control versus TBI (ORBm, ipsilateral),**P = 2.77E-04, control versus TBI (AM, ipsilateral); *n* = 5 mice per group; Two-way repeated measures ANOVA with Bonferroni's post-hoc test. Error bars, s.e.m.. See also **Figs 3.17**, **3.18**, **3.19.** PL, prelimbic area; ACAd, anterior cingulate area, dorsal part; ACAv, anterior cingulate area, ventral part;

MOs, secondary motor area; ORBm, orbital area, medial part; ORBvl, orbital area, ventrolateral part; ILA, infralimbic area, FRP, frontal pole; PL, prelimbic area; MOp, primary motor area; AI, agranular insular area; PIR, piriform area; AON, anterior olfactory nucleus; TT, tenia tecta; DP, dorsal peduncular area; ACB, nucleus accumbens; MS, medial septal nucleus; NDB, diagonal band nucleus; LPO, lateral preoptic area; AM, anteromedial nucleus; PVT, periventricular nucleus; PT, parataenial nucleus; RE, nucleus of reuniens; CLA, claustrum; SI, substantia innominata; SSp, primary somatosensory area; MD, mediodorsal nucleus; VM, ventromedial nucleus; BLA, basolateral amygdala; VISp, primary visual area; RSP, retrosplenial area; CA1, cornu ammonis 1; PERI, perirhinal area; ENTm, medial entorhinal area; ENTl, lateral entorhinal area; CS, superior central nucleus raphe; TH, thalamus; CTX, isocortex, CTXsp, cortical subplate; OLF, olfactory areas; HPF, hippocampal formation; STR, striatum; PAL, pallidum; HY, hypothalamus; MB, midbrain; HB, hindbrain; ATN, anterior group of the dorsal thalamus; MED, medial group of the dorsal thalamus; ILM, intralaminar nuclei of the dorsal thalamus; LAT, lateral group of the dorsal thalamus; MTN, midline group of the dorsal thalamus; VENT, ventral group of the dorsal thalamus; EPI, epithalamus.

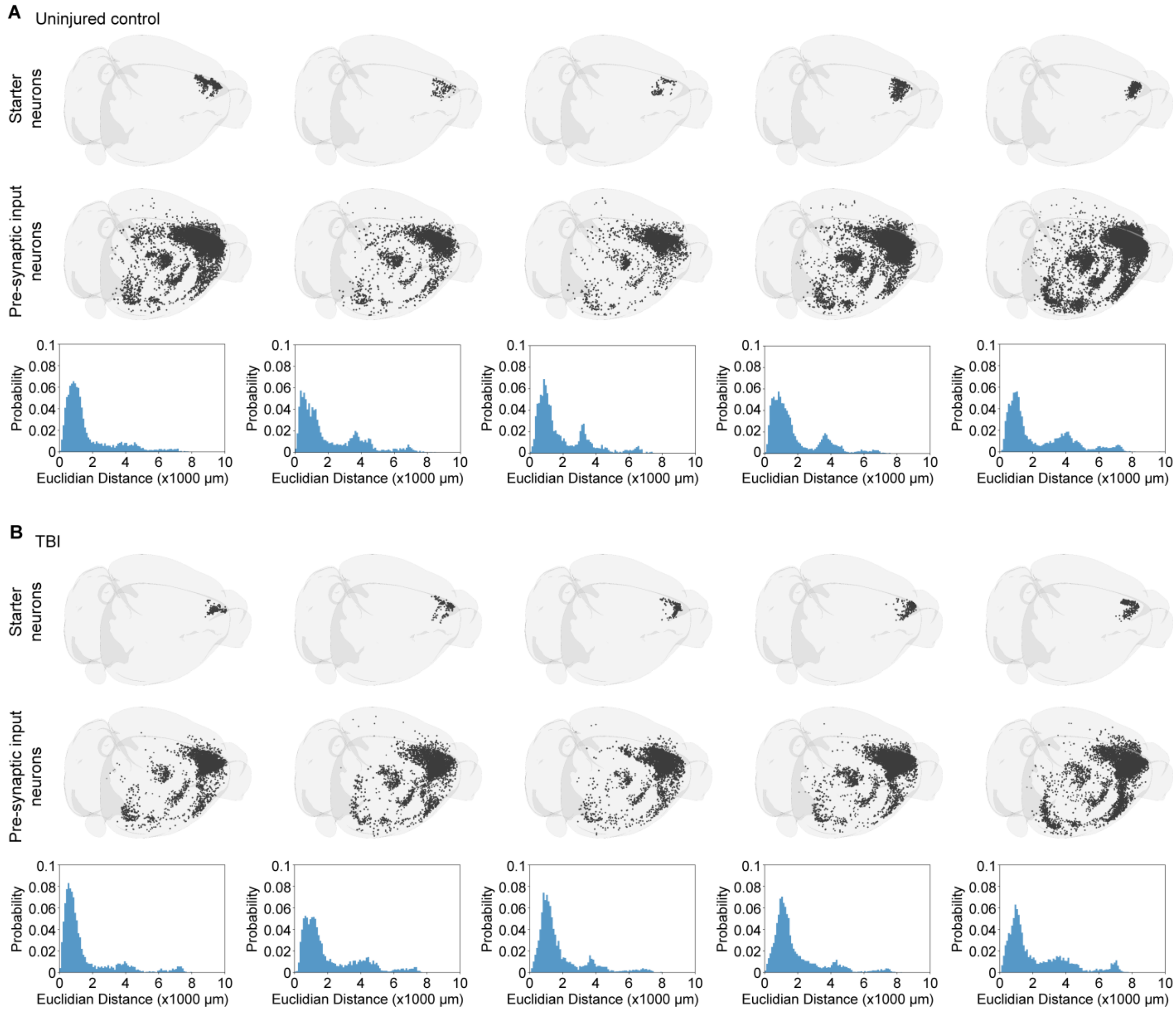

Figure 3.17: Individual animal plots of input to PFC SST interneurons. A, B. Top: whole-brain plots of starter cells and pre-synaptic input neurons annotated in standardized atlas space. Bottom: histograms showing Euclidian distances at 100 µm bins in uninjured controls (A) and brain injured animals (B). Black dots represent individual cells registered in standardized atlas space.

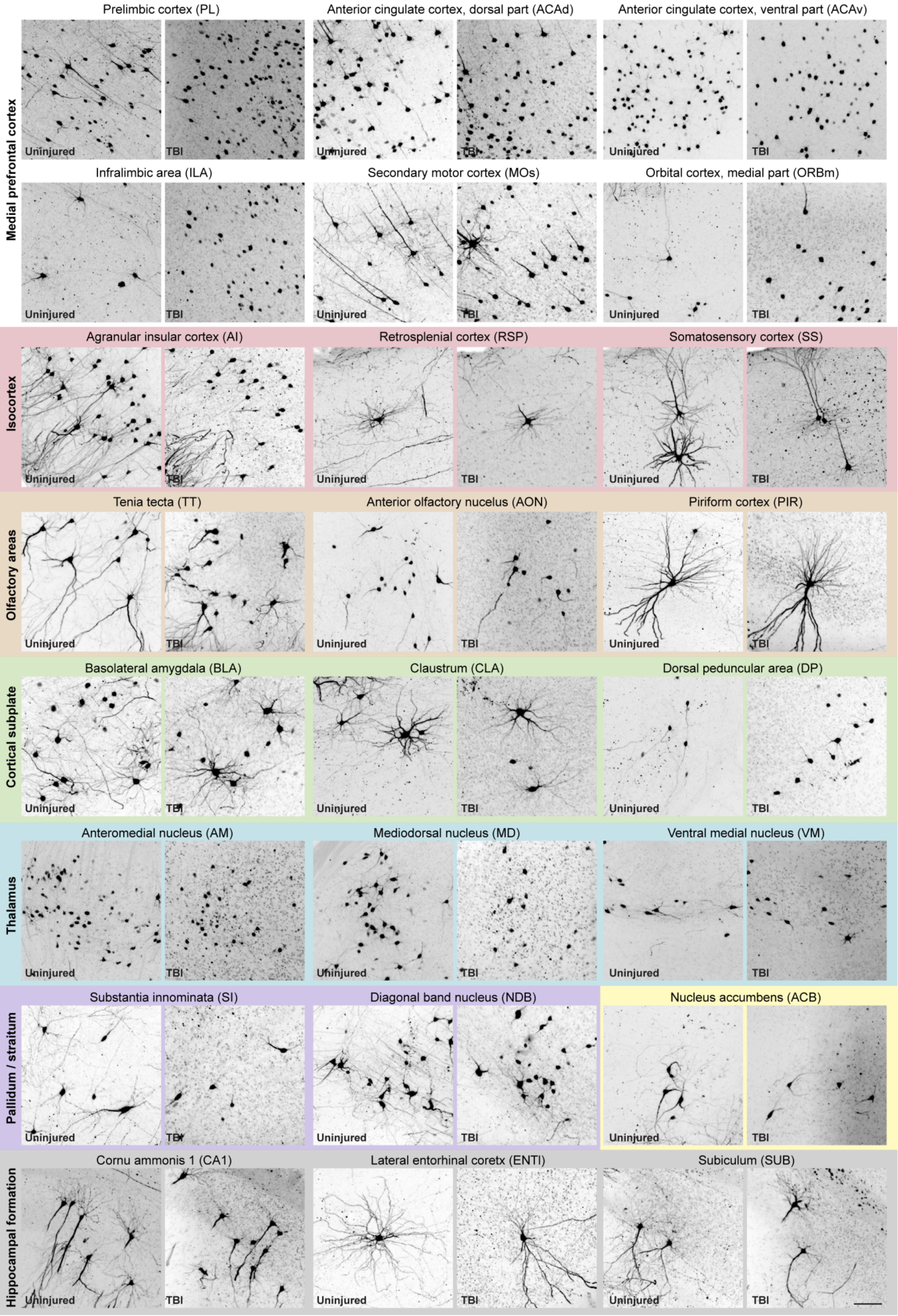

Figure 3.18: Input neurons innervating PFC SST interneurons. Maximum intensity projections (100 μm) of neurons providing direct input to PFC SST interneurons in the intact and damaged brain. Scale bar, 100 μm.

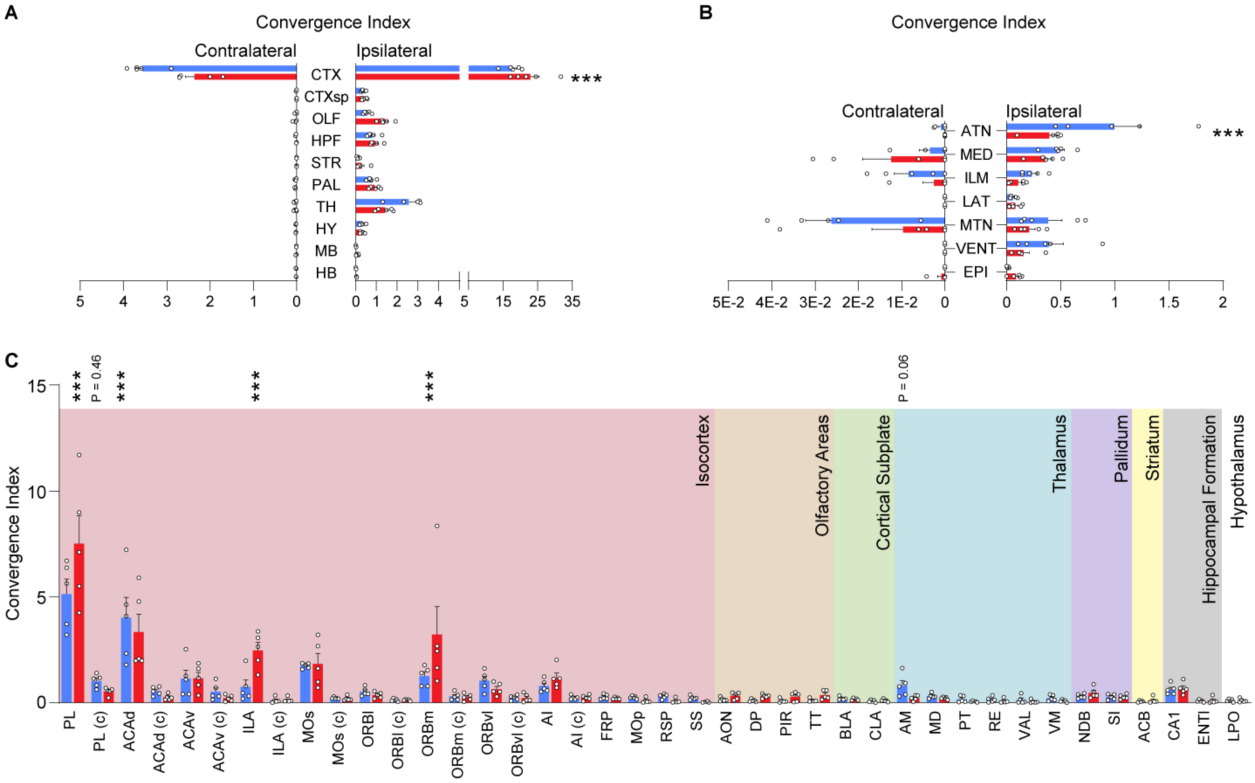

Figure 3.19: Retrograde circuit tracing data in PFC represented as a convergence index. A. Average convergence index for each brain area grouped according to large functional divisions. **B.** Average convergence index for individual thalamic nuclei. **C.** Average convergence index for the top 40 discrete brain areas with the greatest amount of input to SST interneurons in PFC. *** $P < 0.001$; two-way ANOVA with Bonferroni's post-hoc test. Error bars, s.e.m.

Transplanted SST interneurons establish orthotopic brain-wide connections

Grafts of embryonic-derived interneuron progenitors enable robust restoration of inhibition and are therapeutic in a wide range of acquired brain disorders, including epilepsy (Hunt *et al.*, 2013b), Alzheimer's disease (Martinez-Losa et al., 2018) and TBI (Zhu et al., 2019). However, the circuit basis for this regeneration is unknown. Therefore, we tested whether interneuron progenitors are capable of establishing appropriate local and long-range connections in a damaged brain. For this purpose, we harvested GABA progenitors from the medial ganglionic eminence (MGE), the developmental origin of nearly all SST-expressing cortical interneurons (Pelkey et al., 2017). Then, 7 days after TBI, we transplanted 3×10^4 MGE cells into ipsilateral hippocampus at the injury epicenter. This corresponds to the period of maximal deafferentation after TBI (Scheff et al., 2005). We first examined grafts of SST interneurons harvested from E13.5 SST-Cre donor mice crossed with Ai6 reporter to allow for their visualization after transplantation. At 35 days after transplantation (DAT), transplanted interneurons were found throughout hippocampal subfields (*n* = 3 animals) (**Fig 3.20A, B, Fig 3.21**). The majority of Ai6-labeled cells expressed SST (83 ± 2.1%, **Fig 3.20C**), confirming selective Cre expression in the SST population of transplanted MGE cells.

Finally, we performed whole-brain mapping to identify local and long-range inputs to transplanted SST interneurons in the injured brain. For these experiments, donor cells were obtained from SST-Cre+ embryos. Transplants were performed 7 days after TBI, virus injections were made into hippocampus at 8 weeks (AAV8-hSyn-FLEX-TVA-P2A-eGFP-2A-oG) and 11 weeks (RV-ΔG-mCherry) after injury, and animals were processed for brain clearing and analysis 7 days after the final virus injection. This period corresponds to a time when MGE transplantation shows robust therapeutic effects on memory and seizures in brain injured animals (Zhu et al., 2019). We found substantial numbers of input neurons across the brain were labeled by rabies virus (**Fig 3.22A-C**). Notably, input neurons were identified in 14 distinct brain areas, including all regions of hippocampus, ENTm, ENTl, medial septum and NDB (**Fig 3.22D-F, Fig 3.23**). The majority of input came from hippocampus, including robust input from area CA3 and CA1. Compared to uninjured controls, there was a significant reduction in the mean distance of rabies-labeled neurons to the MGE-transplanted starter cell centroid (**Fig 3.22G, Fig 3.24**) as well as the percentage of contralateral (**Fig 3.24**) and extra-hippocampal input (**Fig 3.22G, Fig 3.24**). This pattern of input was similar to what we observed in brain injured animals that did not receive transplants. Indeed, UMAP analysis showed that the majority of injured animals containing transplanted interneurons clustered with brain injured animals rather than controls (**Fig 3.22H**). To determine whether regional inputs co-vary, we calculated Pearsons's correlation coefficients for each pair of input regions. This showed a significant positive correlation between several input regions including CA1, CA2, magnocellular nucleus, prosubiculum, subiculum, and perirhinal cortex, indicating that when transplanted neurons receive input from one region, they generally received input from the other correlated regions (**Fig 3.22I**). Thus, transplanted SST interneurons had highly similar global input patterns as compared to native-born SST interneurons, but transplanted cells showed enhanced local input seen after TBI.

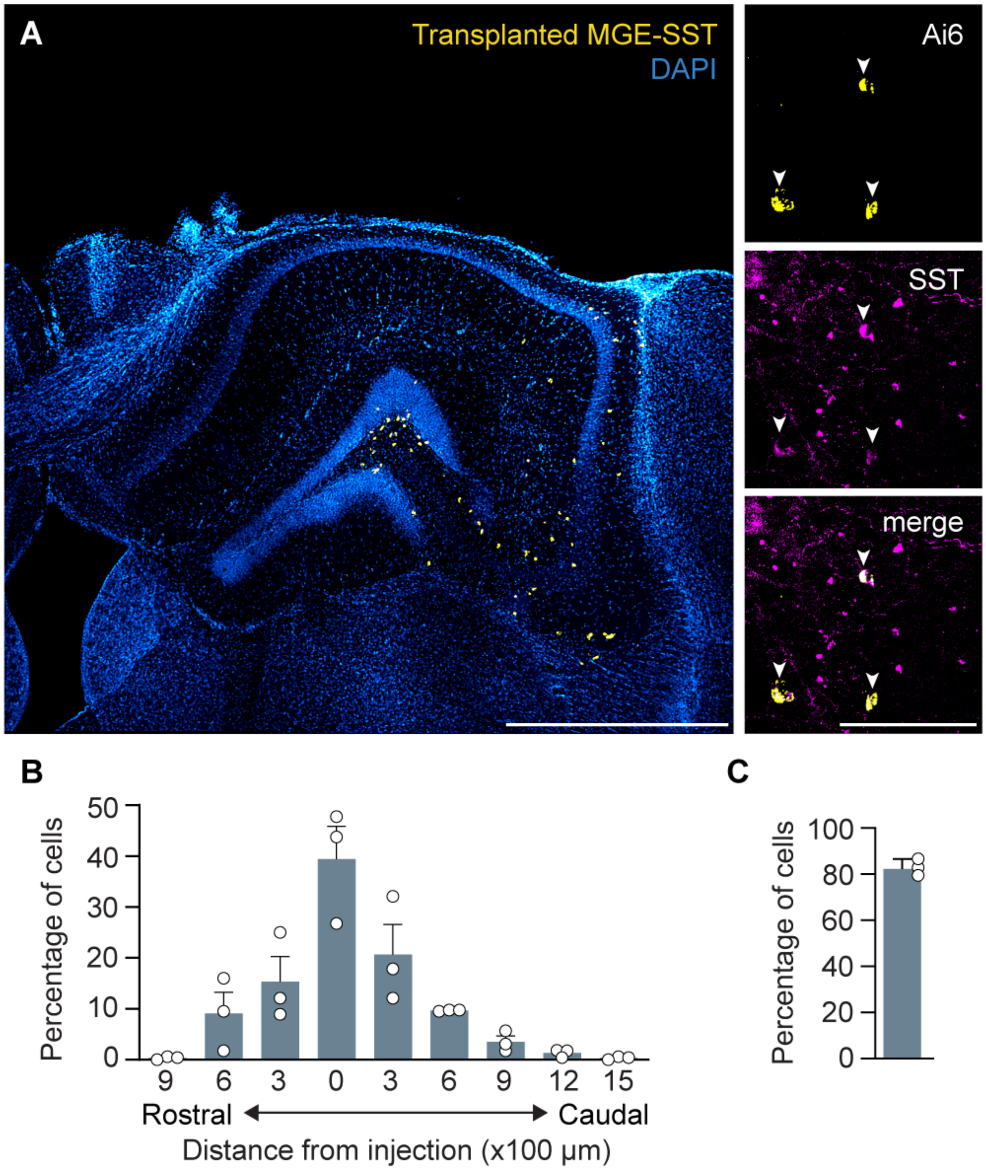

Figure 3.20: Transplanted SST interneurons integrate into brain injured hippocampus. A. Left: Coronal section of dorsal hippocampus five weeks after transplantation labeled for Ai6-expressing transplanted interneurons (yellow) and DAPI (blue). Scale bar, 1 mm. Right: Ai6-expressing neurons (yellow) co-labeled for somatostatin (magenta). Scale bar, 100 µm. **B.** Distribution of transplanted SST interneurons 35 DAT (*n* = 3 mice). **C.** Proportion of Ai6-expressing cells that expressed somatostatin. See also **Fig S15**.

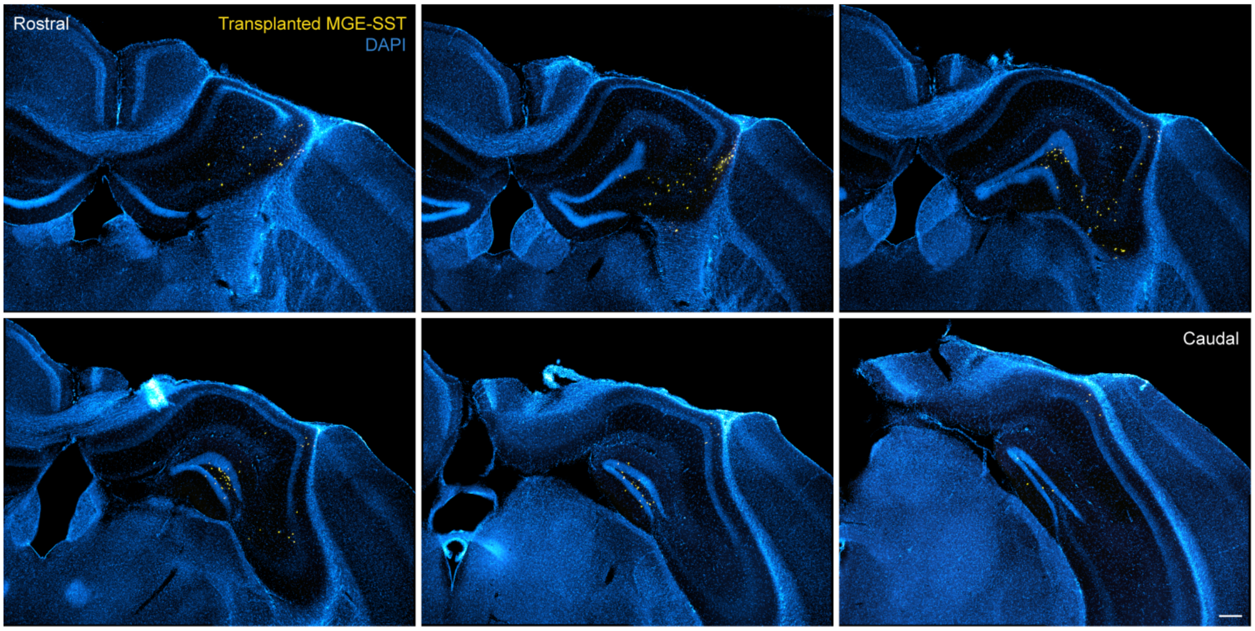

Figure 3.21: Distribution of transplanted MGE-SST cells. Coronal sections spaced 300 μm apart showing the distribution of SST::Ai6-expressing interneurons 35 DAT into a mouse with TBI. Scale bar, 250 μm.

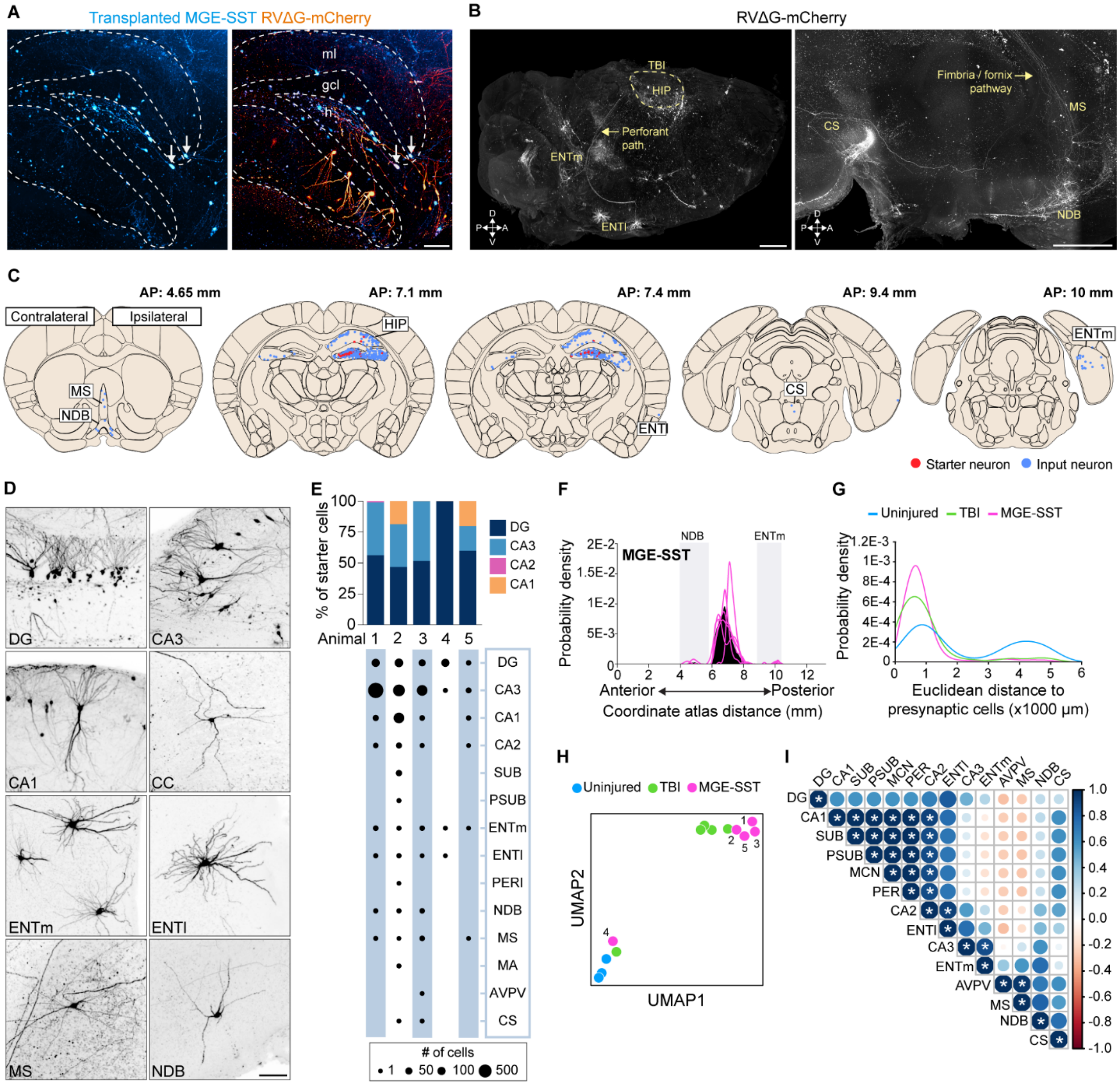

Figure 3.22: Transplanted SST interneurons receive local and long-range input. A. A 100 µm sagittal optical section of dentate gyrus labeled for transplanted starter cells (blue) and input neurons (orange). Scale bar, 100 µm. **B.** Left: 3D render of the entire ipsilateral hemisphere labeled of the same animal shown in A labeled for input neurons (white). Dotted circle outlines the injury border. Right: Whole-brain render labeled for input neurons in superior central nucleus raphae, medial septum and NDB. **C.** Schematic coronal sections (250 µm) showing individual starter cells (red) and input neurons (blue) registered in standardized atlas space. One dot represents one neuron. *n* = 5 animals. **D.** Maximum intensity projections (100 µm) of neurons providing input to transplanted SST interneurons in the intact injured brain. **E.** Top: proportion of transplanted starter cells found in each layer of hippocampus. Bottom: bubble plot of brain regions containing rabies-labeled input neurons. **F.** Gaussian kernel cell density plot of the whole-brain distribution of input neurons along the anterior-posterior axis. Black shading represents the pooled population with individual lines representing each animal. **G.** Gaussian kernel cell density plots showing pooled Euclidian distances of input neurons to nearest starter neuron. **H.** Uniform Manifold Approximation and Projection (UMAP) clustering of retrograde mapping data. **I.** Correlation matrix of input to transplanted SST interneurons. *P < .05; Pearson's correlation. Scale bars, 100 µm (A, G), 1 mm (B). See also **Fig 3.23** and **3.24**. MS, medial septal nucleus; NDB, diagonal band nucleus; HIP, hippocampus; PERI, perirhinal area; ENTl, lateral entorhinal cortex; ENTm, medial entorhinal cortex; DG, dentate gyrus; CA3, cornu ammonis 3; CA1, cornu ammonis 1; CA2, cornu ammonis 2; SUB, subiculum; PSUB, prosubiculum; VISpor, postrhinal area; MA, magnocellular nucleus; AVP, anteroventral preoptic nucleus; AVPV, anteroventral periventricular nucleus; CS, superior central nucleus raphe.

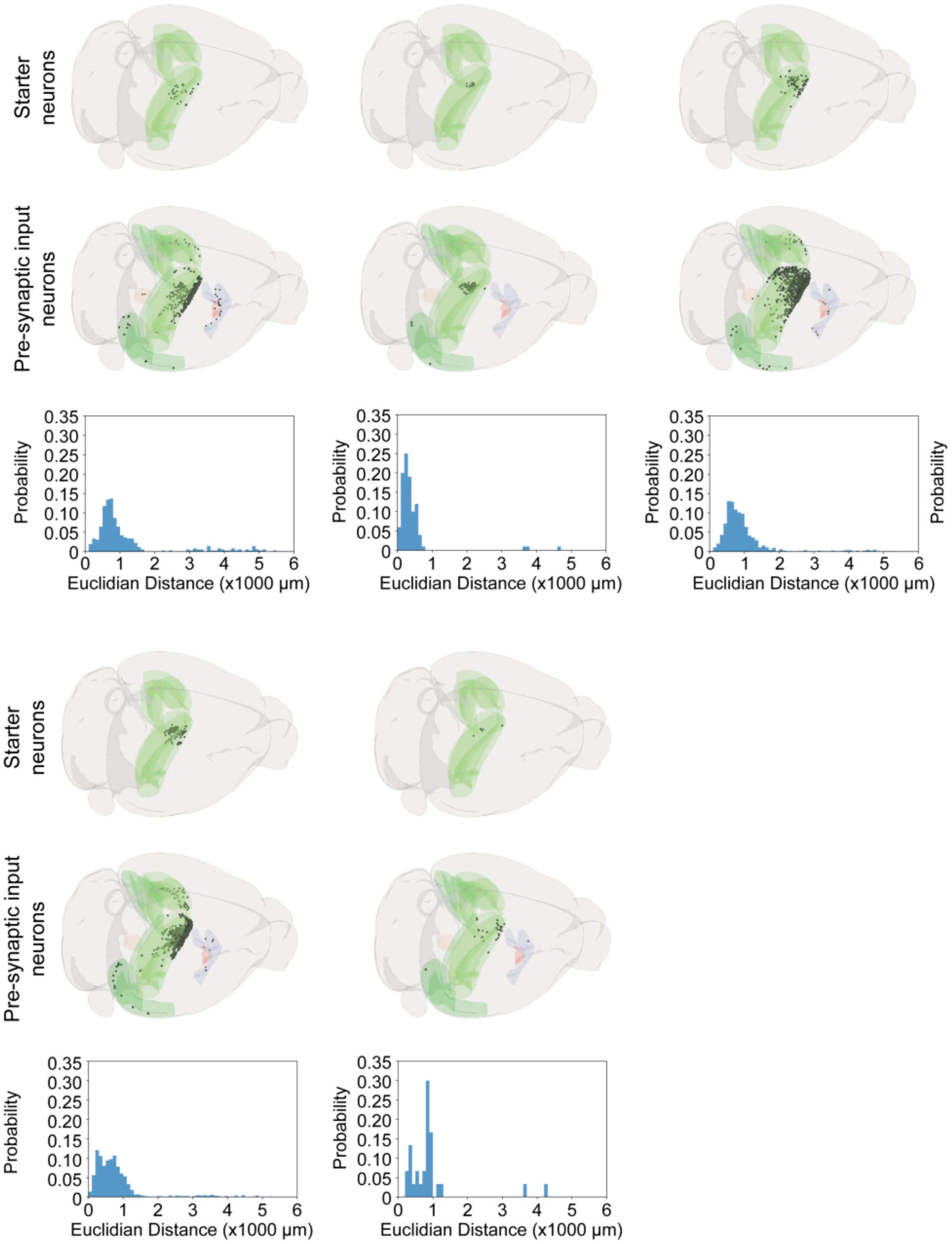

Figure 3.23: Individual animal plots of input to transplanted SST interneurons A. Top: whole-brain plots of starter cells and pre-synaptic input neurons annotated in standardized atlas space. Bottom: histograms showing Euclidian distances at 100 µm bins. Black dots represent individual cells registered in standardized atlas space. Shading indicates hippocampal formation (green), pallial regions (blue) and hypothalamus (red).

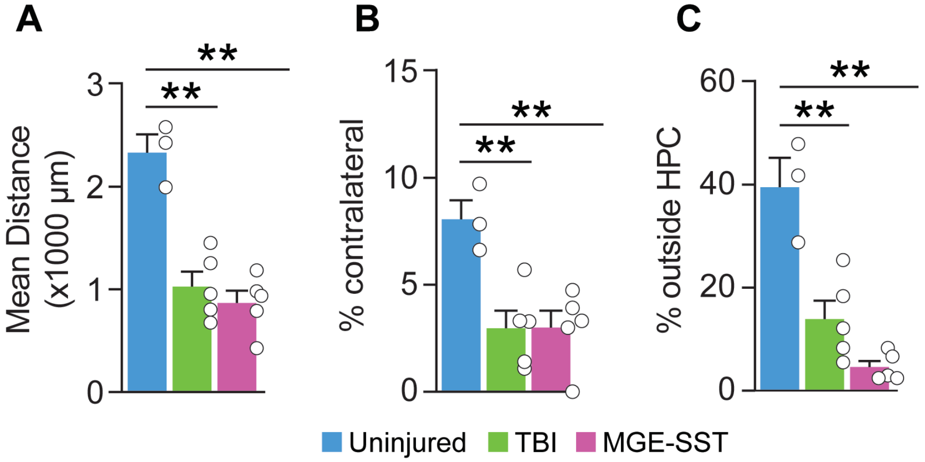

Figure 3.24: Input to transplanted interneurons. A. Quantification of average Euclidian distance between transplanted starter cell centroid and input neuron positions. Control: 2331 ± 174.1 µm, TBI: 1029 ± 142.5 µm, MGE-SST: 865.0± 125.9 µm; **P = 3.89E-04, control versus TBI; **P = 1.49E-04, control versus MGE-SST; one-way ANOVA with Tukey's post-hoc test, *n* = 3-5 mice per group. **B.** Proportion of input neurons found in contralateral hemisphere. Control: 8.05 ± 0.89 %, TBI: 2.97 ± 0.83 %, MGE-SST: 3.00 ± 0.81 %; **P = 7.34E-03, control versus TBI; **P = 7.62E-03, control versus MGE-SST; one-way ANOVA with Tukey's post-hoc test, *n* = 3-5 mice per group. **C.** Proportion of input neurons found outside hippocampus. Control: 39.52 ± 5.63 %, TBI: 13.92 ± 3.58 %, MGE-SST: 4.60± 1.23 %; **P = 1.27E-03, control versus TBI; **P = 1.10E-04, control versus MGE-SST; one-way ANOVA with Tukey's post-hoc test, *n* = 3-5 mice per group. Error bars, s.e.m.

Discussion

Using a mouse model of focal TBI, we report the first systematic assessment of large-scale circuit reorganization in a damaged brain. We mapped the brain-wide input to a single cell type with high therapeutic relevance, SST interneurons, in uninjured controls, after brain injury and after transplantation into brain injured animals. Our data demonstrate that surviving SST interneurons gain new local input after TBI, but they are largely disconnected from distant brain regions. This occurred at two spatially distinct but interacting limbic areas: the injury site in hippocampus and far away from the injury in PFC, which was not directly damaged by TBI. Our observation of circuit reorganization far away from the injury was unexpected. This suggests that post-traumatic circuit rewiring is not restricted only to damaged areas, but occurs broadly throughout the brain in response to focal injury. We further show that the diminished long-range connections did not result from cell loss in these distant brain areas. Transplanted SST interneurons integrated robustly into brain injured hippocampus and received local and long-range host input that resembled the connections of native-born interneurons. This is consistent with previous *ex vivo* functional studies documenting robust excitatory drive onto transplanted interneurons from the host brain (Hunt *et al.*, 2013b; Larimer *et al.*, 2016; Zhu *et al.*, 2019), although the source of these inputs was previously unknown.

TBI produces major structural and functional alterations in neural circuitry – resulting from progressive brain damage and secondary neuroplasticity responses – which develop over time (Hunt *et al.*, 2013a; Povlishock and Katz, 2005). Until recently, our understanding of how TBI damages the brain's wiring diagram has been limited to standard neuroanatomy and slice electrophysiology approaches. These studies show principal neurons undergo initial deafferentation after TBI, possibly due to loss of input neurons (Ribak and Reiffenstein, 1982; Scheff *et al.*, 2005). This is followed by a progressive increase in the number of synaptic contacts and formation of new excitatory circuits within injured areas of the brain (Hunt *et al.*, 2009; 2011; Kharatishvili et al., 2007; Kharatishvili et al., 2006; Purpura and Housepain, 1961; Santhakumar *et al.*, 2000; Scheff *et al.*, 2005). Excitatory drive onto hippocampal SST interneurons, which normally receive sparse input from local principal neurons, is also increased after brain injury (Hunt et al., 2011). However, slice recordings are limited to resolving functional connections of a few neurons within local circuits, because they are surgically isolated from long-range afferent input. By comprehensively mapping brain-wide inputs to SST interneurons at cellular resolution, we identified previously unknown sources of input in controls, such as a back-projection pathway from CA1 to hilar SST interneurons which is enhanced after TBI. Notably, CA1 interneurons are also capable of projecting to dentate gyrus in temporal lobe epilepsy models (Peng et al., 2013), but these cells primarily innervate granule cells.

Previous functional connectivity studies assume that TBI shifts the brain away from a small-world architecture, defined as densely connected local networks linked by sparse long-range input that connects discrete brain areas (Sharp et al., 2014). In line with this concept, interhemispheric resting-state fMRI connectivity is reduced after TBI (Marquez de la Plata et al., 2011), possibly a result of diffuse axonal injury (Sharp et al., 2014), and there is a temporary increase in hyper-connectivity of local networks that generally weakens over time (Harris et al., 2016). While these methods are useful for general hypotheses about brain connectivity, they are unable to identify a precise structural basis for circuit dysfunction in TBI. Our structural data are not entirely consistent with this idea at the cell type level. In both hippocampus and PFC, we found the most prominent sources of long-range input to SST interneurons, including input from contralateral hemisphere, were diminished after focal TBI, but local connections are chronically increased. Thus, TBI may permanently enhance small worldness by increasing local network connections and making long-range input more sparse. There is support for this idea from human functional connectivity studies (Nakamura et al., 2009). We cannot exclude that the structural reorganization we observed after focal TBI is influenced by damage to white matter tracts (Hall *et al.*, 2008). However, our finding that transplanted interneurons are capable of establishing long-distance connections at all suggests that the potential for re-growing these diminished inputs were retained in all brain injured animals. Taken together, our results suggest that even focal TBI leads to widespread remapping of inputs to SST interneurons across the brain regardless of whether there was direct injury or cell loss.

With far fewer inhibitory neurons in the damaged hippocampus, TBI puts extraordinary demands on surviving interneurons. There are three physiological features of SST interneurons that might explain why a loss of long-range input might reflect a compensatory response to damage. First, the strongly facilitiating excitatory synaptic input and other membrane properties of SST interneurons allow these cells to be activated by a high frequency burst from just one pre-synaptic neuron (Kapfer et al., 2007; Silberberg and Markram, 2007). In hippocampus, gaining input from pyramidal neurons and losing ENTm input may help stabilize local network activity after TBI (Cholvin et al., 2021). Second, muscarinic-mediated depolarization can produce prolonged spiking in SST interneurons (Kawaguchi, 1997). Given the rich local innervations after TBI, the loss of CHAT input from basal forebrain could reflect a strategy to balance excitatory drive to this important cell type in the injured hippocampus. Third, even a single dendrite-targeting interneuron can control spike generation in cortical principal neurons (Larkum *et al.*, 1999). Thus, a shift from feed forward to feed back inhibition to dendrites – through the loss of long-range input and enhanced local back-projections – may reflect a potential strategy to gate input integration and maintain the sparse activation of dentate granule cells that enables memory and prevents seizures (Kahn et al., 2019; Pignatelli et al., 2019). Alternatively, increased local input may synchronize SST interneurons, support patterns of pathological activity or impede the coordination between discrete brain regions. Further work combining *in vivo* neurophysiology with selective manipulation of hippocampal cell types will be required to clarify these possibilities.

The ability of transplanted SST interneurons to incorporate structurally into damaged hippocampus was striking given the dramatic reorganization of inhibitory circuits across the injured brain. Although host-donor cell connectivity has been broadly documented (Doerr et al., 2017; Tornero et al., 2017), the precise anatomical input to individual neuron types has not. Cell-type specificity is an important consideration, especially for understanding the circuit basis of disease. Despite massive reactive plasticity in the damaged brain, we found that transplanted interneurons receive highly orthotopic input that is cell-type-specific rather than region-specific. We propose that the beneficial effects of interneuron transplantation seen in various preclinical disease models are driven by the precise integration of interneuron precursors into host brain circuits. This view is supported by a large body of evidence reporting the general structure and function of transplanted interneurons closely resemble their native-born counterparts (Alvarez-

Dolado *et al.*, 2006; Bráz *et al.*, 2012; Etlin et al., 2016; Hunt *et al.*, 2013b; Larimer *et al.*, 2016) as well as recent DREADD-inactivation and VGAT loss-of-function studies demonstrating that therapeutic effects are linked to the electrophysiological integration of the transplanted interneurons (Priya et al., 2019; Zhu *et al.*, 2019). An alternate view suggests interneuron precursors form only weak contacts with the host brain (Southwell et al., 2010) and work indirectly by releasing rejuvenation factors that modify host brain circuits (Zheng et al., 2021). Yet detailed electrophysiological studies consistently report strong synaptic connections (Howard and Baraban, 2016; Hsieh and Baraban, 2017; Larimer *et al.*, 2016; Zhu *et al.*, 2019) and direct evidence for a circuit rejuvenator remains to be identified.

The pattern of synaptic circuit rewiring after TBI is complex. Our results suggest that focal brain damage reorganizes inhibitory circuits on a global scale. We expect this experimental approach will serve as a useful framework for considering whole-brain analyses of network dysfunction in TBI and related brain disorders.

CHAPTER FOUR

Traumatic brain injury to primary visual cortex produces long-lasting circuit dysfunction

Abstract

Primary sensory areas of the mammalian neocortex have a remarkable degree of plasticity, allowing neural circuits to adapt to dynamic environments. However, little is known about the effects of traumatic brain injury on visual circuit function. Here we used anatomy and *in vivo* electrophysiological recordings in adult mice to quantify neuron responses to visual stimuli two weeks and three months after mild controlled cortical impact injury to primary visual cortex (V1). We found that, although V1 remained largely intact in brain-injured mice, there was ~35% reduction in the number of neurons that affected inhibitory cells more broadly than excitatory neurons. V1 neurons showed dramatically reduced activity, impaired responses to visual stimuli and weaker size selectivity and orientation tuning *in vivo*. Our results show a single, mild contusion injury produces profound and long-lasting impairments in the way V1 neurons encode visual input. These findings represent the first demonstration of cortical circuit dysfunction following central visual system neurotrauma.

Introduction

Posterior impact injuries to occipital cortex are extremely common in human. Traumatic brain injury (TBI) can lead to long-lasting visual impairments, such as visual acuity and field loss, binocular dysfunction and spatial perceptual deficits (Armstrong, 2018; Sano et al., 1967; Stelmack et al., 2009), and as many as 75% of military Service members affected by TBI live with permanent visual dysfunction or cortical blindness (Stelmack *et al.*, 2009). Restrictive lesions applied to visual cortex have been shown to trigger cortical plasticity and functional disturbances (Eysel and Schweigart, 1999; Girard et al., 1991; Imbrosci et al., 2010). However, TBI involves mechanical brain damage and a wide range of cortical network abnormalities including cell death, inflammation and synaptic circuit remodeling (Hunt *et al.*, 2013a). There is essentially nothing known about how visual circuit function is affected by TBI.

Following TBI in human, histological studies have documented a reduction in the number of neurons in hippocampus (Swartz *et al.*, 2006) and neocortex (Buriticá *et al.*, 2009). In non-human animal models, TBI produces region- and subtype-specific reductions of neurons in various brain areas (Anderson *et al.*, 2005; Cantu *et al.*, 2015; Fox *et al.*, 1998; Frankowski *et al.*, 2019; Goodman et al., 1994; Hall *et al.*, 2005b; Huusko *et al.*, 2015; Lowenstein *et al.*, 1992; Nichols *et al.*, 2018; Santhakumar *et al.*, 2000; Toth *et al.*, 1997; Vascak et al., 2018) dramatic circuit rewiring (Cajal, 1928; Echlin and Battista, 1963; Hunt *et al.*, 2009; 2010; 2011; Jin et al., 2006; Johnstone et al., 2014; Johnstone et al., 2015; Salin et al., 1995; Scheff *et al.*, 2005) and a loss of inhibition that does not recover with time (Almeida-Suhett *et al.*, 2014; 2015; Butler *et al.*, 2016; Gupta *et al.*, 2012; Hunt *et al.*, 2011; Koenig *et al.*, 2019; Li and Prince, 2002; Pavlov *et al.*, 2011; Toth *et al.*, 1997; Vascak *et al.*, 2018; Witgen et al., 2005). However, nearly all of the information about neocortical responses to TBI comes from studies evaluating somatosensory, motor or frontal cortex. Each of these areas receives numerous intra- and inter-hemispheric inputs from throughout the topographic map (Hafner *et al.*, 2019; Luo et al., 2019; Ährlund-Richter *et al.*, 2019), whereas callosal connectivity of visual cortex is limited to the vertical meridian representation along the V1 border (Lyon and Kaas, 2002; Wang and Burkhalter, 2007). Therefore, a deeper understanding of functional disturbances in brain injured visual cortex is important, because it has potential to provide a rational basis for the development of new circuit-level therapies for visual cortex injury.

To produce central visual system TBI in adult mice, we applied a focal controlled cortical impact (CCI) injury to primary visual cortex (V1). We show that although mild contusion injury did not produce a sizable lesion, there was a subtype- and layer-specific loss of neurons in brain injured

V1. Then, using *in vivo* electrophysiological recordings of visually-evoked responses, we found that mild contusion injury chronically impairs the response of V1 neurons to a variety of visual stimuli. These findings suggest there are profound long-lasting impairments in visual circuit function that result from a single, mild contusive injury to the central visual system. As the first characterization of central visual system neurotrauma, our results also lay the foundation for future mechanistic investigations of altered cortical network activity and pre-clinical studies to restore circuit function in the traumatically injured visual cortex.

Methods

Animals

Mice were maintained in standard housing conditions on a 12h light/dark cycle with food and water provided *ad libitum*. All protocols and procedures followed the guidelines of the University Laboratory Animal Resources at the University of California, Irvine and adhered to National Institutes of Health Guidelines for the Care and Use of Laboratory Animals. For electrophysiology experiments, we used C57Bl/6J mice (Jackson Laboratories, cat no. 000664), and for anatomy experiments, we used a hemizygous glutamic acid decarboxylase - enhanced green fluorescence protein (GAD67-GFP) knock-in line (Tamamaki et al., 2003) maintained on a CD-1 background for > 10 generations.

Experimental design

Male and female mice were randomly allocated to experimental groups prior to TBI. Brain injury was performed at P60, and experiments were performed 0.5 or 3 months after TBI. Brain injuries were only considered to be successful if the lesion was found to be centered over the rostral end of V1. Three animals were excluded from the immunostaining analysis, because upon histological inspection the lesion was not found to be centered over the rostral end of V1. No additional animals were generated to replace these mice. All other brain-injured mice survived and remained otherwise healthy until the day of experimentation.

Controlled cortical impact (CCI)

Unilateral controlled cortical impact was performed as previously described (Frankowski et al., 2019; Zhu et al., 2019), with modifications to the location and depth of injury. Mice were anesthetized with 2% isoflurane until unresponsive to toe-pinch, then placed into a stereotactic frame and maintained on 1% isoflurane. The fur overlying the skull was trimmed and the scalp was scrubbed with betadine before exposing the skull with a midline incision. The skull was rotated 20 degrees counterclockwise along the rostral-caudal axis and the rostral end of the skull was lowered 20 degrees relative to skull-flat. This orientation centered the impactor tip at the rostral end of V1. A ~4-5 mm craniotomy was centered 3 mm lateral to midline and 3 mm rostral to the lambdoid suture in the right hemisphere. The skull cap was removed leaving the dura intact. A computer-controlled pneumatically driven impactor (TBI-0310, Precision Systems and Instrumentation) with a 3 mm beveled stainless-steel tip was used to deliver a 0.2 mm depth contusive injury perpendicular to the dura at 3.5m/s velocity and 500ms of impactor dwell time. The skull cap was not replaced, and the incision was closed with silk sutures. Animals undergoing surgical procedures received buprenorphine hydrochloride (Buprenex, 0.05mg/kg, delivered i.p.) pre-operatively and once daily for 3d. A post-operative health assessment was performed for 5d following surgical procedures.

Immunostaining

At 0.5 or 3 months after injury, mice were transcardially perfused with 4% paraformaldehyde (PFA) and free-floating vibratome sections (50 µm) were processed using standard immunostaining procedures (Zhu et al., 2019). Sections were stained with the following primary antibodies: GFP (1:1000; cat. no. GFP-1020, Aves Labs), NEUN (1:1000; cat. no. MAB377, Millipore), GFAP (1:500, cat. no. MAB3402, Millipore) and IBA1 (1:1000, cat. no. 019-19740, Fujifilm). Secondary antibodies were Alexa 488, 546, 594 and 647 (1:1000; cat. nos. A-11039, A-11005, A-11030 and A-21244, Fisher Scientific). Sections were then mounted on charged slides (Superfrost plus; Fisher Scientific) with Fluoromount-G containing DAPI (Southern Biotech). Images were obtained with a Leica DM6 epifluorescence microscope. Brightness and contrast were adjusted manually using Adobe Photoshop; z-stacks were generated using Leica software.

Volumetric Analysis

Quantification of cortical lesion volume was performed by measuring the area of cortical tissue remaining in both hemispheres in eight DAPI-labeled coronal sections along ~2400 μm of the rostral-caudal axis spaced 300 μm apart as previously described (Frankowski et al., 2019; Zhu et al., 2019). Borders of the cortical plate were drawn between the dorsal aspect of the corpus callosum and the pial surface using ImageJ. Regions of the cortical subplate (e.g., amygdala) were excluded from analysis. The % of the ipsilateral cortex remaining for each animal was calculated using the following formula:

$$\%\ \text{Cortex Remaining} = \left(\frac{\sum i_n}{\sum c_n}\right) \times 100$$

where i = the area of the ipsilateral cortex and c = the area of the contralateral cortex and n = the section number.

Cortical thickness measurement

Average cortical thickness was measured from a series of three DAPI-labeled x10 images of the entire cortical column centered at the injury epicenter and two 300 μm serial sections caudal to the epicenter. The area of tissue between the pial surface and the ventral aspect of layer V/VI was divided by the width of the frame (958.29 μm) to obtain an average cortical thickness value along the width of the frame. For uninjured- controls, images were taken in corresponding brain sections at the most central portion of V1 as defined in the 2017 Allen Reference Atlas.

Cell quantification

Fluorescently labeled coronal brain sections (50 µm) were imaged using a Leica DM6 fluorescence microscope with an x20 objective and quantification was performed in ImageJ, as previously described (Frankowski et al., 2019; Zhu et al., 2019). For quantification of cell density, three brain sections spaced 300 µm apart were counted, with the rostral-most section at the injury epicenter and the next two additional sections caudal to the epicenter. For layer analysis, the border of each layer (layers I, II/III, IV, and V/VI) were defined manually by visual inspection of neuron densities in NEUN epifluorescence images, as previously described (Stanco et al., 2014; Vogt et al., 2014). For quantification of GFAP and IBA1 immunostaining, measurements were analyzed at three different locations and the percentage of area above fluorescence threshold was applied using ImageJ according to a previous protocol (Zhu et al., 2019). The same settings were used for all sections.

Neurophysiology

Animals were initially anesthetized with 2% isoflurane in a mixture of N_2O/O_2 (70%/30%) then placed into a stereotaxic apparatus. A small, custom-made plastic chamber was secured to the exposed skull using dental acrylic. After one day of recovery, re-anesthetized animals were placed in a custom-made hammock, maintained under isoflurane anesthesia (1-2% in N_2O/O_2) and multiple single tungsten electrodes were inserted into V1 layers II-VI using the same craniotomy produced during the injury phase. All recording locations were within the CCI damaged region of V1 (defined as being within the craniotomy). Following electrode placement, the chamber was filled with sterile agar and sealed with sterile bone wax. Animals were then sedated with chlorprothixene hydrochloride (1 mg/kg; IM; (Camillo et al., 2018)) and kept under light isoflurane anesthesia (0.2 – 0.4% in 30% O_2) throughout the recording procedure. EEG and EKG were monitored throughout and body temperature was maintained with a heating pad (Harvard Apparatus, Holliston, MA).

Data was acquired using a multi-channel Scout recording system (Ripple, UT, USA). Local field potentials (LFP) from multiple locations at matching cortical depths were band-pass filtered from 0.1 Hz to 250 Hz and stored along with spiking data at 1 kHz sampling rate. LFP signal was aligned to stimulus time stamps and averaged across trials for each recording depth in order to calculate visually evoked potentials (VEP) (Foik et al., 2015; Suh et al., 2021; Kordecka et al., 2020). Single neuron spike signals were band-pass filtered from 500 Hz to 7 kHz and stored at a 30 kHz sampling frequency. Spikes were sorted online in Trellis (Ripple, UT, USA) while performing visual stimulation. Action potentials were detected based on negative and positive thresholds that were at least twice as large (S/N > 2:1) as the background noise. For each recording location, thresholds were adjusted to maintain a high signal-to-noise ratio. Waveforms were sorted by marking templates based on the clear amplitude difference, positive or negative peak detection, and the slope between negative and positive component, which can be defined as the spike width. Visual stimuli were generated in Matlab (Mathworks, USA) using Psychophysics Toolbox (Brainard, 1997; Pelli, 1997) and displayed on a gamma-corrected LCD monitor (55 inches, 60 Hz; 1920 x 1080 pixels; 52 cd/m^2 mean luminance). Stimulus onset times were corrected for monitor delay using an in-house designed photodiode system (Foik et al., 2018).

Visual responses were assessed according to previously published methods (Foik *et al.*, 2018; Foik et al., 2020; Suh et al., 2021). For recordings of visually evoked responses, cells were first tested with 100 repetitions of a 500 ms bright flash stimulus (105 cd/m^2). Receptive fields for visually responsive cells were then located using square-wave drifting gratings, after which optimal orientation, direction, and spatial and temporal frequencies were determined using sine wave gratings. Shown at optimal orientation, spatial frequencies used ranged from 0.001 to 0.5 cycles/º; Temporal frequencies used were from 0.1 to 10 cycles/s. Using optimal parameters, size tuning was assessed with apertures ranging from 1 to 110º at 100% contrast. With optimal size, orientation tuning of the cell was re-assessed using 8 orientations x 2 directions each, stepped by 22.5º increments. Background activity was calculated as average activity from 500 ms before stimulus onset for each repetition. A cell was determined to be visually responsive if the average firing rate was more than 2 standard deviations above background activity and at least 3 spikes/s. Any cell that was non-responsive to the flash stimulus was not probed using sine wave gratings. A percentage of flash-responsive cells in the 0.5 and 3 month conditions did not respond to every sine wave stimulus condition used. Non-responses to sine wave stimuli were excluded from population analyses because they could not be fit to a curve.

Local Field Potential (LFP) Analysis

Amplitude of response was calculated as a difference between the peak of the positive and negative components of the VEP. Response latency was defined as the time from stimulus onset to maximum response. Maximum of the response was defined at the larger of the negative or positive peak. For uninjured control animals, depths corresponding to layer 5 were always used (~500 μm). This is because layer 5 amplitude responses were the highest in control animals. For TBI animals, the depth with the highest amplitude was used. This is because VEPs were more erratic in TBI animals and not always the most responsive at layer 5.

Single Unit Analysis

Tuning curves were calculated based on average spike rate centered around the preferred direction (peak response). Optimal visual parameters were chosen as the maximum response value. Orientation tuning was measured in degrees at the half-width at half-height (HWHH; 1.18

x σ) based on fits to Gaussian distributions (Alitto and Usrey, 2004; Carandini and Ferster, 2000; Foik *et al.*, 2018; Foik *et al.*, 2020; Liu et al., 2011; 2015) using:

$$R_{O_s} = baseline + \ R_p e^{-\frac{(O_s - O_p)^2}{2\sigma^2}} + R_n e^{-\frac{(O_s - O_p + 180)^2}{2\sigma^2}},$$

where O_s is the stimulus orientation, R_{Os} is the response to different orientations, O_p is the preferred orientation, R_p and R_n are the responses at the preferred and non-preferred direction, σ is the tuning width, and 'baseline' is the offset of the Gaussian distribution. Gaussian fits were estimated without subtracting spontaneous activity, similar to the procedures of Alitto and Usrey (Alitto and Usrey, 2004).

Size tuning curves were fitted by a difference of Gaussian (DoG) function:

$$R_s = K_e \int_{-s}^{s} e^{(-\frac{x}{r_e})^2} dx - K_i \int_{-s}^{s} e^{(-x/r_i)^2} dx + R_0,$$

in which R_s is the response evoked by different aperture sizes. The free parameters, K_e and re, describe the strength and the size of the excitatory space, respectively; Ki and ri represent the strength and the size of the inhibitory space, respectively; and R_0 is the spontaneous activity of the cell.

The optimal spatial and temporal frequency was extracted from the data fitted to Gaussian distributions using the following equation (DeAngelis et al., 1993; Foik *et al.*, 2018; Foik *et al.*, 2020; Van den Bergh et al., 2010):

$$R_{SF/TF} = baseline + \ R_{pref} e^{-\frac{(SF/TF - SF/TF_{pref})^2}{2\sigma^2}},$$

Where $R_{SF/TF}$ is the estimated response, R_{pref} indicates response at preferred spatial or temporal frequency, SF/TF indicates spatial or temporal frequency, σ is the standard deviation of the Gaussian, and baseline is Gaussian offset.

Statistics and Reproducibility

Anatomical data analysis was performed in Graphpad Prism 9, Microsoft Excel and SAS 9.4 software. Experimental groups were averaged across groups (i.e., N = animals) compared by two-way ANOVA with Tukey's post-hoc test, or repeated measures two-way ANOVA followed by Sidak's post-hoc test. For layer analysis, data were fitted to a random intercept mixed model followed by Tukey-Kramer post-hoc. Cell density was defined as the response variable and distance from the injury, cell layer, group, the interaction of layer by group and the interaction of distance by layer by group as explanatory variables. Neurophysiology data analysis was performed in Matlab (Mathworks, USA). Neural responses were averaged across recording locations (i.e., N = animals; *n* = recording locations) or cells (in single-unit recordings) and groups were compared by Kruskal-Wallis H test followed by multiple comparisons using Dunn's post-hoc. All data are expressed as mean ± SEM. Significance was set at $P < 0.05$.

Results

Occipital CCI produces a mild contusion in V1

To evaluate the effect of a single, mild contusion injury to the central visual system, we delivered mild CCI injury centered over the rostral end of V1 in young-adult mice at P60 (**Fig 4.1**). We selected CCI as a model, because the injury is highly reproducible from animal to animal, reliably recapitulates structural and functional deficits of TBI and focal contusion injuries are among the most common posterior impact injuries observed in human (Armstrong, 2018; Sano *et al.*, 1967; Stelmack *et al.*, 2009). In all CCI-injured animals (N = 7 mice), the lesion consisted of mild tissue compression that was restricted to superficial layers of the cortex at the injury epicenter (**Fig 4.2**).

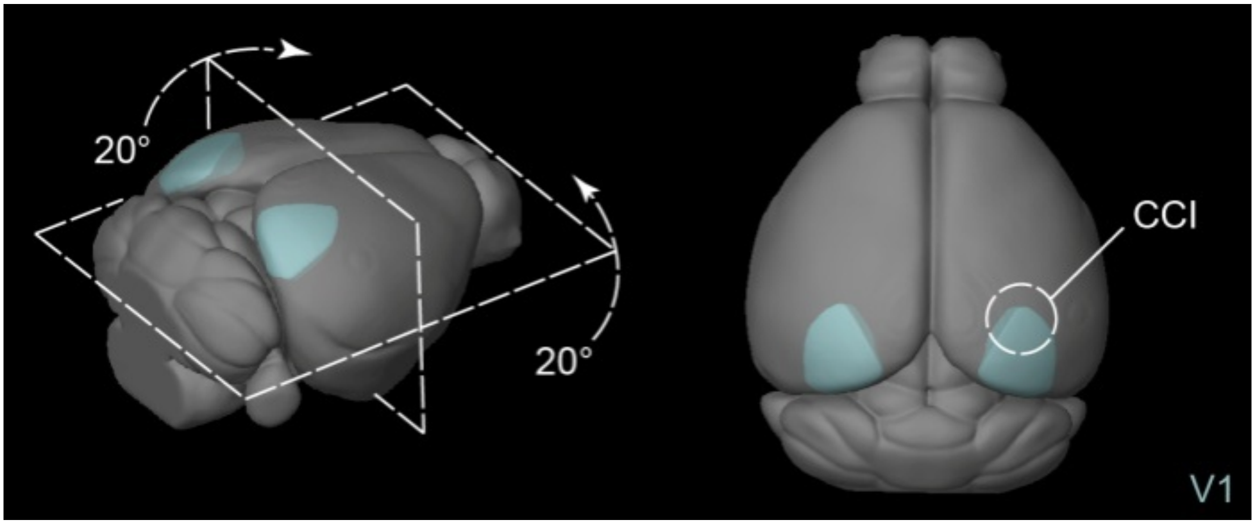

Figure 4.1. Schematic of Allen Mouse Common Coordinate Framework showing the head rotation used to produce CCI injury over V1 (cyan). CCI injury was centered over rostral primary visual cortex (white circle).

To define the lesion location, we examined glial responses in V1 following mild CCI injury (**Fig 4.3a**). To do this, we performed an immunostaining analysis at 0.5 months and 3 months after injury for glial fibrillary acidic protein (GFAP), a marker of astrocytes, and ionizing calcium-binding adaptor molecule 1 (IBA1), a marker of activated microglia. In brain injured animals, the impact site could be clearly identified by a dense pattern of GFAP and IBA1 staining in V1 ipsilateral to the injury. A significant increase in GFAP expression was found in V1 surrounding the injury at 0.5 months, as compared to uninjured controls, sham animals that received a craniotomy but no injury and contralateral tissue sections (**Fig 4.3**), and it remained significantly elevated 3 months post-CCI (**Fig 4.3b**). IBA1 immunostaining was also significantly increased ipsilateral to the injury, but only at 0.5 months after injury (**Fig 4.3c**). Uninjured and sham controls did not have an identifiable cortical lesion in any animal. At 0.5 months post-CCI, a time point when lesion volume is considered to be largely stable (Hall (Hall *et al.*, 2005b; Pleasant *et al.*, 2011), there was no significant difference in cortical volume between uninjured control and brain-injured littermates (TBI: 96 ± 3%, sham: 102 ± 2%, compared to 99 ± 1% in uninjured control; P= 0.15; one-way ANOVA; N = 4-6 mice per group; **Fig 4.3d**).

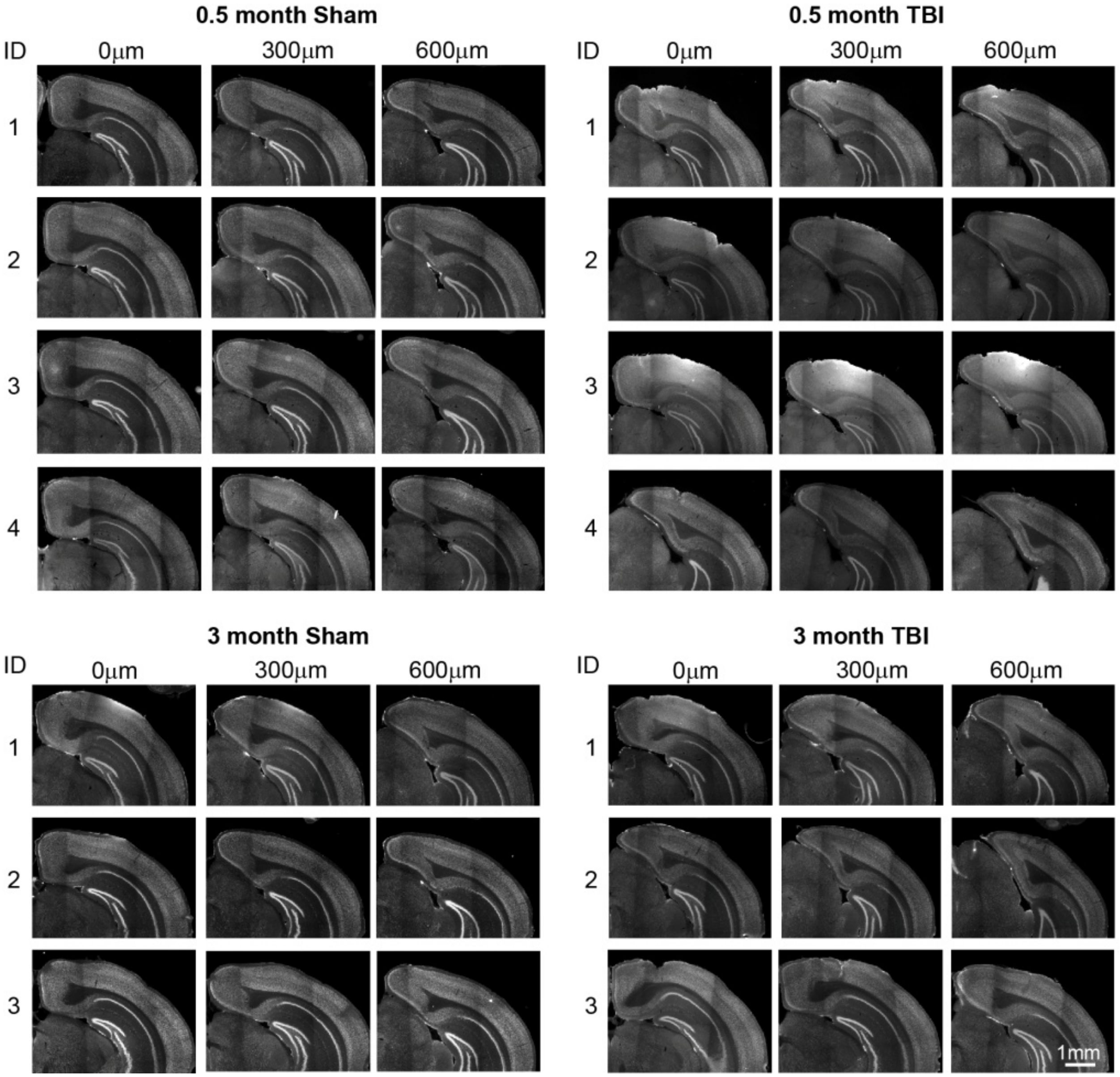

Figure 4.2. Coronal sections of ipsilateral V1 showing NEUN labeling in all sham and brain injured animals used for histological quantifications in this study. ID, animal identification. Scale bar, 1mm

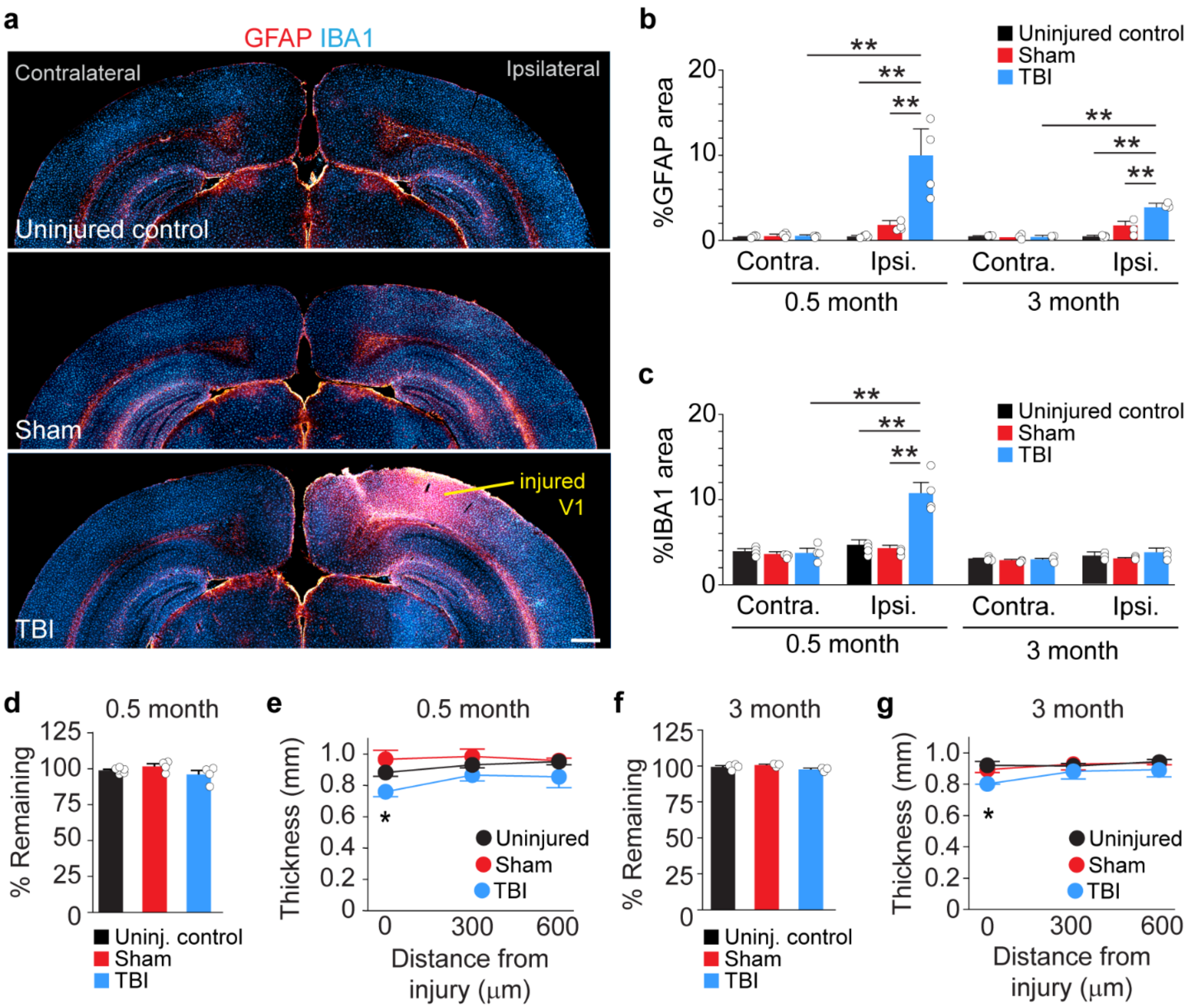

Figure 4.3. Visual cortex TBI produces a mild cortical lesion. a. Coronal sections of GFAP (red) and IBA1 (blue) labeling in a control animal and 0.5 months after sham or CCI injury. **b.** Quantification of GFAP expression in V1 at 0.5 and 3 months post-injury. $^{**}P = 2.9E\text{-}07$, ipsilateral control versus ipsilateral TBI; $^{**}P = 1.3E\text{-}05$, ipsilateral sham versus ipsilateral TBI; $^{**}P = 1.3E\text{-}06$, ipsilateral TBI versus contralateral TBI at 0.5 months; $^{**}P = 1.3E\text{-}06$, ipsilateral control versus ipsilateral TBI; $^{**}P = 8.7E\text{-}05$, ipsilateral sham versus ipsilateral TBI; $^{**}P = 6.0E\text{-}06$, ipsilateral TBI versus contralateral TBI at 3 months two-way ANOVA with Tukey's post-hoc test, N = 3 - 6 mice per group. **c.** Quantification of IBA1 expression in V1 at 0.5 and 3 months post-injury. $^{**}P = 2.4E\text{-}08$, ipsilateral control versus ipsilateral TBI, $^{**}P = 2.9E\text{-}08$, ipsilateral sham versus ipsilateral TBI, $^{**}P = 2.3E\text{-}08$, ipsilateral TBI versus contralateral TBI at 0.5 months; two-way ANOVA with Tukey's post-hoc test, N = 3 - 6 mice per group. **d.** Quantification of cortical tissue volume in control, sham and CCI-injured mice 0.5 months post-CCI. **e.** Average thickness of cortex with distance from the injury 0.5 months post-CCI. $^{*}P = 0.048$, Control versus TBI, two-way repeated measures ANOVA with Tukey's post-hoc test, N = 4 - 6 mice per group. **f.** Quantification of cortical tissue volume in control, sham and CCI-injured mice 3 months post-CCI. **g.** Average cortex thickness with distance from the injury 3 months post-CCI. $^{*}P = 0.023$, Uninjured versus TBI, two-way repeated-measures ANOVA with Tukey's post-hoc test, N = 3 - 4 mice per group. Scale bar, 500 µm; error bars, SEM.

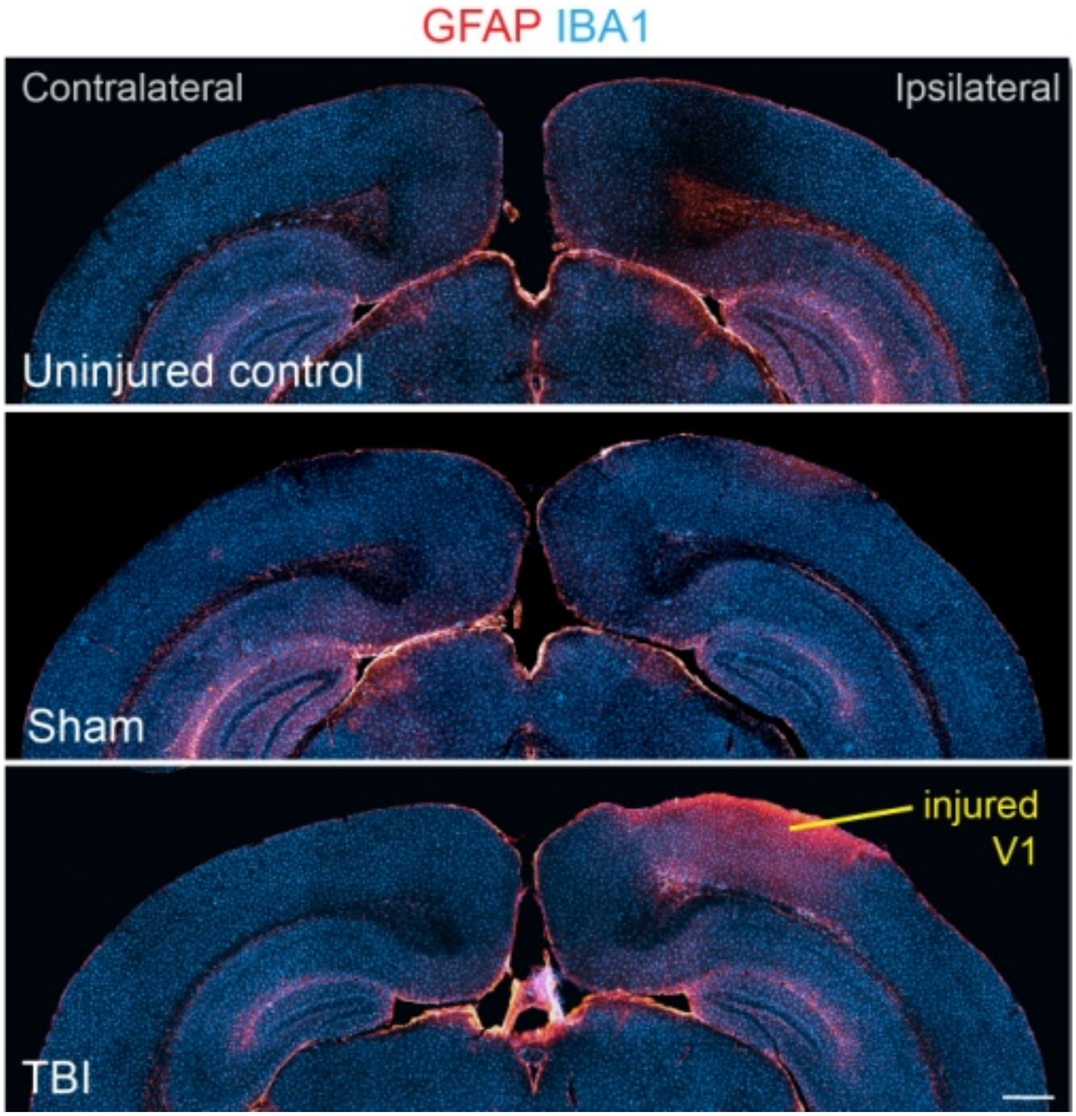

Figure 4.4. Coronal sections of GFAP (red) and IBA1 (blue) labeling in an uninjured control animal and 3 months after sham or CCI injury. Scale bar, 500 μm

However, when we evaluated the thickness of cortical tissue remaining in the contused portion of visual cortex, we found a 14% decrease in cortical thickness in brain injured animals at the injury epicenter, as compared to controls (uninjured: 883 ± 25 μm, sham: 966 ± 58μm, TBI: 760 ± 32μm, P= 0.048; two-way rmANOVA; N = 3-4 mice per group; **Fig 4.3e**). This difference was only observed at the injury epicenter (0μm); no difference in cortical thickness was observed in tissue sections 300μm and 600μm caudal to the epicenter. We found a similar degree of mild tissue loss at 90d post-CCI (**Fig 4.3f,g**). Thus, CCI produced a mild focal injury with minimal structural damage to V1.

Neuron loss after V1 injury

Next, we quantified neuron density in V1 using GAD67-GFP reporter mice that label nearly all GABAergic neurons (Tamamaki et. al, 2003). Sections were immunostained for GFP to identify inhibitory interneurons and NEUN to identify putative excitatory neurons (i.e., NEUN-positive/GAD67-GFP-negative) (**Fig 4.5**). At 0.5 months after TBI, we found a ~35% reduction in NEUN+/GAD67-GFP- cell density in V1 ipsilateral to the injury (**Fig 4.5a,b**). The reduction in excitatory neurons was most profound at the injury epicenter (45% reduction after TBI) and rapidly decreased with distance away from the impact site (**Fig 4.5c**). We also observed ~35% decrease in the overall density of GAD67-GFP+ cells in V1 ipsilateral to the injury (P = 1.07E-06, TBI versus uninjured control, two-way ANOVA; **Fig 4.5d**). However, unlike excitatory neurons, GFP+ interneuron density was reduced by ~35% at each distance from the impact site (**Fig 4.5e**). No change in cell density was observed in the contralateral hemisphere. These findings suggest mild contusion to visual cortex produces substantial neuron loss in V1, and the loss of inhibitory neurons is more widespread than excitatory neurons. To determine if post-traumatic neuron loss was layer-specific, we quantified neuron density in cortical layers I, II/III, IV, and V/VI of brain-injured and uninjured control littermates (**Fig 4.6**). For this analysis, we fitted a random intercept mixed model for each cell type to account for distance from the injury, layer and treatment condition. We found that excitatory cell loss extended throughout the cortical column ipsilateral to the injury, with significant reductions in NEUN+/ GAD67-GFP- cells in cortical layers II/III, IV, and V/VI (**Fig 4.6b,f,j**); no significant differences were found in layer I where excitatory neurons are rarely found. In contrast, GFP+ inhibitory neuron density was most profoundly affected in superficial layers, with significant reductions in GAD67-GFP+ neurons in layers I-IV (**Fig 4.6c,g,k**). However, no change in inhibitory neuron density was observed in layers V/VI.

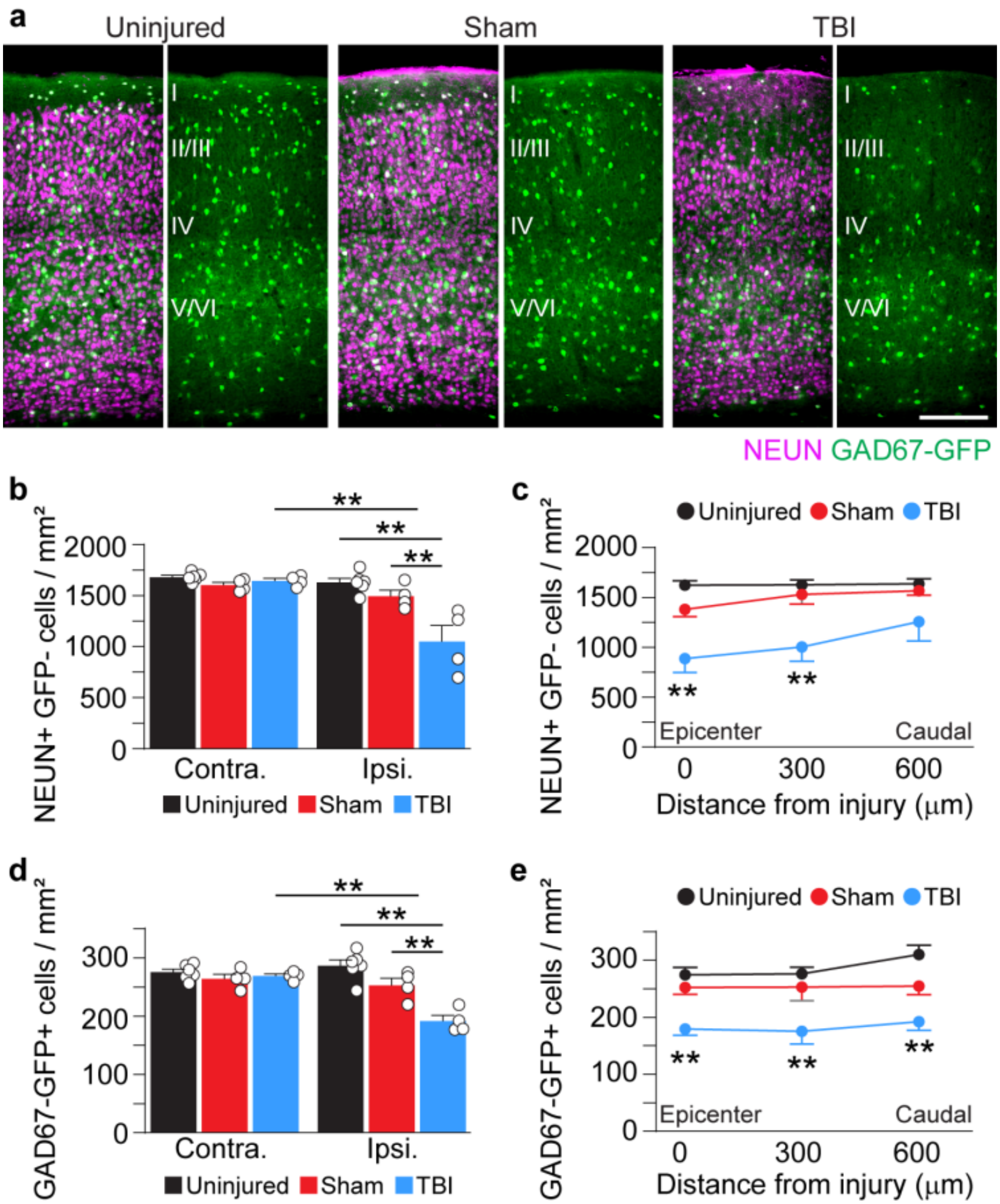

Figure 4.5. Neuron loss in V1 0.5 months after TBI. a. Coronal images of control, sham and CCI-injured V1 labeled for NEUN (magenta) and GAD67-GFP (green). **b.** Quantification of NEUN+/GFP- cell density in uninjured control, sham and brain-injured mice 0.5 months after CCI. **P = 1.79E-05, ipsilateral control versus ipsilateral TBI, **P = 1.77E-03, ipsilateral sham versus ipsilateral TBI, **P = 4.56E-05, ipsilateral TBI versus contralateral TBI; two-way ANOVA with Tukey's post-hoc test, N = 4-6 mice per group. **c.** NEUN+/GFP- cell density at 0 - 600μm from the injury epicenter. **P = 7.86E-05, control versus TBI (0 μm), **P = 1.01E-03, control versus TBI (300 μm); two-way repeated-measures ANOVA with Tukey's post-hoc test; N = 4-6 mice per group. **d.** Quantification of GAD67-GFP+ cell density in uninjured control, sham and brain-injured mice 0.5 months after CCI. **P = 1.07E-06, ipsilateral control versus ipsilateral TBI, **P = 1.58E-03, ipsilateral sham versus ipsilateral TBI, **P = 9.25E-05, ipsilateral TBI versus contralateral TBI, two-way ANOVA with Tukey's post-hoc test, n = 4-6 per group. **e.** GAD67-GFP+ cell density at 0 - 600μm from the injury epicenter. **P = 3.53E-03, control versus TBI (0μm), **P = 1.66E-03, control versus TBI (300 μm), **P = 1.74E-04, control versus TBI (600 μm); two-way repeated-measures ANOVA with Tukey's post-hoc test; N = 4-6 mice per group. Scale bar, 500μm; error bars, SEM.

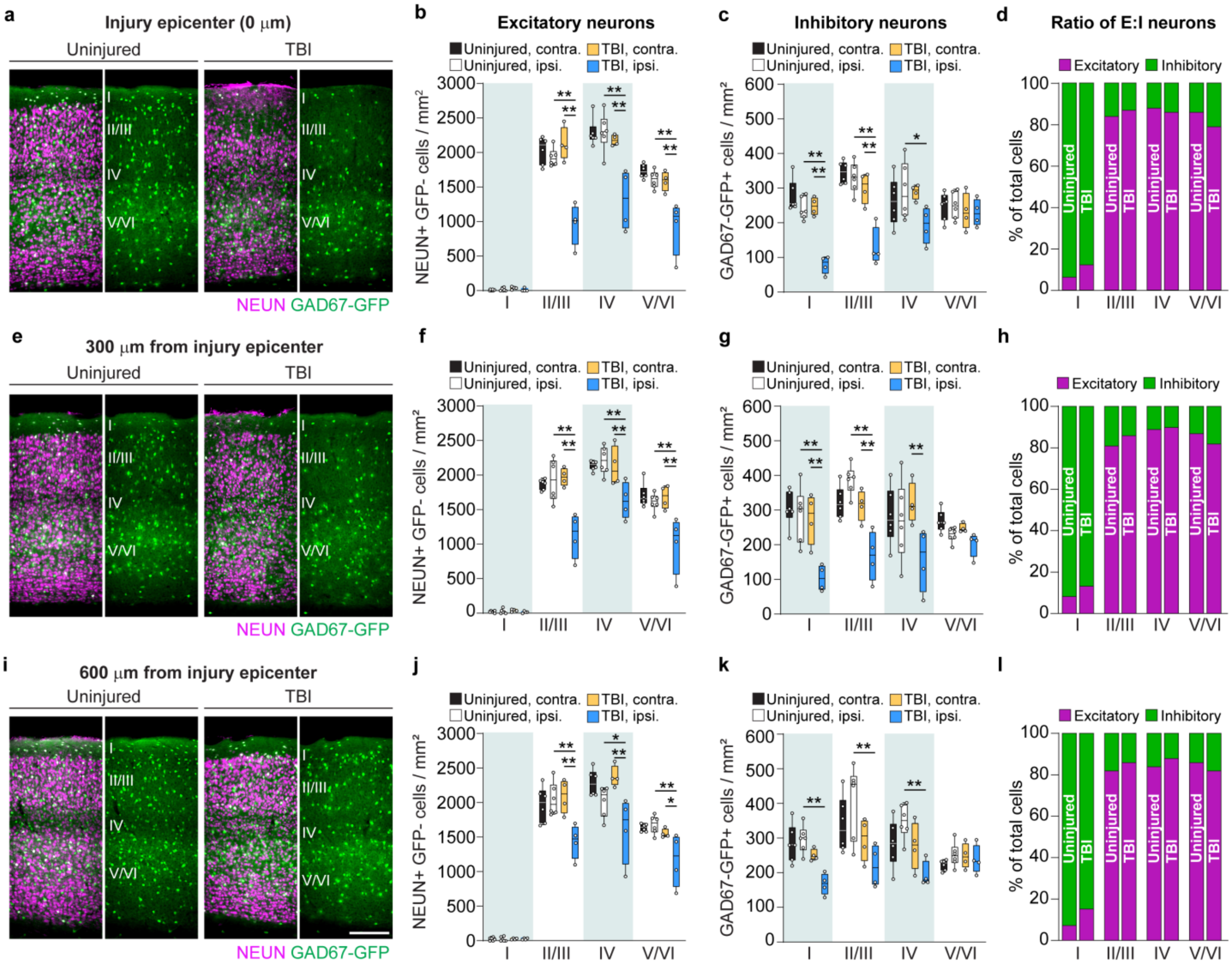

Figure 4.6. V1 injury produces subtype- and layer-specific loss of neurons. a, e, i. Coronal images of control and CCI-injured V1 labeled for NEUN (magenta) and GAD67-GFP (green) at 0 (a), 300 (e) and 600 μm (i) from the injury. **b, f, j.** Quantification of NEUN+/GFP- cell density in layers I, II/III, IV, and V/VI. N = 4-6 mice per group. **c, g, k.** Quantification of GAD67-GFP cell density in layers I, II/III, IV, and V/VI. N = 4-6 mice per group. **d, h, l.** Analysis of the proportion of excitatory to inhibitory neuron density at the injury site (Chi-square = 2.17, df = 3, P = 0.54; **d**), 300μm (Chi-square = 1.32, df = 3, P = 0.72; **h**), or 600μm caudal to the epicenter (Chi-square = 2.68, df = 3, P = 0.44; **l**). Scale bar, 500μm. Box and whisker plots show median, 25th and 75th percentiles, and the whisker bars represent maximum and minimum values. $**P<0.01$, $*P<0.05$; random intercept mixed model with Tukey-Kramer post-hoc test.

Despite these cell- type specific changes in cell density, the ratio of excitatory to inhibitory neurons did not change in any layer of V1 (**Fig. 4.6d,h,l**). We conclude that there are subtype- and layer-specific differences in the degree and extent of neuron loss after visual cortex injury. We next asked whether the loss of neurons at the injury site persisted long term. At 3 months after injury, NEUN+/GAD67-GFP- cell density remained reduced by 32% ipsilateral to the injury (**Fig 4.7a, b**). GAD67-GFP+ interneuron density was also reduced 3 months post-CCI by 32% (**Fig 4.7a, c**).

These data reproduce our observations at 0.5 months and are consistent with a chronic loss of excitatory and inhibitory neurons after mild contusion injury to visual cortex.

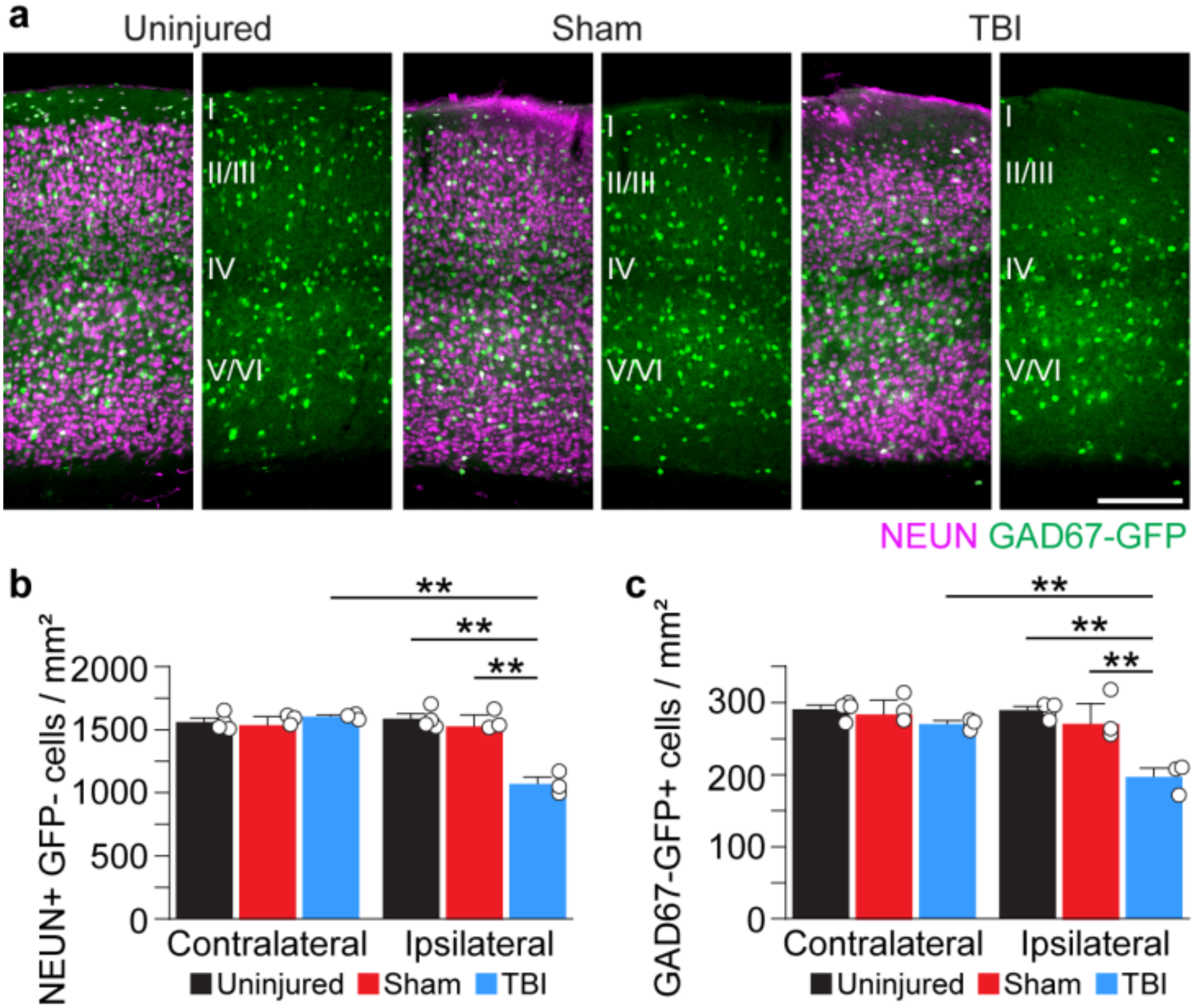

Figure 4.7. Chronic neuron loss in V1 after TBI. a. Coronal images of control, sham and CCI-injured V1 labeled for NEUN (magenta) and GAD67-GFP (green) 3 months after TBI. **b.** Quantification of NEUN+/GFP- cell density in control, sham and brain-injured mice 3 months after CCI. **P = 1.33E-06, ipsilateral control versus ipsilateral TBI, **P = 4.23E-06, ipsilateral sham versus ipsilateral TBI, **P = 1.99E-06, ipsilateral TBI versus contralateral TBI; two-way ANOVA with Tukey's post-hoc test, N = 3-4 mice per group. **c.** Quantification of GAD67-GFP+ cell density in control, sham and brain-injured mice 90d after CCI. **P = 1.60E-04, ipsilateral control versus ipsilateral TBI, **P = 1.02E-03, ipsilateral sham versus ipsilateral TBI, **P = 2.96E-03, ipsilateral TBI versus contralateral TBI; two-way ANOVA with Tukey's post-hoc test, N = 3-4 mice per group. Scale bar, 500µm; error bars, SEM.

Early and long-term disruption of visually evoked responses after TBI

To evaluate the *in vivo* functional state of visual cortex following TBI, we measured visually evoked potentials (VEPs) and single unit responses to a range of stimuli across a wide extent of injured

V1 at 0.5 and 3 months after injury (**Figs 4.8-4.13**). First, we recorded VEPs in response to brief flashes of light. These local field potential responses represent the electrical response of a population of V1 neurons to light stimuli. Representative examples of flash-evoked responses are shown in individual animals (**Fig 4.8a**), along with group averages (**Fig 4.8b**). Compared to uninjured controls, evoked VEP amplitudes were significantly reduced by more than 80% in brain injured mice (control: 277 ± 39 μV, 0.5 months after TBI: 24 ± 4 μV, 3 months after TBI: 53 ± 7 μV; P = 9.95E-09, Kruskal-Wallis H test; **Fig 4.8c**), and response latencies rose to more than 60% longer (control: 88 ± 6 ms, 0.5 months after TBI: 146 ± 17 ms, 3 months after TBI: 100 ± 6 ms; P = 0.02, Kruskal-Wallis H test; **Fig 4.8d**). Of note, response latencies between light flash and maximal response were longer only at 0.5 months after injury and were similar to controls at 3 months. At both time points, we found that wave profiles in the injured brain lacked a negative wave component normally present in deeper cortical layers (**Fig 4.9**). Single neuron responses to the same flashes of light were also measured (**Fig. 4.10a; Fig 4.11**). Average response profiles showed moderate to negligible activity at both 0.5 and 3 months, respectively, compared to the high average spike rate in control mice (**Fig. 4.10b**). After TBI, less than half of the isolated neurons were visually responsive (32% at 0.5 months; 49% at 3 months), compared to 90% of control V1 cells (Chi-square = 56.3, df = 2, P = 5.94E-13; **Fig 4.10c**). Similarly, average peak firing rates were significantly lower in brain injured V1 (control: 42.7 ± 5.7 spikes/s, compared to 5.2 ± 0.4 spikes/s 0.5 months after TBI and 9.9 ± 1.7 spikes/s 3 months after TBI; P = 3.6E-20, Kruskal-Wallis H test; **Fig. 4.10d**). Prior to stimulation, background activity was highest for the uninjured control group (7.6 ± 2.8 spikes/s) and included one outlier with a baseline firing rate over 150 spikes/second; whereas background activity for cells 0.5 months (2.7 ± 2.5 spikes/s) and 3 months (1.6 ± 2.2 spikes/s) after TBI was significantly lower than in uninjured controls (P = 3.59E-20, Kruskal-Wallis H test; **Fig. 4.10e**). Together, these findings suggest there is damage to the local V1 neuron population that lasts for several months after TBI.

To evaluate the functional profile of injured V1 in more detail, we next measured single neuron responses to a range of fundamental visual stimuli, including orientation, size, spatial frequency and temporal frequency *in vivo* (**Fig 4.12; Fig 4.13**). For these analyses, only visually responsive cells were included (see criteria in Methods). Brain injured mice showed weaker tuning and selectivity to all four types of stimulus parameters compared to uninjured controls (**Fig 4.12**) and had a substantial percentage of cells that were non-responsive to one or more stimulus conditions (**Fig. 4.13**). For the cell population, these differences were significant for orientation (**Fig 4.12b**), size (**Fig 4.12d**) and spatial frequency (**Fig 4.12f**), but not temporal frequency (**Fig 4.12h**). The difference was quite striking for orientation and size tuning, both of which are strongly mediated through local cortical inhibition (Liu et al., 2011; Liu et al., 2015; Liu et al., 2017). For orientation, the tuning width, measured as the half-width at half-height (HWHH) of the preferred direction (90º in the example cells) was nearly twice as sharp in the control example (23.7º) compared to 0.5 months after injury (45.0º), and more than 50% broader 3 months after injury (36.3º; **Fig 4.12a**). These differences were also seen for the population (control: 30.9º ± 1.9º, 0.5 months after TBI: 43.1º ± 4.0º; 3 months after TBI: 42.6º ± 2.8º; P = 0.0013, Kruskal-Wallis H test; **Fig 4.12b**). Broader tuning after TBI is consistent with orientation tuning mediated more through intact thalamocortical feed-forward mechanisms and impairments in cortical inhibition (Liu *et al.*, 2015; 2017). Similarly, the larger size preference in TBI compared to control neuron examples (73º and 60º at 0.5 and 3 months post-TBI vs. 35º in uninjured controls; **Fig 4.12c**) and populations (control: 41.5 ± 2.1º, compared to 79.3 ± 3.4º at 0.5 months and 52.1 ± 3.1º at 3 months post-injury; P = 1.16E-13, Kruskal-Wallis H test; **Fig 4.12d**) is also consistent with a loss of cortical inhibition (Liu et al., 2011). This is because stimulus size is normally kept small through a process of lateral suppression mediated by long-range intrinsic excitatory V1 neurons synapsing onto local inhibitory neurons (Liu et al., 2011; Liu et al., 2013). We note that the 3 months post-injury group had a statistically smaller preferred size than the 0.5 month group (P = 2.04E-05,Kruskal-Wallis

H test; **Fig 4.12d**). This could be a sign of recovery, however, a larger percentage of 3 month animal cells did not even respond to the size stimuli (**Fig 4.13**).

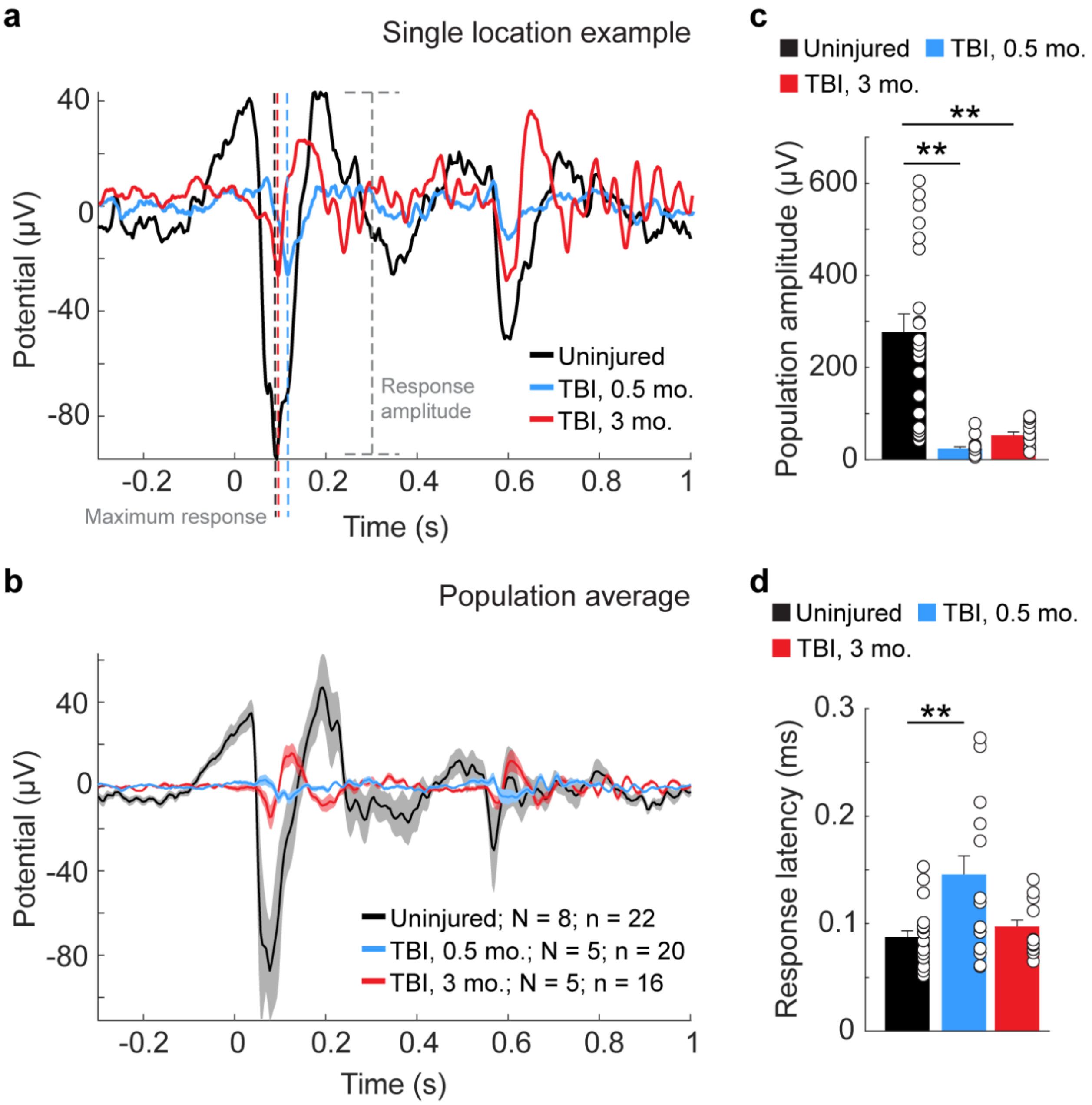

Figure 4.8. TBI disrupts V1 responses to visual stimuli. a. Representative example of VEPs in layer 5 of an uninjured control animal (black trace) and animals 0.5 months (blue trace) and 3 months after CCI (red trace). The maximum response for each trace is indicated by dotted black, blue and red lines. Response amplitude for the control condition is indicated by the dotted grey line. **b.** Average evoked potentials from recording sites in uninjured control (black) and 0.5 months (blue) and 3 months (red) after TBI. N = number of animals; n = number of recording locations. Shading indicates S.E.M. **c.** Quantification of average evoked amplitude. **P=6.23E-09, control versus 0.5 months after TBI; **P = 1.88E-03, control versus 3 months after TBI; Kruskal-Wallis H with Dunn's post-hoc. **d.** Quantification of average response latency. **P=0.02, control versus 0.5 months after TBI, Kruskal-Wallis H with Dunn's post-hoc. Individual data points represent the value for each of the recording locations. N, animals; n, recording location; error bars, SEM.

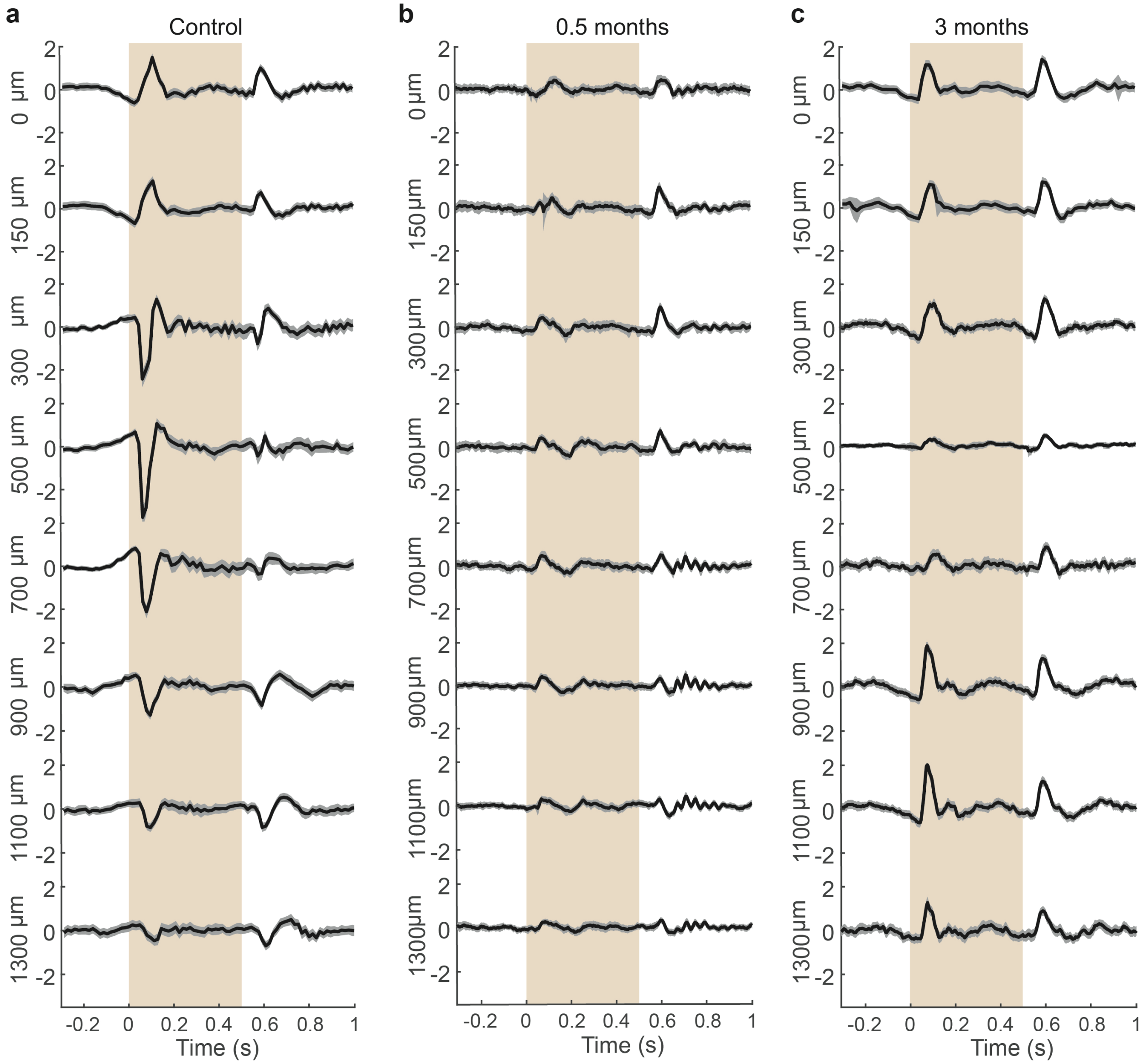

Figure 4.9. a-c. Representative examples of LFP responses through the cortical depth in a control animal (a), and at the site of injury 0.5 months (b) and 3 months (c) after TBI. Grey shading indicates S.E.M. Visual stimulus was presented for 500 ms at Time 0 (brown background shading).

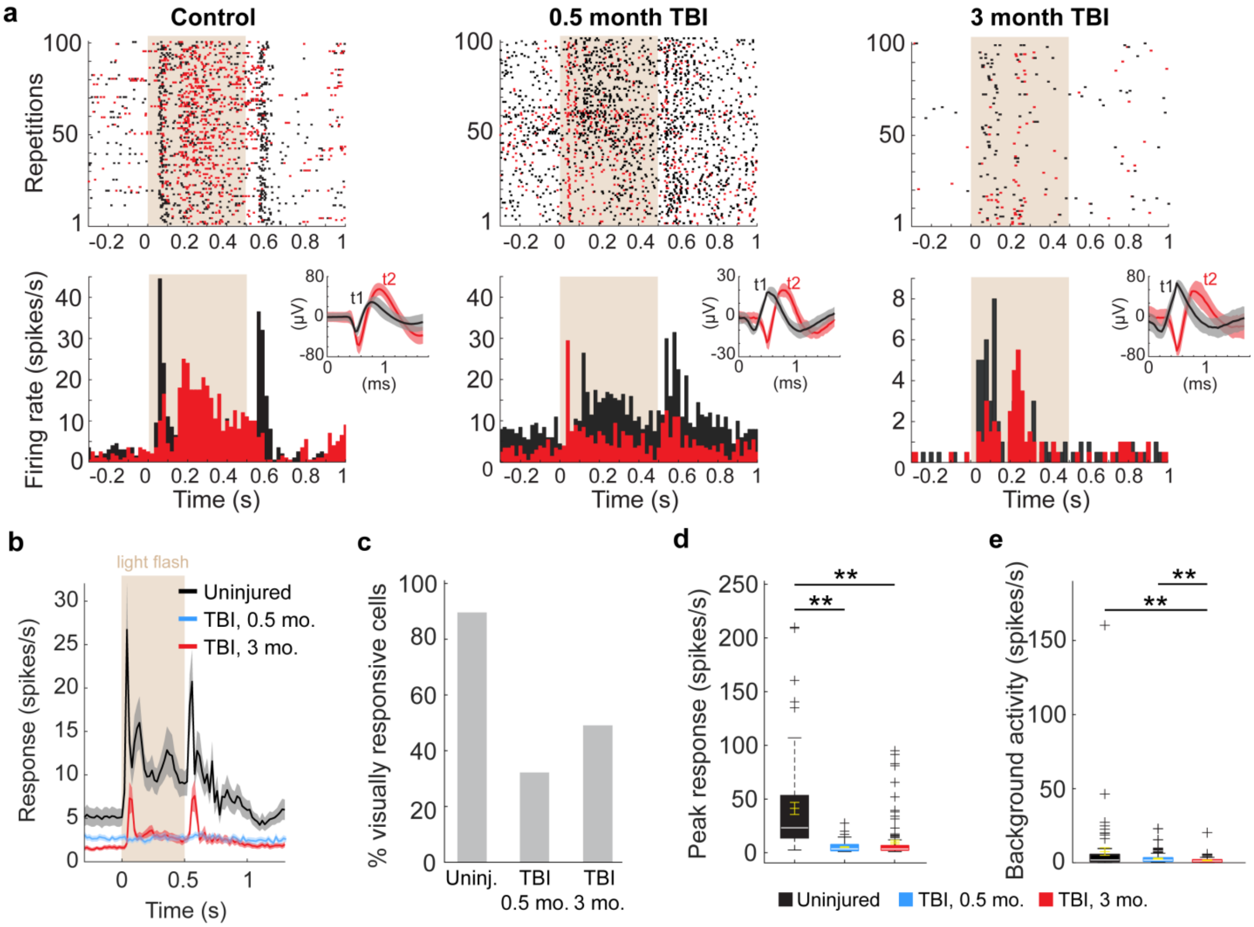

Figure 4.10. Reduced V1 neuron firing following TBI. a. Light-evoked responses of action potential firing for two example neurons (black and red) for each animal group: control (left), 0.5 months (middle) and 3 months after injury (right). Top row shows raster plots to 100 repetitions of the flash stimulus. The bottom row shows the spikes/s averaged over 20 ms bins. In both rows, the 500 ms light stimulus is indicated by beige background shading. Insets in the upper right of the bottom row show raw wave forms isolated by two templates (t1, black and t2, red) based on differences in spike amplitude (uV) and timing (ms). Shading indicates spike variability. **b.** Population averages of light-evoked single-unit responses of action potential firing in uninjured controls (black) and CCI-injured mice 0.5 months (blue) and 3 months after injury (red). n = 67 cells from 8 controls, 110 cells from 5 mice 0.5 months after TBI and 115 cells from 5 mice 3 months after TBI. Shading indicates S.E.M. The 500 ms light stimulus is indicated by beige background shading. **c.** Percentage of visually-responsive cells. **d.** Quantification of peak single-neuron firing rates from each group in response to light stimulus. **P = 9.56E-10, control versus 0.5 months after TBI, **P = 9.56E-10, control versus 3 months after TBI; Kruskal-Wallis H with Dunn's post-hoc. **e.** Quantification of single-neuron firing rates from each group in the 500 ms prior to the light stimulus. **P = 2.00E-03, control versus 0.5 months after TBI, **P = 3.02E-04, control versus 3 months after TBI; Kruskal-Wallis H with Dunn's post-hoc. For box plots, dashed error bars represent the maximum and minimum observations within 1.5 inter-quartile range of the 25th and 75th percentile; values greater than 1.5 inter-quartile range of the 75th percentile are indicated by +.

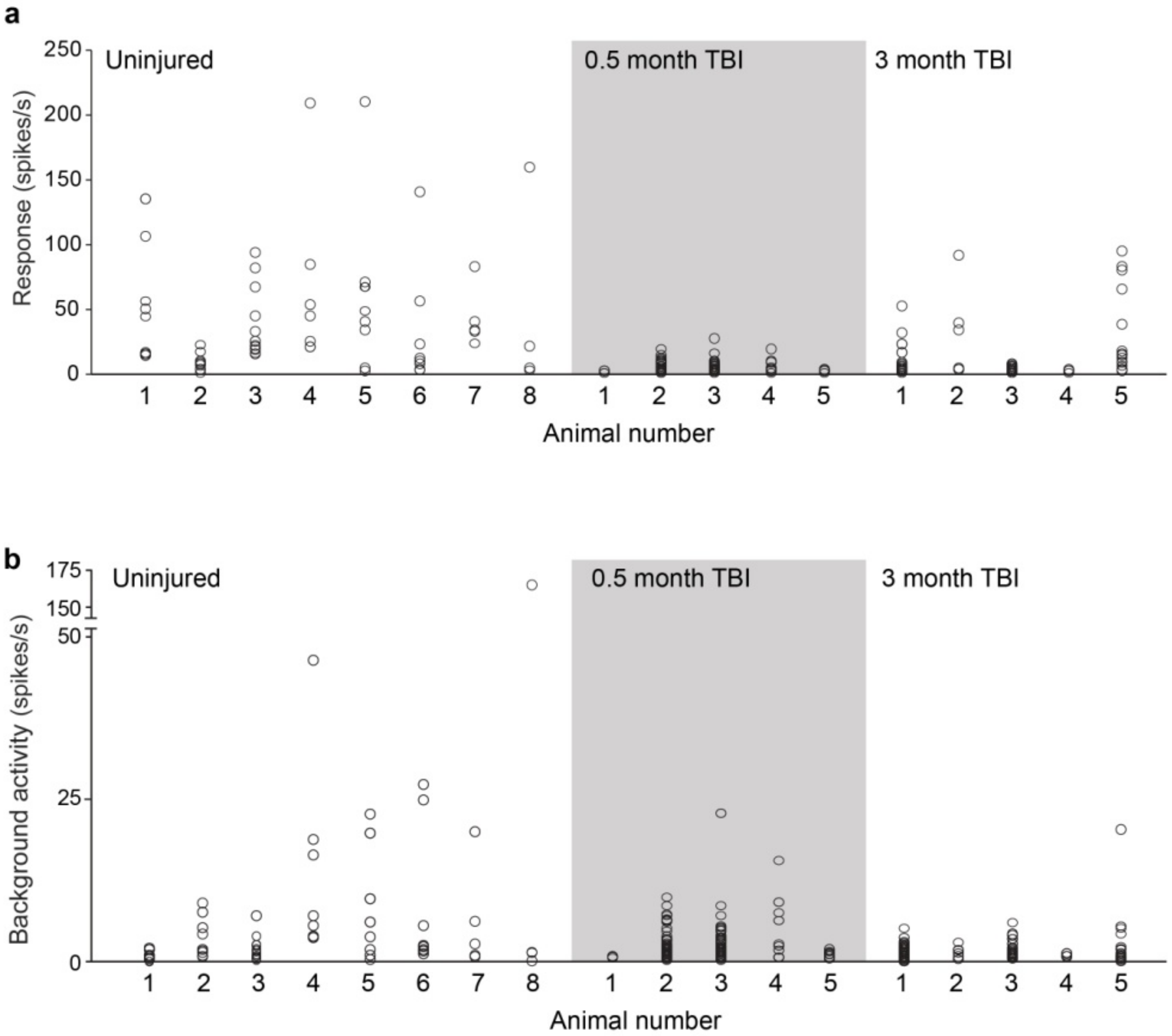

Figure 4.11a,b. Distribution of peak response (a) and background activity (b) for each animal in the uninjured (left, 1-8), 0.5 months (middle, 1-5, gray shading) and 3 months (right, 1-5) after TBI groups.

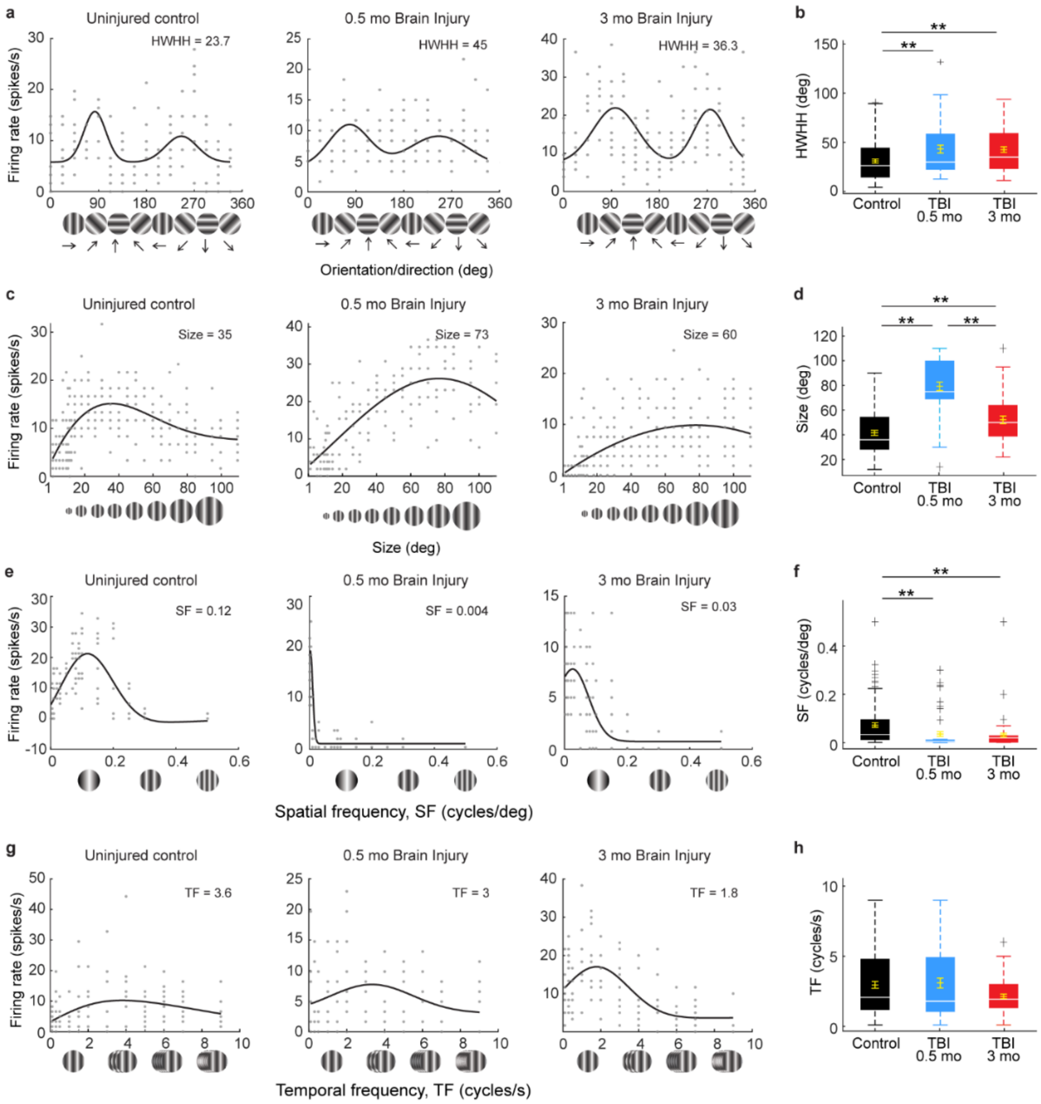

Figure 4.12. TBI disrupts V1 neuron tuning curves in response to drifting gratings. a, b. Orientation tuning curves for single neurons in an uninjured control (black) and CCI-injured mice 0.5 months (blue) and 3 months (red) after injury. To facilitate comparisons across examples orientation preferences have been aligned to 90º and 270º, with 90º representing the preferred direction. Tuning values are given as the half-width at half-height (HWHH) in degrees in each panel (a) and the population averages are quantified in (b). **P = 0.03, control versus 0.5 months after TBI, **P = 1.99E-03, control versus 3 months after TBI; Kruskal-Wallis H with Dunn's post-hoc. n=109 cells from 7 uninjured controls, 54 cells from 5 mice 0.5 months after TBI and 75 cells from 5 mice 3 months after TBI. **c, d.** Single neuron examples and population average quantification of aperture size (in degrees). **P = 9.56E-10, control versus 0.5 months after TBI, *P = 0.042, control versus 3 months after TBI, **P = 2.04E-05, 0.5 versus 3 months after TBI; Kruskal-Wallis H with Dunn's post-hoc. n = 81 cells for control, 45 cells 0.5 months after TBI and 41 cells 3 months after TBI. **e, f.** Single neuron examples and quantification of spatial frequency (SF). **P = 3.80E-06, control versus 0.5 months after TBI, **P = 6.51E-03, control versus 3 months after TBI, Kruskal-Wallis H with Dunn's post-hoc. n =105 cells for control, 55 cells 0.5 months after TBI, 71 cells 3 months after TBI. **g, h.** Single neuron examples and quantification of temporal frequency (TF). P = 0.26; Kruskal-Wallis H test. Optimal values for each parameter are given in each panel. n=95 cells for control, 59 cells 0.5 months after TBI and 70 cells 3 months after TBI. Background activity for each cell is indicated by grey dashed lines. For box plots, dashed error bars represent the maximum and minimum observations within 1.5 inter-quartile range of the 25th and 75th percentile; values greater than 1.5 inter-quartile range of the 75th percentile are indicated by +.

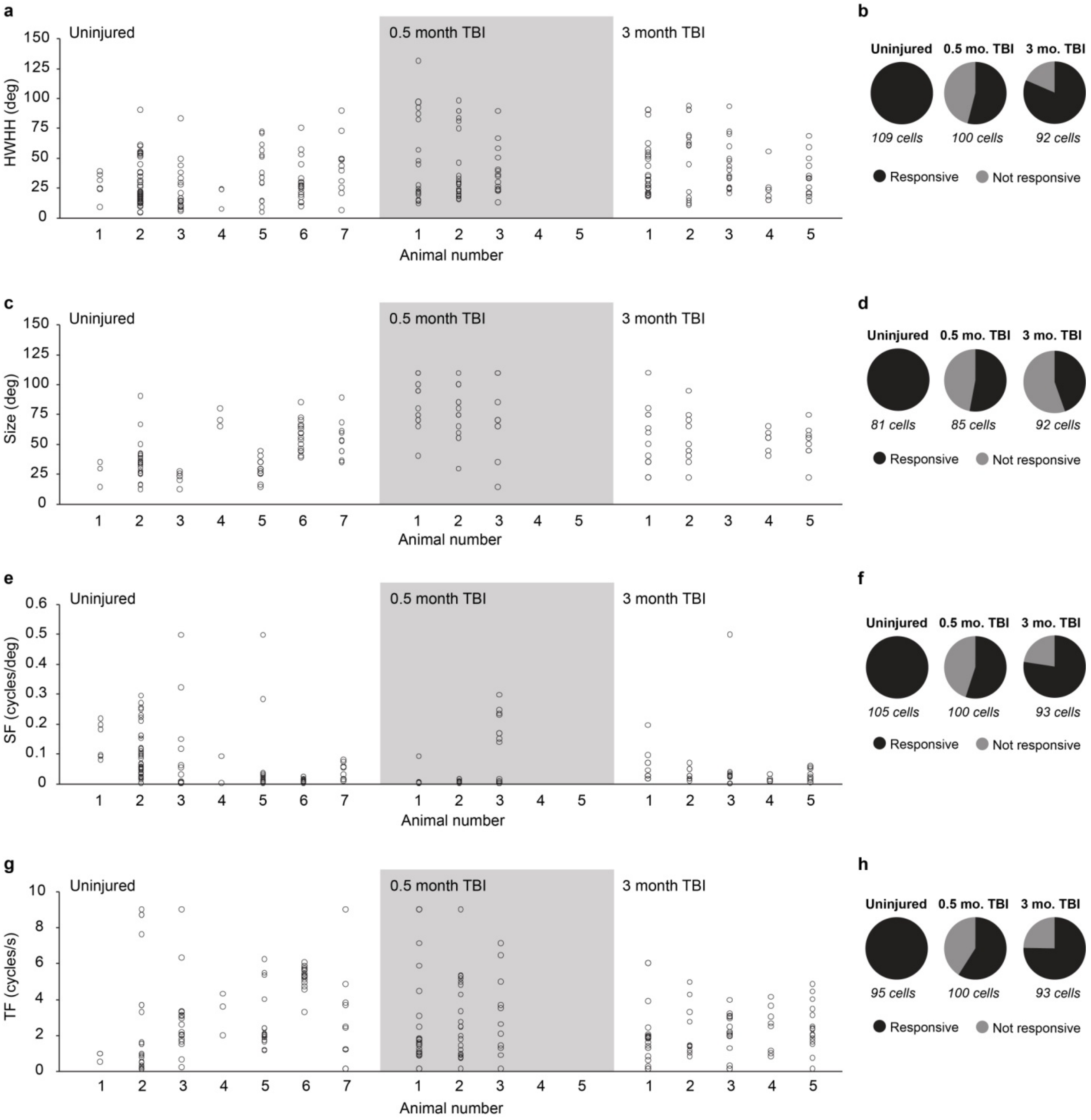

Figure 4.13. a,c,e,g. Distribution of half-width at half-height (a), preferred stimulus size (c), preferred spatial (e) and temporal (g) frequencies for each animal in the uninjured (left, 1-7), 0.5 months (middle, 1-5, gray shading) and 3 months (right, 1-5) after TBI groups. **b,d,f,h.** Proportion of cells that were responsive (black) and not-responsive (gray) to each stimulus parameter: orientation (b), size (d), spatial frequency (f), and temporal frequency (h).

Discussion

Patients with TBI can show long-lasting deficits in visual system function, such as visual acuity and field loss, binocular dysfunction and spatial perceptual deficits (Armstrong, 2018). Here, we delivered a mild focal contusion injury directly to V1 to model occipital contusion injuries, which occur almost exclusively after a direct blow to the back of the head (Ommaya *et al.*, 1971; Sano *et al.*, 1967). Although V1 was relatively well-preserved, compared to traditional approaches that produce substantial tissue damage (Frankowski *et al.*, 2019; Huusko *et al.*, 2015; Nichols *et al.*, 2018), we found neuron loss at the injury site that extended into deep cortical layers. Interestingly, the degree of neuron loss was different in excitatory versus inhibitory systems. Excitatory neurons were lost throughout all layers of brain injured V1, but the greatest degree of cell loss was contained at the injury site. In contrast, inhibitory neurons were uniformly lost by ~35% across all sections examined, but cell loss was restricted to superficial layers I-IV of V1. These observations are different from TBI to hippocampus, where hilar interneurons are widely considered to be the most vulnerable to injury despite being the deepest layer from the site of impact (Frankowski *et al.*, 2019; Lowenstein *et al.*, 1992; Toth *et al.*, 1997). The cellular mechanism for these cell-type-specific responses to injury is unknown. *In vivo* recordings revealed a massive reduction in VEP amplitudes, consistent with damage to the local V1 neuron population, and dramatically altered single neuron tuning to visual stimuli, including changes in orientation and size, which have been shown to be modulated by cortical interneurons (Lee et al., 2012). These findings are consistent with human studies showing visual field dysfunction can occur in individuals with no measurable lesion (Silverman et al., 1993).

Structural and functional damage following V1 injury appear to be permanent. This is different from damage to other sensory areas. For example, in whisker barrel cortex, previous *in vivo* electrophysiology studies have shown there is an initial hypoactivity of neuronal responses 24 hrs after TBI that recovers within 12 weeks after injury, despite persistent structural changes

(Johnstone et al., 2014, 2015). In the current study, we evaluated the effect of V1 TBI on all GABAergic neurons, but specific subtypes may be more or less vulnerable to injury, as has been seen in other brain areas (Frankowski et. al, 2019). Further studies evaluating synaptic plasticity and neuronal connectivity in brain injured V1 will ultimately be required to determine potential candidate mechanisms underlying the permanent disruption of V1 neuron tuning after TBI.

Individuals with TBI can develop visual impairments independent from other injury-induced motor or cognitive deficits (Du et al., 2005; McKenna et al., 2006; Padula et al., 1994; Zihl and Kerkhoff, 1990). Increases in light intensity evoke inhibitory synaptic activity to prevent changes in luminance intensity from disrupting cortical circuit function (Tucker and Fitzpatrick, 2006), and inability to modulate cortical gain has been proposed as a potential mechanism of injury-related photosensitivity (Du *et al.*, 2005; Zihl and Kerkhoff, 1990). Here we show that basic visual processes in V1 are altered to reflect a loss of cortically mediated inhibition. We found significantly broader orientation tuning widths consistent with reduced local inhibitory neuron activity (Lee et al., 2012). Instead, in brain injured animals, V1 orientation tuning resembles the broader widths mediated through feed-forward mechanisms from the thalamus (Liu et al., 2015; Liu et al., 2017), which are likely more intact. Similarly, increased spatial summation indicated by larger stimulus size preference in TBI is consistent with the loss of local inhibitory neurons mediating surround suppression (Adesnik *et al.*, 2012) and likely reflects preservation of feed-forward mediated mechanisms (Liu et al., 2011).

In V1, GABAergic inhibition is essential for a wide range of basic V1 functions, such as tuning a neuron's preference for stimulus contrast, size and orientation (Cardin et al., 2007; Lee *et al.*, 2012; Sillito et al., 1985) as well as higher-order processing, such as contrast perception (Cone et al., 2019). During development, cortical inhibition modulates critical periods, a transient time of enhanced sensitivity to sensory experience. This has been most extensively studied in juvenile

V1, in which obstructing vision through one eye results in cortical blindness to this eye, even after normal vision is restored (Wiesel, 1982). Cortical inhibition is required for opening the developmental critical period in visual cortex (Hensch et al., 1998) and inactivating interneurons can prolong the critical period (Espinosa and Stryker, 2012) or impair cortical plasticity (Fagiolini et al., 2004). Even in adulthood, after binocular vision is well established, manipulating inhibition through pharmacology (Fagiolini and Hensch, 2000; Sillito *et al.*, 1985) or interneuron transplantation (Davis et al., 2015; Larimer *et al.*, 2016) can have dramatic effects on cortical plasticity in response to monocular visual deprivation. Given our recent success using interneuron transplantation to treat post-traumatic memory problems and epilepsy (Hunt *et al.*, 2013b; Zhu *et al.*, 2019), future studies evaluating the effect of manipulating excitatory versus inhibitory activity in brain injured V1 may reveal new avenues for circuit-based therapy.

CONCLUSIONS

Traumatic brain injury has devastating consequences on the affected individual, the caregivers who support those individuals, and our society. Individuals are frequently left with life-long deficits that affect multiple domains. For these reasons, it is important to understand how TBI affects brain circuit structure and function globally, and to consider the development of future therapeutic interventions from a circuit-based perspective. The overall conclusions of the work described here is that traumatic brain injury profoundly reorganizes brain circuit structure and function from microscopic to mesoscopic scales. In Chapter One, I review the history of TBI research with a specific focus on CCI as a useful model to produce brain injuries in animals that recapitulate many of the characteristics of brain injuries sustained in humans. In Chapter Two, I show that the cellular responses to traumatic brain injury vary depending on the interaction of injury severity, regional and laminar position, and neurochemical identity. After analyzing five distinct neurochemically-defined subtypes in each layer of DG and CA1, we identified hilar somatostatin-expressing interneurons as the most vulnerable interneuron subtype to injury. Considering the importance of this specific interneuron subtype in circuit function and previous work showing SST+ interneurons are highly plastic in response to insult, this led us to investigate how the inputs onto surviving SST+ interneurons are changed during the chronic post-injury phase using a monosynaptic rabies virus tracing paradigm. In Chapter Three, I show that the surviving SST+ interneurons in DG and PFC show a similar pattern of changes, with a loss of long-range input and an increase in local input. These results were remarkable because circuit reorganization occurred not only at the injury site, but also distal from the injury where cellular injury was undetectable. SST+ interneurons introduced into the injured DG via MGE transplantation show a remarkable ability to re-establish connections with appropriate brain regions in the entorhinal cortex, basal forebrain, and brain stem. These results indicate that the therapeutic effects of MGE transplantation may involve integration of input from distant brain regions, similar to their endogenous counterparts. In Chapter Four, we shifted our focus to the visual cortex and show that a mild focal injury produces differential cell loss in excitatory and inhibitory neurons, and that the surviving neurons show altered responses to fundamental features of visual stimuli. Taken together, these results support the notion that TBI should be investigated and treated from the perspective of a brain circuit disorder. Severe focal injuries can have widespread and profound effects that ripple across the brain, affecting multiple systems. Even mild superficial injuries can completely alter the cellular and electrophysiological properties of affected regions. Finally, cell-based therapeutics may have tremendous therapeutic potential to alleviate the devastating consequences of TBI in the future.

Mechanisms underlying selective vulnerability of hilar SST interneurons

Vulnerability of GABAergic interneurons to injury is a common feature across many neurological diseases. Hilar interneuron loss has been demonstrated in models of temporal lobe epilepsy (Obenaus et al., 1993), fluid-percussion TBI (Lowenstein *et al.*, 1992), cerebral ischemia (Johansen et al., 1987), electrical stimulation of the perforant pathway (Sloviter, 1987), and Alzheimer's disease (Ramos et al., 2006). These results in animal models recapitulate findings in post-mortem human tissue samples that show hilar neuron loss in the hippocampus of epileptic patients (de Lanerolle *et al.*, 1989; Robbins et al., 1991) or after trauma (Swartz *et al.*, 2006). In Chapter Two, I show that SST+ neurons are the most vulnerable subtype to injury of the five neurochemically defined subtypes studied. The particular vulnerability of hilar SST interneurons may be due to a confluence of several factors including the biomechanics of injury, activity dependent mechanisms related to laminar position, and intrinsic electrophysiological and neurochemical properties. When delivering CCI injury we use a beveled-tip impactor tip, which has been shown to produce a high degree of principle strain and shearing forces at the edges of the impactor (Pleasant *et al.*, 2011). The impactor tip is oriented perpendicular to midline and offset ~1mm from midline, which would direct the maximal principle strain directly towards the dentate gyrus. Injury biomechanics alone do not explain why the hilus would be most vulnerable across subtypes, considering that it is the farthest hippocampal subfield from the impact site. Differential patterns of synaptic connectivity likely contribute to stark contrast between differential susceptibility of hilar interneurons compared to interneurons in other cell layers such as molecular layer interneurons, which are completely unaffected by injury. Hilar interneurons receive excitatory input from mossy fiber synapses in addition to perforant path axons (Leranth *et al.*, 1990). Following a TBI, cortical spreading depolarization occurs, which involves massive unregulated depolarization of cortical neurons (Taş et al., 2019). This unregulated activity may activate the entorhinal cortex, which would lead to increased excitatory drive directly onto hilar interneurons as well as increased drive onto dentate granule cells. Greater excitatory drive may overwhelm hilar SST+ neurons which have relatively high input resistance compared to other interneuron subtypes (Hunt *et al.*, 2013b), leading to substantial change in voltage in response to current injection. Another potential contributing mechanism is the lack of calcium binding protein expression in hilar SST+ neurons, which may render them more vulnerable to toxic increases in calcium after sustained depolarization (Nitsch et al., 1990). In the hilus, SST-expressing interneurons do not co-label with parvalbumin, calretinin, or calbindin (Bouilleret et al., 2000). However, in CA3 and in CA1, approximately half of SST-expressing interneurons co-label with calretinin or calbindin (Bouilleret *et al.*, 2000). The presence of calcium binding proteins may reduce activity-dependent increases in calcium enough to prevent cell death. Supporting this hypothesis, calcium chelation can protect hilar interneurons from prolonged electrical stimulation-induced cell death (Scharfman and Schwartzkroin, 1989). Another potential contributing factor could be the structural characteristics of the hilus. Neurons in the hilus are instantaneously damaged by the biomechanics of fluid percussion injury, even without the recruitment of active physiological processes. This was demonstrated in a series of experiments where fluid percussion injury was delivered and silver staining was used to reveal patterns of structural damage immediately after injury (Toth *et al.*, 1997). Animals perfused immediately after injury showed selective silver staining in the hilus, but not in the granule cell layer, suggesting that hilar neurons showed a greater degree of damage after injury. The role of activity-dependent processes was ruled out by performing fluid percussion injury in animals that were perfused prior to injury, and in a second experiment where animals were fixed, cooled, and perfused with a glutamate receptor blocker prior to injury. These experiments also revealed selective silver staining in the hilus, indicating that hilar neurons were selectively vulnerable even without the recruitment of active physiological processes. One possible explanation could be related to damage to the extensive axonal arborization characteristic of hilar SST+ interneurons. Compared to granule cells, hilar SST+ axons are 40-times longer, and a single SST+ neuron may arborize over 80% of the septotemporal axis of the dentate gyrus (Buckmaster *et al.*, 2002). Cells with smaller arborization are subjected to a lesser degree of stretching induced by injury biomechanics (Toth *et al.*, 1997), thus the extensive axonal arborization characteristic of hilar interneurons may contribute to their selective vulnerability. Hilar SST+ play important roles in microcircuit operations supporting memory formation through feed-back and lateral inhibition (Katona *et al.*, 1999; Raza et al., 2017; Stefanelli *et al.*, 2016). As a major source of inhibition in the dentate gyrus, the loss of hilar interneurons could have profound consequences on the function of the dentate circuit after TBI. In the healthy dentate gyrus, granule cells outnumber HIPP cells 50:1 (Buckmaster and Jongen-Rêlo, 1999). Thus, loss of hilar interneurons could significantly increase the granule cells to interneuron ratio, placing increased demand on remaining hilar SST+ neurons. Surviving SST+ neurons also receive increased excitatory drive after TBI (Butler *et al.*, 2017; Hunt *et al.*, 2011), further increasing the demand placed on individual neurons. Excessive cation influx and depolarization can result in depolarization block, the failure to support continuous action potential generation. Given that fewer hilar interneurons are present after TBI and surviving interneurons receive increased excitatory input, the likelihood of depolarization block may be higher and may contribute to spontaneous seizure generation if SST+ neurons fail to activate. In mouse models of TLE, the loss of GABAergic interneurons in dentate gyrus is correlated with seizure frequency

(Buckmaster *et al.*, 2017). While this has not been demonstrated after trauma, interneuron transplantation abrogates spontaneous seizures after CCI injury (Zhu *et al.*, 2019). In summary, the vulnerability of hilar SST+ interneurons to injury likely involves multiple converging mechanisms and injury-induced loss likely contributes to DG circuit dysfunction.

Consequences of circuit reorganization after TBI

A neuron's function is strongly influenced by its synaptic inputs. In Chapter Three, we used rabies virus tracing and whole-brain clearing to provide the first cellular-resolution maps of synaptic input onto somatostatin neurons after traumatic brain injury. We demonstrate that a single focal contusive injury reorganizes circuit connectivity in two brain regions involved in learning and memory, the dentate gyrus and prefrontal cortex. In both regions we found a common theme - the formation of hyper-connected local hubs and the loss of the largest sources of long-range input.

TBI is often considered to be disorder of circuit connectivity typically attributed to diffuse axonal injury (Sharp et al., 2014). However, even a focal contusive injury is sufficient to remodel brain-wide circuit connectivity in two regions critical to learning and memory, the DG and PFC. One common finding in both regions is an increase in local input after injury. In DG, these changes may occur as a result of compensatory mechanisms that restore imbalances in excitation and inhibition after TBI. Some of the earliest changes in the hippocampus after injury include interneuron loss and reduced synaptic inhibition. Silver staining methods have revealed that damage to the hilus occurs within minutes after TBI (Toth et al., 1997). This likely contributes to interneuron loss and subsequently reduced synaptic inhibition, detectable within one week after injury (Toth et al., 1997, Santhakumar et al., 2000). After TBI, expression and activity of neuronal chloride transporter KCC2 is reduced, reducing intracellular chloride concentrations and impairing the efficacy of inhibitory synaptic transmission (Bonislawski et al., 2007). Together, these mechanisms contribute to a loss of synaptic inhibition. In addition to a loss of inhibition, post-traumatic mossy fiber sprouting forms recurrent excitatory connections between dentate granule cells (Hunt et al., 2009), which may enhance excitability of the dentate gyrus. Together, these alterations to the circuit may reduce the filtering capacity of the dentate gyrus and result in greater excitatory input passing through the hippocampal circuit. One possible compensatory mechanism would involve additional recruitment of surviving SST neurons by sprouting of their dendrites and axons. Morphological changes to support this compensatory response have been previously described in temporal lobe epilepsy models, where hilar SST neurons show increased soma size, axonal sprouting, and increased dendrite length after insult (Buckmaster and Wen, 2011; Zhang *et al.*, 2009). After CCI, dentate granule cells show slower IPSC decay times, which is consistent a shift towards dendritic synaptic inhibition over perisomatic inhibition due to axonal sprouting of surviving SST neurons in the outer molecular layer (Hunt et al., 2011). Hilar SST neurons also show increased spontaneous action potential firing, greater sEPSC and mEPSC frequency, and increased input from CA3 after CCI (Hunt et al., 2011). These results suggest that compensatory recruitment of surviving SST interneurons is a potential strategy to restore lost feedback inhibition. This compensatory mechanism may also explain greater CA1 and subicular input after injury. Hilar SST neurons can extend dendrites into the molecular layer (Leranth et al., 1990), which may also sprout in response to injury. These molecular layer dendrites may be the anatomical substrate mediating connectivity between hilar SST neurons and principal neurons in CA1 and the subiculum. In CA1, pyramidal neuron axons sprout within weeks after TBI (Norris and Scheff, 2009). Sprouted axons may also cross the hippocampal fissure, which is known to occur in epilepsy models (Peng et al., 2013), suggesting a similar mechanism could occur after TBI. Greater CA1 to hilar SST connectivity could reflect additional compensatory recruitment of feedback inhibition after injury. A potential molecular mechanism mediating post-injury may involve autophogy signaling pathways. The phosphatidylinositol/protein kinase B Akt/mammalian target of rapamycin (PI3K/Akt/mTOR) autophagy pathway plays a critical role in regulation of cell body size and outgrowth of axons and dendrites during normal development and after injury (Fingar et al., 2002). Pharmacological inhibition of mTOR signaling using rapamycin suppresses mossy fiber sprouting after TBI (Butler *et al.*, 2015; 2017), and abolishes axonal sprouting in hilar SST neurons in epilepsy models (Buckmaster and Wen, 2011), demonstrating the importance of this signaling pathway in post-injury sprouting responses.

Similar to our results in DG, PFC SST neurons received greater local input after TBI. Increased prefrontal connectivity and activation has been frequently reported in functional imaging studies in patients affected by TBI and may reflect a compensatory mechanism of the altered brain network in response to cognitive demands (Hillary et al., 2006; Hillary et al., 2015). The mechanisms by which the PFC reorganizes to increase local input onto SST+ neurons may involve interactions between the hippocampus, PFC, and anterior thalamic nuclei. Our data shows that PFC receives direct monosynaptic input from CA1 and subiculum, confirming previous reports (Ährlund-Richter *et al.*, 2019). After TBI, the hippocampus can become hyperexcitable and generate seizure activity, which could increase excitatory input from subiculum and CA1 into PFC. This increased excitatory input could promote hyperconnectivity within the PFC. A recent study using optogenetic kindling of the ventral hippocampus identified the medial PFC as one of the brain regions showing greatest evoked responses to hippocampal kindling. Optogenetic kindling of the ventral hippocampus resulted in greater interconnectivity within the medial PFC, and more widespread and intense activation measured by fMRI (Choy et al., 2021). It is possible that after TBI, a similar mechanism is at play, with output from CA1 promoting greater interconnectivity of prefrontal cortical regions. If so, changes in the PFC may emerge after the hippocampus becomes hyperexcitable. Future work could elucidate whether elevated hippocampal output contributes to this mechanism by transplanting MGE cells into the injured hippocampus and repeat the rabies tracing experiments, whole-cell patch clamp electrophysiology, or calcium imaging to determine whether SST+ neurons receive greater input after TBI when hippocampal activity is normalized by interneuron transplantation. Another contributing factor may involve disrupted feedback between the PFC and hippocampus. The PFC does not directly project back to the hippocampus but can interact through the anterior nuclei that receive input from PFC and project back to the subiculum (Shibata, 1993; van Groen et al., 1999). Since TBI also disrupts the connectivity between PFC and anterior thalamic nuclei, feedback from the PFC back to the subiculum may be disrupted. Taken together, it is possible that TBI shifts the balance of the bidirectional communication between the PFC and hippocampus more towards a unilateral flow of excitatory input from the hippocampus into PFC which could promote an increase in local connectivity after TBI.

Another common finding in both regions was a reduction in long-range inputs involved in memory. In DG, cholinergic input from the basal forebrain is known to contribute to memory formation (Raza et al., 2017). We found a significant reduction in this input arriving onto hilar SST interneurons, which could be due to cell loss in the region of origin or damage to the axons connecting the two regions. While cell loss in the basal forebrain has been previously been reported after diffuse TBI (Leonard *et al.*, 1994; Schmidt and Grady, 1995), we found no cell loss in two separate cohorts of animals. This may be due to differences in the injury model used, as fluid percussion injury produces a more diffuse injury compared to CCI. Nonetheless this is surprising because neuronal activity based-mechanisms have been implicated in ChAT+ cell loss after TBI (Wurtman, 1992). We also found a loss of reelin+ input from the entorhinal cortex, which is known to provide spatial and contextual information to the DG (Kitamura et al., 2015; Rowland et al., 2018). However when we quantified reelin+ cell density, no cell loss was detected in brain-injured animals. These results suggests that the loss of long-range input could be due to axonal injury rather than distal cell death, consistent with previous reports of damage to the major white matter pathways innervating the hippocampus after CCI (Hall *et al.*, 2008; Lighthall et al., 1990). In the PFC, we also found that SST neurons lose thalamic input, the major source of input outside the neocortex. In TBI patients, reduced prefrontal-thalamic connectivity is associated with impaired memory, attention, and executive function (Little et al., 2010). Specifically, we found reduced input from the anterior thalamic nuclei including the anteromedial nucleus, which is a major relay for memory circuits through direct connections with the prefrontal cortex, hippocampus, and entorhinal cortex (Aggleton and Brown, 1999; Xiao and Barbas, 2002). The loss of input from the anterior nuclei specifically may contribute to the cognitive deficits associated with TBI. The role of the anterior thalamic nuclei in various forms of memory has been demonstrated in humans and in rodents, as anterior thalamic lesions impair episodic, recognition, and spatial memory (Aggleton et al., 1996; Byatt and Dalrymple-Alford, 1996; Sziklas and Petrides, 2007). Case studies of individuals with lesions localized to the anteromedial nucleus specifically show long-lasting episodic and recognition memory (Ghika-Schmid and Bogousslavsky, 2000; Kishiyama et al., 2005; Parkin et al., 1994). We found that input from the anterior thalamic nuclei broadly and specifically the anteromedial nucleus was reduced. Given the importance of these regions in multiple memory domains, the loss of this input may in part contribute to cognitive deficits after TBI. Another consistent effect between the DG and PFC was a significant decrease in the proportion of input arising from the contralateral hemisphere. Previous work using functional imaging in TBI patients has shown that both the hippocampus and frontal lobes show decreased bilateral connectivity, which is associated with impaired memory recall (Marquez de la Plata *et al.*, 2011). Our results are also consistent with results from diffusion tensor imaging, with brain injured patients showed reduced connectivity between the fornix and hippocampus in addition to reduced frontal lobe connectivity (Kinnunen et al., 2011). Taken together, our tracing results indicate that a single focal injury can produce widespread circuit reorganization affecting multiple brain circuits affecting memory, attention, and executive function similar to those described after diffuse injury. While we only investigated changes in a single cell type across two brain regions, our results suggest that changes in connectivity could extend to other neuronal subtypes and is not necessarily restricted to circuits within contused brain regions.

Connectivity of transplanted interneurons in the injured brain

While TBI therapies often focus on sparing tissue at-risk of atrophy or preserving neurons acutely, in the case of treating chronic injury these approaches are of limited value. Interneuron transplantation for treating individuals affected by severe TBI is a promising candidate for a disease with no approved treatments. Interneurons replacement is a logical approach for treating TBI because hippocampal interneuron loss is a consistent feature after TBI and previous work has demonstrated tremendous potential to ameliorate cognitive deficits after injury and post-traumatic epilepsy (Zhu *et al.*, 2019). To date, it is the only effective intervention to prevent the development of post-traumatic epilepsy in animal models of TBI (Dulla and Pitkänen, 2021). While the mechanism by which transplanted interneurons mediate their effects has been suggested to be indirect secretion of trophic factors (Zheng *et al.*, 2021), accumulating evidence supports the hypothesis that integration into host-brain networks and subsequent activity of transplanted cells is involved. The integration of interneuron progenitors into host-brain networks has been demonstrated previously using electron microscopy (Daadi *et al.*, 2009), paired electrophysiological recordings (Howard and Baraban, 2016), and optogenetics (Hsieh and Baraban, 2017). Chemogenetic inactivation of transplanted interneurons reverses the therapeutic effects of interneuron transplantation in brain injured mice (Zhu *et al.*, 2019), and transplanting interneuron progenitors lacking vesicular GABA transporters fail to induce cortical plasticity (Priya *et al.*, 2019). These results suggest that integration into host-brain networks and synaptic activity of grafted interneurons underlie the beneficial effects. Our results further support this hypothesis by showing robust monosynaptic input onto transplanted interneurons from local neurons in addition to long-range inputs in the entorhinal cortex and basal forebrain, similar to those seen in endogenous SST neurons. These results are promising for several reasons. First, the adult brain retains the capacity to appropriately integrate neuron subtypes only generated during early embryonic development. Second, despite damage to white matter pathways innervating the hippocampus, long-range inputs can be established onto interneurons grafted into the injury site. Third, synaptic input is appropriate for the particular cell type within the region where they are found, as transplanted interneurons received input from the same regions that endogenous hilar SST neurons receive in control or injured conditions. Our results show that the brain is inherently capable to rewiring the proper connections after injury if the proper neuron subtypes are introduced into the right regions, which is supports the development of future cell-based therapies for circuit repair.

Tissue clearing and the future of mesoscopic neuroanatomy

Advances in tissue clearing have made whole mouse brain (Ertürk *et al.*, 2012), whole mouse (Pan *et al.*, 2016), and whole human brain (Zhao *et al.*, 2020) clearing possible. Modern light sheet microscopes can resolve brain structures with resolution up to two orders of magnitude greater than the highest resolution structural magnetic resonance scanners (Helthuis et al., 2018). Although these advances permit acquisition of unprecedented amounts of volumetric data, one outstanding challenge is labeling structures of interest with commercially available antibodies. Over the past several years several approaches have tried to address the issues surrounding the limited capacity for antibodies to diffuse deep into cleared tissue, although with some drawbacks. Centrifugal or convective flow improve antibody penetration in cleared tissue, however labeling is still limited to approximately ~1mm from the surface (Lee *et al.*, 2016). Stochastic electrotransport uses a rotating electric field to enhance the movement of charged antibody particles to obtain deep and even immunolabeling, however this requires very specialized equipment for this purpose (Kim *et al.*, 2015b). With approximately 10-fold smaller molecular weights, single domain nanobodies paired with peristaltic perfusion pumps have been used to achieve deep labeling, although target probes are only available against commonly used fluorophores such as GFP or mCherry (Cai *et al.*, 2019). The most promising developments for enhancing antibody penetration include the use of small micelle forming detergents such as CHAPS (Zhao *et al.*, 2020). Most clearing protocols use antibody diluent solutions that closely resemble those used for traditional slice immunohistochemistry with detergents such as Triton-X, sodium dodecyl sulphate, or Tween-20. These detergents have a hydrophilic charged head group and a long hydrophobic tail group, which assemble into large micelles. While these are effective for permeabilizing tissue sections less than 100 microns thick, they are incapable of penetrating tissues that are millimeters or centimeters thick. We incorporated CHAPS detergent into the iDISCO+ protocol and achieved whole-brain immunolabeling of structures deep in the brain and were even able to resolve neuronal processes in midline thalamic nuclei. The major advantages of this approach include the ability to use commercially available antibodies, no need for specialized equipment, and the ability to immunolabel entire brains without separating the hemispheres. One outstanding question is whether the approach described here is effective for labeling densely expressed antigens. Our data involved labeling up to ~10,000 mCherry- and GFP-expressing neurons in the whole brain, which is only a small fraction of the total in the entire brain. It is possible that to label highly expressed antigens such as NeuN, additional steps may need to be taken to achieve even and consistent labeling. One easily implemented approach would be to pair CHAPS detergent and centrifugation together to enhance the diffusion of antibody-laden CHAPS micelles through cleared tissue. This approach may also significantly reduce the amount of time needed for antibody incubation which currently takes over two weeks. Approaches incorporating multiple permeabilization improvements may also be necessary for immunolabeling larger species. As neuroscience research moves more towards using larger brains, it will be necessary to incorporate new approaches to label these structures. While the volume of a mouse brain is only ~1cm^3, the volume of a marmoset brain is approximately 50-fold larger (Woodward et al., 2018), and the volume of a human brain is approximately 1300-fold larger (Cosgrove et al., 2007). Free diffusion of antibodies would require months or years of incubation time to evenly label these larger brains, which would be prohibitively costly. A recent report imaged a whole macaque brain and traced cortico-thalamic axons using an approach similar to serial two-photon tomography approaches but at larger scale. The brain was first sectioned into 250 consecutive 300 μm slices which were then individually stained, imaged, and aligned (Xu et al., 2021). While this approach was successful, staining and imaging an intact brain would be ideal as a less computationally intensive approach that does not introduce error along the sectioning planes.

The reverse clearing protocol described and applied to study the long-range projections to the dentate gyrus in Chapter 3 has great potential to supplement mesoscale tracing data in novel ways. Typically, cleared tissue is not considered to be useful after the initial round of immunostaining. In the troubleshooting section of the iDISCO+ protocol it is explicitly stated that “We do not know of a method to reverse the clearing” (Renier *et al.*, 2016). The methods described here provide a framework for rehydrating and immunolabeling previously cleared tissue which can be adapted to probe cell-type identities of cells, quantification of cell density, or to obtain information about structures that cannot be easily resolved using a light sheet microscope, such as synapses. We used this method to identify the cell-type markers of rabies-labeled cells innervating hilar SST interneurons, demonstrating that the major extrahippocampal inputs from the basal forebrain and medial entorhinal cortex express acetylcholine transferase and reelin, respectively. We also demonstrated that the density of CHAT+ or Reelin+ cells is not reduced after injury, indicating that distal cell loss is not the primary driver of the loss of long-range presynaptic input. These experiments could be expanded upon in many ways. One potential application would be to identify the pre- and post-synaptic receptors mediating interactions between two connected neurons previously identified using light sheet imaging. Another potential application is pairing reverse cleared tissue with super-resolution methods, allowing for imaging and analysis beyond the diffraction limit of light microscopy. This would feasibly allow researchers to approach their question of interest across six orders of magnitude of resolution in the same animal, from intact-brain resolution (~1cm for mouse) to single molecule resolution (20 nm) (Rust et al., 2006). Future experiments could use reverse clearing to demonstrate that a transplanted human neuron is fully integrated into a circuit with mature morphology, cell-type marker expression, and functionally connectivity with cell-type specific long-range input neurons mapped in atlas space, all within a single animal. To do this, human interneuron progenitors could be transplanted into the hippocampus of a mouse after CCI injury. Then, the human cells could be infected with AAVs expressing a fluorescent reporter, TVA, G protein, and a calcium indicator under human cell-type specific promoters. After AAV expression, transplanted neurons could be infected with a rabies virus expressing channelrhodopsin-mCherry. Using two photon microscopy or an endoscopic microscope, calcium transients could be recorded while optogenetically stimulating the entorhinal cortex. After demonstrating functional connectivity, brains could be immunolabeled, cleared, and imaged using a light sheet microscope to map the locations of ChR2-rabies cells in standard atlas space and obtain whole-cell morphology of transplanted cells. Then, the same brains could be reverse cleared to stain for subtype markers expected in the transplanted cell (I.e., somatostatin, human nuclear marker) and the presynaptic input marker (i.e, reelin). This experiment would demonstrate that a human cell transplanted into the damaged brain shows mature morphology, expresses the correct cell type markers, and receives functional monosynaptic input from the appropriate presynaptic source, all within a single animal.

Future directions

While we focused on SST+ interneurons which are known to be highly plastic in various neurological disease models, it is unknown whether the connectivity of other neuronal subtypes is differentially affected after TBI. Cell-type specific patterns of input vary, with SST+ interneurons in PFC receiving greater input from CA1 than PV- or VIP-expressing interneurons (Sun et al., 2019b). Future rabies tracing experiments using cell type specific cre-driver lines for excitatory neurons, PV-, or VIP-expressing interneurons would elucidate whether SST+ neurons are particularly susceptible, or if the patterns of circuit reorganization we observed are a common feature across different neuronal subtypes. Another outstanding question is what brain regions are involved in post-injury circuit reorganization and the time course of region-specific changes. It is possible that increased output driven by post-injury hyperexcitability and spontaneous seizures within the hippocampus promotes circuit reorganization in many other regions targeted by the CA1 and subiculum. Known targets of subiculum and CA1 include basolateral amygdala, agranular insular areas, retrosplenial, auditory, somatosensory, gustatory, olfactory, and visual areas (Cenquizca and Swanson, 2007). Circuit-level changes in these areas may contribute to the wide range of deficits associated with TBI. Further experiments using rabies virus tracing could reveal whether inputs to other brain regions distant from the injury site are altered after TBI. While we performed tracing experiments at a chronic time point, another open question is the time course of changes after injury. One approach would be to use single-cell RNA sequencing to determine when injury induced transcriptional changes occur in regions distal to injury. Previous work has shown that after mild TBI, hippocampal neurons show changes in genes involved in glutamate transport, metabolism, neuroplasticity, and cell-cell signaling (Arneson et al., 2018), suggesting similar processes may be involved after focal injury. This approach could be paired with fluorescent in situ hybridization to quantify spatial patterns of gene expression changes.

Another approach that would provide insight into changes in network activity across of large swaths of the cortex is mesoscopic imaging (Sofroniew et al., 2016). With a ~5 mm field of view, it would be possible to image calcium dynamics across the perilesional zone into prefrontal areas. This would enable chronic imaging over the course of the animal's lifetime and provide insight into the time course of injury-induced activity changes spanning the brain. This information would potentially inform the timing of cell-based therapies. Introducing interneuron progenitors into the hippocampus during the early versus chronic phase of injury could have differential effects on downstream regions. Another future direction would be to determine whether the capacity for new neurons introduced into the damaged brain to incorporate the appropriate inputs is possible in larger brains. The results presented here show that interneurons grafted into the damaged mouse hippocampus are capable of re-reestablishing long-range inputs, however whether this translates to other species is an open question. Transplantation experiments and rabies virus tracing after TBI in pigs, ferrets, or non-human primates could provide insight into whether these findings translate to higher species.

Future experiments could address outstanding questions regarding the role of long-range input in mediating the therapeutic effects of interneuron transplantation. To do this, CCI and MGE-Flp transplants could be performed in mice carrying a floxed allele for an inhibitory opsin. A Flp-dependent AAV could then express rabies G protein and TVA in transplanted MGE cells. Then, using a non-toxic double mutant G- and L-deleted rabies virus coding for Cre recombinase (Chatterjee *et al.*, 2018), the long-range inputs from the basal forebrain or entorhinal cortex specifically innervating transplanted neurons could be driven to express inhibitory opsins. Then, the individual contributions of long-range inputs could be probed by inhibiting input neurons during behavior or while recording local field potential in the hippocampus. Reelin-expressing neurons in layer II of medial entorhinal cortex are involved in spatial coding (Rowland et al., 2018). By activating the inhibitory opsins in entorhinal cortex during a spatial navigation task, the contribution of these cell's input onto transplanted neurons during task performance could be tested. Another outstanding question is whether interneuron transplants affect network oscillations after TBI. Previous work has shown that TBI attenuates theta oscillations in hippocampus, and that electrical stimulation of the basal forebrain improves oscillation deficits and improves spatial memory task performance (Lee et al., 2013; Lee et al., 2015). Given that hilar interneurons that target distal granule cell dendrites are involved in hippocampal theta generation (Buzsáki, 2002), and that these interneurons receive input from the basal forebrain, it is possible that long-range input onto transplanted interneurons is involved in theta oscillatory activity. To test this, the tracing strategy described above could be used, except inhibitory opsins could be driven in basal forebrain while recording the local field potential in hippocampus. This experiment would provide insight into whether network oscillations in the injured hippocampus are mediated by input from the basal forebrain onto transplanted interneurons.

Final concluding remarks

While considerable effort has been made in recent years to map the cell-type specific circuits of endogenous neurons in the healthy brain, our results indicate that understanding how these circuits are changed in the context of disease will require considerable effort. After injury, neuron loss is variable depending on severity of insult and the regional, laminar, and neurochemical identity. Surviving neurons undergo profound circuit reorganization, even in regions not directly damaged. These changes are likely to evolve over time and influence other brain regions that may otherwise assumed to be healthy. Future work could reveal that TBI reorganizes many more circuits across the brain. Diseases such as epilepsy or Alzheimer's disease that have unique patterns of pathophysiology that evolve over space and time will require considerable effort to decipher and understand how disease progression affects the organization of circuits related to cognition. Finally, interneuron-based therapeutics have shown great potential in alleviating the burden of neurological disease. For the first time, we show that these cells can properly integrate into the damaged brain which bodes well for potential therapeutic applications not only after TBI, but a host of other neurological diseases.

APPENDIX A

Modeling traumatic brain injury using controlled cortical impact injury

Abstract

Traumatic brain injury (TBI) occurs when an external mechanical force damages the brain. Controlled cortical impact (CCI) is an experimental neurotrauma model that has been widely used to produce graded, reproducible injuries in animals that mimic important histological, physiological and behavioral aspects of closed-head TBI seen clinically. CCI takes advantage of an electronically controlled pneumatic piston to deliver a precise contusion injury to neocortex. Here, we describe a step-by-step protocol for performing CCI in mice. Expected histological outcomes of injury as well as strengths and limitations of the model are also discussed.

Introduction

Traumatic brain injury (TBI) afflicts nearly 6 million Americans (National Institute of Neurological Disorders and Stroke, 2015). It is a serious neurological disorder that occurs after an external mechanical force damages the brain (e.g., from a bump, blow, or jolt to the head). Trauma substantially increases the risk for a variety of physical, cognitive, emotional, social and psychiatric health problems, and it is one of the most common causes of drug-resistant epilepsy in humans (Faul and Coronado, 2015; Frey, 2003; Herman, 2002; Rao and Lyketsos, 2000; Scholten *et al.*, 2015). Despite the prevalence of TBI, there are no effective therapies for brain trauma. A number of animal models have been developed to investigate basic mechanisms of TBI, injury dynamics and to test new therapies. Here, we describe a protocol for performing controlled cortical impact (CCI) injury in mice, a widely used experimental model of closed head injury. We routinely use CCI to study injury-related synaptic reorganization in the hippocampus, and we recently adapted the model to investigate neural circuit mechanisms of post-traumatic epilepsy (Hunt *et al.*, 2012; Hunt *et al.*, 2009; 2010; 2011). CCI uses an electronically controlled pneumatic (or electromagnetic) impactor to deliver a precise, focal contusion injury to the brain surface. Initially described in ferrets (Lighthall, 1988), the CCI device has since been adapted for use in rats (Dixon *et al.*, 1991), mice (Smith *et al.*, 1995), sheep (Anderson *et al.*, 2003), pigs (Alessandri et al., 2003), and non-human primates (King *et al.*, 2010). The CCI injury device described here (TBI-0310, **Fig. A.1**) uses a small bore, double acting stroke-constrained steel pneumatic cylinder. The impactor is mounted vertically on a crossbar perpendicular to the brain surface (though the animal can be angled in the stereotactic device). A removable impactor tip (3-5 mm, with either a flat or rounded edge) is attached to the end of the lower rod, and the upper rod is attached to a sensor system that detects impactor velocity. The impactor tip is pneumatically-driven by a control unit to compress brain tissue at a user-selected velocity, dwell time (i.e., the amount of time the cortical tissue remains depressed) and depth. Our laboratory typically uses a target velocity of 3.5 m/s, dwell time of 400-500 ms and injury depths of 0.5 mm (moderate injury) to 1 mm (severe injury).

Materials

Reagents

- Adult, 6-8 wk old CD-1 mice weighing approx. 30g on the day of surgery (Charles River Laboratories, cat. no. 022)
- Isoflurane (Western Medical, cat. no. 7263)
- Buprenex (Buprenorphine hydrochloride; Western Medical, cat. no. 7292)
- Ketaset (Ketamine hydrochloride; Western Medical, cat. no. 565)
- Anased (Xylazine hydrochloride; Western Medical, cat. no. 5530)
- Oxygen gas (100%, Airgas, cat. no. OX USP200)
- Betadine surgical scrub (Fisher, cat. no. 19-027132)

- Puralube vet ointment (Fisher, cat. no. NC0138063)
- Cotton-tipped applicators (Fisher, cat. no. 23-400-115)
- SILK 6/0 C-3 18″ sutures (CP Medical Sutures, cat. no. 667S)
- Surgicel absorbable hemostat (Ethicon, cat. no. ETH1951)
- Ethanol (use as 70% v/v)

Equipment

- Head Impactor (Precision Systems Inc., cat. no. TBI0310)
- Jun-Air 3-4 air compressor (Precision Systems Inc., supplied with TBI-0310)
- Small Animal Stereotaxic U-Frame Assembly (David Kopf Instruments, Model 900R-B)
- Universal Clamp (David Kopf Instruments, Model 925- A-C)
- Mouse Gas Anesthesia Head Holder (David Kopf Instruments, Model 923-B)
- Mouse Non-Rupture 60 Degree Tip Ear Bars (David Kopf Instruments, Model 922)
- Dumont SS Forceps - Standard Tips/Straight/13.5cm (Fine Science Tools, cat. no. 11203-23)
- Student Fine Scissors - Straight/11.5cm (Fine Science Tools, cat. no. 91460-11)
- Graefe Forceps - Serrated/Straight/10cm (Fine Science Tools, cat. no. 11050-10)
- Halsey Needle Holder - Straight/Serrated/13cm/with Lock (Fine Science Tools, cat. no. 12501-13)
- Ideal micro drill (CellPoint Scientific, cat. no. CP67- 1200)
- Burrs for Micro Drill - 0.5mm Tip Diameter/Carbon Steel (Fine Science Tools, cat. no. 19007-05)
- Compact mini rodent anesthesia machine (DRE Veterinary, cat. no. 9280)
- Passive scavenging hose, 19 mm Blue Corr-A-Flex II Circuit Hose (DRE Veterinary, cat no. 12384)

- Oster™ Animal Clippers (Fisher Scientific, cat. no. 01- 305-10)

Procedures

Assembling the device

Assemble the PSI TBI-0310 Head Impactor and connect the Jun-Air compressor and DRE anesthesia machine according to the manufacturer instructions. Two impactor tips are supplied by PSI; one 3 mm beveled (flat) tip and one 5 mm rounded tip. We typically use the beveled impactor tip in our studies, because we have found that it produces more consistent hippocampal damage and epilepsy in mice (Hunt *et al.*, 2012; Hunt *et al.*, 2009). The KOPF 900 small animal stereotactic U-frame is attached to the stand post (1 cm diameter) with the KOPF model 925 swivel mount.

Preparation of the CCI device

1. Turn on the air compressor to pressurize the CCI device (**Fig A.1a**). The compressor tank gauge should display between 90-110 PSI of pressure while the outflow gauge should display approximately 80 PSI of pressure.
2. Turn on the control box.
3. Prior to surgery, it is necessary to calibrate and test the CCI device to confirm that it produces the desired impact velocity and dwell time. This can be accomplished by following the step-by-step procedures on the control box.

Surgery

4. All procedures must be approved by and comply with Institutional Animal Care and Use Committee (IACUC) regulations and should be performed using aseptic techniques. Record all surgical and procedural items on Form 1 or a similar form (see Form 1).

5. To induce anesthesia, place a mouse into a vented induction chamber supplied with 2-4% isoflurane for 60s. ALTERNATE APPROACH: An injection of ketamine/xylazine (80-100 Ketamine + 5 - 10 Xylazine; mg/kg) delivered IP may be used in place of isoflurane gas anesthesia. Record the pre-operative body weight.

6. Ensure the mouse is deeply anesthetized by a suppression of a toe-pinch response.

7. Shave the scalp using scissors or an electronic hair clipper.

8. Secure the mouse into the stereotactic frame and insert the ear bars. Supply 2-4% isoflurane through KOPF Model 923-B mouse gas anesthesia head holder. Adjust the inspired concentration of isoflurane as necessary, and ensure suppression of a toe-pinch response.

9. Administer a preemptive injection of buprenorphine (0.05mg/kg, IP) prior to initiating surgery.

10. Apply Puralube ointment to eyes, to keep eyes moist during the procedure.

11. Apply Betadine surgical scrub to the scalp using a sterile cotton swab.

12. Make an approx. 1 inch midline incision to the scalp. Reflect the skin and clean skull with sterile cotton swab (**Fig A.2a**). ALTERNATE APPROACH: The skin on either side of the incision can be retracted using hemostat forceps.

13. Make a 4-5mm craniotomy centered between lambda and bregma, ~1mm lateral to the sagittal suture using the hand-held Ideal micro drill with a 0.6mm round carbide drill bit (**Fig A.2b**). This is achieved by lightly scoring the surface of the skull to produce the circular craniotomy. It is critical not to penetrate the skull with the drill, as this could damage the underlying dura mater and/or brain.

14. Using fine micro-dissection forceps, carefully remove the bone flap from the craniotomy (**Fig A.2c**). If necessary, the craniotomy can be enlarged further to ensure sufficient clearance for the impactor tip by carefully drilling along the edge of the craniotomy. Make sure not to damage the dura mater. This procedure should not result in bleeding at the craniotomy site.

Delivering contusion injury

15. Adjust the position of the head in the frame to achieve skull-flat; i.e., lambda and bregma should be approximately level.

16. Select "Experiment" on the electronic control unit and choose the desired experimental parameters. Our laboratory typically uses a velocity of 3.5m/s, dwell time of 400-500ms and injury depths of 0.5 mm (moderate injury) to 1 mm (severe injury).

17. Follow the instruction on the control box to zero the impactor tip to the cortical surface. Use the X and Y control wheels on the base of the impactor to move the animal into position and align the impactor tip directly above the area to be impacted.

18. Initiate the cortical impact by pressing the "Impact" button.

19. A sterile cotton swab can be used to control any bleeding that may occur immediately following impact.

20. Apply Surgicel to the dorsal surface of the brain, and close the incision using 6-0 silk sutures. ALTERNATE APPROACH: A circular plastic disk (cranioplasty) can be glued to the skull, covering the craniotomy site.

21. Remove the mouse from the stereotactic frame and return to a clean holding cage for recovery. Animals should be monitored until evidence of withdrawal reflex after foot pinch and righting reflex can be observed. Mice may occasionally experience seizures during the first couple hours after severe trauma (Hunt et al., 2009).

22. Animals should be closely monitored for recovery, signs and symptoms of pain and distress or other adverse effects after surgery. A post-operative injection of buprenorphine (0.05mg/kg, IP) should be administered within 24hr after surgery. Skin sutures should be removed within 14d of surgery. We perform a qualitative postoperative health assessment each day for the first 5d after surgery and periodically thereafter. Record all findings on Form 2 or a similar form. (See Form 2). Animals normally recover from the CCI procedure without complication and remain otherwise healthy.

Expected outcomes

CCI produces a graded morphological and histological injury response, but craniotomy in the absence of injury does not produce an overt cortical lesion (Fig. 2). In hippocampus, cell death peaks around 48hr after CCI and 5 is nearly complete by seven days following injury (Baldwin *et al.*, 1997; Hall *et al.*, 2005b; Kaya et al., 1999). In mice, impact depths of 0.5 mm typically produce "moderate" injuries that include a cortical cavity generally restricted to the neocortex, and depths of 1.0 mm produce "severe" injuries extending through the thickness of the neocortex and occasionally impinge upon hippocampus (Saatman (Hunt *et al.*, 2012; Hunt *et al.*, 2009; Saatman *et al.*, 2006). Often, very severe injuries also include distortion of the principal cell layers in hippocampus (Fig. A.2). In addition, mice develop axon sprouting in CA1 of hippocampus (Norris and Scheff, 2009) and dentate gyrus (Hunt *et al.*, 2012; Hunt *et al.*, 2009; 2010; 2011; Semple *et al.*, 2017) within weeks following injury. Sprouting is more robust following 1.0 mm impact depths as compared to more moderate injuries (Hunt *et al.*, 2009). Many laboratories routinely use a battery of neurobehavioral assays to evaluate neurological function after CCI and to test preclinical therapies. Injured mice exhibit gross motor impairments during the first week after injury that typically recover to sham-control levels within two weeks of injury, though some fine motor deficits may persist (Fox et al., 1999). Cognitive deficits are also observed shortly after CCI and are long lasting (Hamm et al., 1996; Scheff et al., 1997). In our hands, approximately 15% of mice will experience behavioral seizures within 2 hrs after CCI injury of 1.0 mm depth, and spontaneous seizures are observed in at least 40% of the animals within 10 weeks following injury (Hunt *et al.*, 2009).

Advantages and limitations

An advantage of CCI is the high degree of precision that can be achieved over injury dynamics. Injury severity is primarily managed by adjusting the depth of tissue compression and impactor tip shape and size (Mao *et al.*, 2010a; Mao *et al.*, 2010b; Pleasant *et al.*, 2011), but other external injury parameters can also be controlled with precision, such as impact velocity, dwell time, number of impacts, and number of craniotomies. The ability to produce accurate, reproducible contusion injuries relies on appropriate calibration of the device and precisely zeroing the impactor tip to the cortical surface using the provided contact sensor. The use of a stereotactic frame allows one to choose whether the tip is perpendicular or angled with respect to the injury site. CCI is a model of focal, closed-head contusion injury. However, histopathology following neurotrauma is not exclusive to the site of injury (Hall *et al.*, 2005b), and there is likely a diffuse component to the injury (Hall *et al.*, 2008). Although injury is delivered through a craniotomy, it is considered a “closed-head” and not “penetrating” injury, because the dura remains intact. The presence of a craniotomy likely alters injury-related changes in intracranial pressure following TBI (Zweckberger et al., 2003); this concern can be somewhat alleviated by attaching a cranioplasty over the craniotomy after impact. Alternatives to single unilateral CCI in adult mice include recent adaptations of the model for use in juvenile mice (i.e., at P21; (Semple *et al.*, 2017), repeated mild injuries (Bolton Hall et al., 2016) and multifocal injuries (Vonder Haar et al., 2013). In all, these features allow for good control over biomechanical parameters in order to generate relatively consistent and reproducible focal injuries that can be adapted for use in a variety of animal species and developmental ages.

Acknowledgements

This work was supported by funding from the National Institutes of Health grants R01– NS096012 and T32– NS082174.

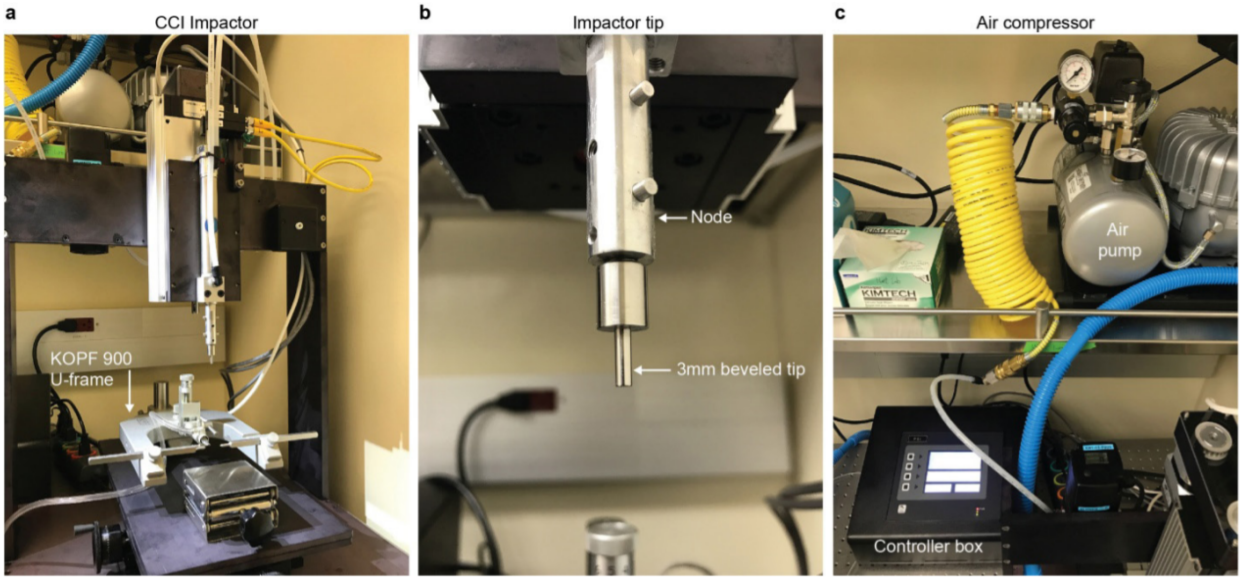

Figure A.1. PSI TBI-0310 controlled cortical impact injury device. The PSI TBI-0310 CCI injury device equipped with KOPF Model 900R-B frame with Model 923-B Mouse Gas Anesthesia Head Holder and Model 922 Non-Rupture 60 Degree Tip Ear Bars. a. CCI impactor. b. Image showing the 3mm beveled impactor tip attached to the node. c. Top, Jun-Air air compressor. Bottom, electronic controller box used to control the injury device.

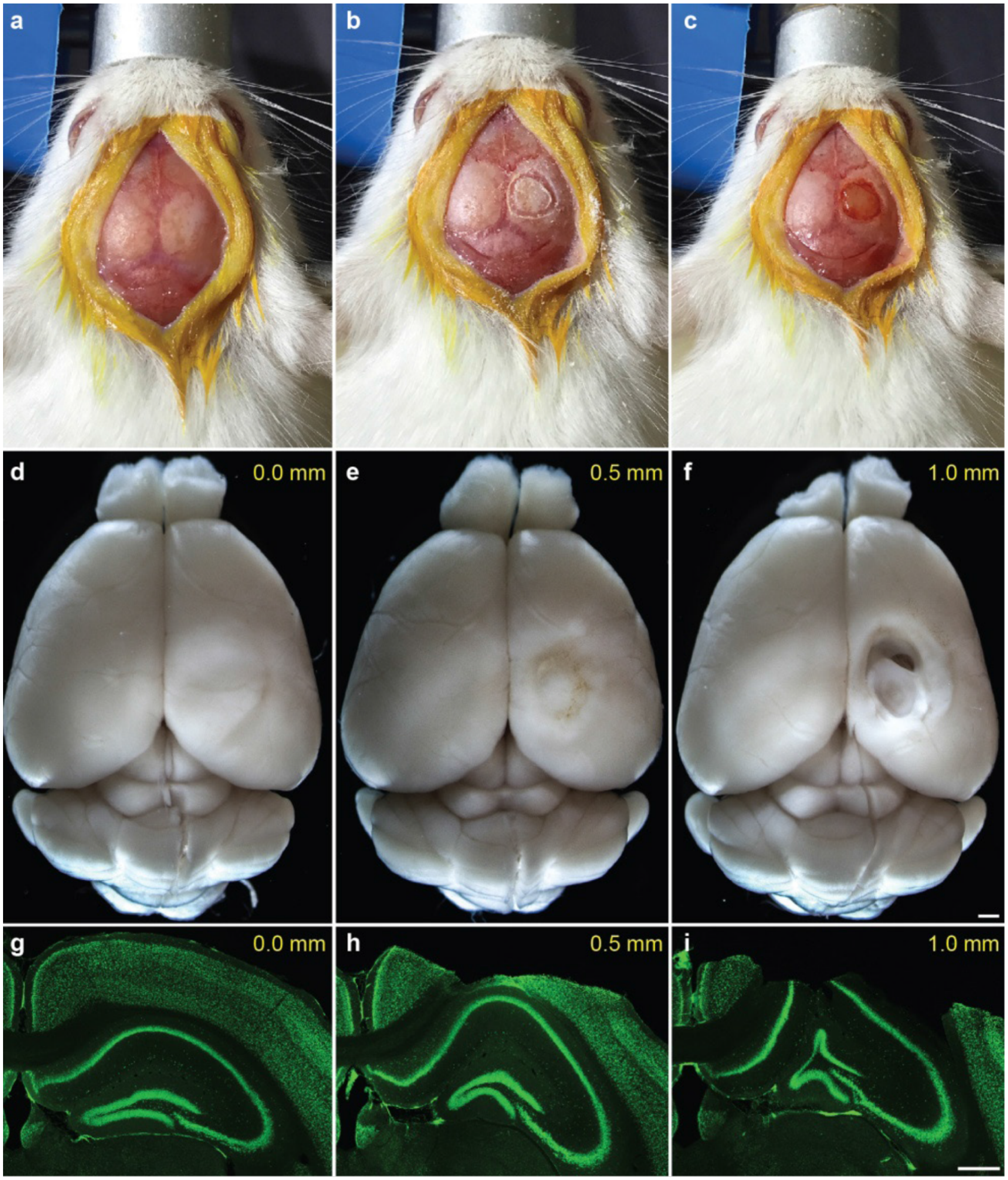

Figure A.2. Graded injury after controlled cortical impact. CCI can be used to deliver graded, reproducible injuries. a Mouse in Model 900R-B small animal Stereotaxic U-Frame. The mouse's nose is placed in the Model 923-B mouse gas anesthesia head holder. The head is held in position by Model 922 non-rupture 60 degree tip ear bars, and the skin cleaned with surgical scrub prior to making the incision. b. A 4-5 mm craniotomy is made over the right somatosensory neocortex approximately halfway between bregma (B) and lambda (l). c. Skull cap is carefully removed, leaving the underlying dura intact. d-f. Whole-brain images 30 days following CCI injury in a sham injured control mouse, 0.0 mm (d), moderate 0.5 mm (e) and severe 1.0 mm (f) impact. g-i. NeuN immunostaining (green) 30 days following sham (g), 0.5 mm injury (h) and 1.0 mm injury (i). Cavitation into the underlying hippocampus and distortion of hippocampal principal layers is common following 1.0 mm injuries. Scale bars: 250 um.

APPENDIX B

Modified iDISCO and Reverse Clearing Protocols

The iDISCO+ protocol (Renier et al., 2016) can clear whole mouse brains with isotropic shrinkage and is compatible with antibody labeling. However, antibody penetration is poor. Immunolabeling intensity rapidly decreases in deep neocortex and subcortical structures if brains are not halved prior to starting the protocol. Here, I incorporated additional steps to enhance antibody penetration and improve decolorization based on the SHANEL protocol (Zhao et al., 2020). Changes to the original protocol include:

1. Decolorization and permeabilization with CHAPS to remove residual blood which absorbs light.
2. Loosening extracellular matrix with guanidine hydrochloride.
3. Permeabilization with CHAPS before antibody incubation
4. Adding CHAPS to primary and secondary diluent for greater antibody penetration.
5. Multiple DBE incubations for improved refractive index (RI) matching.

Materials

Abbreviated Name	Full Name	Supplier / Cat. No.
CHAPS	3-[(3-Cholamidopropyl) dimethylammonio]-1-propanesulfonate	Anatrace / C316
NMDEA	N-Methyldiethanolamine	Sigma / 471828
Guanidine HCL	Carbamimidoylazanium chloride	Alfa Aesar / A13543
Heparin	Heparin sodium	Serva / 24590.01
10X PBS	Phosphate-Buffered Saline	Gibco / 70011044
NDS	Normal Donkey Serum	Fisher / 50413115
Tween-20	Polyoxyethylene (20) sorbitan monolaurate	Fisher / BP337
Triton X-100	2-[4-(2,4,4-trimethylpentan-2-yl) phenoxy]ethanol	Sigma / T9284
Na_3N	Sodium Azide	Sigma / S2002
H_2O_2	Hydrogen Peroxide	Sigma / 216763
MeOH	Methanol	Fisher / AC268280010
DCM	Dichloromethane	Sigma / 270997-12X100mL
DBE	Dibenzyl ether	Sigma / 108014
DMSO	Dimethyl sulfoxide	Sigma / M81802

Solutions:

10% CHAPS/ 25% NMDEA Permeabilization / Decolorization Solution (10mL)

- 1 g CHAPS
- 2.5 mL MDEA
- 20 µL10% Na_3N

Complete to 10 mL 1X PBS

4M Guanidine Solution (10mL)

- 3.82 g Guanidine HCL
- 0.1 g CHAPS

Complete to 10 mL 1X PBS

PTx.2 (1L)

- 100 mL 10X PBS
- 2 mL Triton-X
- 2 mL 10% Na3N

Complete to 1L with dH20

PTwH (1L)

- 100 mL 10X PBS
- 2 mL Tween-20
- 1 mL 10mg/mL Heparin
- 2 mL 10% Na3N

Complete to 1 L with dH20

PBS w/ Heparin

- 100 mL 10X PBS (1M)
- 1 mL 10 mg/mL Heparin

Complete to 1 L with dH20

5% H2O2 in 80% MeOH (30mL)

- 5 mL 30% H2O2
- 25 mL 100% Methanol

Blocking Solution (50 mL)

- 3 mL NDS
- 5 mL DMSO

Complete to 50 mL with PTx.2

Antibody Diluent (50 mL)

- 1.5 mL NDS
- 0.125 g CHAPS

Complete to 50 mL with PTwH

Notes:

- All steps are performed in 5mL Eppendorf centrifuge tubes (Eppendorf cat. no. 0030119401). The same tube can be used until refractive index matching in DBE, where a fresh tube should be used after the first DBE change.

- When labeling your samples, write in the inside (sticky side) of a piece of lab tape. Many of the solutions used will dissolve ink, so this prevents your labels from disappearing.
- Solutions containing DCM will cause brains to float to the top of the tube. Since the tubes cannot be filled completely, if brains are shaken with the tubes horizontally, they will be repeatedly exposed to air. This can be prevented by lifting the tapered end of the tube slightly so that the air bubble is trapped in the narrow part of the tube.
- Wherever nutation is specified, do not shake instead. Nutation involves inversion of the tube.
- Solutions containing DCM should be handled in a fume hood with proper PPE.
- DBE is not volatile and can be used on a bench, but it is very difficult to clean up if spilled. 100% ethanol spray can be used to clean spills.
- Peroxide in methanol will bleach skin, wear PPE when handling.
- CHAPS is compatible with anti-DsRed Polyclonal Antibody (Takara cat. no 632496) and anti-GFP (Aves cat. no. GFP-1020). However, we have not tested it with other antibodies. Test your antibodies in tissue sections with the antibody diluent containing CHAPS before starting the protocol. CHAPS concentration may need to be changed on a case-by-case basis.
- Our room temperature is 23C

Perfusion (0d)

1. Transcardially perfuse with freshly made PBS w/ heparin (~25mL)
    - Heparin improves perfusion by reducing clotting and improves staining specificity
    - Once perfusate runs clear, switch to 4% PFA (~25mL)
2. Postfix overnight at 4C in 4% PFA in PBS

Permeabilization/Decolorization (+1d)

3. Dispose PFA in hazardous waste and wash samples in PBS for 10 min to remove residual PFA
4. Incubate brains in CHAPS/MDEA solution w/ nutation at 37C for 48h
    - Both CHAPS and MDEA are light sensitive, wrap the tubes in foil
    - Solution will turn green after 48h; this is the reaction of MDEA with heme

Wash (+3d)

5. Wash with PBS, five solution changes then overnight at room temp w/ 115RPM shaking

1st Dehydration and Delipidation (+4d)

All steps at room temperature w/ 115RPM shaking

6. 20% MeOH in dH_20; 1h
7. 40% MeOH in dH_20; 1h
8. 60% MeOH in dH_20; 1h
9. 80% MeOH in dH_20; 1h
10. 100% MeOH; 1h
11. 100% MeOH; 1h
12. 66% DCM / 33% MeOH; overnight

Peroxide Bleaching (+5d)

Steps 12 & 13 at room temperature w/ 115RPM shaking

13. 100% MeOH; 4h
14. 100% MeOH; 4h

15. 5% H_2O_2 in 80% MeOH; 4C in fridge, no shaking

Rehydration and extracellular matrix treatment with guanidine (+6d)

Steps 15 - 20 at room temperature w/ 115RPM shaking

16. 60% MeOH in dH_20; 1h
17. 40% MeOH in dH_20; 1h
18. 20% MeOH in dH_20; 1h
19. PTx.2; 1h
20. 4M guanidine wash; 24h at room temperature w/ 115RPM shaking
    - After guanidine wash, brains will appear swollen and almost clear. They will shrink and turn opaque after PBS washing.

Wash (+7d)

21. 3X PBS washes; leave overnight

Permeabilization (+8d)

22. Incubate brains in CHAPS/MDEA solution w/ nutation at 37C overnight

Blocking (+9d)

23. Incubate brains in blocking solution w/ nutation at 37C overnight

Primary Staining (+10d)

24. Incubate brains in antibody diluent containing primary antibody for 7d at 37C with nutation
    - Wrap samples in foil, CHAPS is light-sensitive

Wash (+17d)

25. 5X washes over 24h in PTwH

Secondary Staining (+18d)

26. Incubate brains in antibody diluent containing secondary antibody for 7d at 37C with nutation
    - 0.2um syringe filter diluent after adding secondary antibody and dispense into a clean centrifuge tube to reduce secondary antibody aggregates
    - Wrap in foil, CHAPS is light-sensitive

Wash (+25d)

27. 5X washes over 24h in PTwH

Dehydration (+26d)

Steps 27-32 at room temperature w/ 115RPM shaking

28. 20% MeOH in dH_20; 1h
29. 40% MeOH in dH_20; 1h
30. 60% MeOH in dH_20; 1h
31. 80% MeOH in dH_20; 1h
32. 100% MeOH; 1h
33. 100% MeOH; 1h
34. 100% MeOH; o/n @ 4C, no shaking

Clearing (+27d)

35. 2:1 DCM/MeOH wash w/ shaking @ RT; 3h

36. DCM wash w/ shaking @ RT; 15 min
37. DCM wash w/ shaking @ RT; 15 min
38. 5X DBE changes over 48h, leave o/n @ 4C
    - Multiple DBE changes are required for proper refractive index matching. The first DBE wash can be done in the same tube used for the protocol but use a fresh tube after that. Residual DCM will affect refractive index matching.
    - Samples are RI matched once the edges of the sample are not visible. However, multiple DBE washes are required for complete RI matching. When tissue is placed into a fresh DBE solution, there should be no fluid turbulence visible, and the edges of the tissue should not be visible. This may take two overnight incubations to complete.
    - Use the <u>same</u> DBE used for RI matching to fill the imaging chamber.
    - Wash solutions containing DCM, which cause brains to float to the top of the tube. Air bubbles can get caught in the ventricles if brains are exposed to air. If air bubbles are present after DBE incubation, they can be removed by centrifugation at 500g for 10 min. This can be repeated until bubbles are gone.

Reverse Clearing

Cleared samples can be rehydrated and sectioned to perform traditional immunohistochemistry. We have found rehydrated tissue to be compatible will all antibodies we have tested including NeuN, ChAT, Reelin, and DsRed.

Notes:

- Rehydrated tissue sections are more hydrophobic than typical PFA-fixed tissue. If rehydrated tissue is placed into PBS without detergent, it will float to the top of the solution.

- Vibratome sectioning should be performed using PBS containing 0.05% Triton-X and cutting speed should be reduced by ~50% of typical speed used for PFA-fixed tissue.
- We have not tried cryostat sectioning rehydrated tissue, however it is likely to be challenging due to the sticky nature of rehydrated tissue
- When mounting tissue onto charged slides, use PBS containing 0.05% Triton-X, otherwise the tissue will adhere to the glass and is prone to tearing.

Protocol

1. Remove cleared tissue from DBE and place into a clean tube containing 100% DCM, wash for 15 min with shaking. Samples will turn opaque.
2. Wash in fresh DCM; 15 min with shaking
3. Overnight wash in 2:1 DCM/MeOH at room temperature with shaking
1. All subsequent washes are 1h with 115 RPM shaking
4. 100% MeOH; 1h
5. 80% MeOH in dH20; 1h
6. 60% MeOH in dH20; 1h
7. 40% MeOH in dH20; 1h
8. 20% MeOH in dH20; 1h
9. 0.1M PBS; 1h
10. Samples can be stored at 4C in 0.1M PBS containing sodium azide

APPENDIX C

Interneuron loss in Chd2$^{+/-}$ mice

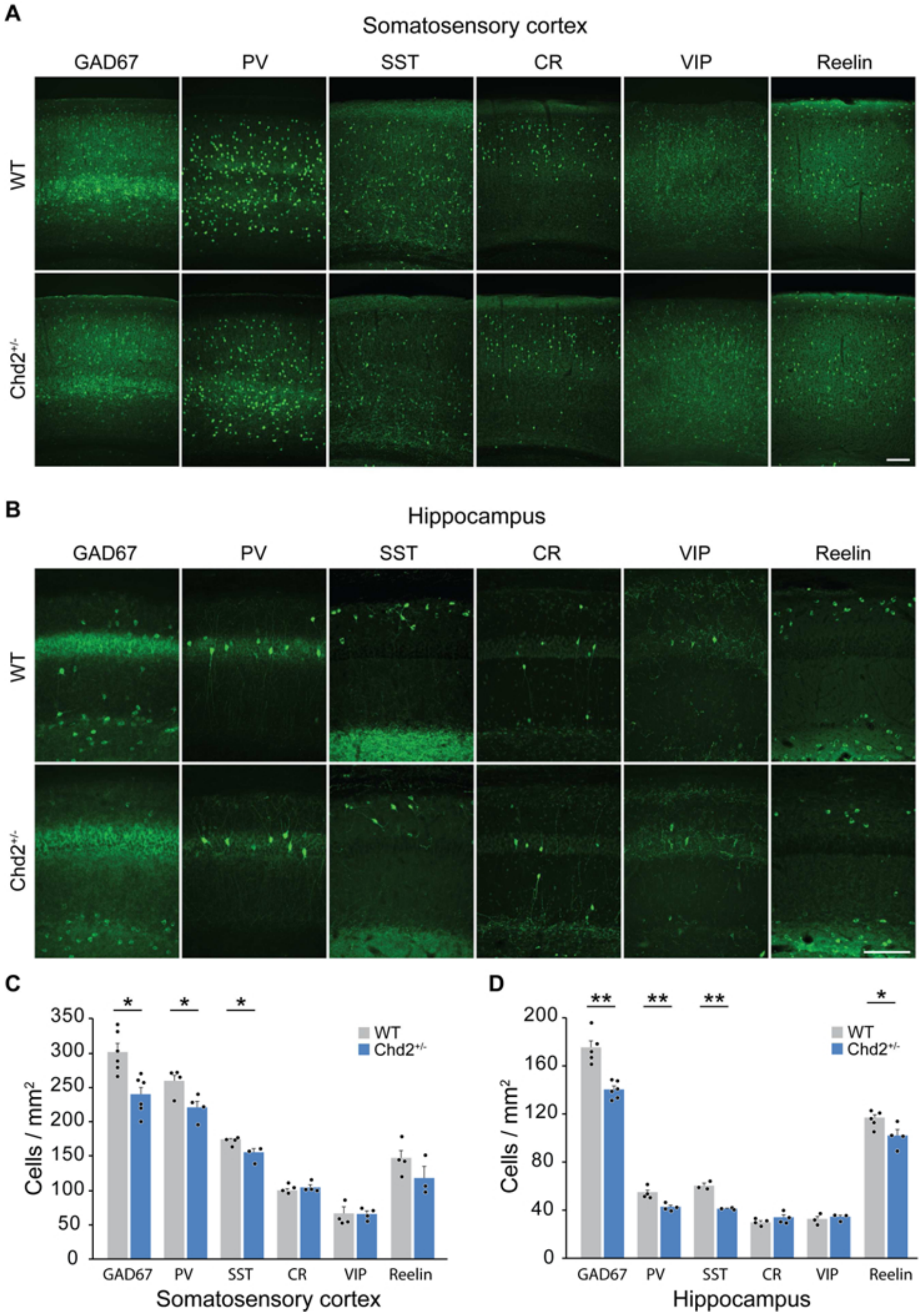

C.1 Chd2+/− mice exhibit decreased density of GABAergic interneurons. A, B. Immunostaining of coronal sections through somatosensory neocortex (A) and CA1 region of hippocampus (B) for GAD67, PV, SST, CR, VIP and reelin at P30. C, D. Quantification of each subtype marker shows Chd2+/− mice had decreased density of cells expressing GAD67, PV and SST in somatosensory cortex (C) and decreased density of cells expressing GAD67 PV, SST and reeling in hippocampus (D) compared to WT littermates (n=3–6 mice per genotype). Error bars, s.e.m.; ∗ $p < 0.05$. ∗∗ $p < 0.01$; scale bars, 150 μm in A and B.

REFERENCES

Abbas, A.I., Sundiang, M.J.M., Henoch, B., Morton, M.P., Bolkan, S.S., Park, A.J., Harris, A.Z., Kellendonk, C., and Gordon, J.A. (2018). Somatostatin Interneurons Facilitate Hippocampal-Prefrontal Synchrony and Prefrontal Spatial Encoding. Neuron *100*, 926-939.e923. 10.1016/j.neuron.2018.09.029.

Acsády, L., Kamondi, A., Sík, A., Freund, T., and Buzsáki, G. (1998). GABAergic cells are the major postsynaptic targets of mossy fibers in the rat hippocampus. J Neurosci *18*, 3386-3403.

Adelson, P.D., Fellows-Mayle, W., Kochanek, P.M., and Dixon, C.E. (2013). Morris water maze function and histologic characterization of two age-at-injury experimental models of controlled cortical impact in the immature rat. Childs Nerv Syst *29*, 43-53. 10.1007/s00381-012-1932-4.

Adesnik, H., Bruns, W., Taniguchi, H., Huang, Z.J., and Scanziani, M. (2012). A neural circuit for spatial summation in visual cortex. Nature *490*, 226-231. 10.1038/nature11526.

Aggleton, J., and Brown, M. (1999). Episodic memory, amnesia, and the hippocampal-anterior thalamic axis. Behavioral and Brain Sciences *22*, 425-444.

Aggleton, J.P., Hunt, P.R., Nagle, S., and Neave, N. (1996). The effects of selective lesions within the anterior thalamic nuclei on spatial memory in the rat. Behav Brain Res *81*, 189-198. 10.1016/s0166-4328(96)89080-2.

Ährlund-Richter, S., Xuan, Y., van Lunteren, J.A., Kim, H., Ortiz, C., Pollak Dorocic, I., Meletis, K., and Carlén, M. (2019). A whole-brain atlas of monosynaptic input targeting four different cell types in the medial prefrontal cortex of the mouse. Nat Neurosci *22*, 657-668. 10.1038/s41593-019-0354-y.

Albertini, A.A., Ruigrok, R.W., and Blondel, D. (2011). Rabies virus transcription and replication. Adv Virus Res *79*, 1-22. 10.1016/B978-0-12-387040-7.00001-9.

Albisetti, G.W., Ghanem, A., Foster, E., Conzelmann, K.K., Zeilhofer, H.U., and Wildner, H. (2017). Identification of Two Classes of Somatosensory Neurons That Display Resistance to Retrograde Infection by Rabies Virus. J Neurosci *37*, 10358-10371. 10.1523/JNEUROSCI.1277-17.2017.

Alessandri, B., Heimann, A., Filippi, R., Kopacz, L., and Kempski, O. (2003). Moderate controlled cortical contusion in pigs: effects on multi-parametric neuromonitoring and clinical relevance. J Neurotrauma *20*, 1293-1305. 10.1089/089771503322686094.

Alexander, M.P. (1995). Mild traumatic brain injury: pathophysiology, natural history, and clinical management. Neurology *45*, 1253-1260. 10.1212/wnl.45.7.1253.

Alitto, H.J., and Usrey, W.M. (2004). Influence of contrast on orientation and temporal frequency tuning in ferret primary visual cortex. J Neurophysiol *91*, 2797-2808. 10.1152/jn.00943.2003.

Allan, S.M., and Rothwell, N.J. (2001). Cytokines and acute neurodegeneration. Nat Rev Neurosci *2*, 734-744. 10.1038/35094583.

Allen, G.V., Saper, C.B., Hurley, K.M., and Cechetto, D.F. (1991). Organization of visceral and limbic connections in the insular cortex of the rat. J Comp Neurol *311*, 1-16. 10.1002/cne.903110102.

Almeida-Suhett, C.P., Prager, E.M., Pidoplichko, V., Figueiredo, T.H., Marini, A.M., Li, Z., Eiden, L.E., and Braga, M.F. (2014). Reduced GABAergic inhibition in the basolateral amygdala and the development of anxiety-like behaviors after mild traumatic brain injury. PLoS One *9*, e102627. 10.1371/journal.pone.0102627.

Almeida-Suhett, C.P., Prager, E.M., Pidoplichko, V., Figueiredo, T.H., Marini, A.M., Li, Z., Eiden, L.E., and Braga, M.F. (2015). GABAergic interneuronal loss and reduced inhibitory synaptic transmission in the hippocampal CA1 region after mild traumatic brain injury. Exp Neurol *273*, 11-23. 10.1016/j.expneurol.2015.07.028.

Alvarez-Dolado, M., Calcagnotto, M.E., Karkar, K.M., Southwell, D.G., Jones-Davis, D.M., Estrada, R.C., Rubenstein, J.L., Alvarez-Buylla, A., and Baraban, S.C. (2006). Cortical inhibition modified by embryonic neural precursors grafted into the postnatal brain. J Neurosci *26*, 7380-7389. 10.1523/JNEUROSCI.1540-06.2006.

Amaral, D.G. (1978). A Golgi study of cell types in the hilar region of the hippocampus in the rat. J Comp Neurol *182*, 851-914. 10.1002/cne.901820508.

Amaral, D.G., Insausti, R., and Campbell, M.J. (1988). Distribution of somatostatin immunoreactivity in the human dentate gyrus. J Neurosci *8*, 3306-3316.

Amaral, D.G., Scharfman, H.E., and Lavenex, P. (2007). The dentate gyrus: fundamental neuroanatomical organization (dentate gyrus for dummies). Prog Brain Res *163*, 3-22. 10.1016/S0079-6123(07)63001-5.

Andersen, P., Bliss, T.V., Lomo, T., Olsen, L.I., and Skrede, K.K. (1969). Lamellar organization of hippocampal excitatory pathways. Acta Physiol Scand *76*, 4A-5A. 10.1111/j.1748-1716.1969.tb04499.x.

Andersen, P., Holmqvist, B., and Voorhoeve, P.E. (1966). Entorhinal activation of dentate granule cells. Acta Physiol Scand *66*, 448-460. 10.1111/j.1748-1716.1966.tb03223.x.

Anderson, K.J., Miller, K.M., Fugaccia, I., and Scheff, S.W. (2005). Regional distribution of fluoro-jade B staining in the hippocampus following traumatic brain injury. Exp Neurol *193*, 125-130. 10.1016/j.expneurol.2004.11.025.

Anderson, R.W., Brown, C.J., Blumbergs, P.C., McLean, A.J., and Jones, N.R. (2003). Impact mechanics and axonal injury in a sheep model. J Neurotrauma *20*, 961-974. 10.1089/089771503770195812.

Anderson, S.A., Eisenstat, D.D., Shi, L., and Rubenstein, J.L. (1997). Interneuron migration from basal forebrain to neocortex: dependence on Dlx genes. Science *278*, 474-476. 10.1126/science.278.5337.474.

Anderson, S.A., Marín, O., Horn, C., Jennings, K., and Rubenstein, J.L. (2001). Distinct cortical migrations from the medial and lateral ganglionic eminences. Development *128*, 353-363.

Annegers, J.F., and Coan, S.P. (2000). The risks of epilepsy after traumatic brain injury. Seizure *9*, 453-457. 10.1053/seiz.2000.0458.

Armstrong, R.A. (2018). Visual problems associated with traumatic brain injury. Clin Exp Optom *101*, 716-726. 10.1111/cxo.12670.
Arneson, D., Zhang, G., Ying, Z., Zhuang, Y., Byun, H.R., Ahn, I.S., Gomez-Pinilla, F., and Yang, X. (2018). Single cell molecular alterations reveal target cells and pathways of concussive brain injury. Nat Commun *9*, 3894. 10.1038/s41467-018-06222-0.

Ascoli, G.A., Alonso-Nanclares, L., Anderson, S.A., Barrionuevo, G., Benavides-Piccione, R., Burkhalter, A., Buzsáki, G., Cauli, B., Defelipe, J., Fairén, A., et al. (2008). Petilla terminology: nomenclature of features of GABAergic interneurons of the cerebral cortex. Nat Rev Neurosci *9*, 557-568. 10.1038/nrn2402.

Bakst, I., Avendano, C., Morrison, J.H., and Amaral, D.G. (1986). An experimental analysis of the origins of somatostatin-like immunoreactivity in the dentate gyrus of the rat. J Neurosci *6*, 1452-1462.

Bakst, I., Morrison, J.H., and Amaral, D.G. (1985). The distribution of somatostatin-like immunoreactivity in the monkey hippocampal formation. J Comp Neurol *236*, 423-442. 10.1002/cne.902360402.

Balabanov, R., Goldman, H., Murphy, S., Pellizon, G., Owen, C., Rafols, J., and Dore-Duffy, P. (2001). Endothelial cell activation following moderate traumatic brain injury. Neurol Res *23*, 175-182. 10.1179/016164101101198514.

Baldwin, S.A., Fugaccia, I., Brown, D.R., Brown, L.V., and Scheff, S.W. (1996). Blood-brain barrier breach following cortical contusion in the rat. J Neurosurg *85*, 476-481. 10.3171/jns.1996.85.3.0476.

Baldwin, S.A., Gibson, T., Callihan, C.T., Sullivan, P.G., Palmer, E., and Scheff, S.W. (1997). Neuronal cell loss in the CA3 subfield of the hippocampus following cortical contusion utilizing the optical disector method for cell counting. J Neurotrauma *14*, 385-398. 10.1089/neu.1997.14.385.

Baraban, S.C., Southwell, D.G., Estrada, R.C., Jones, D.L., Sebe, J.Y., Alfaro-Cervello, C., García-Verdugo, J.M., Rubenstein, J.L., and Alvarez-Buylla, A. (2009). Reduction of seizures by transplantation of cortical GABAergic interneuron precursors into Kv1.1 mutant mice. Proc Natl Acad Sci U S A *106*, 15472-15477. 10.1073/pnas.0900141106.

Barbay, S., Zhang, H., Frost, S.B., Peterson, J.C., Guggenmos, D.J., Hudson, H.M., Bundy, D.T., DeJong, S.L., and Nudo, R.J. (2021). A cortical injury model in a non-human primate to assess execution of reach and grasp actions: implications for recovery after traumatic brain injury. J Neurosci Methods *361*, 109283. 10.1016/j.jneumeth.2021.109283.

Barnes, D.E., Kaup, A., Kirby, K.A., Byers, A.L., Diaz-Arrastia, R., and Yaffe, K. (2014). Traumatic brain injury and risk of dementia in older veterans. Neurology *83*, 312-319. 10.1212/WNL.0000000000000616.

Beal, M.F., Mazurek, M.F., Svendsen, C.N., Bird, E.D., and Martin, J.B. (1986). Widespread reduction of somatostatin-like immunoreactivity in the cerebral cortex in Alzheimer's disease. Ann Neurol *20*, 489-495. 10.1002/ana.410200408.

Bolkvadze, T., and Pitkänen, A. (2012). Development of post-traumatic epilepsy after controlled cortical impact and lateral fluid-percussion-induced brain injury in the mouse. J Neurotrauma *29*, 789-812. 10.1089/neu.2011.1954.
Bolton Hall, A.N., Joseph, B., Brelsfoard, J.M., and Saatman, K.E. (2016). Repeated Closed Head Injury in Mice Results in Sustained Motor and Memory Deficits and Chronic Cellular Changes. PLoS One *11*, e0159442. 10.1371/journal.pone.0159442.

Bonislawski, D.P., Schwarzbach, E.P., and Cohen, A.S. (2007). Brain injury impairs dentate gyrus inhibitory efficacy. Neurobiol Dis *25*, 163-169. 10.1016/j.nbd.2006.09.002.

Bouilleret, V., Schwaller, B., Schurmans, S., Celio, M.R., and Fritschy, J.M. (2000). Neurodegenerative and morphogenic changes in a mouse model of temporal lobe epilepsy do not depend on the expression of the calcium-binding proteins parvalbumin, calbindin, or calretinin. Neuroscience *97*, 47-58. 10.1016/s0306-4522(00)00017-8.

Boychuk, J.A., Butler, C.R., Halmos, K.C., and Smith, B.N. (2016). Enduring changes in tonic GABAA receptor signaling in dentate granule cells after controlled cortical impact brain injury in mice. Exp Neurol *277*, 178-189. 10.1016/j.expneurol.2016.01.005.

Brainard, D.H. (1997). The Psychophysics Toolbox. Spat Vis *10*, 433-436.

Brazeau, P., Vale, W., Burgus, R., Ling, N., Butcher, M., Rivier, J., and Guillemin, R. (1973). Hypothalamic polypeptide that inhibits the secretion of immunoreactive pituitary growth hormone. Science *179*, 77-79. 10.1126/science.179.4068.77.

Brownstein, M., Arimura, A., Sato, H., Schally, A.V., and Kizer, J.S. (1975). The regional distribution of somatostatin in the rat brain. Endocrinology *96*, 1456-1461. 10.1210/endo-96-6-1456.

Bráz, J.M., Sharif-Naeini, R., Vogt, D., Kriegstein, A., Alvarez-Buylla, A., Rubenstein, J.L., and Basbaum, A.I. (2012). Forebrain GABAergic neuron precursors integrate into adult spinal cord and reduce injury-induced neuropathic pain. Neuron *74*, 663-675. 10.1016/j.neuron.2012.02.033.

Buckmaster, P.S., Abrams, E., and Wen, X. (2017). Seizure frequency correlates with loss of dentate gyrus GABAergic neurons in a mouse model of temporal lobe epilepsy. J Comp Neurol *525*, 2592-2610. 10.1002/cne.24226.

Buckmaster, P.S., and Dudek, F.E. (1997). Neuron loss, granule cell axon reorganization, and functional changes in the dentate gyrus of epileptic kainate-treated rats. J Comp Neurol *385*, 385-404.

Buckmaster, P.S., and Jongen-Rêlo, A.L. (1999). Highly specific neuron loss preserves lateral inhibitory circuits in the dentate gyrus of kainate-induced epileptic rats. J Neurosci *19*, 9519-9529.

Buckmaster, P.S., Kunkel, D.D., Robbins, R.J., and Schwartzkroin, P.A. (1994). Somatostatin-immunoreactivity in the hippocampus of mouse, rat, guinea pig, and rabbit. Hippocampus *4*, 167-180. 10.1002/hipo.450040207.

Buckmaster, P.S., and Lew, F.H. (2011). Rapamycin suppresses mossy fiber sprouting but not seizure frequency in a mouse model of temporal lobe epilepsy. J Neurosci *31*, 2337-2347. 10.1523/JNEUROSCI.4852-10.2011.

Buckmaster, P.S., and Wen, X. (2011). Rapamycin suppresses axon sprouting by somatostatin interneurons in a mouse model of temporal lobe epilepsy. Epilepsia *52*, 2057-2064. 10.1111/j.1528-1167.2011.03253.x.

Buckmaster, P.S., Yamawaki, R., and Zhang, G.F. (2002). Axon arbors and synaptic connections of a vulnerable population of interneurons in the dentate gyrus in vivo. J Comp Neurol *445*, 360-373. 10.1002/cne.10183.

Bullock, R., Zauner, A., Woodward, J.J., Myseros, J., Choi, S.C., Ward, J.D., Marmarou, A., and Young, H.F. (1998). Factors affecting excitatory amino acid release following severe human head injury. J Neurosurg *89*, 507-518. 10.3171/jns.1998.89.4.0507.

Buriticá, E., Villamil, L., Guzmán, F., Escobar, M.I., García-Cairasco, N., and Pimienta, H.J. (2009). Changes in calcium-binding protein expression in human cortical contusion tissue. J Neurotrauma *26*, 2145-2155. 10.1089/neu.2009.0894.

Butler, C.R., Boychuk, J.A., and Smith, B.N. (2015). Effects of Rapamycin Treatment on Neurogenesis and Synaptic Reorganization in the Dentate Gyrus after Controlled Cortical Impact Injury in Mice. Front Syst Neurosci *9*, 163. 10.3389/fnsys.2015.00163.

Butler, C.R., Boychuk, J.A., and Smith, B.N. (2016). Differential effects of rapamycin treatment on tonic and phasic GABAergic inhibition in dentate granule cells after focal brain injury in mice. Exp Neurol *280*, 30-40. 10.1016/j.expneurol.2016.03.022.

Butler, C.R., Boychuk, J.A., and Smith, B.N. (2017). Brain Injury-Induced Synaptic Reorganization in Hilar Inhibitory Neurons Is Differentially Suppressed by Rapamycin. eNeuro *4*. 10.1523/ENEURO.0134-17.2017.

Butt, S.J., Fuccillo, M., Nery, S., Noctor, S., Kriegstein, A., Corbin, J.G., and Fishell, G. (2005). The temporal and spatial origins of cortical interneurons predict their physiological subtype. Neuron *48*, 591-604. 10.1016/j.neuron.2005.09.034.

Buzsáki, G. (2002). Theta oscillations in the hippocampus. Neuron *33*, 325-340. 10.1016/s0896-6273(02)00586-x.

Byatt, G., and Dalrymple-Alford, J.C. (1996). Both anteromedial and anteroventral thalamic lesions impair radial-maze learning in rats. Behav Neurosci *110*, 1335-1348. 10.1037//0735-7044.110.6.1335.

Cai, R., Pan, C., Ghasemigharagoz, A., Todorov, M.I., Förstera, B., Zhao, S., Bhatia, H.S., Parra-Damas, A., Mrowka, L., Theodorou, D., et al. (2019). Panoptic imaging of transparent mice reveals whole-body neuronal projections and skull-meninges connections. Nat Neurosci *22*, 317-327. 10.1038/s41593-018-0301-3.

Cajal, S.R.y. (1928). Study of traumatic degeneration in the cerebral cortex.

Callaway, E.M. (1998). Local circuits in primary visual cortex of the macaque monkey. Annu Rev Neurosci *21*, 47-74. 10.1146/annurev.neuro.21.1.47.

Cantu, D., Walker, K., Andresen, L., Taylor-Weiner, A., Hampton, D., Tesco, G., and Dulla, C.G. (2015). Traumatic Brain Injury Increases Cortical Glutamate Network Activity by Compromising GABAergic Control. Cereb Cortex *25*, 2306-2320. 10.1093/cercor/bhu041.

Carandini, M., and Ferster, D. (2000). Membrane potential and firing rate in cat primary visual cortex. J Neurosci *20*, 470-484.

Cardin, J.A., Palmer, L.A., and Contreras, D. (2007). Stimulus feature selectivity in excitatory and inhibitory neurons in primary visual cortex. J Neurosci *27*, 10333-10344. 10.1523/JNEUROSCI.1692-07.2007.

Casalia, M.L., Howard, M.A., and Baraban, S.C. (2017). Persistent seizure control in epileptic mice transplanted with gamma-aminobutyric acid progenitors. Ann Neurol *82*, 530-542. 10.1002/ana.25021.

Caveness, W.F., Meirowsky, A.M., Rish, B.L., Mohr, J.P., Kistler, J.P., Dillon, J.D., and Weiss, G.H. (1979). The nature of posttraumatic epilepsy. J Neurosurg *50*, 545-553. 10.3171/jns.1979.50.5.0545.

Cenquizca, L.A., and Swanson, L.W. (2007). Spatial organization of direct hippocampal field CA1 axonal projections to the rest of the cerebral cortex. Brain Res Rev *56*, 1-26. 10.1016/j.brainresrev.2007.05.002.

Centers for Disease Control and Prevention (2014). Report to congress on traumatic brain injury in the United States: epidemiology and rehabilitation. Atlanta, GA: National Center for Injury Prevention and Control, 1-72.

Chatterjee, S., Sullivan, H.A., MacLennan, B.J., Xu, R., Hou, Y., Lavin, T.K., Lea, N.E., Michalski, J.E., Babcock, K.R., Dietrich, S., et al. (2018). Nontoxic, double-deletion-mutant rabies viral vectors for retrograde targeting of projection neurons. Nat Neurosci *21*, 638-646. 10.1038/s41593-018-0091-7.

Cholvin, T., Hainmueller, T., and Bartos, M. (2021). The hippocampus converts dynamic entorhinal inputs into stable spatial maps. Neuron *109*, 3135-3148.e3137. 10.1016/j.neuron.2021.09.019.

Chung, K., Wallace, J., Kim, S.Y., Kalyanasundaram, S., Andalman, A.S., Davidson, T.J., Mirzabekov, J.J., Zalocusky, K.A., Mattis, J., Denisin, A.K., et al. (2013). Structural and molecular interrogation of intact biological systems. Nature *497*, 332-337. 10.1038/nature12107.

Clark, R.S., Carcillo, J.A., Kochanek, P.M., Obrist, W.D., Jackson, E.K., Mi, Z., Wisneiwski, S.R., Bell, M.J., and Marion, D.W. (1997). Cerebrospinal fluid adenosine concentration and uncoupling of cerebral blood flow and oxidative metabolism after severe head injury in humans. Neurosurgery *41*, 1284-1292; discussion 1292-1283. 10.1097/00006123-199712000-00010.

Claudi, F., Tyson, A.L., Petrucco, L., Margrie, T.W., Portugues, R., and Branco, T. (2021). Visualizing anatomically registered data with brainrender. Elife *10*. 10.7554/eLife.65751.

Cone, J.J., Scantlen, M.D., Histed, M.H., and Maunsell, J.H.R. (2019). Different Inhibitory Interneuron Cell Classes Make Distinct Contributions to Visual Contrast Perception. eNeuro *6*. 10.1523/ENEURO.0337-18.2019.

Coons, A.H., Creech, H.J., and Jones, R.N. (1941). Immunological properties of an antibody containing a fluorescent group.

Coronado, V.G., Thomas, K.E., Sattin, R.W., and Johnson, R.L. (2005). The CDC traumatic brain injury surveillance system: characteristics of persons aged 65 years and older hospitalized with a TBI. J Head Trauma Rehabil *20*, 215-228. 10.1097/00001199-200505000-00005.

Corso, P., Finkelstein, E., Miller, T., Fiebelkorn, I., and Zaloshnja, E. (2006). Incidence and lifetime costs of injuries in the United States. Inj Prev *12*, 212-218. 10.1136/ip.2005.010983.

Cosgrove, K.P., Mazure, C.M., and Staley, J.K. (2007). Evolving knowledge of sex differences in brain structure, function, and chemistry. Biol Psychiatry *62*, 847-855. 10.1016/j.biopsych.2007.03.001.

Cronin, A.F. (2001). Traumatic brain injury in children: issues in community function. Am J Occup Ther *55*, 377-384. 10.5014/ajot.55.4.377.

Cummings, K.A., and Clem, R.L. (2020). Prefrontal somatostatin interneurons encode fear memory. Nat Neurosci *23*, 61-74. 10.1038/s41593-019-0552-7.

Cunningham, A.S., Salvador, R., Coles, J.P., Chatfield, D.A., Bradley, P.G., Johnston, A.J., Steiner, L.A., Fryer, T.D., Aigbirhio, F.I., Smielewski, P., et al. (2005). Physiological thresholds for irreversible tissue damage in contusional regions following traumatic brain injury. Brain *128*, 1931-1942. 10.1093/brain/awh536.

Daadi, M.M., Lee, S.H., Arac, A., Grueter, B.A., Bhatnagar, R., Maag, A.L., Schaar, B., Malenka, R.C., Palmer, T.D., and Steinberg, G.K. (2009). Functional engraftment of the medial ganglionic eminence cells in experimental stroke model. Cell Transplant *18*, 815-826. 10.3727/096368909X470829.

Davis, M.F., Figueroa Velez, D.X., Guevarra, R.P., Yang, M.C., Habeeb, M., Carathedathu, M.C., and Gandhi, S.P. (2015). Inhibitory Neuron Transplantation into Adult Visual Cortex Creates a New Critical Period that Rescues Impaired Vision. Neuron *86*, 1055-1066. 10.1016/j.neuron.2015.03.062.

de Carlos, J.A., López-Mascaraque, L., and Valverde, F. (1996). Dynamics of cell migration from the lateral ganglionic eminence in the rat. J Neurosci *16*, 6146-6156.

de Lanerolle, N.C., Kim, J.H., Robbins, R.J., and Spencer, D.D. (1989). Hippocampal interneuron loss and plasticity in human temporal lobe epilepsy. Brain Res *495*, 387-395.

DeAngelis, G.C., Ohzawa, I., and Freeman, R.D. (1993). Spatiotemporal organization of simple-cell receptive fields in the cat's striate cortex. II. Linearity of temporal and spatial summation. J Neurophysiol *69*, 1118-1135. 10.1152/jn.1993.69.4.1118.

Denk, W., Strickler, J.H., and Webb, W.W. (1990). Two-photon laser scanning fluorescence microscopy. Science *248*, 73-76. 10.1126/science.2321027.

Dinday, M.T., Girskis, K.M., Lee, S., Baraban, S.C., and Hunt, R.F. (2017). PAFAH1B1 haploinsufficiency disrupts GABA neurons and synaptic E/I balance in the dentate gyrus. Sci Rep *7*, 8269. 10.1038/s41598-017-08809-x.

Dixon, C.E., Clifton, G.L., Lighthall, J.W., Yaghmai, A.A., and Hayes, R.L. (1991). A controlled cortical impact model of traumatic brain injury in the rat. J Neurosci Methods *39*, 253-262.

Dixon, C.E., Lyeth, B.G., Povlishock, J.T., Findling, R.L., Hamm, R.J., Marmarou, A., Young, H.F., and Hayes, R.L. (1987). A fluid percussion model of experimental brain injury in the rat. J Neurosurg *67*, 110-119. 10.3171/jns.1987.67.1.0110.

Do, J.P., Xu, M., Lee, S.H., Chang, W.C., Zhang, S., Chung, S., Yung, T.J., Fan, J.L., Miyamichi, K., Luo, L., and Dan, Y. (2016). Cell type-specific long-range connections of basal forebrain circuit. Elife *5*. 10.7554/eLife.13214.

Dodt, H.U., Leischner, U., Schierloh, A., Jährling, N., Mauch, C.P., Deininger, K., Deussing, J.M., Eder, M., Zieglgänsberger, W., and Becker, K. (2007). Ultramicroscopy: three-dimensional visualization of neuronal networks in the whole mouse brain. Nat Methods *4*, 331-336. 10.1038/nmeth1036.

Doerr, J., Schwarz, M.K., Wiedermann, D., Leinhaas, A., Jakobs, A., Schloen, F., Schwarz, I., Diedenhofen, M., Braun, N.C., Koch, P., et al. (2017). Whole-brain 3D mapping of human neural transplant innervation. Nat Commun *8*, 14162. 10.1038/ncomms14162.

Du, T., Ciuffreda, K.J., and Kapoor, N. (2005). Elevated dark adaptation thresholds in traumatic brain injury. Brain Inj *19*, 1125-1138. 10.1080/02699050500149817.

Duhaime, A.C., Margulies, S.S., Durham, S.R., O'Rourke, M.M., Golden, J.A., Marwaha, S., and Raghupathi, R. (2000). Maturation-dependent response of the piglet brain to scaled cortical impact. J Neurosurg *93*, 455-462. 10.3171/jns.2000.93.3.0455.

Dulla, C.G., and Pitkänen, A. (2021). Novel Approaches to Prevent Epileptogenesis After Traumatic Brain Injury. Neurotherapeutics. 10.1007/s13311-021-01119-1.

Echlin, F.A., and Battista, A. (1963). Epileptiform Seizures from Chronic Isolated Cortex. Arch Neurol *9*, 154-170. 10.1001/archneur.1963.00460080064009.

Ertürk, A., Becker, K., Jährling, N., Mauch, C.P., Hojer, C.D., Egen, J.G., Hellal, F., Bradke, F., Sheng, M., and Dodt, H.U. (2012). Three-dimensional imaging of solvent-cleared organs using 3DISCO. Nat Protoc *7*, 1983-1995. 10.1038/nprot.2012.119.

Esclapez, M., and Houser, C.R. (1995). Somatostatin neurons are a subpopulation of GABA neurons in the rat dentate gyrus: evidence from colocalization of pre-prosomatostatin and glutamate decarboxylase messenger RNAs. Neuroscience *64*, 339-355. 10.1016/0306-4522(94)00406-u.

Espinosa, J.S., and Stryker, M.P. (2012). Development and plasticity of the primary visual cortex. Neuron *75*, 230-249. 10.1016/j.neuron.2012.06.009.

Etlin, A., Bráz, J.M., Kuhn, J.A., Wang, X., Hamel, K.A., Llewellyn-Smith, I.J., and Basbaum, A.I. (2016). Functional Synaptic Integration of Forebrain GABAergic Precursors into the Adult Spinal Cord. J Neurosci *36*, 11634-11645. 10.1523/JNEUROSCI.2301-16.2016.

Euston, D.R., Gruber, A.J., and McNaughton, B.L. (2012). The role of medial prefrontal cortex in memory and decision making. Neuron *76*, 1057-1070. 10.1016/j.neuron.2012.12.002.
Eyre, M.D., and Bartos, M. (2019). Somatostatin-Expressing Interneurons Form Axonal Projections to the Contralateral Hippocampus. Front Neural Circuits *13*, 56. 10.3389/fncir.2019.00056.

Eysel, U.T., and Schweigart, G. (1999). Increased receptive field size in the surround of chronic lesions in the adult cat visual cortex. Cereb Cortex *9*, 101-109. 10.1093/cercor/9.2.101.

Faber, D.J., Mik, E.G., Aalders, M.C., and van Leeuwen, T.G. (2003). Light absorption of (oxy-)hemoglobin assessed by spectroscopic optical coherence tomography. Opt Lett *28*, 1436-1438. 10.1364/ol.28.001436.

Faden, A.I., Demediuk, P., Panter, S.S., and Vink, R. (1989). The role of excitatory amino acids and NMDA receptors in traumatic brain injury. Science *244*, 798-800. 10.1126/science.2567056.

Fagiolini, M., Fritschy, J.M., Löw, K., Möhler, H., Rudolph, U., and Hensch, T.K. (2004). Specific GABAA circuits for visual cortical plasticity. Science *303*, 1681-1683. 10.1126/science.1091032.

Fagiolini, M., and Hensch, T.K. (2000). Inhibitory threshold for critical-period activation in primary visual cortex. Nature *404*, 183-186. 10.1038/35004582.

Faul, M., and Coronado, V. (2015). Epidemiology of traumatic brain injury. Handb Clin Neurol *127*, 3-13. 10.1016/B978-0-444-52892-6.00001-5.

Feeney, D.M., Boyeson, M.G., Linn, R.T., Murray, H.M., and Dail, W.G. (1981). Responses to cortical injury: I. Methodology and local effects of contusions in the rat. Brain Res *211*, 67-77. 10.1016/0006-8993(81)90067-6.

Ferrell, R.B., and Tanev, K.S. (2002). Traumatic brain injury in older adults. Curr Psychiatry Rep *4*, 354-362. 10.1007/s11920-002-0083-9.

Fingar, D.C., Salama, S., Tsou, C., Harlow, E., and Blenis, J. (2002). Mammalian cell size is controlled by mTOR and its downstream targets S6K1 and 4EBP1/eIF4E. Genes Dev *16*, 1472-1487. 10.1101/gad.995802.

Fogarty, M., Grist, M., Gelman, D., Marín, O., Pachnis, V., and Kessaris, N. (2007). Spatial genetic patterning of the embryonic neuroepithelium generates GABAergic interneuron diversity in the adult cortex. J Neurosci *27*, 10935-10946. 10.1523/JNEUROSCI.1629-07.2007.

Foik, A.T., Lean, G.A., Scholl, L.R., McLelland, B.T., Mathur, A., Aramant, R.B., Seiler, M.J., and Lyon, D.C. (2018). Detailed Visual Cortical Responses Generated by Retinal Sheet Transplants in Rats with Severe Retinal Degeneration. J Neurosci *38*, 10709-10724. 10.1523/JNEUROSCI.1279-18.2018.

Foik, A.T., Scholl, L.R., Lean, G.A., and Lyon, D.C. (2020). Visual Response Characteristics in Lateral and Medial Subdivisions of the Rat Pulvinar. Neuroscience *441*, 117-130. 10.1016/j.neuroscience.2020.06.030.

Forslund, M.V., Perrin, P.B., Røe, C., Sigurdardottir, S., Hellstrøm, T., Berntsen, S.A., Lu, J., Arango-Lasprilla, J.C., and Andelic, N. (2019). Global Outcome Trajectories up to 10 Years After Moderate to Severe Traumatic Brain Injury. Front Neurol *10*, 219. 10.3389/fneur.2019.00219.
Fox, G.B., Fan, L., Levasseur, R.A., and Faden, A.I. (1998). Sustained sensory/motor and cognitive deficits with neuronal apoptosis following controlled cortical impact brain injury in the mouse. J Neurotrauma *15*, 599-614. 10.1089/neu.1998.15.599.

Fox, G.B., LeVasseur, R.A., and Faden, A.I. (1999). Behavioral responses of C57BL/6, FVB/N, and 129/SvEMS mouse strains to traumatic brain injury: implications for gene targeting approaches to neurotrauma. J Neurotrauma *16*, 377-389. 10.1089/neu.1999.16.377.

Fox, W.C., Park, M.S., Belverud, S., Klugh, A., Rivet, D., and Tomlin, J.M. (2013). Contemporary imaging of mild TBI: the journey toward diffusion tensor imaging to assess neuronal damage. Neurol Res *35*, 223-232. 10.1179/1743132813Y.0000000162.

Frankowski, J.C., Kim, Y.J., and Hunt, R.F. (2019). Selective vulnerability of hippocampal interneurons to graded traumatic brain injury. Neurobiol Dis *129*, 208-216. 10.1016/j.nbd.2018.07.022.

Freund, T.F. (2003). Interneuron Diversity series: Rhythm and mood in perisomatic inhibition. Trends Neurosci *26*, 489-495. 10.1016/S0166-2236(03)00227-3.

Freund, T.F., and Buzsáki, G. (1996). Interneurons of the hippocampus. Hippocampus *6*, 347-470. 10.1002/(SICI)1098-1063(1996)6:4<347::AID-HIPO1>3.0.CO;2-I.

Frey, L.C. (2003). Epidemiology of posttraumatic epilepsy: a critical review. Epilepsia *44 Suppl 10*, 11-17.

Frotscher, M., Jonas, P., and Sloviter, R.S. (2006). Synapses formed by normal and abnormal hippocampal mossy fibers. Cell Tissue Res *326*, 361-367. 10.1007/s00441-006-0269-2.

Gabbott, P.L., Warner, T.A., Jays, P.R., Salway, P., and Busby, S.J. (2005). Prefrontal cortex in the rat: projections to subcortical autonomic, motor, and limbic centers. J Comp Neurol *492*, 145-177. 10.1002/cne.20738.

Gennarelli, T.A., Thibault, L.E., Adams, J.H., Graham, D.I., Thompson, C.J., and Marcincin, R.P. (1982). Diffuse axonal injury and traumatic coma in the primate. Ann Neurol *12*, 564-574. 10.1002/ana.410120611.

Gentry, L.R., Godersky, J.C., and Thompson, B. (1988). MR imaging of head trauma: review of the distribution and radiopathologic features of traumatic lesions. AJR Am J Roentgenol *150*, 663-672. 10.2214/ajr.150.3.663.

Ghika-Schmid, F., and Bogousslavsky, J. (2000). The acute behavioral syndrome of anterior thalamic infarction: a prospective study of 12 cases. Ann Neurol *48*, 220-227.

Girard, P., Salin, P.A., and Bullier, J. (1991). Visual activity in areas V3a and V3 during reversible inactivation of area V1 in the macaque monkey. J Neurophysiol *66*, 1493-1503. 10.1152/jn.1991.66.5.1493.

Gold, E.M., Vasilevko, V., Hasselmann, J., Tiefenthaler, C., Hoa, D., Ranawaka, K., Cribbs, D.H., and Cummings, B.J. (2018). Repeated Mild Closed Head Injuries Induce Long-Term White Matter Pathology and Neuronal Loss That Are Correlated With Behavioral Deficits. ASN Neuro *10*, 1759091418781921. 10.1177/1759091418781921.

Gong, H., Zeng, S., Yan, C., Lv, X., Yang, Z., Xu, T., Feng, Z., Ding, W., Qi, X., Li, A., et al. (2013). Continuously tracing brain-wide long-distance axonal projections in mice at a one-micron voxel resolution. Neuroimage *74*, 87-98. 10.1016/j.neuroimage.2013.02.005.

Goodman, J.C., Cherian, L., Bryan, R.M., and Robertson, C.S. (1994). Lateral cortical impact injury in rats: pathologic effects of varying cortical compression and impact velocity. J Neurotrauma *11*, 587-597. 10.1089/neu.1994.11.587.

Grinberg, L.T., Anghinah, R., Nascimento, C.F., Amaro, E., Leite, R.P., Martin, M.a.G., Naslavsky, M.S., Takada, L.T., Filho, W.J., Pasqualucci, C.A., and Nitrini, R. (2016). Chronic Traumatic Encephalopathy Presenting as Alzheimer's Disease in a Retired Soccer Player. J Alzheimers Dis *54*, 169-174. 10.3233/JAD-160312.

Guo, D., Zeng, L., Brody, D.L., and Wong, M. (2013). Rapamycin attenuates the development of posttraumatic epilepsy in a mouse model of traumatic brain injury. PLoS One *8*, e64078. 10.1371/journal.pone.0064078.

Gupta, A., Elgammal, F.S., Proddutur, A., Shah, S., and Santhakumar, V. (2012). Decrease in tonic inhibition contributes to increase in dentate semilunar granule cell excitability after brain injury. J Neurosci *32*, 2523-2537. 10.1523/JNEUROSCI.4141-11.2012.

Guskiewicz, K.M., Marshall, S.W., Bailes, J., McCrea, M., Cantu, R.C., Randolph, C., and Jordan, B.D. (2005). Association between recurrent concussion and late-life cognitive impairment in retired professional football players. Neurosurgery *57*, 719-726; discussion 719-726. 10.1093/neurosurgery/57.4.719.

Hafner, G., Witte, M., Guy, J., Subhashini, N., Fenno, L.E., Ramakrishnan, C., Kim, Y.S., Deisseroth, K., Callaway, E.M., Oberhuber, M., et al. (2019). Mapping Brain-Wide Afferent Inputs of Parvalbumin-Expressing GABAergic Neurons in Barrel Cortex Reveals Local and Long-Range Circuit Motifs. Cell Rep *28*, 3450-3461.e3458. 10.1016/j.celrep.2019.08.064.

Hajos, N., Acsady, L., and Freund, T.F. (1996). Target selectivity and neurochemical characteristics of VIP-immunoreactive interneurons in the rat dentate gyrus. Eur J Neurosci *8*, 1415-1431. 10.1111/j.1460-9568.1996.tb01604.x.

Halabisky, B., Parada, I., Buckmaster, P.S., and Prince, D.A. (2010). Excitatory input onto hilar somatostatin interneurons is increased in a chronic model of epilepsy. J Neurophysiol *104*, 2214-2223. 10.1152/jn.00147.2010.

Halasy, K., and Somogyi, P. (1993). Distribution of GABAergic synapses and their targets in the dentate gyrus of rat: a quantitative immunoelectron microscopic analysis. J Hirnforsch *34*, 299-308.

Halaweish, I., Bambakidis, T., Nikolian, V.C., Georgoff, P., Bruhn, P., Piascik, P., Buckley, L., Srinivasan, A., Liu, B., Li, Y., and Alam, H.B. (2016). Early resuscitation with lyophilized plasma provides equal neuroprotection compared with fresh frozen plasma in a large animal survival model of traumatic brain injury and hemorrhagic shock. J Trauma Acute Care Surg *81*, 1080-1087. 10.1097/TA.0000000000001204.

Hall, E.D., Bryant, Y.D., Cho, W., and Sullivan, P.G. (2008). Evolution of post-traumatic neurodegeneration after controlled cortical impact traumatic brain injury in mice and rats as assessed by the de Olmos silver and fluorojade staining methods. J Neurotrauma *25*, 235-247. 10.1089/neu.2007.0383.

Hall, E.D., Gibson, T.R., and Pavel, K.M. (2005a). Lack of a gender difference in post-traumatic neurodegeneration in the mouse controlled cortical impact injury model. J Neurotrauma *22*, 669-679. 10.1089/neu.2005.22.669.

Hall, E.D., Sullivan, P.G., Gibson, T.R., Pavel, K.M., Thompson, B.M., and Scheff, S.W. (2005b). Spatial and temporal characteristics of neurodegeneration after controlled cortical impact in mice: more than a focal brain injury. J Neurotrauma *22*, 252-265. 10.1089/neu.2005.22.252.

Hamm, R.J., Temple, M.D., Pike, B.R., O'Dell, D.M., Buck, D.L., and Lyeth, B.G. (1996). Working memory deficits following traumatic brain injury in the rat. J Neurotrauma *13*, 317-323. 10.1089/neu.1996.13.317.

Han, Z.S., Buhl, E.H., Lörinczi, Z., and Somogyi, P. (1993). A high degree of spatial selectivity in the axonal and dendritic domains of physiologically identified local-circuit neurons in the dentate gyrus of the rat hippocampus. Eur J Neurosci *5*, 395-410. 10.1111/j.1460-9568.1993.tb00507.x.

Harris, J.A., Mihalas, S., Hirokawa, K.E., Whitesell, J.D., Choi, H., Bernard, A., Bohn, P., Caldejon, S., Casal, L., Cho, A., et al. (2019). Hierarchical organization of cortical and thalamic connectivity. Nature *575*, 195-202. 10.1038/s41586-019-1716-z.

Harris, N.G., Verley, D.R., Gutman, B.A., Thompson, P.M., Yeh, H.J., and Brown, J.A. (2016). Disconnection and hyper-connectivity underlie reorganization after TBI: A rodent functional connectomic analysis. Exp Neurol *277*, 124-138. 10.1016/j.expneurol.2015.12.020.

Hayes, R.L., Stalhammar, D., Povlishock, J.T., Allen, A.M., Galinat, B.J., Becker, D.P., and Stonnington, H.H. (1987). A new model of concussive brain injury in the cat produced by extradural fluid volume loading: II. Physiological and neuropathological observations. Brain Inj *1*, 93-112. 10.3109/02699058709034449.

Heidbreder, C.A., and Groenewegen, H.J. (2003). The medial prefrontal cortex in the rat: evidence for a dorso-ventral distinction based upon functional and anatomical characteristics. Neurosci Biobehav Rev *27*, 555-579. 10.1016/j.neubiorev.2003.09.003.

Heinemann, U., Beck, H., Dreier, J.P., Ficker, E., Stabel, J., and Zhang, C.L. (1992). The dentate gyrus as a regulated gate for the propagation of epileptiform activity. Epilepsy Res Suppl *7*, 273-280.

Helthuis, J.H.G., van der Zwan, A., van Doormaal, T.P.C., Bleys, R.L.A.W., Harteveld, A.A., van der Toorn, A., Brozici, M., Hendrikse, J., and Zwanenburg, J.J.M. (2018). High resolution 7T and 9.4T-MRI of human cerebral arterial casts enables accurate estimations of the cerebrovascular morphometry. Sci Rep *8*, 14235. 10.1038/s41598-018-32427-w.

Hensch, T.K., Fagiolini, M., Mataga, N., Stryker, M.P., Baekkeskov, S., and Kash, S.F. (1998). Local GABA circuit control of experience-dependent plasticity in developing visual cortex. Science *282*, 1504-1508. 10.1126/science.282.5393.1504.
Herman, S.T. (2002). Epilepsy after brain insult: targeting epileptogenesis. Neurology *59*, S21-26.

Hernández-Miranda, L.R., Parnavelas, J.G., and Chiara, F. (2010). Molecules and mechanisms involved in the generation and migration of cortical interneurons. ASN Neuro *2*, e00031. 10.1042/AN20090053.

Hillary, F.G., Genova, H.M., Chiaravalloti, N.D., Rypma, B., and DeLuca, J. (2006). Prefrontal modulation of working memory performance in brain injury and disease. Hum Brain Mapp *27*, 837-847. 10.1002/hbm.20226.

Hillary, F.G., Roman, C.A., Venkatesan, U., Rajtmajer, S.M., Bajo, R., and Castellanos, N.D. (2015). Hyperconnectivity is a fundamental response to neurological disruption. Neuropsychology *29*, 59-75. 10.1037/neu0000110.

Holbourn, A.H.S. (1943). Mechanics of head injuries.

Houser, C.R. (2007). Interneurons of the dentate gyrus: an overview of cell types, terminal fields and neurochemical identity. Prog Brain Res *163*, 217-232. 10.1016/S0079-6123(07)63013-1.
Houser, C.R., and Esclapez, M. (1994). Localization of mRNAs encoding two forms of glutamic acid decarboxylase in the rat hippocampal formation. Hippocampus *4*, 530-545. 10.1002/hipo.450040503.

Howard, M.A., and Baraban, S.C. (2016). Synaptic integration of transplanted interneuron progenitor cells into native cortical networks. J Neurophysiol *116*, 472-478. 10.1152/jn.00321.2016.

Hsieh, J.Y., and Baraban, S.C. (2017). Medial Ganglionic Eminence Progenitors Transplanted into Hippocampus Integrate in a Functional and Subtype-Appropriate Manner. eNeuro *4*. 10.1523/ENEURO.0359-16.2017.

Hunt, R.F., Boychuk, J.A., and Smith, B.N. (2013a). Neural circuit mechanisms of post-traumatic epilepsy. Front Cell Neurosci *7*, 89. 10.3389/fncel.2013.00089.

Hunt, R.F., Girskis, K.M., Rubenstein, J.L., Alvarez-Buylla, A., and Baraban, S.C. (2013b). GABA progenitors grafted into the adult epileptic brain control seizures and abnormal behavior. Nat Neurosci *16*, 692-697. 10.1038/nn.3392.

Hunt, R.F., Haselhorst, L.A., Schoch, K.M., Bach, E.C., Rios-Pilier, J., Scheff, S.W., Saatman, K.E., and Smith, B.N. (2012). Posttraumatic mossy fiber sprouting is related to the degree of cortical damage in three mouse strains. Epilepsy Res *99*, 167-170. 10.1016/j.eplepsyres.2011.10.011.

Hunt, R.F., Scheff, S.W., and Smith, B.N. (2009). Posttraumatic epilepsy after controlled cortical impact injury in mice. Exp Neurol *215*, 243-252. 10.1016/j.expneurol.2008.10.005.

Hunt, R.F., Scheff, S.W., and Smith, B.N. (2010). Regionally localized recurrent excitation in the dentate gyrus of a cortical contusion model of posttraumatic epilepsy. J Neurophysiol *103*, 1490-1500. 10.1152/jn.00957.2009.
Hunt, R.F., Scheff, S.W., and Smith, B.N. (2011). Synaptic reorganization of inhibitory hilar interneuron circuitry after traumatic brain injury in mice. J Neurosci *31*, 6880-6890. 10.1523/JNEUROSCI.0032-11.2011.

Huusko, N., Römer, C., Ndode-Ekane, X.E., Lukasiuk, K., and Pitkänen, A. (2015). Loss of hippocampal interneurons and epileptogenesis: a comparison of two animal models of acquired epilepsy. Brain Struct Funct *220*, 153-191. 10.1007/s00429-013-0644-1.

Hånell, A., Clausen, F., Björk, M., Jansson, K., Philipson, O., Nilsson, L.N., Hillered, L., Weinreb, P.H., Lee, D., McIntosh, T.K., et al. (2010). Genetic deletion and pharmacological inhibition of Nogo-66 receptor impairs cognitive outcome after traumatic brain injury in mice. J Neurotrauma *27*, 1297-1309. 10.1089/neu.2009.1255.

Ibrahim, L.A., Mesik, L., Ji, X.Y., Fang, Q., Li, H.F., Li, Y.T., Zingg, B., Zhang, L.I., and Tao, H.W. (2016). Cross-Modality Sharpening of Visual Cortical Processing through Layer-1-Mediated Inhibition and Disinhibition. Neuron *89*, 1031-1045. 10.1016/j.neuron.2016.01.027.

Ibrahim, L.A., Schuman, B., Bandler, R., Rudy, B., and Fishell, G. (2020). Mining the jewels of the cortex's crowning mystery. Curr Opin Neurobiol *63*, 154-161. 10.1016/j.conb.2020.04.005.

Imbrosci, B., Eysel, U.T., and Mittmann, T. (2010). Metaplasticity of horizontal connections in the vicinity of focal laser lesions in rat visual cortex. J Physiol *588*, 4695-4703. 10.1113/jphysiol.2010.198192.

Iwasaki, Y., and Clark, H.F. (1975). Cell to cell transmission of virus in the central nervous system. II. Experimental rabies in mouse. Lab Invest *33*, 391-399.

Jacobs, H.E. (1988). The Los Angeles Head Injury Survey: procedures and initial findings. Arch Phys Med Rehabil *69*, 425-431.

Ji, X.Y., Zingg, B., Mesik, L., Xiao, Z., Zhang, L.I., and Tao, H.W. (2016). Thalamocortical Innervation Pattern in Mouse Auditory and Visual Cortex: Laminar and Cell-Type Specificity. Cereb Cortex *26*, 2612-2625. 10.1093/cercor/bhv099.

Jin, X., Prince, D.A., and Huguenard, J.R. (2006). Enhanced excitatory synaptic connectivity in layer v pyramidal neurons of chronically injured epileptogenic neocortex in rats. J Neurosci *26*, 4891-4900. 10.1523/JNEUROSCI.4361-05.2006.

Johansen, F.F., Zimmer, J., and Diemer, N.H. (1987). Early loss of somatostatin neurons in dentate hilus after cerebral ischemia in the rat precedes CA-1 pyramidal cell loss. Acta Neuropathol *73*, 110-114.

Johnstone, V.P., Shultz, S.R., Yan, E.B., O'Brien, T.J., and Rajan, R. (2014). The acute phase of mild traumatic brain injury is characterized by a distance-dependent neuronal hypoactivity. J Neurotrauma *31*, 1881-1895. 10.1089/neu.2014.3343.

Johnstone, V.P., Wright, D.K., Wong, K., O'Brien, T.J., Rajan, R., and Shultz, S.R. (2015). Experimental Traumatic Brain Injury Results in Long-Term Recovery of Functional

Responsiveness in Sensory Cortex but Persisting Structural Changes and Sensorimotor, Cognitive, and Emotional Deficits. J Neurotrauma *32*, 1333-1346. 10.1089/neu.2014.3785.
Jonas, P., Bischofberger, J., Fricker, D., and Miles, R. (2004). Interneuron Diversity series: Fast in, fast out--temporal and spatial signal processing in hippocampal interneurons. Trends Neurosci *27*, 30-40. 10.1016/j.tins.2003.10.010.

Jones, E., Fear, N.T., and Wessely, S. (2007). Shell shock and mild traumatic brain injury: a historical review. Am J Psychiatry *164*, 1641-1645. 10.1176/appi.ajp.2007.07071180.

Kahn, J.B., Port, R.G., Yue, C., Takano, H., and Coulter, D.A. (2019). Circuit-based interventions in the dentate gyrus rescue epilepsy-associated cognitive dysfunction. Brain *142*, 2705-2721. 10.1093/brain/awz209.

Kandel, E.R., Schwartz, J. H., Jessell, T. M., Siegelbaum, S., Hudspeth, A. J., & Mack, S. (2000). Principles of neural science (McGraw-hill).

Kapfer, C., Glickfeld, L.L., Atallah, B.V., and Scanziani, M. (2007). Supralinear increase of recurrent inhibition during sparse activity in the somatosensory cortex. Nat Neurosci *10*, 743-753. 10.1038/nn1909.

Karnani, M.M., Jackson, J., Ayzenshtat, I., Hamzehei Sichani, A., Manoocheri, K., Kim, S., and Yuste, R. (2016). Opening Holes in the Blanket of Inhibition: Localized Lateral Disinhibition by VIP Interneurons. J Neurosci *36*, 3471-3480. 10.1523/JNEUROSCI.3646-15.2016.

Katayama, Y., Becker, D.P., Tamura, T., and Hovda, D.A. (1990). Massive increases in extracellular potassium and the indiscriminate release of glutamate following concussive brain injury. J Neurosurg *73*, 889-900. 10.3171/jns.1990.73.6.0889.

Katona, I., Acsády, L., and Freund, T.F. (1999). Postsynaptic targets of somatostatin-immunoreactive interneurons in the rat hippocampus. Neuroscience *88*, 37-55. 10.1016/s0306-4522(98)00302-9.

Kawaguchi, Y. (1997). Selective cholinergic modulation of cortical GABAergic cell subtypes. J Neurophysiol *78*, 1743-1747. 10.1152/jn.1997.78.3.1743.

Kaya, S.S., Mahmood, A., Li, Y., Yavuz, E., Göksel, M., and Chopp, M. (1999). Apoptosis and expression of p53 response proteins and cyclin D1 after cortical impact in rat brain. Brain Res *818*, 23-33.

Kelly, K.M., Miller, E.R., Lepsveridze, E., Kharlamov, E.A., and Mchedlishvili, Z. (2015). Posttraumatic seizures and epilepsy in adult rats after controlled cortical impact. Epilepsy Res *117*, 104-116. 10.1016/j.eplepsyres.2015.09.009.

Kelly, R.M., and Strick, P.L. (2000). Rabies as a transneuronal tracer of circuits in the central nervous system. J Neurosci Methods *103*, 63-71.

Kemper, V.G., De Martino, F., Emmerling, T.C., Yacoub, E., and Goebel, R. (2018). High resolution data analysis strategies for mesoscale human functional MRI at 7 and 9.4T. Neuroimage *164*, 48-58. 10.1016/j.neuroimage.2017.03.058.

Kepecs, A., and Fishell, G. (2014). Interneuron cell types are fit to function. Nature *505*, 318-326. 10.1038/nature12983.
Kessaris, N., Magno, L., Rubin, A.N., and Oliveira, M.G. (2014). Genetic programs controlling cortical interneuron fate. Curr Opin Neurobiol *26*, 79-87. 10.1016/j.conb.2013.12.012.

Kharatishvili, I., Immonen, R., Gröhn, O., and Pitkänen, A. (2007). Quantitative diffusion MRI of hippocampus as a surrogate marker for post-traumatic epileptogenesis. Brain *130*, 3155-3168. 10.1093/brain/awm268.

Kharatishvili, I., Nissinen, J.P., McIntosh, T.K., and Pitkänen, A. (2006). A model of posttraumatic epilepsy induced by lateral fluid-percussion brain injury in rats. Neuroscience *140*, 685-697. 10.1016/j.neuroscience.2006.03.012.

Kim, E.J., Jacobs, M.W., Ito-Cole, T., and Callaway, E.M. (2016). Improved Monosynaptic Neural Circuit Tracing Using Engineered Rabies Virus Glycoproteins. Cell Rep *15*, 692-699. 10.1016/j.celrep.2016.03.067.

Kim, E.J., Juavinett, A.L., Kyubwa, E.M., Jacobs, M.W., and Callaway, E.M. (2015a). Three Types of Cortical Layer 5 Neurons That Differ in Brain-wide Connectivity and Function. Neuron *88*, 1253-1267. 10.1016/j.neuron.2015.11.002.

Kim, S.Y., Cho, J.H., Murray, E., Bakh, N., Choi, H., Ohn, K., Ruelas, L., Hubbert, A., McCue, M., Vassallo, S.L., et al. (2015b). Stochastic electrotransport selectively enhances the transport of highly electromobile molecules. Proc Natl Acad Sci U S A *112*, E6274-6283. 10.1073/pnas.1510133112.

Kim, Y.J., Khoshkhoo, S., Frankowski, J.C., Zhu, B., Abbasi, S., Lee, S., Wu, Y.E., and Hunt, R.F. (2018). Chd2 Is Necessary for Neural Circuit Development and Long-Term Memory. Neuron *100*, 1180-1193.e1186. 10.1016/j.neuron.2018.09.049.

King, C., Robinson, T., Dixon, C.E., Rao, G.R., Larnard, D., and Nemoto, C.E. (2010). Brain temperature profiles during epidural cooling with the ChillerPad in a monkey model of traumatic brain injury. J Neurotrauma *27*, 1895-1903. 10.1089/neu.2009.1178.

Kinnunen, K.M., Greenwood, R., Powell, J.H., Leech, R., Hawkins, P.C., Bonnelle, V., Patel, M.C., Counsell, S.J., and Sharp, D.J. (2011). White matter damage and cognitive impairment after traumatic brain injury. Brain *134*, 449-463. 10.1093/brain/awq347.

Kirst, C., Skriabine, S., Vieites-Prado, A., Topilko, T., Bertin, P., Gerschenfeld, G., Verny, F., Topilko, P., Michalski, N., Tessier-Lavigne, M., and Renier, N. (2020). Mapping the Fine-Scale Organization and Plasticity of the Brain Vasculature. Cell *180*, 780-795.e725. 10.1016/j.cell.2020.01.028.

Kishiyama, M.M., Yonelinas, A.P., Kroll, N.E., Lazzara, M.M., Nolan, E.C., Jones, E.G., and Jagust, W.J. (2005). Bilateral thalamic lesions affect recollection- and familiarity-based recognition memory judgments. Cortex *41*, 778-788. 10.1016/s0010-9452(08)70296-x.

Klausberger, T., and Somogyi, P. (2008). Neuronal diversity and temporal dynamics: the unity of hippocampal circuit operations. Science *321*, 53-57. 10.1126/science.1149381.

Klug, J.R., Engelhardt, M.D., Cadman, C.N., Li, H., Smith, J.B., Ayala, S., Williams, E.W., Hoffman, H., and Jin, X. (2018). Differential inputs to striatal cholinergic and parvalbumin interneurons imply functional distinctions. Elife *7*. 10.7554/eLife.35657.
Koenig, J.B., Cantu, D., Low, C., Sommer, M., Noubary, F., Croker, D., Whalen, M., Kong, D., and Dulla, C.G. (2019). Glycolytic inhibitor 2-deoxyglucose prevents cortical hyperexcitability after traumatic brain injury. JCI Insight *5*. 10.1172/jci.insight.126506.

Krzic, U., Gunther, S., Saunders, T.E., Streichan, S.J., and Hufnagel, L. (2012). Multiview light-sheet microscope for rapid in toto imaging. Nat Methods *9*, 730-733. 10.1038/nmeth.2064.

Larimer, P., Spatazza, J., Espinosa, J.S., Tang, Y., Kaneko, M., Hasenstaub, A.R., Stryker, M.P., and Alvarez-Buylla, A. (2016). Caudal Ganglionic Eminence Precursor Transplants Disperse and Integrate as Lineage-Specific Interneurons but Do Not Induce Cortical Plasticity. Cell Rep *16*, 1391-1404. 10.1016/j.celrep.2016.06.071.

Larkum, M.E., Zhu, J.J., and Sakmann, B. (1999). A new cellular mechanism for coupling inputs arriving at different cortical layers. Nature *398*, 338-341. 10.1038/18686.

Lavin, T.K., Jin, L., Lea, N.E., and Wickersham, I.R. (2020). Monosynaptic Tracing Success Depends Critically on Helper Virus Concentrations. Front Synaptic Neurosci *12*, 6. 10.3389/fnsyn.2020.00006.

Le Merre, P., Ährlund-Richter, S., and Carlén, M. (2021). The mouse prefrontal cortex: Unity in diversity. Neuron *109*, 1925-1944. 10.1016/j.neuron.2021.03.035.

Lee, D.J., Gurkoff, G.G., Izadi, A., Berman, R.F., Ekstrom, A.D., Muizelaar, J.P., Lyeth, B.G., and Shahlaie, K. (2013). Medial septal nucleus theta frequency deep brain stimulation improves spatial working memory after traumatic brain injury. J Neurotrauma *30*, 131-139. 10.1089/neu.2012.2646.

Lee, D.J., Gurkoff, G.G., Izadi, A., Seidl, S.E., Echeverri, A., Melnik, M., Berman, R.F., Ekstrom, A.D., Muizelaar, J.P., Lyeth, B.G., and Shahlaie, K. (2015). Septohippocampal Neuromodulation Improves Cognition after Traumatic Brain Injury. J Neurotrauma *32*, 1822-1832. 10.1089/neu.2014.3744.

Lee, E., Choi, J., Jo, Y., Kim, J.Y., Jang, Y.J., Lee, H.M., Kim, S.Y., Lee, H.J., Cho, K., Jung, N., et al. (2016). ACT-PRESTO: Rapid and consistent tissue clearing and labeling method for 3-dimensional (3D) imaging. Sci Rep *6*, 18631. 10.1038/srep18631.

Lee, S.H., Kwan, A.C., Zhang, S., Phoumthipphavong, V., Flannery, J.G., Masmanidis, S.C., Taniguchi, H., Huang, Z.J., Zhang, F., Boyden, E.S., et al. (2012). Activation of specific interneurons improves V1 feature selectivity and visual perception. Nature *488*, 379-383. 10.1038/nature11312.

Leonard, J.R., Maris, D.O., and Grady, M.S. (1994). Fluid percussion injury causes loss of forebrain choline acetyltransferase and nerve growth factor receptor immunoreactive cells in the rat. J Neurotrauma *11*, 379-392. 10.1089/neu.1994.11.379.

Leranth, C., Malcolm, A.J., and Frotscher, M. (1990). Afferent and efferent synaptic connections of somatostatin-immunoreactive neurons in the rat fascia dentata. J Comp Neurol *295*, 111-122. 10.1002/cne.902950110.

Li, H., and Prince, D.A. (2002). Synaptic activity in chronically injured, epileptogenic sensory-motor neocortex. J Neurophysiol *88*, 2-12. 10.1152/jn.00507.2001.
Li, Y., Bao, H., Luo, Y., Yoan, C., Sullivan, H.A., Quintanilla, L., Wickersham, I., Lazarus, M., Shih, Y.I., and Song, J. (2020). Supramammillary nucleus synchronizes with dentate gyrus to regulate spatial memory retrieval through glutamate release. Elife *9*. 10.7554/eLife.53129.

Liepert, J., Storch, P., Fritsch, A., and Weiller, C. (2000). Motor cortex disinhibition in acute stroke. Clin Neurophysiol *111*, 671-676.

Lighthall, J.W. (1988). Controlled cortical impact: a new experimental brain injury model. J Neurotrauma *5*, 1-15. 10.1089/neu.1988.5.1.

Lighthall, J.W., Goshgarian, H.G., and Pinderski, C.R. (1990). Characterization of axonal injury produced by controlled cortical impact. J Neurotrauma *7*, 65-76. 10.1089/neu.1990.7.65.

Little, D.M., Kraus, M.F., Joseph, J., Geary, E.K., Susmaras, T., Zhou, X.J., Pliskin, N., and Gorelick, P.B. (2010). Thalamic integrity underlies executive dysfunction in traumatic brain injury. Neurology *74*, 558-564. 10.1212/WNL.0b013e3181cff5d5.

Littlejohn, E.L., Scott, D., and Saatman, K.E. (2020). Insulin-like growth factor-1 overexpression increases long-term survival of posttrauma-born hippocampal neurons while inhibiting ectopic migration following traumatic brain injury. Acta Neuropathol Commun *8*, 46. 10.1186/s40478-020-00925-6.

Liu, L., Xu, H., Wang, J., Li, J., Tian, Y., Zheng, J., He, M., Xu, T.L., Wu, Z.Y., Li, X.M., and Duan, S.M. (2020). Cell type-differential modulation of prefrontal cortical GABAergic interneurons on low gamma rhythm and social interaction. Sci Adv *6*, eaay4073. 10.1126/sciadv.aay4073.

Liu, Y.J., Hashemi-Nezhad, M., and Lyon, D.C. (2011). Dynamics of extraclassical surround modulation in three types of V1 neurons. J Neurophysiol *105*, 1306-1317. 10.1152/jn.00692.2010.

Liu, Y.J., Hashemi-Nezhad, M., and Lyon, D.C. (2015). Contrast invariance of orientation tuning in cat primary visual cortex neurons depends on stimulus size. J Physiol *593*, 4485-4498. 10.1113/JP271180.

Liu, Y.J., Hashemi-Nezhad, M., and Lyon, D.C. (2017). Differences in orientation tuning between pinwheel and domain neurons in primary visual cortex depend on contrast and size. Neurophotonics *4*, 031209. 10.1117/1.NPh.4.3.031209.

Long, J.E., Cobos, I., Potter, G.B., and Rubenstein, J.L. (2009). Dlx1&2 and Mash1 transcription factors control MGE and CGE patterning and differentiation through parallel and overlapping pathways. Cereb Cortex *19 Suppl 1*, i96-106. 10.1093/cercor/bhp045.

Lothman, E.W., Stringer, J.L., and Bertram, E.H. (1992). The dentate gyrus as a control point for seizures in the hippocampus and beyond. Epilepsy Res Suppl *7*, 301-313.

Lovett-Barron, M., Kaifosh, P., Kheirbek, M.A., Danielson, N., Zaremba, J.D., Reardon, T.R., Turi, G.F., Hen, R., Zemelman, B.V., and Losonczy, A. (2014). Dendritic inhibition in the hippocampus supports fear learning. Science *343*, 857-863. 10.1126/science.1247485.

Lowenstein, D.H., Thomas, M.J., Smith, D.H., and McIntosh, T.K. (1992). Selective vulnerability of dentate hilar neurons following traumatic brain injury: a potential mechanistic link between head trauma and disorders of the hippocampus. J Neurosci *12*, 4846-4853.
Luo, P., Li, A., Zheng, Y., Han, Y., Tian, J., Xu, Z., Gong, H., and Li, X. (2019). Whole Brain Mapping of Long-Range Direct Input to Glutamatergic and GABAergic Neurons in Motor Cortex. Front Neuroanat *13*, 44. 10.3389/fnana.2019.00044.

Lur, G., Vinck, M.A., Tang, L., Cardin, J.A., and Higley, M.J. (2016). Projection-Specific Visual Feature Encoding by Layer 5 Cortical Subnetworks. Cell Rep *14*, 2538-2545. 10.1016/j.celrep.2016.02.050.

Lyon, D.C., and Kaas, J.H. (2002). Evidence for a modified V3 with dorsal and ventral halves in macaque monkeys. Neuron *33*, 453-461. 10.1016/s0896-6273(02)00580-9.

Léránth, C., and Frotscher, M. (1987). Cholinergic innervation of hippocampal GAD- and somatostatin-immunoreactive commissural neurons. J Comp Neurol *261*, 33-47. 10.1002/cne.902610104.

Madathil, S.K., Carlson, S.W., Brelsfoard, J.M., Ye, P., D'Ercole, A.J., and Saatman, K.E. (2013). Astrocyte-Specific Overexpression of Insulin-Like Growth Factor-1 Protects Hippocampal Neurons and Reduces Behavioral Deficits following Traumatic Brain Injury in Mice. PLoS One *8*, e67204. 10.1371/journal.pone.0067204.

Mao, H., Jin, X., Zhang, L., Yang, K.H., Igarashi, T., Noble-Haeusslein, L.J., and King, A.I. (2010a). Finite element analysis of controlled cortical impact-induced cell loss. J Neurotrauma *27*, 877-888. 10.1089/neu.2008.0616.

Mao, H., and Yang, K.H. (2011). Investigation of brain contusion mechanism and threshold by combining finite element analysis with in vivo histology data.

Mao, H., Yang, K.H., King, A.I., and Yang, K. (2010b). Computational neurotrauma--design, simulation, and analysis of controlled cortical impact model. Biomech Model Mechanobiol *9*, 763-772. 10.1007/s10237-010-0212-z.

Marquez de la Plata, C.D., Garces, J., Shokri Kojori, E., Grinnan, J., Krishnan, K., Pidikiti, R., Spence, J., Devous, M.D., Moore, C., McColl, R., et al. (2011). Deficits in functional connectivity of hippocampal and frontal lobe circuits after traumatic axonal injury. Arch Neurol *68*, 74-84. 10.1001/archneurol.2010.342.

Martinez-Losa, M., Tracy, T.E., Ma, K., Verret, L., Clemente-Perez, A., Khan, A.S., Cobos, I., Ho, K., Gan, L., Mucke, L., et al. (2018). Nav1.1-Overexpressing Interneuron Transplants Restore Brain Rhythms and Cognition in a Mouse Model of Alzheimer's Disease. Neuron *98*, 75-89.e75. 10.1016/j.neuron.2018.02.029.

Martland, H.S. (1928). Punch drunk. *Journal of the American Medical Association 91*, 1103-1107.

Martínez-Cerdeño, V., Noctor, S.C., Espinosa, A., Ariza, J., Parker, P., Orasji, S., Daadi, M.M., Bankiewicz, K., Alvarez-Buylla, A., and Kriegstein, A.R. (2010). Embryonic MGE precursor cells grafted into adult rat striatum integrate and ameliorate motor symptoms in 6-OHDA-lesioned rats. Cell Stem Cell *6*, 238-250. 10.1016/j.stem.2010.01.004.

Marín, O., and Rubenstein, J.L. (2001). A long, remarkable journey: tangential migration in the telencephalon. Nat Rev Neurosci *2*, 780-790. 10.1038/35097509.
Matsumoto, K., Mitani, T.T., Horiguchi, S.A., Kaneshiro, J., Murakami, T.C., Mano, T., Fujishima, H., Konno, A., Watanabe, T.M., Hirai, H., and Ueda, H.R. (2019). Advanced CUBIC tissue clearing for whole-organ cell profiling. Nat Protoc *14*, 3506-3537. 10.1038/s41596-019-0240-9.

Maxwell, W.L., Watt, C., Graham, D.I., and Gennarelli, T.A. (1993). Ultrastructural evidence of axonal shearing as a result of lateral acceleration of the head in non-human primates. Acta Neuropathol *86*, 136-144. 10.1007/BF00334880.

McKenna, K., Cooke, D.M., Fleming, J., Jefferson, A., and Ogden, S. (2006). The incidence of visual perceptual impairment in patients with severe traumatic brain injury. Brain Inj *20*, 507-518. 10.1080/02699050600664368.

Mebatsion, T., Weiland, F., and Conzelmann, K.K. (1999). Matrix protein of rabies virus is responsible for the assembly and budding of bullet-shaped particles and interacts with the transmembrane spike glycoprotein G. J Virol *73*, 242-250. 10.1128/JVI.73.1.242-250.1999.

Mez, J., Daneshvar, D.H., Kiernan, P.T., Abdolmohammadi, B., Alvarez, V.E., Huber, B.R., Alosco, M.L., Solomon, T.M., Nowinski, C.J., McHale, L., et al. (2017). Clinicopathological Evaluation of Chronic Traumatic Encephalopathy in Players of American Football. JAMA *318*, 360-370. 10.1001/jama.2017.8334.

Minsky, M. (1988). Memoir on inventing the confocal scanning microscope.

Miyoshi, G., Butt, S.J., Takebayashi, H., and Fishell, G. (2007). Physiologically distinct temporal cohorts of cortical interneurons arise from telencephalic Olig2-expressing precursors. J Neurosci *27*, 7786-7798. 10.1523/JNEUROSCI.1807-07.2007.

Morales, C., Morici, J.F., Espinosa, N., Sacson, A., Lara-Vasquez, A., García-Pérez, M.A., Bekinschtein, P., Weisstaub, N.V., and Fuentealba, P. (2021). Dentate Gyrus Somatostatin Cells are Required for Contextual Discrimination During Episodic Memory Encoding. Cereb Cortex *31*, 1046-1059. 10.1093/cercor/bhaa273.

Morgan, R.J., Santhakumar, V., and Soltesz, I. (2007). Modeling the dentate gyrus. Prog Brain Res *163*, 639-658. 10.1016/S0079-6123(07)63035-0.

Morganti-Kossmann, M.C., Rancan, M., Otto, V.I., Stahel, P.F., and Kossmann, T. (2001). Role of cerebral inflammation after traumatic brain injury: a revisited concept. Shock *16*, 165-177. 10.1097/00024382-200116030-00001.

Mori, T., and Morimoto, K. (2014). Rabies virus glycoprotein variants display different patterns in rabies monosynaptic tracing. Front Neuroanat *7*, 47. 10.3389/fnana.2013.00047.

Nakamura, T., Hillary, F.G., and Biswal, B.B. (2009). Resting network plasticity following brain injury. PLoS One *4*, e8220. 10.1371/journal.pone.0008220.

National Institute of Neurological Disorders and Stroke (2015). Traumatic

brain injury: hope through research. https://www.ninds.nih.gov/Disorders/Patient-Caregiver-Education/Hope-Through-Research/Traumatic-Brain-Injury-Hope-Through.

Nery, S., Fishell, G., and Corbin, J.G. (2002). The caudal ganglionic eminence is a source of distinct cortical and subcortical cell populations. Nat Neurosci *5*, 1279-1287. 10.1038/nn971.

Nichols, J., Bjorklund, G.R., Newbern, J., and Anderson, T. (2018). Parvalbumin fast-spiking interneurons are selectively altered by paediatric traumatic brain injury. J Physiol *596*, 1277-1293. 10.1113/JP275393.

Nichols, J., Perez, R., Wu, C., Adelson, P.D., and Anderson, T. (2015). Traumatic brain injury induces rapid enhancement of cortical excitability in juvenile rats. CNS Neurosci Ther *21*, 193-203. 10.1111/cns.12351.

Niedworok, C.J., Brown, A.P., Jorge Cardoso, M., Osten, P., Ourselin, S., Modat, M., and Margrie, T.W. (2016). aMAP is a validated pipeline for registration and segmentation of high-resolution mouse brain data. Nat Commun *7*, 11879. 10.1038/ncomms11879.

Nilsson, B., Pontén, U., and Voigt, G. (1977). Experimental head injury in the rat. Part 1: Mechanics, pathophysiology, and morphology in an impact acceleration trauma model. J Neurosurg *47*, 241-251. 10.3171/jns.1977.47.2.0241.

Nilsson, P., Hillered, L., Olsson, Y., Sheardown, M.J., and Hansen, A.J. (1993). Regional changes in interstitial K+ and Ca2+ levels following cortical compression contusion trauma in rats. J Cereb Blood Flow Metab *13*, 183-192. 10.1038/jcbfm.1993.22.

Nilsson, P., Hillered, L., Pontén, U., and Ungerstedt, U. (1990). Changes in cortical extracellular levels of energy-related metabolites and amino acids following concussive brain injury in rats. J Cereb Blood Flow Metab *10*, 631-637. 10.1038/jcbfm.1990.115.

Nitsch, R., Leranth, C., and Frotscher, M. (1990). Most somatostatin-immunoreactive neurons in the rat fascia dentata do not contain the calcium-binding protein parvalbumin. Brain Res *528*, 327-329. 10.1016/0006-8993(90)91676-8.

Norris, C.M., and Scheff, S.W. (2009). Recovery of afferent function and synaptic strength in hippocampal CA1 following traumatic brain injury. J Neurotrauma *26*, 2269-2278. 10.1089/neu.2009.1029.

Obenaus, A., Esclapez, M., and Houser, C.R. (1993). Loss of glutamate decarboxylase mRNA-containing neurons in the rat dentate gyrus following pilocarpine-induced seizures. J Neurosci *13*, 4470-4485.

Oliva, A.A., Jiang, M., Lam, T., Smith, K.L., and Swann, J.W. (2000). Novel hippocampal interneuronal subtypes identified using transgenic mice that express green fluorescent protein in GABAergic interneurons. J Neurosci *20*, 3354-3368.

Olivas, N.D., Quintanar-Zilinskas, V., Nenadic, Z., and Xu, X. (2012). Laminar circuit organization and response modulation in mouse visual cortex. Front Neural Circuits *6*, 70. 10.3389/fncir.2012.00070.

Ommaya, A.K., Grubb, R.L., and Naumann, R.A. (1971). Coup and contre-coup injury: observations on the mechanics of visible brain injuries in the rhesus monkey. J Neurosurg *35*, 503-516. 10.3171/jns.1971.35.5.0503.

Overstreet-Wadiche, L., and McBain, C.J. (2015). Neurogliaform cells in cortical circuits. Nat Rev Neurosci *16*, 458-468. 10.1038/nrn3969.

Padula, W.V., Argyris, S., and Ray, J. (1994). Visual evoked potentials (VEP) evaluating treatment for post-trauma vision syndrome (PTVS) in patients with traumatic brain injuries (TBI). Brain Inj *8*, 125-133. 10.3109/02699059409150964.

Pan, C., Cai, R., Quacquarelli, F.P., Ghasemigharagoz, A., Lourbopoulos, A., Matryba, P., Plesnila, N., Dichgans, M., Hellal, F., and Ertürk, A. (2016). Shrinkage-mediated imaging of entire organs and organisms using uDISCO. Nat Methods *13*, 859-867. 10.1038/nmeth.3964.

Parga Becerra, A., Logsdon, A.F., Banks, W.A., and Ransom, C.B. (2021). Traumatic Brain Injury Broadly Affects GABAergic Signaling in Dentate Gyrus Granule Cells. eNeuro *8*. 10.1523/ENEURO.0055-20.2021.

Parkin, A.J., Rees, J.E., Hunkin, N.M., and Rose, P.E. (1994). Impairment of memory following discrete thalamic infarction. Neuropsychologia *32*, 39-51. 10.1016/0028-3932(94)90067-1.

Pavlov, I., Huusko, N., Drexel, M., Kirchmair, E., Sperk, G., Pitkänen, A., and Walker, M.C. (2011). Progressive loss of phasic, but not tonic, GABAA receptor-mediated inhibition in dentate granule cells in a model of post-traumatic epilepsy in rats. Neuroscience *194*, 208-219. 10.1016/j.neuroscience.2011.07.074.

Pelkey, K.A., Chittajallu, R., Craig, M.T., Tricoire, L., Wester, J.C., and McBain, C.J. (2017). Hippocampal GABAergic Inhibitory Interneurons. Physiol Rev *97*, 1619-1747. 10.1152/physrev.00007.2017.

Pelli, D.G. (1997). The VideoToolbox software for visual psychophysics: transforming numbers into movies. Spat Vis *10*, 437-442.

Peng, Z., Zhang, N., Wei, W., Huang, C.S., Cetina, Y., Otis, T.S., and Houser, C.R. (2013). A reorganized GABAergic circuit in a model of epilepsy: evidence from optogenetic labeling and stimulation of somatostatin interneurons. J Neurosci *33*, 14392-14405. 10.1523/JNEUROSCI.2045-13.2013.

Pesold, C., Impagnatiello, F., Pisu, M.G., Uzunov, D.P., Costa, E., Guidotti, A., and Caruncho, H.J. (1998). Reelin is preferentially expressed in neurons synthesizing gamma-aminobutyric acid in cortex and hippocampus of adult rats. Proc Natl Acad Sci U S A *95*, 3221-3226. 10.1073/pnas.95.6.3221.

Pignatelli, M., Ryan, T.J., Roy, D.S., Lovett, C., Smith, L.M., Muralidhar, S., and Tonegawa, S. (2019). Engram Cell Excitability State Determines the Efficacy of Memory Retrieval. Neuron *101*, 274-284.e275. 10.1016/j.neuron.2018.11.029.

Pischiutta, F., Micotti, E., Hay, J.R., Marongiu, I., Sammali, E., Tolomeo, D., Vegliante, G., Stocchetti, N., Forloni, G., De Simoni, M.G., et al. (2018). Single severe traumatic brain injury produces progressive pathology with ongoing contralateral white matter damage one year after injury. Exp Neurol *300*, 167-178. 10.1016/j.expneurol.2017.11.003.

Pleasant, J.M., Carlson, S.W., Mao, H., Scheff, S.W., Yang, K.H., and Saatman, K.E. (2011). Rate of neurodegeneration in the mouse controlled cortical impact model is influenced by impactor tip shape: implications for mechanistic and therapeutic studies. J Neurotrauma *28*, 2245-2262. 10.1089/neu.2010.1499.

Pollak Dorocic, I., Fürth, D., Xuan, Y., Johansson, Y., Pozzi, L., Silberberg, G., Carlén, M., and Meletis, K. (2014). A whole-brain atlas of inputs to serotonergic neurons of the dorsal and median raphe nuclei. Neuron *83*, 663-678. 10.1016/j.neuron.2014.07.002.

Ponsford, J., Draper, K., and Schönberger, M. (2008). Functional outcome 10 years after traumatic brain injury: its relationship with demographic, injury severity, and cognitive and emotional status. J Int Neuropsychol Soc *14*, 233-242. 10.1017/S1355617708080272.

Povlishock, J.T., and Katz, D.I. (2005). Update of neuropathology and neurological recovery after traumatic brain injury. J Head Trauma Rehabil *20*, 76-94. 10.1097/00001199-200501000-00008.

Priya, R., Rakela, B., Kaneko, M., Spatazza, J., Larimer, P., Hoseini, M.S., Hasenstaub, A.R., Alvarez-Buylla, A., and Stryker, M.P. (2019). Vesicular GABA Transporter Is Necessary for Transplant-Induced Critical Period Plasticity in Mouse Visual Cortex. J Neurosci *39*, 2635-2648. 10.1523/JNEUROSCI.1253-18.2019.

Purpura, D.P., and Housepain, E.M. (1961). Morphological and physiological properties of chronically isolated immature neocortex. Exp Neurol *4*, 377-401. 10.1016/0014-4886(61)90025-5.

Qi, Y., Yu, T., Xu, J., Wan, P., Ma, Y., Zhu, J., Li, Y., Gong, H., Luo, Q., and Zhu, D. (2019). FDISCO: Advanced solvent-based clearing method for imaging whole organs. Sci Adv *5*, eaau8355. 10.1126/sciadv.aau8355.

Ragan, T., Kadiri, L.R., Venkataraju, K.U., Bahlmann, K., Sutin, J., Taranda, J., Arganda-Carreras, I., Kim, Y., Seung, H.S., and Osten, P. (2012). Serial two-photon tomography for automated ex vivo mouse brain imaging. Nat Methods *9*, 255-258. 10.1038/nmeth.1854.

Raible, D.J., Frey, L.C., Del Angel, Y.C., Carlsen, J., Hund, D., Russek, S.J., Smith, B., and Brooks-Kayal, A.R. (2015). JAK/STAT pathway regulation of GABAA receptor expression after differing severities of experimental TBI. Exp Neurol *271*, 445-456. 10.1016/j.expneurol.2015.07.001.

Ramos, B., Baglietto-Vargas, D., del Rio, J.C., Moreno-Gonzalez, I., Santa-Maria, C., Jimenez, S., Caballero, C., Lopez-Tellez, J.F., Khan, Z.U., Ruano, D., et al. (2006). Early neuropathology of somatostatin/NPY GABAergic cells in the hippocampus of a PS1xAPP transgenic model of Alzheimer's disease. Neurobiol Aging *27*, 1658-1672. 10.1016/j.neurobiolaging.2005.09.022.

Rao, V., and Lyketsos, C. (2000). Neuropsychiatric sequelae of traumatic brain injury. Psychosomatics *41*, 95-103. 10.1176/appi.psy.41.2.95.

Raza, S.A., Albrecht, A., Çalışkan, G., Müller, B., Demiray, Y.E., Ludewig, S., Meis, S., Faber, N., Hartig, R., Schraven, B., et al. (2017). HIPP neurons in the dentate gyrus mediate the cholinergic modulation of background context memory salience. Nat Commun *8*, 189. 10.1038/s41467-017-00205-3.

Reardon, T.R., Murray, A.J., Turi, G.F., Wirblich, C., Croce, K.R., Schnell, M.J., Jessell, T.M., and Losonczy, A. (2016). Rabies Virus CVS-N2c(ΔG) Strain Enhances Retrograde Synaptic Transfer and Neuronal Viability. Neuron *89*, 711-724. 10.1016/j.neuron.2016.01.004.

Renier, N., Adams, E.L., Kirst, C., Wu, Z., Azevedo, R., Kohl, J., Autry, A.E., Kadiri, L., Umadevi Venkataraju, K., Zhou, Y., et al. (2016). Mapping of Brain Activity by Automated Volume Analysis of Immediate Early Genes. Cell *165*, 1789-1802. 10.1016/j.cell.2016.05.007.

Renier, N., Wu, Z., Simon, D.J., Yang, J., Ariel, P., and Tessier-Lavigne, M. (2014). iDISCO: a simple, rapid method to immunolabel large tissue samples for volume imaging. Cell *159*, 896-910. 10.1016/j.cell.2014.10.010.

Rennó-Costa, C., Lisman, J.E., and Verschure, P.F. (2010). The mechanism of rate remapping in the dentate gyrus. Neuron *68*, 1051-1058. 10.1016/j.neuron.2010.11.024.

Ribak, C.E., and Reiffenstein, R.J. (1982). Selective inhibitory synapse loss in chronic cortical slabs: a morphological basis for epileptic susceptibility. Can J Physiol Pharmacol *60*, 864-870. 10.1139/y82-122.

Robbins, R.J., Brines, M.L., Kim, J.H., Adrian, T., de Lanerolle, N., Welsh, S., and Spencer, D.D. (1991). A selective loss of somatostatin in the hippocampus of patients with temporal lobe epilepsy. Ann Neurol *29*, 325-332. 10.1002/ana.410290316.

Rodríguez-Baeza, A., Reina-de la Torre, F., Poca, A., Martí, M., and Garnacho, A. (2003). Morphological features in human cortical brain microvessels after head injury: a three-dimensional and immunocytochemical study. Anat Rec A Discov Mol Cell Evol Biol *273*, 583-593. 10.1002/ar.a.10069.

Rowland, D.C., Obenhaus, H.A., Skytøen, E.R., Zhang, Q., Kentros, C.G., Moser, E.I., and Moser, M.B. (2018). Functional properties of stellate cells in medial entorhinal cortex layer II. Elife *7*. 10.7554/eLife.36664.

Royer, S., Zemelman, B.V., Losonczy, A., Kim, J., Chance, F., Magee, J.C., and Buzsáki, G. (2012). Control of timing, rate and bursts of hippocampal place cells by dendritic and somatic inhibition. Nat Neurosci *15*, 769-775. 10.1038/nn.3077.

Rudy, B., Fishell, G., Lee, S., and Hjerling-Leffler, J. (2011). Three groups of interneurons account for nearly 100% of neocortical GABAergic neurons. Dev Neurobiol *71*, 45-61. 10.1002/dneu.20853.

Ruff, R.M., and Jurica, P. (1999). In search of a unified definition for mild traumatic brain injury. Brain Inj *13*, 943-952. 10.1080/026990599120963.

Rust, M.J., Bates, M., and Zhuang, X. (2006). Sub-diffraction-limit imaging by stochastic optical reconstruction microscopy (STORM). Nat Methods *3*, 793-795. 10.1038/nmeth929.

Rutland-Brown, W., Langlois, J.A., Thomas, K.E., and Xi, Y.L. (2006). Incidence of traumatic brain injury in the United States, 2003. J Head Trauma Rehabil *21*, 544-548. 10.1097/00001199-200611000-00009.

Saatman, K.E., Duhaime, A.C., Bullock, R., Maas, A.I., Valadka, A., Manley, G.T., and Members, W.S.T.a.A.P. (2008). Classification of traumatic brain injury for targeted therapies. J Neurotrauma *25*, 719-738. 10.1089/neu.2008.0586.

Saatman, K.E., Feeko, K.J., Pape, R.L., and Raghupathi, R. (2006). Differential behavioral and histopathological responses to graded cortical impact injury in mice. J Neurotrauma *23*, 1241-1253. 10.1089/neu.2006.23.1241.

Salazar, A.M., Jabbari, B., Vance, S.C., Grafman, J., Amin, D., and Dillon, J.D. (1985). Epilepsy after penetrating head injury. I. Clinical correlates: a report of the Vietnam Head Injury Study. Neurology *35*, 1406-1414. 10.1212/wnl.35.10.1406.

Salin, P., Tseng, G.F., Hoffman, S., Parada, I., and Prince, D.A. (1995). Axonal sprouting in layer V pyramidal neurons of chronically injured cerebral cortex. J Neurosci *15*, 8234-8245.

Sano, K., Nakamura, N., Hirakawa, K., Masuzawa, H., and Hashizume, K. (1967). Mechanism and dynamics of closed head injuries (preliminary report). Neurol Med Chir (Tokyo) *9*, 21-33. 10.2176/nmc.9.21.

Santhakumar, V., Bender, R., Frotscher, M., Ross, S.T., Hollrigel, G.S., Toth, Z., and Soltesz, I. (2000). Granule cell hyperexcitability in the early post-traumatic rat dentate gyrus: the 'irritable mossy cell' hypothesis. J Physiol *524 Pt 1*, 117-134.

Satoh, J., Tabira, T., Sano, M., Nakayama, H., and Tateishi, J. (1991). Parvalbumin-immunoreactive neurons in the human central nervous system are decreased in Alzheimer's disease. Acta Neuropathol *81*, 388-395.

Scharfman, H.E., Goodman, J.H., and Sollas, A.L. (1999). Actions of brain-derived neurotrophic factor in slices from rats with spontaneous seizures and mossy fiber sprouting in the dentate gyrus. J Neurosci *19*, 5619-5631.

Scharfman, H.E., and Schwartzkroin, P.A. (1989). Protection of dentate hilar cells from prolonged stimulation by intracellular calcium chelation. Science *246*, 257-260. 10.1126/science.2508225.
Scheff, S.W., Baldwin, S.A., Brown, R.W., and Kraemer, P.J. (1997). Morris water maze deficits in rats following traumatic brain injury: lateral controlled cortical impact. J Neurotrauma *14*, 615-627. 10.1089/neu.1997.14.615.

Scheff, S.W., Price, D.A., Hicks, R.R., Baldwin, S.A., Robinson, S., and Brackney, C. (2005). Synaptogenesis in the hippocampal CA1 field following traumatic brain injury. J Neurotrauma *22*, 719-732. 10.1089/neu.2005.22.719.

Scheggia, D., Managò, F., Maltese, F., Bruni, S., Nigro, M., Dautan, D., Latuske, P., Contarini, G., Gomez-Gonzalo, M., Requie, L.M., et al. (2020). Somatostatin interneurons in the prefrontal cortex control affective state discrimination in mice. Nat Neurosci *23*, 47-60. 10.1038/s41593-019-0551-8.

Schiavone, S., Neri, M., Trabace, L., and Turillazzi, E. (2017). The NADPH oxidase NOX2 mediates loss of parvalbumin interneurons in traumatic brain injury: human autoptic immunohistochemical evidence. Sci Rep *7*, 8752. 10.1038/s41598-017-09202-4.

Schmidt, R.H., and Grady, M.S. (1995). Loss of forebrain cholinergic neurons following fluid-percussion injury: implications for cognitive impairment in closed head injury. J Neurosurg *83*, 496-502. 10.3171/jns.1995.83.3.0496.

Schmitt, J.M., and Kumar, G. (1996). Turbulent nature of refractive-index variations in biological tissue. Opt Lett *21*, 1310-1312. 10.1364/ol.21.001310.

Schmued, L.C., Stowers, C.C., Scallet, A.C., and Xu, L. (2005). Fluoro-Jade C results in ultra high resolution and contrast labeling of degenerating neurons. Brain Res *1035*, 24-31. 10.1016/j.brainres.2004.11.054.

Scholten, A.C., Haagsma, J.A., Andriessen, T.M., Vos, P.E., Steyerberg, E.W., van Beeck, E.F., and Polinder, S. (2015). Health-related quality of life after mild, moderate and severe traumatic brain injury: patterns and predictors of suboptimal functioning during the first year after injury. Injury *46*, 616-624. 10.1016/j.injury.2014.10.064.

Schuman, B., Machold, R.P., Hashikawa, Y., Fuzik, J., Fishell, G.J., and Rudy, B. (2019). Four Unique Interneuron Populations Reside in Neocortical Layer 1. J Neurosci *39*, 125-139. 10.1523/JNEUROSCI.1613-18.2018.

Schwab, N., Wennberg, R., Grenier, K., Tartaglia, C., Tator, C., and Hazrati, L.N. (2021). Association of Position Played and Career Duration and Chronic Traumatic Encephalopathy at Autopsy in Elite Football and Hockey Players. Neurology *96*, e1835-e1843. 10.1212/WNL.0000000000011668.

Seeman, S.C., Campagnola, L., Davoudian, P.A., Hoggarth, A., Hage, T.A., Bosma-Moody, A., Baker, C.A., Lee, J.H., Mihalas, S., Teeter, C., et al. (2018). Sparse recurrent excitatory connectivity in the microcircuit of the adult mouse and human cortex. Elife *7*. 10.7554/eLife.37349.

Semple, B.D., O'Brien, T.J., Gimlin, K., Wright, D.K., Kim, S.E., Casillas-Espinosa, P.M., Webster, K.M., Petrou, S., and Noble-Haeusslein, L.J. (2017). Interleukin-1 Receptor in Seizure Susceptibility after Traumatic Injury to the Pediatric Brain. J Neurosci *37*, 7864-7877. 10.1523/JNEUROSCI.0982-17.2017.

Sharp, D.J., Scott, G., and Leech, R. (2014). Network dysfunction after traumatic brain injury. Nat Rev Neurol *10*, 156-166. 10.1038/nrneurol.2014.15.

Shibley, H., and Smith, B.N. (2002). Pilocarpine-induced status epilepticus results in mossy fiber sprouting and spontaneous seizures in C57BL/6 and CD-1 mice. Epilepsy Res *49*, 109-120. 10.1016/s0920-1211(02)00012-8.

Shlosberg, D., Benifla, M., Kaufer, D., and Friedman, A. (2010). Blood-brain barrier breakdown as a therapeutic target in traumatic brain injury. Nat Rev Neurol *6*, 393-403. 10.1038/nrneurol.2010.74.

Silberberg, G., and Markram, H. (2007). Disynaptic inhibition between neocortical pyramidal cells mediated by Martinotti cells. Neuron *53*, 735-746. 10.1016/j.neuron.2007.02.012.

Sillito, A.M., Salt, T.E., and Kemp, J.A. (1985). Modulatory and inhibitory processes in the visual cortex. Vision Res *25*, 375-381. 10.1016/0042-6989(85)90062-8.

Silverman, I.E., Galetta, S.L., Gray, L.G., Moster, M., Atlas, S.W., Maurer, A.H., and Alavi, A. (1993). SPECT in patients with cortical visual loss. J Nucl Med *34*, 1447-1451.

Simchick, G., Scheulin, K.M., Sun, W., Sneed, S.E., Fagan, M.M., Cheek, S.R., West, F.D., and Zhao, Q. (2021). Detecting functional connectivity disruptions in a translational pediatric traumatic brain injury porcine model using resting-state and task-based fMRI. Sci Rep *11*, 12406. 10.1038/s41598-021-91853-5.

Sloviter, R.S. (1982). A simplified Timm stain procedure compatible with formaldehyde fixation and routine paraffin embedding of rat brain. Brain Res Bull *8*, 771-774. 10.1016/0361-9230(82)90104-6.

Sloviter, R.S. (1987). Decreased hippocampal inhibition and a selective loss of interneurons in experimental epilepsy. Science *235*, 73-76. 10.1126/science.2879352.

Smith, D.H., Soares, H.D., Pierce, J.S., Perlman, K.G., Saatman, K.E., Meaney, D.F., Dixon, C.E., and McIntosh, T.K. (1995). A model of parasagittal controlled cortical impact in the mouse: cognitive and histopathologic effects. J Neurotrauma *12*, 169-178. 10.1089/neu.1995.12.169.

Soares, H.D., Thomas, M., Cloherty, K., and McIntosh, T.K. (1992). Development of prolonged focal cerebral edema and regional cation changes following experimental brain injury in the rat. J Neurochem *58*, 1845-1852. 10.1111/j.1471-4159.1992.tb10061.x.

Sofroniew, N.J., Flickinger, D., King, J., and Svoboda, K. (2016). A large field of view two-photon mesoscope with subcellular resolution for in vivo imaging. Elife *5*. 10.7554/eLife.14472.

Somogyi, P., Hodgson, A.J., Smith, A.D., Nunzi, M.G., Gorio, A., and Wu, J.Y. (1984). Different populations of GABAergic neurons in the visual cortex and hippocampus of cat contain somatostatin- or cholecystokinin-immunoreactive material. J Neurosci *4*, 2590-2603.

Southwell, D.G., Froemke, R.C., Alvarez-Buylla, A., Stryker, M.P., and Gandhi, S.P. (2010). Cortical plasticity induced by inhibitory neuron transplantation. Science *327*, 1145-1148. 10.1126/science.1183962.

Spalteholz, W. (1911). Über das Durchsichtigmachen von Menchlichen und Tierichen Präparaten und Seine Theoretischen Bedingungen. S. Hirzel.

Spruston, N. (2008). Pyramidal neurons: dendritic structure and synaptic integration. Nat Rev Neurosci *9*, 206-221. 10.1038/nrn2286.

Stanco, A., Pla, R., Vogt, D., Chen, Y., Mandal, S., Walker, J., Hunt, R.F., Lindtner, S., Erdman, C.A., Pieper, A.A., et al. (2014). NPAS1 represses the generation of specific subtypes of cortical interneurons. Neuron *84*, 940-953. 10.1016/j.neuron.2014.10.040.

Statler, K.D., Scheerlinck, P., Pouliot, W., Hamilton, M., White, H.S., and Dudek, F.E. (2009). A potential model of pediatric posttraumatic epilepsy. Epilepsy Res *86*, 221-223. 10.1016/j.eplepsyres.2009.05.006.

Stefanelli, T., Bertollini, C., Lüscher, C., Muller, D., and Mendez, P. (2016). Hippocampal Somatostatin Interneurons Control the Size of Neuronal Memory Ensembles. Neuron *89*, 1074-1085. 10.1016/j.neuron.2016.01.024.

Stelmack, J.A., Frith, T., Van Koevering, D., Rinne, S., and Stelmack, T.R. (2009). Visual function in patients followed at a Veterans Affairs polytrauma network site: an electronic medical record review. Optometry *80*, 419-424. 10.1016/j.optm.2009.02.011.

Steward, O. (1976). Topographic organization of the projections from the entorhinal area to the hippocampal formation of the rat. J Comp Neurol *167*, 285-314. 10.1002/cne.901670303.

Suh, S., Choi, E.H., Leinonen, H., Foik, A.T., Newby, G.A., Yeh, W.H., Dong, Z., Kiser, P.D., Lyon, D.C., Liu, D.R., and Palczewski, K. (2021). Restoration of visual function in adult mice with an inherited retinal disease via adenine base editing. Nat Biomed Eng *5*, 169-178. 10.1038/s41551-020-00632-6.

Sun, L., Tang, Y., Yan, K., Yu, J., Zou, Y., Xu, W., Xiao, K., Zhang, Z., Li, W., Wu, B., et al. (2019a). Differences in neurotropism and neurotoxicity among retrograde viral tracers. Mol Neurodegener *14*, 8. 10.1186/s13024-019-0308-6.

Sun, Q., Li, X., Ren, M., Zhao, M., Zhong, Q., Ren, Y., Luo, P., Ni, H., Zhang, X., Zhang, C., et al. (2019b). A whole-brain map of long-range inputs to GABAergic interneurons in the mouse medial prefrontal cortex. Nat Neurosci *22*, 1357-1370. 10.1038/s41593-019-0429-9.

Sun, Y., Nguyen, A.Q., Nguyen, J.P., Le, L., Saur, D., Choi, J., Callaway, E.M., and Xu, X. (2014). Cell-type-specific circuit connectivity of hippocampal CA1 revealed through Cre-dependent rabies tracing. Cell Rep *7*, 269-280. 10.1016/j.celrep.2014.02.030.

Sun, Z., Liu, S., Kharlamov, E.A., Miller, E.R., and Kelly, K.M. (2018). Hippocampal neuropeptide Y protein expression following controlled cortical impact and posttraumatic epilepsy. Epilepsy Behav *87*, 188-194. 10.1016/j.yebeh.2018.08.002.

Sutula, T., Cascino, G., Cavazos, J., Parada, I., and Ramirez, L. (1989). Mossy fiber synaptic reorganization in the epileptic human temporal lobe. Ann Neurol *26*, 321-330. 10.1002/ana.410260303.

Swartz, B.E., Houser, C.R., Tomiyasu, U., Walsh, G.O., DeSalles, A., Rich, J.R., and Delgado-Escueta, A. (2006). Hippocampal cell loss in posttraumatic human epilepsy. Epilepsia *47*, 1373-1382. 10.1111/j.1528-1167.2006.00602.x.

Szabadics, J., Lorincz, A., and Tamás, G. (2001). Beta and gamma frequency synchronization by dendritic gabaergic synapses and gap junctions in a network of cortical interneurons. J Neurosci *21*, 5824-5831.

Sziklas, V., and Petrides, M. (2007). Contribution of the anterior thalamic nuclei to conditional learning in rats. Hippocampus *17*, 456-461. 10.1002/hipo.20286.

Szu, J.I., Chaturvedi, S., Patel, D.D., and Binder, D.K. (2020). Aquaporin-4 Dysregulation in a Controlled Cortical Impact Injury Model of Posttraumatic Epilepsy. Neuroscience *428*, 140-153. 10.1016/j.neuroscience.2019.12.006.

Tamamaki, N., Fujimori, K.E., and Takauji, R. (1997). Origin and route of tangentially migrating neurons in the developing neocortical intermediate zone. J Neurosci *17*, 8313-8323.

Tamamaki, N., Yanagawa, Y., Tomioka, R., Miyazaki, J., Obata, K., and Kaneko, T. (2003). Green fluorescent protein expression and colocalization with calretinin, parvalbumin, and somatostatin in the GAD67-GFP knock-in mouse. J Comp Neurol *467*, 60-79. 10.1002/cne.10905.

Taylor, B.C., Hagel, E.M., Carlson, K.F., Cifu, D.X., Cutting, A., Bidelspach, D.E., and Sayer, N.A. (2012). Prevalence and costs of co-occurring traumatic brain injury with and without psychiatric disturbance and pain among Afghanistan and Iraq War Veteran V.A. users. Med Care *50*, 342-346. 10.1097/MLR.0b013e318245a558.

Taş, Y., Solaroğlu, İ., and Gürsoy-Özdemir, Y. (2019). Spreading Depolarization Waves in Neurological Diseases: A Short Review about its Pathophysiology and Clinical Relevance. Curr Neuropharmacol *17*, 151-164. 10.2174/1570159X15666170915160707.

Teasdale, G., and Jennett, B. (1974). Assessment of coma and impaired consciousness. A practical scale. Lancet *2*, 81-84. 10.1016/s0140-6736(74)91639-0.

Tong, L.M., Djukic, B., Arnold, C., Gillespie, A.K., Yoon, S.Y., Wang, M.M., Zhang, O., Knoferle, J., Rubenstein, J.L., Alvarez-Buylla, A., and Huang, Y. (2014). Inhibitory interneuron progenitor transplantation restores normal learning and memory in ApoE4 knock-in mice without or with Aβ accumulation. J Neurosci *34*, 9506-9515. 10.1523/JNEUROSCI.0693-14.2014.

Tornero, D., Tsupykov, O., Granmo, M., Rodriguez, C., Grønning-Hansen, M., Thelin, J., Smozhanik, E., Laterza, C., Wattananit, S., Ge, R., et al. (2017). Synaptic inputs from stroke-injured brain to grafted human stem cell-derived neurons activated by sensory stimuli. Brain *140*, 692-706. 10.1093/brain/aww347.

Toth, Z., Hollrigel, G.S., Gorcs, T., and Soltesz, I. (1997). Instantaneous perturbation of dentate interneuronal networks by a pressure wave-transient delivered to the neocortex. J Neurosci *17*, 8106-8117.

Tremblay, R., Lee, S., and Rudy, B. (2016). GABAergic Interneurons in the Neocortex: From Cellular Properties to Circuits. Neuron *91*, 260-292. 10.1016/j.neuron.2016.06.033.

Tricoire, L., Pelkey, K.A., Erkkila, B.E., Jeffries, B.W., Yuan, X., and McBain, C.J. (2011). A blueprint for the spatiotemporal origins of mouse hippocampal interneuron diversity. J Neurosci *31*, 10948-10970. 10.1523/JNEUROSCI.0323-11.2011.

Tricoire, L., and Vitalis, T. (2012). Neuronal nitric oxide synthase expressing neurons: a journey from birth to neuronal circuits. Front Neural Circuits *6*, 82. 10.3389/fncir.2012.00082.

Tsiang, H., Koulakoff, A., Bizzini, B., and Berwald-Netter, Y. (1983). Neurotropism of rabies virus. An in vitro study. J Neuropathol Exp Neurol *42*, 439-452. 10.1097/00005072-198307000-00006.

Tubi, M.A., Lutkenhoff, E., Blanco, M.B., McArthur, D., Villablanca, P., Ellingson, B., Diaz-Arrastia, R., Van Ness, P., Real, C., Shrestha, V., et al. (2019). Early seizures and temporal lobe trauma predict post-traumatic epilepsy: A longitudinal study. Neurobiol Dis *123*, 115-121. 10.1016/j.nbd.2018.05.014.

Tucker, T.R., and Fitzpatrick, D. (2006). Luminance-evoked inhibition in primary visual cortex: a transient veto of simultaneous and ongoing response. J Neurosci *26*, 13537-13547. 10.1523/JNEUROSCI.3723-06.2006.

Tyson, A.L., Rousseau, C.V., Niedworok, C.J., Keshavarzi, S., Tsitoura, C., Cossell, L., Strom, M., and Margrie, T.W. (2021). A deep learning algorithm for 3D cell detection in whole mouse brain image datasets. PLoS Comput Biol *17*, e1009074. 10.1371/journal.pcbi.1009074.

Udakis, M., Pedrosa, V., Chamberlain, S.E.L., Clopath, C., and Mellor, J.R. (2020). Interneuron-specific plasticity at parvalbumin and somatostatin inhibitory synapses onto CA1 pyramidal neurons shapes hippocampal output. Nat Commun *11*, 4395. 10.1038/s41467-020-18074-8.

Ueda, H.R., Dodt, H.U., Osten, P., Economo, M.N., Chandrashekar, J., and Keller, P.J. (2020a). Whole-Brain Profiling of Cells and Circuits in Mammals by Tissue Clearing and Light-Sheet Microscopy. Neuron *106*, 369-387. 10.1016/j.neuron.2020.03.004.

Ueda, H.R., Ertürk, A., Chung, K., Gradinaru, V., Chédotal, A., Tomancak, P., and Keller, P.J. (2020b). Tissue clearing and its applications in neuroscience. Nat Rev Neurosci *21*, 61-79. 10.1038/s41583-019-0250-1.

Van den Bergh, G., Zhang, B., Arckens, L., and Chino, Y.M. (2010). Receptive-field properties of V1 and V2 neurons in mice and macaque monkeys. J Comp Neurol *518*, 2051-2070. 10.1002/cne.22321.

Varga, C., Lee, S.Y., and Soltesz, I. (2010). Target-selective GABAergic control of entorhinal cortex output. Nat Neurosci *13*, 822-824. 10.1038/nn.2570.

Vascak, M., Jin, X., Jacobs, K.M., and Povlishock, J.T. (2018). Mild Traumatic Brain Injury Induces Structural and Functional Disconnection of Local Neocortical Inhibitory Networks via Parvalbumin Interneuron Diffuse Axonal Injury. Cereb Cortex *28*, 1625-1644. 10.1093/cercor/bhx058.

Vaughn, M.G., Salas-Wright, C.P., John, R., Holzer, K.J., Qian, Z., and Veeh, C. (2019). Traumatic Brain Injury and Psychiatric Co-Morbidity in the United States. Psychiatr Q *90*, 151-158. 10.1007/s11126-018-9617-0.

Vivar, C., Potter, M.C., Choi, J., Lee, J.Y., Stringer, T.P., Callaway, E.M., Gage, F.H., Suh, H., and van Praag, H. (2012). Monosynaptic inputs to new neurons in the dentate gyrus. Nat Commun *3*, 1107. 10.1038/ncomms2101.

Vogt, D., Hunt, R.F., Mandal, S., Sandberg, M., Silberberg, S.N., Nagasawa, T., Yang, Z., Baraban, S.C., and Rubenstein, J.L. (2014). Lhx6 directly regulates Arx and CXCR7 to determine cortical interneuron fate and laminar position. Neuron *82*, 350-364. 10.1016/j.neuron.2014.02.030.

Voie, A.H., Burns, D.H., and Spelman, F.A. (1993). Orthogonal-plane fluorescence optical sectioning: three-dimensional imaging of macroscopic biological specimens. J Microsc *170*, 229-236. 10.1111/j.1365-2818.1993.tb03346.x.

Vonder Haar, C., Friend, D.M., Mudd, D.B., and Smith, J.S. (2013). Successive bilateral frontal controlled cortical impact injuries show behavioral savings. Behav Brain Res *240*, 153-159. 10.1016/j.bbr.2012.11.029.

Vélez-Fort, M., Rousseau, C.V., Niedworok, C.J., Wickersham, I.R., Rancz, E.A., Brown, A.P., Strom, M., and Margrie, T.W. (2014). The stimulus selectivity and connectivity of layer six principal cells reveals cortical microcircuits underlying visual processing. Neuron *83*, 1431-1443. 10.1016/j.neuron.2014.08.001.

Wang, Q., and Burkhalter, A. (2007). Area map of mouse visual cortex. J Comp Neurol *502*, 339-357. 10.1002/cne.21286.

Wang, Q., Ding, S.L., Li, Y., Royall, J., Feng, D., Lesnar, P., Graddis, N., Naeemi, M., Facer, B., Ho, A., et al. (2020). The Allen Mouse Brain Common Coordinate Framework: A 3D Reference Atlas. Cell *181*, 936-953.e920. 10.1016/j.cell.2020.04.007.

Watabe-Uchida, M., Zhu, L., Ogawa, S.K., Vamanrao, A., and Uchida, N. (2012). Whole-brain mapping of direct inputs to midbrain dopamine neurons. Neuron *74*, 858-873. 10.1016/j.neuron.2012.03.017.

Wendling, F., Bartolomei, F., Bellanger, J.J., and Chauvel, P. (2002). Epileptic fast activity can be explained by a model of impaired GABAergic dendritic inhibition. Eur J Neurosci *15*, 1499-1508. 10.1046/j.1460-9568.2002.01985.x.

Werner, C., and Engelhard, K. (2007). Pathophysiology of traumatic brain injury. Br J Anaesth *99*, 4-9. 10.1093/bja/aem131.

Wichterle, H., Garcia-Verdugo, J.M., Herrera, D.G., and Alvarez-Buylla, A. (1999). Young neurons from medial ganglionic eminence disperse in adult and embryonic brain. Nat Neurosci *2*, 461-466. 10.1038/8131.

Wichterle, H., Turnbull, D.H., Nery, S., Fishell, G., and Alvarez-Buylla, A. (2001). In utero fate mapping reveals distinct migratory pathways and fates of neurons born in the mammalian basal forebrain. Development *128*, 3759-3771.

Wickersham, I.R., Finke, S., Conzelmann, K.K., and Callaway, E.M. (2007a). Retrograde neuronal tracing with a deletion-mutant rabies virus. Nat Methods *4*, 47-49. 10.1038/nmeth999.

Wickersham, I.R., Lyon, D.C., Barnard, R.J., Mori, T., Finke, S., Conzelmann, K.K., Young, J.A., and Callaway, E.M. (2007b). Monosynaptic restriction of transsynaptic tracing from single, genetically targeted neurons. Neuron *53*, 639-647. 10.1016/j.neuron.2007.01.033.

Wiesel, T.N. (1982). Postnatal development of the visual cortex and the influence of environment. Nature *299*, 583-591. 10.1038/299583a0.

Witgen, B.M., Lifshitz, J., Smith, M.L., Schwarzbach, E., Liang, S.L., Grady, M.S., and Cohen, A.S. (2005). Regional hippocampal alteration associated with cognitive deficit following experimental brain injury: a systems, network and cellular evaluation. Neuroscience *133*, 1-15. 10.1016/j.neuroscience.2005.01.052.

Wittner, L., Henze, D.A., Záborszky, L., and Buzsáki, G. (2006). Hippocampal CA3 pyramidal cells selectively innervate aspiny interneurons. Eur J Neurosci *24*, 1286-1298. 10.1111/j.1460-9568.2006.04992.x.

Wonders, C.P., and Anderson, S.A. (2006). The origin and specification of cortical interneurons. Nat Rev Neurosci *7*, 687-696. 10.1038/nrn1954.

Woodward, A., Hashikawa, T., Maeda, M., Kaneko, T., Hikishima, K., Iriki, A., Okano, H., and Yamaguchi, Y. (2018). The Brain/MINDS 3D digital marmoset brain atlas. Sci Data *5*, 180009. 10.1038/sdata.2018.9.

Wurtman, R.J. (1992). Choline metabolism as a basis for the selective vulnerability of cholinergic neurons. Trends Neurosci *15*, 117-122. 10.1016/0166-2236(92)90351-8.

Xiao, D., and Barbas, H. (2002). Pathways for emotions and memory II. Afferent input to the anterior thalamic nuclei from prefrontal, temporal, hypothalmaic areas and the basal ganglia in the rhesus monkey. Thalamus & Related Systems *2*, 33-48.

Xu, F., Shen, Y., Ding, L., Yang, C.Y., Tan, H., Wang, H., Zhu, Q., Xu, R., Wu, F., Xiao, Y., et al. (2021). High-throughput mapping of a whole rhesus monkey brain at micrometer resolution. Nat Biotechnol. 10.1038/s41587-021-00986-5.

Xu, H., Liu, L., Tian, Y., Wang, J., Li, J., Zheng, J., Zhao, H., He, M., Xu, T.L., and Duan, S. (2019). A Disinhibitory Microcircuit Mediates Conditioned Social Fear in the Prefrontal Cortex. Neuron. 10.1016/j.neuron.2019.02.026.

Xu, Q., Cobos, I., De La Cruz, E., Rubenstein, J.L., and Anderson, S.A. (2004). Origins of cortical interneuron subtypes. J Neurosci *24*, 2612-2622. 10.1523/JNEUROSCI.5667-03.2004.

Zaloshnja, E., Miller, T., Langlois, J.A., and Selassie, A.W. (2008). Prevalence of long-term disability from traumatic brain injury in the civilian population of the United States, 2005. J Head Trauma Rehabil *23*, 394-400. 10.1097/01.HTR.0000341435.52004.ac.

Zeisel, A., Muñoz-Manchado, A.B., Codeluppi, S., Lönnerberg, P., La Manno, G., Juréus, A., Marques, S., Munguba, H., He, L., Betsholtz, C., et al. (2015). Brain structure. Cell types in the mouse cortex and hippocampus revealed by single-cell RNA-seq. Science *347*, 1138-1142. 10.1126/science.aaa1934.

Zhang, W., Yamawaki, R., Wen, X., Uhl, J., Diaz, J., Prince, D.A., and Buckmaster, P.S. (2009). Surviving hilar somatostatin interneurons enlarge, sprout axons, and form new synapses with granule cells in a mouse model of temporal lobe epilepsy. J Neurosci *29*, 14247-14256. 10.1523/JNEUROSCI.3842-09.2009.

Zhao, S., Todorov, M.I., Cai, R., -Maskari, R.A., Steinke, H., Kemter, E., Mai, H., Rong, Z., Warmer, M., Stanic, K., et al. (2020). Cellular and Molecular Probing of Intact Human Organs. Cell *180*, 796-812.e719. 10.1016/j.cell.2020.01.030.

Zhao, Y., Flandin, P., Long, J.E., Cuesta, M.D., Westphal, H., and Rubenstein, J.L. (2008). Distinct molecular pathways for development of telencephalic interneuron subtypes revealed through analysis of Lhx6 mutants. J Comp Neurol *510*, 79-99. 10.1002/cne.21772.

Zheng, X., Salinas, K.J., Velez, D.X.F., Nakayama, T., Lin, X., Banerjee, D., Xu, X., and Gandhi, S.P. (2021). Host interneurons mediate plasticity reactivated by embryonic inhibitory cell transplantation in mouse visual cortex. Nat Commun *12*, 862. 10.1038/s41467-021-21097-4.

Zhu, B., Eom, J., and Hunt, R.F. (2019). Transplanted interneurons improve memory precision after traumatic brain injury. Nat Commun *10*, 5156. 10.1038/s41467-019-13170-w.

Zhu, H., Yan, H., Tang, N., Li, X., Pang, P., Li, H., Chen, W., Guo, Y., Shu, S., Cai, Y., et al. (2017). Impairments of spatial memory in an Alzheimer's disease model via degeneration of hippocampal cholinergic synapses. Nat Commun *8*, 1676. 10.1038/s41467-017-01943-0.

Zihl, J., and Kerkhoff, G. (1990). Foveal photopic and scotopic adaptation in patients with brain damage. *Clinical Vision Sciences 5*, 185-195.

Zimmerman, K.A., Laverse, E., Samra, R., Yanez Lopez, M., Jolly, A.E., Bourke, N.J., Graham, N.S.N., Patel, M.C., Hardy, J., Kemp, S., et al. (2021). White matter abnormalities in active elite adult rugby players. Brain Commun *3*, fcab133. 10.1093/braincomms/fcab133.

Zlokovic, B.V. (2008). The blood-brain barrier in health and chronic neurodegenerative disorders. Neuron *57*, 178-201. 10.1016/j.neuron.2008.01.003.

Zweckberger, K., Stoffel, M., Baethmann, A., and Plesnila, N. (2003). Effect of decompression craniotomy on increase of contusion volume and functional outcome after controlled cortical impact in mice. J Neurotrauma *20*, 1307-1314. 10.1089/089771503322686102.